



Journal of Science

Volume: 19, Issue: 1, Year: 2023

Contact

Manisa Celal Bayar University
Institute of Natural and Applied Sciences
Campus of Şehit Prof Dr İlhan Varank 45140 Yunusemre – MANİSA, TÜRKİYE
Tel: (00 90) 236 201 27 05
Fax: (00 90) 236 241 21 49
e-mail: cbujos@gmail.com
Web: <https://dergipark.org.tr/tr/pub/cbayarfbe>

“CBU Journal of Science is indexed by ULAKBIM-TUBITAK TR-DIZIN”



ISSN 1305-130X

E-ISSN 1305-1385

CBUJOS is published quarterly at Manisa Celal Bayar University Printing House

“CBU Journal of Science is a refereed scientific journal”



Celal Bayar University Journal of Science

Owner

Manisa Celal Bayar University,

Editors : Prof. Dr. Kamil ŞİRİN

Assoc. Prof. Dr.. Emine KEMİKLİOĞLU

Assistant Editor: Assoc. Prof. Dr. Mustafa AKYOL

Layout Editor & Secretary

Assoc. Prof. Dr. İlker Çetin KESKİN

International Scientific Advisory Board

Prof. Dr. Arianit REKA; State University of Tetova, Macedonia

Prof. Dr. Tomasz NIEMIEC; Warsaw University of Life Sciences, Poland

Prof. Dr. Alyani ISMAIL; Universiti Putra, Malaysia

Prof. Dr. Iuliana APRODU; Dunarea de Jos University, Romania

Assoc. Prof. Can BAYRAM; University of Illinois, USA

Assoc. Prof. Dr. Johanan Christian PRASANNA; Madras Christian College, South India

Assoc. Prof. Dr. Nouredine ISSAOUI; Université de Monastir, Tunisie.

Assoc. Dr. Edward Albert UECKERMANN; North-West University, South Africa

Assoc. Dr. Zhi-Qiang ZHANG; The University of Auckland, Holland

Assist. Prof. Dr. Young Ki KIM; Pohang University of Science and Technology, South Korea

Assist. Prof. Dr. Mona MIRHEYDARI; Rutgers University, USA

Assist. Prof. Dr. Donatella ALBANESE; Università Degli Studi Di Salerno, Italy

Assist. Prof. Dr. Jinghua JIANG; The University of Memphis, USA

Assist. Prof. Dr. Jens OLDELAND; University of Hamburg, Germany

Dr. Cheng CHENG; Apple Inc., USA

Dr. Sajedah AFGHAH; Microsoft Corporation, USA

Dr. Jinghua JIANG; The University of Memphis

National Scientific Advisory Board

Prof. Dr. Mustafa Ersöz; Selçuk University

Prof. Dr. Oğuz Gürsoy; Mehmet Akif University

Prof. Dr. Mehmet Çevik; İzmir Katip Çelebi University

Prof. Dr. Sezgin Çelik; Yıldız Teknik University

Prof. Dr. Osman Dayan; Çanakkale Onsekiz Mart University

Prof. Dr. Serdar İplikçi; Pamukkale University

Prof. Dr. Yasin Üst; Yıldız Teknik University

Prof. Dr. Mahmut Kuş; Konya Teknik University

Prof. Dr. Ertunç Gündüz; Hacettepe University

Prof. Dr. Tülin Aydemir; Manisa Celal Bayar University

Prof. Dr. Sezai Taşkın; Manisa Celal Bayar University

Prof. Dr. Fatma Şaşmaz Ören; Manisa Celal Bayar University

Prof. Dr. Fatih Selimefendigil; Manisa Celal Bayar University

Prof. Dr. Osman Çulha; Manisa Celal Bayar University

Prof. Dr. Ali Konuralp; Manisa Celal Bayar University

Prof. Dr. Erol Akpınar; Abant İzzet Baysal University

Prof. Dr. Ali Demir; Manisa Celal Bayar University

Prof. Dr. Serap Derman; Yıldız Teknik University

Prof. Dr. Hayati Mamur; Manisa Celal Bayar University

Assoc. Prof. Dr. Fatih Doğan; Çanakkale Onsekiz Mart University

Assoc. Prof. Dr. Yeliz Yıldırım; Ege University

Assoc. Prof. Dr. Özlem Çağındı; Manisa Celal Bayar University

Assoc. Prof. Dr. Mehmet Söylemez, Adıyaman University

Assoc. Prof. Dr. Nil Mansuroğlu; Ahi Evran University

Assist. Prof. Dr. Zeynep Çipiloğlu Yıldız; Manisa Celal Bayar University



CBU Journal of Science

Celal Bayar University Journal of Science (CBUJOS) covers scientific studies in the fields of Engineering and Science and publishes accounts of original research articles concerned with all aspects of experimental and theoretical studies. CBU Journal of Science is a refereed scientific journal published four times annually (March, June, September and December) by Institute of Natural and Applied Sciences of Manisa Celal Bayar University. CBU Journal of Science considers the original research articles written in English for evaluation.

CBU Journal of Science is indexed by TUBİTAK ULAKBİM TR-DİZİN, and also is included in DOAJ, Cite Factor, Journal TOCS, Advanced Science Index and OAJI databases. Digital Object Identifier (DOI) number will be assigned for all the articles being published in CBU Journal of Science.

Instructions for Authors and Article Template can be found on the main page of MCBU Institute of Natural and Applied Sciences (<http://fbe.cbu.edu.tr>)





Vol: 19, Issue: 1, Year: 2023

Contents

Research Article

Pages

Environmental and Economic Analysis of Bioenergy Production and Utilization in Adana Turkey DOI: 10.18466/cbayarfbe.1175413 Deniz Pesen, Görkem Gençay, Berrin Kurşun	1-10
Performance Comparison of PEGASIS, HEED and LEACH Protocols in Wireless Sensor Networks DOI: 10.18466/cbayarfbe.1165816 Kareem Hameed Ali, A. F. M. Shahan Shah	11-18
Determination of Optimal DC/AC Ratio for Grid-Connected Photovoltaic Systems DOI: 10.18466/cbayarfbe.1200284 Mehmet Fatih Beyoğlu, Metin Demirtaş	19-29
Tissue Mimicking Phantom Design and Characterization for Thermal Imaging Applications on Breast Cancer Diagnosis DOI: 10.18466/cbayarfbe.1176244 Zeynep Ayyıldız, İbrahim Akkaya, Mehmet Engin	31-37
Covid-19 Death and Case Numbers Forecasting with ARIMA and LSTM Models DOI: 10.18466/cbayarfbe.1070691 Büşra Çetin, Nida Gökçe Narin	39-46
Refraction simulation of nonlinear wave for Shallow Water-Like equation DOI: 10.18466/cbayarfbe.1145651 Murat Subaşı, Hülya Durur	47-52
Majority Vote Decision Fusion System to Assist Automated Identification of Vertebral Column Pathologies DOI: 10.18466/cbayarfbe.1082067 Akın Özçift, Mehmet Bozuyula	53-65
One-Step Fabrication of Silver Nanostructures Decorated Cu-Grid as an Ideal SERS Platform DOI: 10.18466/cbayarfbe.1170104 Menekşe Şakir	67-72
A Study on Total Phenolic and Flavonoid Content, Antioxidant, Toxicity, and Anthelmintic Activities of Methanol Extract of <i>Crocus cancellatus</i> subsp. <i>lycuis</i> DOI: 10.18466/cbayarfbe.1111317 Mehlika Alper, Mehmet Özgür Atay, Olcay Ceylan, Ramazan Mammadov	73-78
Adsorption behavior of methylene blue onto four different coffee residues DOI: 10.18466/cbayarfbe.1107088 Ecem Tekne, Yeliz Özüdoğru	79-85



Comparison of Microwave, Ultrasonic Bath and Homogenizer Extraction Methods on the Bioactive Molecules Content of Green Tea (*Camellia Sinensis*) Plant.

DOI: 10.18466/cbayarfbe.1169751

Hafize Dilek Tepe, Fatma Doyuk

87-95




An Approach For Determination of Risky Buildings And Building Energy Performance Concerning Urban Renewal In Türkiye

DOI: 10.18466/cbayarfbe.1108873

Ebru Alakavuk, Hande Odaman Kaya

97-106

Environmental and Economic Analysis of Bioenergy Production and Utilization in Adana Turkey

Deniz Pesen¹ , Görkem Gençay¹ , Berrin Kurşun^{1*} 

¹ Marmara University, Faculty of Engineering, Chemical Engineering, İstanbul, Türkiye

*berrin.kursun@marmara.edu.tr

* Orcid No: 0000-0002-2111-4416

Received: 15 September 2022

Accepted: 15 February 2023

DOI: 10.18466/cbayarfbe.1175413

Abstract

This work investigates the most feasible ways of processing biological wastes in Adana from energetic, environmental and economic points of view. Energetically, syngas constitutes 59% of bioenergy produced in Adana whereas biogas constitutes 41%. In total, 9.5×10^5 MWh electricity can be generated from bioenergy of which 5.6×10^5 MWh comes from syngas. Based on 2020 electricity consumption values, 13.3 % of electricity demand can be met by electricity generated from organic wastes. Substitution of Turkish grid electricity by the renewable electricity and prevention of organic waste decay provide 464 thousand and 391 thousand tons of GHG mitigation, respectively. Economically, utilization of certain agricultural wastes as animal feed instead of bioenergy resource appears as a more feasible option. 13.2 billion TL can be gained through sales of animal feed, renewable electricity and organic fertilizer in Adana and 9.25 billion TL of this gain is solely acquired from animal feed. This result confirms the feasibility of evaluating nutritious resources as feed instead of energy resource for syngas production through gasification. Hence, appropriate utilization of biological waste materials can make significant energetic, environmental and economic contributions to a region without creating competition with food or feed resources.

Keywords: Bioenergy production, economic feasibility, greenhouse gas (GHG) mitigation, renewable electricity generation,

1. Introduction

57.7 % of the electricity generation in Turkey for the year 2020 was realized from fossil fuels. Hard coal and natural gas that are imported constitute the majority of the utilized fossil fuels in electricity production. Share of the electricity generated from waste materials was only 1.87 % in the 2020 electricity mix [1]. Excluding hydropower, potentials of other renewable energy resources are underutilized in the country [2]. Electricity generation is responsible for 33% of the greenhouse gas (GHG) emitted in the country for the same year. Also, considering energy resource dependency of the country, it is crucial for Turkey to utilize her renewable energy potential to the fullest [1,3]. Furthermore, Turkey committed to reduce her CO₂ emissions in the ratio of 30% by 2030 under United Nations Framework on Climate Change (UNFCCC). Hence, utilizing her renewable energy resources can help meet this target [4].

Our work aims to evaluate potential and utilization pathways of bioenergy, one of the most promising renewable energy sources, in Adana Turkey. To be able

to place this work into context, available studies should be reviewed. The studies about bioenergy for Turkey cover several aspects. Policy issues hindering wider adoption of bioenergy [2,5,6], potential assessment for electricity and transportation fuel production from bioenergy [7-10], evaluation of energy crops' potential contribution on bioenergy production [11], impact of bioenergy production on ecosystem services [12] and general assessments of bioenergy production and potential from different resources are the aspects studied [13-18].

While evaluating potential of different renewable energy resources (RER) in Turkey, Baris et al conclude that bioenergy is the most feasible RER due to its social benefits including local job creation and clean energy access opportunity for rural communities. Policy wise, they emphasize the necessity of establishment of policies specific to each renewable energy because of different characteristics belonging to each energy type [2]. Kaygusuz [5] and Bahadır [6] point out that inclusion of stakeholder view and wishes, social impacts, local job creation potential, potential environmental impacts in

construction of policies is vital for wider adoption and success of bioenergy projects [5,6]. Potential assessment of bioenergy from animal and agricultural wastes to generate electricity is estimated by Rincon et al for Turkey. However, they did not consider municipal or forestry wastes in their analysis. Adana is found to be a resourceful location in generating electricity from the accounted biomass types and 0.3 million tons of waste potential is estimated for Adana per year [7]. Bilgili analyze electricity generation from biogas in Mediterranean region of Turkey. He concludes that 6.9% of the electricity demand can be met and 2.6 million tons of CO₂ emission reduction can be achieved in the region [8]. Akyürek reveals that 4.0x10¹⁰ MJ energy can be generated from biogas in Mediterranean [9]. Transportation fuel production potential of Turkey from biological materials is investigated by Emeksiz and Yuksel. They find that Turkey's biodiesel and bioethanol potentials are 1.67 and 13.5 million tons, respectively. However, the resources they evaluate are competing ones with feed and food at the same time such as soybean, sunflower, wheat and corn. Adana Province is also found to be a suitable location for biofuel production in this work [10]. Possible contribution of energy crops on bioenergy production based on shrub willows is assessed by Acar and Gokok. Alleviating the problem of competition with food or feed resources, energy crops are found to be "promising" resources for bioenergy production if grown suitably [11]. Deniz and Paletto analyze how the forest management styles and bioenergy production affect ecosystem services and environmental sustainability. The most negatively affected ecosystem services are found as soil protection and biodiversity. They analyze how these services can be protected by changes in forest management [12]. Lastly, bioenergy potential estimation from different feedstocks is made in numerous works [13-18]. Of those, biomethane (biogas) from animal wastes is estimated to provide 2.9%–3.3% of Turkey's natural gas usage [17]. And, Balat states that bioenergy can create 160 thousand jobs with 17 Mtoe technical potential in Turkey [18].

In this context, our work evaluates biogas and synthesis gas production from biological waste materials in Adana Province. Accounted wastes are agricultural, husbandry, forestry and municipal solid wastes produced in the city. Conversion of biogas and synthesis gas into electricity, utilization of certain agricultural wastes as animal feed instead of bioenergy resource, the resulting economic and environmental benefits are assessed. So, this article investigates most feasible ways of utilizing bio-waste by evaluating Adana Province as a case study. Hence, our work neither focuses on specific waste types nor only bioenergy production as the utilization option. And, the holistic assessment structure of the work is what makes it contribute and add to the existing literature. If this assessment performed specific to Adana is generalized to the whole country it can significantly contribute to the national bioenergy planning.

Organization of the article is that Section 2 presents background information about bioenergy production methods, the energy utilization and available waste materials in Adana. Methodology section presents assumptions and techniques utilized in the study calculations. Section 4 includes the assessment results and discussion followed by the main conclusions derived in the last section.

2. Background

2.1. Bioenergy Production Processes

2.1.1. Biogas Production

Biogas is produced through anaerobic digestion and process slurry can be utilized as organic fertilizer. Polysaccharides, proteins and fats in the organic waste are broken into simpler compounds through a sequence of reactions in O₂ free environment. As a result, CO₂ and CH₄ constitutes the main components of the product [19]. In biogas production, wastes that have high moisture content such as animal manures (bovine, ovine, poultry) and vegetable residues are mainly utilized. These feedstocks are more easily processed by the facultative bacteria performing the anaerobic digestion. This clean energy resource can be utilized in electricity generation, heating or transportation after upgrading [19,20]. Table 1 presents available compounds and their volumetric percentage ranges in biogas.

Table 1: Biogas constituents and their volumetric percentage ranges in the composition [19].

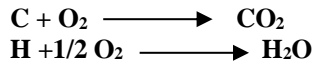
Biogas Constituents	Compound Formula	Volumetric Percentage
Methane	CH ₄	50-80
Hydrogen	H ₂	0-5
Carbon dioxide	CO ₂	20-50
Water	H ₂ O	0-1
Nitrogen	N ₂	0-3
Ammonia	NH ₃	Trace amount
Hydrogen sulfide	H ₂ S	Trace amount

2.1.2. Synthesis Gas (Syngas) Production

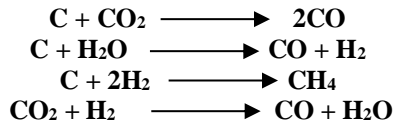
In essence biomass gasification is an incomplete combustion process where O₂ is utilized less than the stoichiometric ratio. Gasification process has 4 phases. Firstly, feedstock is dried to have moisture less than 15%. In following step pyrolysis, volatile organic compounds are evaporated with heat and carbonized compound are left. Carbon and hydrogen in the carbonized feed stock are oxidized in combustion also providing all heat for other process steps. Lastly, reduction takes place to produce mainly CO and H₂ [21]. Small amounts of CH₄ and H₂O are also available in syngas content. Syngas can be utilized in electricity generation as well as H₂ production for hydrogen fuel cells [21, 22].

The reactants and formed products in combustion and reduction zones are given below.

Combustion Zone



Reduction Zone



2.2. Adana Province

Adana has a very high bioenergy potential due to its geographical conditions and climate. It has an annual bio-waste amount of around 6.0 million tons and only 0.71million tons of this amount is processed in Adana Integrated Solid Waste Disposal Facility [23,24]. At the beginning of 2011, this facility that is owned by the ITC company and managed jointly with Adana Metropolitan Municipality started its operations. In the facility, domestic solid wastes of fifteen districts, commercial and institutional domestic solid wastes are sorted, composted and stored regularly, and medical wastes originating from hospitals, treatment and preventive health services are disposed of. The integrated facility consists of a mechanical separation and biomethanization system, a power generation facility, a medical waste sterilization facility and a sanitary landfill. On average, 1950 tons of solid waste collected from residential, commercial and institutional areas are processed daily [24]. Table 2 presents total amount of products and resulting bio-waste in Adana annually.

Table 2: Annual bio-waste quantities from different sources in Adana [23]. (TOE: Tons of oil equivalent)

Animal Type	Number	Waste Quantity (tons/year)	Economic Energy Equivalent (TOE/year)
Bovine	2.68x10 ⁵	2.07 x10 ⁶	4.23 x10 ³
Ovine	8.08 x10 ⁵	7.29 x10 ⁵	1.20 x10 ²
Poultry	7.25 x10 ⁶	2.22 x10 ⁵	4.10 x10 ⁴
Total	8.32 x10 ⁵	3.02 x10 ⁶	4.54 x10 ⁴
Plant Type	Amount (tons)	Waste Quantity (tons/year)	Economic Energy Equivalent (TOE/year)
Field	5.53 x10 ⁶	2.71 x10 ⁶	6.76 x10 ⁵
Garden	2.20 x10 ⁶	4.07E+04	1.75 x10 ⁴
Vegetable	1.72 x10 ⁶	5.93 x10 ⁵	1.78 x10 ⁵
Total	9.45 x10 ⁶	3.34 x10 ⁶	8.71 x10 ⁵
Forestry	NA	7.88 x10 ⁵	1.76 x10 ⁵
Municipal	NA	7.62 x10 ⁵	1.18 x10 ⁴

Around 68.5 % of the husbandry waste comes from bovines that also have the highest energy content. Field wastes constitutes the major part of the waste originating from plant material. Forestry and municipal wastes are almost equal in quantity while forestry wastes have higher energy content than municipal solid wastes [23]. Breakdown of municipal solid waste in Adana for the year 2019 is shown in Figure 1. Of the 762 thousand tons of municipal waste, 495 thousand tons (65%) are organic. 8% of wastes are of plastic while wastes that cannot be sorted (classified as other) constitute 23% of the whole [24].

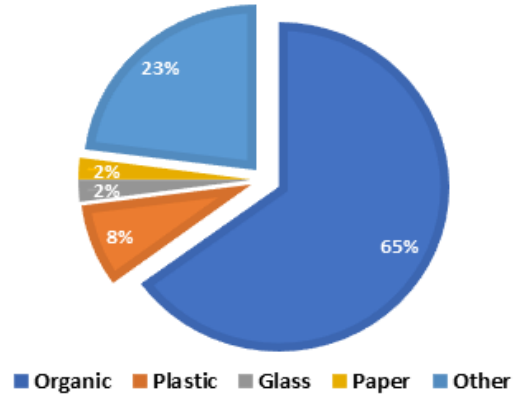


Figure 1: Breakdown of municipal waste in Adana [20].

Adana Province is the most populated city of Mediterranean region and the 6th largest city of Turkey. Beyond agricultural activities, it is also highly industrialized [24]. Hence, produced bioenergy can be utilized in several sectors increasing self-sufficiency of the city. Electricity and natural gas consumption quantities in Adana by different sectors in 2018, 2019 and 2020 are presented in Table 3 [25-30]. On average, 3% of Turkish electricity consumption realizes in Adana. When electricity and natural gas consumption data are analyzed, industrial and household sectors stand out as the main users of both energy resource.

3. Methodology

The scope of this work covers three main parts. The electricity that can be generated from biogas or syngas that are obtained from the waste material in Adana; GHG mitigation potential due to prevention of waste material decay, renewable electricity generation and chemical fertilizer replacement; lastly economic benefits of these activities are examined. This section presents the assumptions and calculation details utilized in our work.

3.1. Renewable Electricity Generation

Biomass energy potential atlas (BEPA) prepared by the General Directorate of Energy Affairs (GDEA) presents biomass energy potential at the country, city and district level sourcing from several biological waste material [23]. Waste data belonging to different biomass types in Adana were classified as suitable for biogas (anaerobic

Table 3: Annual electricity and natural gas consumption in Adana [25-30].

Electricity Consumption (MWh)						
Year	Lighting	Household	Industry	Irrigation	Commercial	Total
2020	1.22 x10 ⁵	1.98x10 ⁶	3.37 x10 ⁶	1.79 x10 ⁵	1.50 x10 ⁶	7.15 x10 ⁶
2019	1.23 x10 ⁵	1.80 x10 ⁶	3.09 x10 ⁶	1.61 x10 ⁵	1.58 x10 ⁶	6.75 x10 ⁶
2018	1.08 x10 ⁵	1.71 x10 ⁶	3.15 x10 ⁶	1.41 x10 ⁵	1.60 x10 ⁶	6.71 x10 ⁶
Natural Gas Consumption (Sm ³)						
Year	Conversion /Cycle	Industry	Service	Household	Other	Total
2020	7.38 x10 ⁷	3.32E+08	2.73 x10 ⁷	1.08 x10 ⁸	2.33 x10 ⁷	5.64 x10 ⁸
2019	7.67 x10 ⁷	2.48E+08	2.84 x10 ⁷	9.67 x10 ⁷	2.29 x10 ⁶	4.52 x10 ⁸
2018	3.17 x10 ⁷	2.83E+08	2.67 x10 ⁷	7.63 x10 ⁷	8.41 x10 ⁶	4.27 x10 ⁸

digestion) or syngas (gasification) production. Animal (bovine, ovine, poultry), vegetable and organic municipal wastes are evaluated as the wet waste types suitable for biogas production. On the other hand, dry wastes that cannot be efficiently used in anaerobic digestion are chosen to be used in syngas production.

3.1.1. Biogas Electricity

In biogas production from animal waste, biogas energy equivalences were readily available as data. Hence, direct conversion of biogas into electricity is calculated according to Equation 1, where j_i is the biogas energy content of waste in question and e_i is the efficiency factor. Energy efficiency for electricity generation from biogas ranges from 8% to 54%. Conversion of biogas into electricity with 31% average efficiency is accepted here [31]. Lastly, the electrical energy calculated in MJ has been converted into MWh electricity by dividing 3600 (1 MWh equals 3600 MJ).

$$E_j = \sum_1^i (j_i e_i) / 3600 \quad (1)$$

The annual average temperature in Adana is 19.2 °C and the annual minimum is 13.9 °C [32]. Because of its temperate climate and that mesophilic bacteria like this warm environment, 40% efficiency for biogas production is accepted in Adana [33]. For vegetable and organic municipal wastes, the economic calorific energy values given in TOE (tons of oil equivalent) units are converted to MJ (1 TOE equals 41840 MJ), multiplied by biogas (e_i) and electricity (c_i) efficiency factors and then converted to MWh as presented in Equation 2 [23].

$$E_w = \sum_1^i (41840 t_i e_i c_i / 3600) \quad (2)$$

3.1.2. Electricity from Syngas

The economic energy equivalents for plant, forest and dry organic municipal wastes suitable for gasification were converted from TOE to MJ [19]. For synthesis gas, the thermal efficiency is determined as 0.755. The syngas

equivalence was calculated by multiplying 0.755 by the economic energy equivalents in MJ unit. The electrical equivalence is calculated by multiplying the calculated syngas equivalences by using conversion factor of 0.30 [34]. The gasification electrical equivalence was calculated using Equation 3, where t_i is the thermal efficiency, c_i is the conversion factor and j_i is the calorific value of the feedstock in MJ.

$$E_c = \sum_1^i (j_i t_i W_i c_i) \quad (3)$$

3. Greenhouse Gas (GHG) Mitigation

3.1.3. Substitution of Grid Electricity by Renewable Electricity

When global warming potential (GWP) of the 2020 Turkish electricity mix is examined, GHG emissions of each resource in the mix and their corresponding shares are required. Table 4 presents the share and GWP of each energy resource in the 2020 Turkish electricity mix [1, 35,36]. GWP of 2020 mix is found as 494 g CO₂ eq/kWh when GWP of each resource is multiplied by its share in the mix and results are added up. However, the GWP of the electricity obtained from wastes alone is 4.10 g CO₂ eq/kWh [35,36].

In Equation 4, g_i is the coefficient found by subtracting GWP of waste electricity from the grid GWP value (494-4,1). Using equation 4, the magnitude of GHG emissions mitigated due to substitution of grid electricity by electricity generated from bio-waste is calculated.

$$GHGM_i = \sum_1^i (E_{w_i} g_i) \quad (4)$$

3.1.4. Prevention of Chemical Fertilizer Production

Utilization of the organic fertilizer produced in anaerobic digestion process replaces chemical fertilizer use needs and the GHG emissions due to chemical fertilizer production can be avoided. 0.03% of the weight of wet

vegetable waste and 0.051% of wet animal waste is N [37]. Therefore, wet waste amounts are multiplied by 0.3 and 0.51 and the amount of nitrogen in kg per ton of waste is found.

Table 4: Share and GWP potential of different resources in the Turkish electricity mix in 2020 [1,35,36].

Energy Resource	GWP (g CO ₂ eq/kWh)	Share in the Mix (%)
Hard Coal	1.06 x10 ³	22.14
Lignite	1.1310 ³	12.38
Natural Gas	4.9910 ²	23.14
Hydro (Reservoir)	8.30x10 ⁰	18.75
Hydro (Stream)	4.10 x10 ⁰	6.74
Wind	7.30 x10 ⁰	8.11
Waste	4.10 x10 ⁰	1.88
Geothermal	6.30 x10 ¹	3.28
Sun	2.95x10 ¹	3.58

In Table 6 section 2, the quantities of CO₂, CH₄, NO₂ emissions corresponding to 1 kg of nitrogen content in the waste are given in grams. In equation 5, m_i is the organic waste amount, N_i is the coefficient used to calculate the amount of nitrogen contained in the chemical fertilizer. Through Equation 5, the quantities of CO₂, CH₄, NO₂ emissions that are reduced by using organic fertilizer instead of chemical fertilizer are calculated.

$$GHGM_2 = \sum_1^i (m_i e_i N_i) \quad (5)$$

3.1.5. Prevention of Decay of Organic Wastes with Biogas Production.

Prevention of the GHG emissions due organic material decay creates a big opportunity for GHG mitigation as well as having a renewable energy source. Here, the dry weights of organic wastes are needed to calculate the amount of mitigated GHG emissions.

Table 5: Moisture and dry solid values utilized in biogas and electricity production efficiency calculations.

Inputs	Moisture	Dry Solid (d _i)	Ref.
Municipal Organic Wastes	89.0%	11.0%	[39]
Cow Dung	80.0%	20.0%	[40]
Chicken Manure	28.7%	71.3%	[41]
Vegetable Waste	89.0%	11.0%	[39]

Therefore, using the ratios in Table 5, dry weights of bovine, ovine, poultry, plant and organic municipal waste are calculated [39-41].

In Table 6 section 3, the GHG emissions due to decay of each organic material type are presented. Hence, these emissions are avoided by biogas production. Equation 6 stands for the calculation of the mitigated GHG emissions by organic fertilizer production where m_i is the amount of organic waste, d_i is dry solid content ratio, C_i is the grams of CO₂ emitted when 1 kg of dry feedstock decays.

$$GHGM_3 = \sum_1^i (m_i d_i C_i) \quad (6)$$

Table 6: GHG coefficients utilized in calculations.

GHG Mitigation Sources	Turkey Energy Mix (gCO ₂ /kWh)	Ref.
1. Fossil fuel sourced electricity replacement	494	[35,36]
2. Chemical fertilizer replacement	g/kg of N	
CO ₂	3200	[38]
CH ₄	3.1	[38]
NO ₂	18	[38]
3. Organic Waste Processed	g CO ₂ /kg of dry feedstock (C _i)	
Organic Municipal Wastes	420	[42]
Cow Dung	447	[40]
Chicken Manure	447	[41]
Vegetable Waste	420	[42]

3.2. Economic Assessment

3.2.1. Animal Feed

Majority of the agricultural wastes are burned in Adana. The economic return of using these nutritious wastes as animal feed instead of burning is particularly important. By using the current feed prices in 2022 [43-45], the financial value of the feed is calculated by multiplying the quantity by the unit price for each feed type as presented in Table 7. Although these dry feedstocks could have been used to produce syngas and from syngas electricity, utilizing them as animal feed is determined to be more feasible for Adana's economy.

3.2.2. Sales of Generated Renewable Electricity

The active energy unit price for electricity that is being sold to the grid before transmission is determined to be 0.78919 TL/kWh [46]. In the light of this information, the income that can be obtained from electricity is calculated by multiplying the unit price with the amount of electricity as shown in Equation 7. Here, u_i is the unit

price of electricity in 2022 and E_i electricity generated in kWh.

$$EG_1 = \sum_1^i (E_i u_i) \quad (7)$$

Table 7: Amounts of nutritious wastes in Adana and their market value in 2022 [43-45].

Plant	Waste Amount (tons)	Feed Price (TL/ton)
Barley	11837	4100
Safflower	151.50	65000
Sunflower	406270	3750
Wheat	681905	3500
Rye	200.80	1750
Rapeseed	36.800	5000
Corn	1011240	4150
Cotton	220408	4000
Potato	43815	3000
Sugar Beet	1021.2	1000
Sesame	2581.5	26875
Triticale	249.60	1750
Oat	33.6	1900

3.2.3. Sales Revenue of the Organic Fertilizer Produced

Solid and liquid organic fertilizers are produced as byproducts of anaerobic digestion process. The liquid portion is determined to be given free as an incentive in return for the cooperation of the farmers in collecting the waste and delivering it to the facility. 50-75% of the dry weight of organic waste is converted into solid organic fertilizer in biogas production [47]. In this study, 62.5% conversion is accepted. The calculation of the total amount of organic fertilizer obtained is given in Equation 8. Here, f_i is the coefficient used to calculate how much of the organic waste is converted into solid organic fertilizer.

$$O_f = \sum_1^i (m_i f_i) \quad (8)$$

The price of a ton of organic fertilizer varies between 500 and 800 dollars in 2022 [48]. It has a value above the average market price for chemical fertilizers since the organic fertilizer produced will be completely composed of biological content without mixed chemicals. Since the municipality will be selling this fertilizer, it has been decided to sell 1 ton of organic fertilizer for \$400 at a subsidized price. The exchange rate was taken as 14.5 TL/\$ to convert US Dollar to Turkish Lira as presented in Equation 9. Here, l_i is the coefficient representing the unit price of one ton of organic solid fertilizer, b_i is exchange rate between TL to \$.

$$EG_2 = \sum_1^i O_f l_i b_i \quad (9)$$

4. Results and Discussion

4.1. Electricity Generation

Although dry weights of the wastes suitable for biogas production are more than that of the wastes suitable for syngas production (0.82 versus 0.54 million ton) in Adana, higher conversion efficiency of waste to syngas transformation produces more energy than waste to biogas transformation. Hence, syngas constitutes 59% of the energy in electricity generation whereas biogas constitutes 41% (6.7×10^9 MJ syngas versus 4.5×10^9 MJ biogas). Rincon et al. [7] estimate 0.3-2.65 million tons of bio-waste availability per year for Adana Province. Our 1.36 (0.84 and 0.54) million tons of bio-waste calculation is well in accordance with this range. Furthermore, Akyurek [9] calculates biogas energy potential of Adana Province as 1.1×10^{10} MJ per year. 4.5×10^9 MJ biogas potential we calculate is lower than this value since some wastes are dedicated to animal feed and syngas production as more feasible utilization paths in our work.

The electricity generated from different waste resources in Adana can be seen in Figure 2. Animal, plant and municipal wastes are utilized to produce biogas. Dry wastes such as shells of nuts, forest residues are utilized in syngas production through gasification. High energy content of the waste material gasified produces substantial amount of syngas resulting in being the dominant source of energy in renewable electricity generation. A total of 9.5×10^5 MWh electricity is generated from the waste material of which 5.6×10^5 MWh is generated from syngas followed by plant waste sourced biogas. Results show that the electricity generated from waste material can meet 13.3 % of the electricity demand in Adana based on 2020 consumption and production values. Bilgili [8] finds that biogas sourced electricity can meet 6.9% of the electricity demand in Mediterranean Region also stating that Adana is the city with highest bioenergy potential of the region. Hence, 13.3 % meeting ratio for Adana can be explained by Adana's high bioenergy potential and additional syngas production.

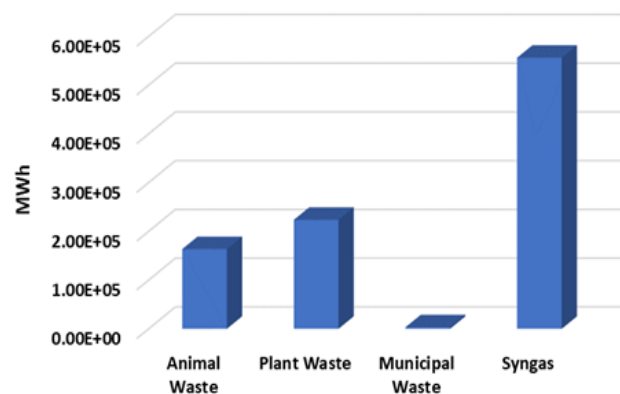


Figure 2: Electricity generation from different organic wastes in Adana Province.

4.2. GHG Mitigation

Figure 3 shows the comparison of nitrogen content of the waste material types. The animal originated organic waste contains more nitrogen than the plant and municipal wastes, proportionally. Bovine waste contains the highest quantity of nitrogen due to both high waste amount and nitrogen content. However, since the amount of plant waste is significantly higher than that of poultry waste, plant waste contains more nitrogen than poultry waste in absolute terms. The nitrogen content of wastes is important in GHG emissions during the course of biological material decay.

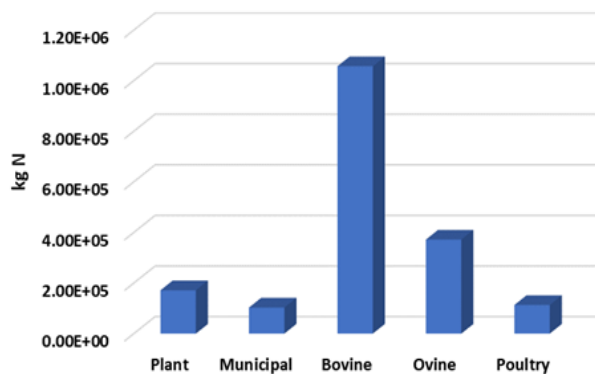


Figure 3: Nitrogen content comparison of different organic waste types in Adana Province.

Turkish electricity grid has a GWP of 494 g CO₂ eq/kWh for the year 2020. Substitution of the grid electricity by the renewable electricity generated from the wastes in Adana results in 464 thousand tons of CO₂ eq. GHG emission mitigation as can be seen in Figure 4. This makes the renewable electricity the major source of GHG emission reduction followed by the avoided emissions due to organic waste decay and chemical fertilizer production. 391 thousand tons of GHG can be avoided due to the prevention of biological waste decay in Adana.

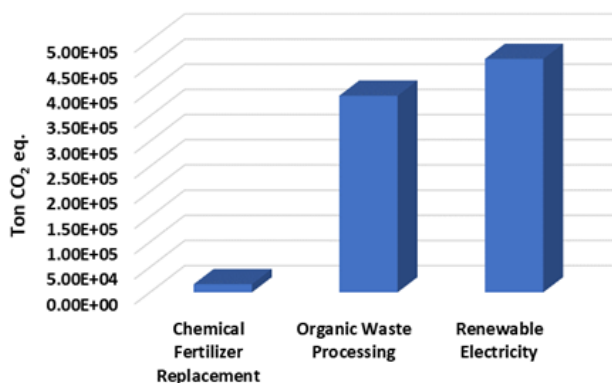


Figure 4: GHG mitigation from different resources in Adana Province.

Bilgili [8] and Akyurek [9] estimate 2.65 and 27.0 million tons of CO₂ emission prevention for Mediterranean region due to substitution of the grid electricity and coal sourced electricity by the electricity from biogas. Akyurek's [9] high result is due to substitution of coal (energy source with the highest GHG emission). 464 thousand tons of GHG mitigation due to grid electricity substitution and 1.01 tons of total GHG mitigation results for Adana are then in harmony with their results.

4.3. Economic Gain

Figure 5 presents the economic benefits acquired from different sales. High level of agricultural activity and the resulting nutritious waste that can be used as animal feed becomes the major source of income gained from the waste material in Adana. Organic fertilizer produced as a by-product of anaerobic digestion together with biogas is sold at a price of 400\$/ton and provides 3.3 billion TL income at an exchange rate of 14.5 TL/\$. Although the renewable electricity is the major GHG reducing factor, the least economic benefit is gained from the renewable electricity sales with 0.79 TL/kWh unit price. Totally, these sales can provide 13.2 billion TL to Adana's economy of which 9.25 billion TL solely comes from the animal feed sales. This result confirms the feasibility of evaluating resources given in Table 6 as feed instead of energy resource for syngas production through gasification.

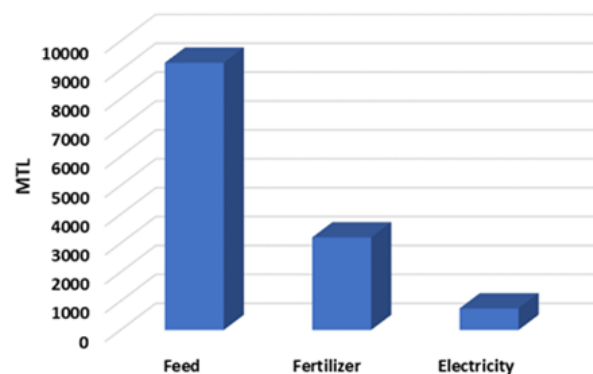


Figure 5: Economic gain from different resources in Adana.

Economic gain acquired from biomass reported in literature depends on utilization pathways and assumptions of the works as well as the value of currency at the time of each study. Hence, stating a robust value is not feasible. However, Balat [18] points that bioenergy can create 160000 jobs in Turkey and can make significant contribution to the economy. That bioenergy has significant economic potential is also the main result of other studies [7, 8, 9] which is also in accordance with our result.

5. Conclusions

This work investigates the bioenergy potential of Adana Province from biological waste materials that are the by-products of agricultural, husbandry, forestry activities and also including municipal organic wastes. Conversion of these materials into biogas and synthesis gas and then into electricity is studied from energetic point of view. Study scope also covers utilization of certain agricultural wastes as animal feed instead of bioenergy resource. Furthermore, the economic and environmental benefits of these interventions are assessed. Hence, our work investigates the most feasible ways of utilizing bio-waste by evaluating Adana Province as a case study. As a result, generalizing this holistic assessment to the whole country can significantly contribute to the national bioenergy planning of Turkey.

Energetically, syngas constitutes 59% of the bioenergy produced whereas the remaining 41% is biogas from 1.36 million tons of biomass in Adana, annually. This situation is due to the higher conversion efficiency of waste to syngas transformation process that produces more energy than waste to biogas transformation. 1.36 million bio-waste amount calculated for Adana is well in accordance with Rincon et al.'s [7] 0.3-2.65 million tons of bio-waste availability estimation range for the city. Although lower biogas potential of 4.5×10^9 MJ than Akyurek's [9] 1.1×10^{10} MJ of biogas estimation is calculated here. This can be explained by dedication of some wastes to animal feed and syngas production as more feasible utilization paths in our work.

Based on 2020 electricity consumption values in Adana, 13.3 % of electricity demand can be met by the electricity generated from organic wastes. This higher ratio than Bilgili's [8] 6.9 % estimation for Mediterranean can be explained by Adana's high bioenergy potential and additional syngas production.

Substitution of Turkish grid electricity mainly generated from fossil resources by the renewable electricity generated from waste in Adana results in 464 thousand tons of CO₂ eq. GHG emission mitigation. This makes the renewable electricity the major source of GHG emission reduction for the city. Nitrogen content is important in GHG emissions during the course of biological material decay. Processing of biological wastes creates a great opportunity for GHG mitigation as well as having a clean and renewable energy resource. In Adana, bovine wastes are found to have the highest quantity of N content and 391 thousand tons of GHG can be avoided due to prevention of biological waste decay in Adana. Also, 1.01 tons of total GHG mitigation calculated for Adana is determined to be in harmony with literature values.

Economically, 13.2 billion TL can be gained through sales of animal feed, renewable electricity and organic fertilizer. 9.25 billion TL of this gain is solely acquired

from animal feed. This result confirms the feasibility of evaluating nutritious resources given in Table 6 as feed instead of energy resource for syngas production through gasification. Organic fertilizer that is a by-product of biogas production contributes 3.3 billion TL to Adana's economy and the least economic benefit is gained from the renewable electricity sales. That bioenergy has significant economic potential is the main result of many studies [7, 8, 9, 18] which is also in accordance with what we conclude economically.

All in all, this work reveals that appropriate utilization of biological waste materials can make significant energetic, environmental and economic contributions to a region without creating competition with food or feed resources.

Author's Contributions

Deniz Pesen: Performed study calculations under supervision of Dr. Berrin Kurşun and drafted the manuscript.

Görkem Gençay: Performed study calculations under supervision of Dr. Berrin Kurşun and drafted the manuscript.

Berrin Kurşun: Supervised the study, rewrote and edited the manuscript.

Ethics

There are no ethical issues after the publication of this manuscript.

References

- [1]. Turkish Electricity Transmission Corporation (TEIAS), Turkish electricity production and transmission statistics. <https://www.teias.gov.tr/tr-TR/turkiye-elektrik-uretim-iletim-istatistikleri> (accessed 06.05. 2022).
- [2]. Baris K, Kucukali, S. 2012. Availability of renewable energy sources in Turkey: Current situation, potential, government policies and the EU perspective. *Energy Policy*: 42:377-391.
- [3]. Organization for Economic Co-operation and Development (OECD), Greenhouse gas emissions. https://stats.oecd.org/Index.aspx?DataSetCode=AIR_GHG (accessed 26.03.2022).
- [4]. United Nations Climate Change, Republic of Turkey intended nationally determined contribution. https://www4.unfccc.int/sites/submissions/INDC/Published%20Documents/Turkey/1/The_INDC_of_TURKEY_v.15.19.30.pdf (accessed 27.10. 2021).
- [5]. Kaygusuz K, Keleş S. 2012. Sustainable bioenergy policies in Turkey. *Journal of Engineering Research and Applied Science*: 1(1): 34-43.
- [6]. Bahadır A, Keleş S, Kaygusuz K. 2013. Bioenergy potential, utilization and policies in Turkey. *Journal of Engineering Research and Applied Science*: 2(2): 167-183.
- [7]. Rincon L, Puri M, Kojakovic A. 2019. The contribution of sustainable bioenergy to renewable electricity generation in Turkey:

- Evidence based policy from an integrated energy and agriculture approach. *Energy Policy*; 130: 69-88.
- [8]. Bilgili ME.2022. Exploitable potential of biomass energy in electrical energy production in the Mediterranean Region of Turkey. *Journal of Agricultural Sciences*; 28 (4): 666 – 676.
- [9]. Akyurek Z. 2019. Energy recovery and greenhouse gas emission reduction potential of bio-waste in the Mediterranean Region of Turkey. *El-Cezeri Journal of Science and Engineering*; 6(3): 482-490.
- [10]. Emeksiz C, Yuksel A. 2022. A suitable site selection for sustainable bioenergy production facility by using hybrid multi-criteria-decision making approach, case study: Turkey. *Fuel*; 315: 123214.
- [11]. Acar P, Gokok E. 2021. Promising resources for bioenergy: shrub willows of Turkey. *Bioenergy Studies*; 2(1): 7-17.
- [12]. Deniz T, Paletto A. 2018. Effects of bioenergy production on environmental sustainability: a preliminary study based on expert opinions in Italy and Turkey. *Journal of Forestry Research*; 29: 1611–1626.
- [13]. Erdogdu E (2008). An exposé of bioenergy and its potential and utilization in Turkey. *Energy Policy*, 36(6): 2182-2190.
- [14]. Ozturk M, Sabab N, Altay V et al., 201). Biomass and bioenergy: An overview of the development potential in Turkey and Malaysia. *Renewable and Sustainable Energy Reviews*, 79:1285-1302.
- [15]. Bilgen S, Keles S, Sarikaya I et al. 2015. A perspective for potential and technology of bioenergy in Turkey: Present case and future view. *Renewable and Sustainable Energy Reviews*; 48:228-239.
- [16]. Gulsen H, Yenigun I. 2021. Investigation of origin plant and animal bioenergy capacity for Turkey. *Periodicals of Engineering and Natural Sciences*; 9(2): 339-346.
- [17]. Melikoglu M, Menekse ZK. 2020. Forecasting Turkey's cattle and sheep manure based biomethane potentials till 2026. *Biomass and Bioenergy*; 132: 105440.
- [18]. Balat M. 2005. Use of biomass sources for energy in Turkey and a view to biomass potential. *Biomass and Bioenergy*; 29 (1): 32-41.
- [19]. Khanal SK. *Anaerobic Biotechnology for Bioenergy Production*. Wiley-Blackwell. Ames, Iowa, 2008; pp 301.
- [20]. Fırat Kalkınma Ajansı, Biyogaz. https://fka.gov.tr/sharepoint/userfiles/Icerik_Dosya_Ekleri/FKA_ARA_STIRMA_RAPORLARI/B%C4%B0YOGAZ.pdf (accessed 24.08.2022).
- [21]. Rajvanshi AK. Biomass gasification. In: Gaswami DY eds. *Alternative Energy in Agriculture*. CRC Press, 1986; Vol II:83-102.
- [22]. Reed TB, Das A. *Handbook of Biomass Downdraft Gasifier Engine Systems*. United States Department of Energy. Golden, Colorado, 1988; 148 pp.
- [23]. General Directorate of Energy Affairs (GDEA), Biomass energy potential atlas (BEPa). <https://bepa.enerji.gov.tr/> (accessed 02.03.2022)
- [24]. Adana Çevre ve Şehircilik İl Müdürlüğü , Adana ili 2019 yılı çevre durum raporu. https://webdosya.csb.gov.tr/db/ced/icerikler/adana_-2019_-cdr-20201023092541.pdf. (accessed 02.03.2022).
- [25]. Enerji Piyasası Düzenleme Kurumu. Elektrik piyasası, 2020 yılı piyasa gelişim raporu . <http://epdk.gov.tr/Detay/Icerik/3-0-0-102/yillik-rapor-elektrik-piyasasi-gelisim-raporlari> (accessed 26.03.2022).
- [26]. Enerji Piyasası Düzenleme Kurumu, Elektrik piyasası, 2019 yılı piyasa gelişim raporu. Available at: <http://epdk.gov.tr/Detay/Icerik/3-0-0-102/yillik-rapor-elektrik-piyasasi-gelisim-raporlari> (accessed 26.03.2022).
- [27]. Enerji Piyasası Düzenleme Kurumu, Elektrik piyasası, 2018 yılı piyasa gelişim raporu. <http://epdk.gov.tr/Detay/Icerik/3-0-0-102/yillik-rapor-elektrik-piyasasi-gelisim-raporlari> (accessed 26.03.2022).
- [28]. Enerji Piyasası Düzenleme Kurumu, Doğal gaz piyasası 2020 yılı sektör raporu. <https://www.epdk.gov.tr/Detay/Icerik/3-0-94/dogal-gaz-yillik-sektor-raporu> (accessed 26.03.2022).
- [29]. Enerji Piyasası Düzenleme Kurumu, Doğal gaz piyasası 2019 yılı sektör raporu. <https://www.epdk.gov.tr/Detay/Icerik/3-0-94/dogal-gaz-yillik-sektor-raporu> (accessed 26.03.2022).
- [30]. Enerji Piyasası Düzenleme Kurumu, Doğal gaz piyasası 2018 yılı sektör raporu. <https://www.epdk.gov.tr/Detay/Icerik/3-0-94/dogal-gaz-yillik-sektor-raporu> (accessed 26.03.2022).
- [31]. Hakawatia R, Smyth BM, McCullough G et al. 2017. What is the most energy efficient route for biogas utilization: heat, electricity or transport. *Applied Energy*; 206: 1076–1087.
- [32]. Turkish State Meteorological Service, Seasonal averages belonging to cities-adana. <https://www.mgm.gov.tr/veridegerlendirme/il-ve-ilceler-istatistik.aspx?m=ADANA> (accessed 26.07.2022).
- [33]. Freitas FF, De Souza SS, Ferreira LRA et al. 2019. The Brazilian market of distributed biogas generation: Overview, technological development and case study. *Renewable and Sustainable Energy Reviews*; 101: 146-157.
- [34]. Chhiti, Y, Kemiha, M. 2013. Thermal conversion of biomass, pyrolysis and gasification. *International Journal of Engineering and Science*; 2(3): 75-85.
- [35]. Kursun B. 2022. Role of solar power in shifting the Turkish electricity sector towards sustainability. *The Clean Energy Journal*; 6(2):1078–1089.
- [36]. Atilgan B, Azapagic A. 2016. An integrated life cycle sustainability assessment of electricity generation in Turkey. *Energy Policy*; 93: 168-186.
- [37]. Türkiye Cumhuriyeti Sanayi ve Teknoloji Bakanlığı, Kimyasal gübre ve azot bileşiklerinin imalatı sektörü kaynak verimliliği rehberi, <https://www.ahika.gov.tr/assets/upload/dosyalar/kimyasalgubreveazot-bilesiklerininimalatirehberi.pdf> (accessed 26.07.2022).
- [38]. Börjesson, P, Berglund M. 2007. Environmental systems analysis of biogas systems—Part II: The environmental impact of replacing various reference systems. *Biomass and Bioenergy*; 31: 326–344.
- [39]. Bouallagui H, Cheikh RB, Marouani L et al. 2003. Mesophilic biogas production from fruit and vegetable waste in a tubular digester. *Bioresource Technology*; 86 :85–89.
- [40]. Hao X, Chang C, Larney FJ et al., G.R. 2001. Greenhouse gas emissions during cattle feedlot manure composting. *Journal of Environmental Quality*; 30: 376–386.
- [41]. Oliveira MO, Somariva R, Ando Junior OH et al. Biomass Electricity Generation Using Industry Poultry waste, International Conference on Renewable Energies and Power Quality (ICREPQ'12) Santiago de Compostela (Spain), 2012, pp. 1650-1654.
- [42]. Lou XF, Nair J. 2009. The impact of landfilling and composting on greenhouse gas emissions – A review. *Bioresource Technology*; 100: 3792–3798.
- [43]. Aybak Tarım, Feed prices 2022. <http://aybaktarim.com/fiyatlarimiz/>(accessed 26.07.2022).



[44]. Turkish Grain Board. Barley, wheat, rye, oat prices. <https://www.tmo.gov.tr/hububat/1/bugday-arpabr-cavdar-yulaf> (accessed 26.07.2022).

[45]. Kırklareli Provincial Directorate of Agriculture and Forestry, Announced beet purchases for Alpullu sugar factory 2022-2023 production year. <https://kirkclareli.tarimorman.gov.tr/Haber/1978/Alpullu-Seker-Fabrikasi-2022-2023-Uretim-Yili-Pancar-Alim-Fiyatlarini-Acikladi> (accessed 26.07.2022).

[46]. Enerji Atlası, 2022 electricity prices. <https://www.enerjiatlası.com/elektrik-fiyatları/> (accessed 26.07.2022).

[47]. Kursun B. Towards Design of Sustainable Energy Systems in Developing Countries: Centralized and Localized Options, Ph. D, The Ohio State University, Ohio, 2013; pp 362.

[48]. Made-in-China, Organic fertilizer for plant 100% water soluble humic and amino acid with good price. <https://xsvagri.en.made-in-china.com/product/IOUTQJFYFDpl/China-Organic-Fertilizer-for-Plant-100-Water-Soluble-Humic-and-Amino-Acid-with-Good-Price.html> (accessed 26.07.2022).

Performance Comparison of PEGASIS, HEED and LEACH Protocols in Wireless Sensor Networks

Kareem Hameed Ali¹ , A. F. M. Shahan Shah^{2*} 

¹ Istanbul Gelisim University, Department of Electrical and Electronics Engineering, Istanbul, Türkiye
^{2,*} Yildiz Technical University, Department of the Electronics and Communication Engineering, Istanbul, Türkiye

* shah@yildiz.edu.tr

* Orcid No: 0000-0002-3133-6557

Received: 23 August 2022

Accepted: 02 March 2023

DOI: 10.18466/cbayarfbe.1165816

Abstract

Wireless sensor networks (WSNs) is one of the most emerging and fastest growing fields in the scientific world. The most widely recognized requirement related with sensor network configuration is that sensor hubs have restricted energy spending plans. Typically, when a sensor node's battery cannot be replaced or recharged, its low battery power becomes a serious problem. The efficient use of energy source in a sensor node is a desirable criterion for scalability and prolonging the lifetime of WSN. Therefore, designing an efficient routing protocol for reducing energy consumption is one of the important issues in the network. A large number of routing protocols have been proposed in the last few decades. Some of the most popular and energy efficient routing protocols are hierarchical routing protocols like LEACH (Low Energy Adaptive Clustering Hierarchy), PEGASIS (Power Efficient GATHERing in Sensor Information Systems), and HEED (Hybrid Energy Efficient Distributed clustering protocol). In this paper, these hierarchical routing protocols are studied for their pros and cons. Finally, a comparative study on these protocols is done based on several metrics such as: energy consumption, stability period, scalability, and network lifetime through simulations on different simulation environments.

Keywords: HEED, LEACH, PEGASIS, Routing Protocol, WSN.

1. Introduction

The super distant association, known as the "Sound Surveillance System (SOSUS)," was made by the United States military during the 1950s to perceive and follow Soviet submarines. This association used brought down acoustic sensors known as hydrophones that were spread across the Atlantic and Pacific oceans [1]. This distinguishing advancement is at this point elaborate today in extra serene applications like noticing undersea untamed life and volcanic activity. Up until 1980, the United States Defense Advanced Research Projects Agency (DARPA) started research in wireless sensor networks (WSNs) known as "Circulated Sensor Networks (DSN)" to officially investigate the difficulties in executing disseminated WSNs. DSNs were assumed to have a large number of spatially distributed low-cost sensing nodes that collaborated and operated autonomously, with information being sent to the appropriate node for use. Coordinated effort with colleges, for example, Carnegie Mellon University and the Massachusetts Institute of Technology Lincoln Labs

permitted DSNs to be incorporated into the scholarly community. Regardless of its uncertainty at that point, WSN innovation immediately tracked down a home in scholarly world and non-military personnel logical exploration [2].

Late headways in semiconductor, systems administration, and material science advancements empower the far reaching sending of enormous scope in WSNs. Together, these innovations have empowered another age of WSNs that offer huge benefits over remote organizations created 5 to quite a while back. Then again, the utilization of Wireless Sensor Networks has detonated in late many years and is as yet developing at a disturbing rate. This is impacting the manner in which we live, as individuals depend on remote network in an ever increasing number of parts of their regular routines [3].

WSNs are comprised of countless sensor hubs that are battery-controlled and have restricted memory as well as correspondence and calculation capacities. WSN

applications are partitioned into two sorts: occasion discovery (ED) and spatial interaction assessment (SPE) [4]. Sensors are conveyed in ED to distinguish an occasion like a backwoods fire, tremor, and so on, while in SPE, WSN plans to screen actual peculiarities like temperature, pressure, etc for a given Region of Interest (ROI). Due to the large number of uses covered by WSN, sensor network execution measurements are rigorously application explicit.. WSNs can work in unattended unforbearing conditions where human mediation is unsafe, wasteful, and here and there unimaginable [5]. Thus, "network lifetime" has turned into a typical presentation metric for practically all WSN applications. The expression "network lifetime" alludes to the time after which an organization becomes inoperable. The hidden WSN's non-usefulness is likewise application subordinate, as a matter of fact [6].

Energy effective steering algorithm [11-13] can be ordered as follows: information driven routing [14] calculation, area based directing calculation [5] and progressive directing calculation [15]. Information driven steering calculation utilizes meta information to track down the course from source to objective before any genuine information transmission to dispose of repetitive information transmission Location based directing calculation requires real area data for each sensor hub. Various levelled steering algorithm [15] separates the organization into bunches. Cluster head (CH) is chosen in each bunch. CH [16] gathers information from its individuals, totals the information and ships off sink. This approach is energy proficient however generally complex than different methodologies.

Recent advancements in wireless technology have resulted in the creation of mobile wireless sensor networks. Aside from sensor mobility, sensors in the network are low-cost and have a limited battery life. They are more material with regards to the central attributes of these organizations [7]. These organizations have an assortment of uses, including search and salvage tasks, wellbeing and ecological observing, and canny traffic signal frameworks. As per the application necessities, portable remote sensor hubs are energy restricted gear, so saving energy is quite possibly the main issues in the plan of these organization. Alongside each of the difficulties brought about by the versatility of the sensor hubs, we can note to the directing and dynamic grouping [9]. Concentrates on show that group models, which have customizable boundaries have critical effect in limiting energy utilization and broaden the lifetime of the organization. Subsequently, the principal objective of this examination is to present and choose the shrewd way involving transformative calculations for grouping in portable remote sensor networks for expanding Lifetime of the Network and right conveyance of bundles [8].

Considering the design issues in WSNs and the sheer number of protocols available to tackle them, it is very difficult to find a routing protocol which suits a specific purpose or fulfills certain requirements with better results as compared to other protocols [9].

Moreover, there are many surveys such as [6], [7] and [8] on energy-efficient hierarchical routing protocols analyzing their strengths and weakness depending upon their implementation, but none of them focused on their performance in energy-efficiency and prolonging network lifetime for large scale WSNs. That is, the scalability of a network is also an important criterion in deciding which routing protocol is more energy-efficient than the other [18].

This motivated us to work on this study where we select three known hierarchical routing protocols, LEACH, PEGASIS and HEED and do a simulation for 100 to 1000 nodes over a network area of (100 X 100) to (1000 X 1000) square meters and compare them on metrics such as load balancing, average energy consumption and lifetime of the network [19]-[20].

The rest of the article is arranged in this manner: Section 2 confers material and method. In Section 3, results and discussion are presented. Finally, the paper wraps up in Section 4.

2. Materials and Methods

Wireless sensor networks (WSN) play an important role in today's world. It is a useful technology for sending and receiving data from various parts of the system via mini sensor nodes spread across a large area. These nodes can perform a variety of data operations such as sensing the environment, gathering and processing data, and so on. The batteries embedded in these nodes provide the necessary energy for these processes. In many applications, sensor nodes are small and equipped with a small, low-energy battery. It is critical to reduce energy consumption and extend the network's lifetime as much as possible [9]. The contributions of this study can be expressed as

- Our work includes simulation of network for various simulation parameters such as number of nodes, network area, initial energy, location of base station, crossover distance, electronics energy per bit, aggregation energy per bit, and length of packets.
- Then we simulated the LEACH, PEGASIS and HEED as directed in their original paper and ran these protocols over the above-mentioned simulated network.
- We then, stored the statistics such as residual energy of network per round, dead nodes per round, average residual energy of a node per round, variance of residual energy per round for each protocol in different simulation environments.

- Finally, the conclusion was drawn after analyzing the statistics obtained by plotting the graphs for each protocol after every simulation.

2.1. LEACH Protocol

LEACH is a straightforward TDMA-based steering convention utilized in WSNs and is one of the most established and first various levelled conventions. Heinzelman (W. R. Heinzelman et al. 2000) proposed it in the year 2000. This group-based convention arose as an energy-proficient correspondence convention for remote miniature sensor networks that utilizations randomized revolution of nearby bunch base stations known as group heads to appropriate energy load consistently among sensor hubs in the organization. The essential elements of LEACH are:

- For the setup and operation of clusters, localized control and coordination.
- The cluster heads and related clusters are rotated randomly.
- To decrease global communication, use local compression.

Filter (S. Lindsey, et al. 2002) is a various levelled directing convention that is ordinarily utilized in WSNs. The idea proposed in LEACH has enlivened the advancement of a few comparable various levelled steering conventions. Sensor hubs in LEACH put together themselves as nearby groups, with one hub going about as the Cluster Head (CH) and different hubs as straightforward individuals from that bunch. Drain utilizes randomized group head pivot to appropriate energy utilization uniformly among hubs. The bunch heads get information from their group individuals and total it to lessen the quantity of messages shipped off the Base Station (BS). In each round, the sensor hubs freely choose themselves as group heads with a foreordained likelihood. To decrease above in group head foundation, every hub pursues a political race choice that is autonomous of different hubs. The organization runtime is separated into adjusts. In each round, every hub chooses an irregular worth somewhere in the range of '0' and '1'. Assuming the arbitrary worth is not exactly the ongoing round's limit, the hub turns into the group head:

$$T(n) = \begin{cases} \frac{p}{1-p(r \bmod \frac{1}{p})} & \text{if } n \in G \\ 0 & \text{otherwise} \end{cases} \quad (1)$$

where n addresses the given hub, p addresses the predefined level of hubs that can be bunch heads, r addresses the ongoing round, and G addresses the arrangement of hubs that didn't become group heads in the past $1/p$ adjusts. Drain's execution time is separated into adjusts.

2.2. PEGASIS Protocol

The convention PEGASIS was supportive of presented by Lindsey and Raghavendra [70] in which a chain of sensor hubs is framed and every hub discusses just with its nearby neighbours. Only one selected node delivers data to the BS; otherwise, data is sent from node to node. The leader node in charge of transmission switches every round. Either the BS determines the chain's creation, or the nodes themselves use a greedy method to do it. Each node collects data from its neighbor during data collection and transfers it to the next neighboring node after fusing it with the data it has already collected. The sensor nodes die out at random areas to strengthen the system. By switching the data transmission leader in each communication cycle, this is accomplished.

2.3. HEED Protocol

The essential presumption in HEED is that every sensor hub is fit for controlling its transmission power level however they are area un-mindful. It was proposed by Younis and Fahmy [16] in 2004, this method was created as a disseminated and energy proficient group development. Notice utilizes a blend of two unique boundaries for CH determination for example remaining energy of every hub and hub degree. A hub can be chosen as a CH relying upon its lingering energy along with some likelihood. The group arrangement happens when different hubs in the organization pick their separate CHs keeping up with least expense of correspondence. The fundamental goal of HEED is to draw out network lifetime as well as supporting versatile information conglomeration.

The two clustering parameters which are used in the algorithm are Residual Energy of the node as a primary parameter and Intra Cluster Communication Cost as a secondary parameter. Higher the residual energy of the node, higher the probability of that node to become a cluster head (CH).

3. Results and Discussion

Today, the greater part of the exploration is done to create super low fueled WSN which is just conceivable provided that the general organization lifetime increments, energy utilization [16] diminishes and the organization run with high security and unwavering quality. To accomplish this, numerous calculations have been executed. They are called energy-productive calculations. These calculations in their fundamental structure have previously been carried out on different organization conventions including LEACH, PEGASIS, HEED and so on. Be that as it may, these calculations need further examination for expansion in network lifetime, energy productivity and so forth. So, the proposed algorithm is one of the energy productive conventions intended to build the organization lifetime.

3.1. Experiment Results

The simulation of LEACH, PEGASIS and HEED was done in MATLAB. Some simulation plots has been shown in Figures 1, 2 and 3. Here, we are going to describe some of the important aspects of the simulation like assumptions, simulation parameters, simulation network environments and energy dissipation model. Table 1 represent simulation parameters.

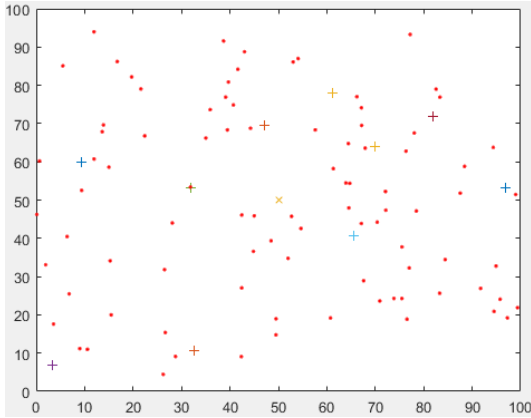


Figure 1. LEACH plot for 100 nodes at round 1334, dead nodes 20, cluster heads 6.

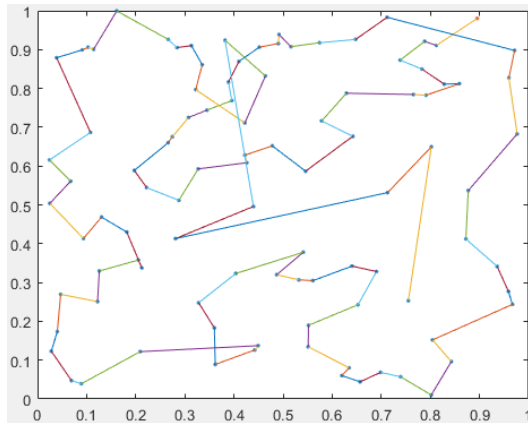


Figure 2. Chain formation in PEGASIS for 20 nodes.

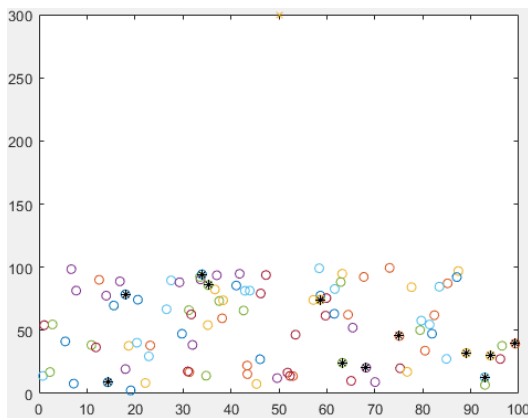


Figure 3. Chain formation in HEED for 20 nodes.

Table 1. The simulation parameters.

Simulation Parameters	Values
E_{elec} (Electronics energy loss per bit)	50 nJ
E_{fs} (Free space energy loss per bit per m^2)	10 pJ
E_{mp} (Multi-path fading energy loss per bit per m^4)	0.0013 pJ
E_{aggr} (Data Aggregation energy loss per bit)	5 nJ
Packet length (bits)	2000
P (Desired fraction of cluster heads in LEACH)	0.05
P_{min} (Minimum probability to be a cluster head in HEED)	5×10^{-4}
C_{prob} (Initial probability to be a cluster head in HEED)	0.05

3.1.1. Radio Energy Dissipation Model

Remote correspondence is the primary piece of energy dispersal in WSN. The energy dissemination model utilized in our re-enactment is displayed in Figure 4 [21] and is depicted beneath in Eq. 2. Depending on the distance between the transmitter and the receiver, the effective radio energy dissipation model employed both the free space (d^2 power loss) and the multipath fading (d^4 power loss) channel models. The free space model is employed if the distance is below a certain threshold, d_0 ; otherwise, the multipath model is used. The energy required to send a message of length k across a distance d is shown. Additionally, we expect that the radio divert is symmetric in nature for example energy expected to send a parcel from hub A to hub B will be equivalent to energy expected to send a bundle of same length from hub B to hub A.

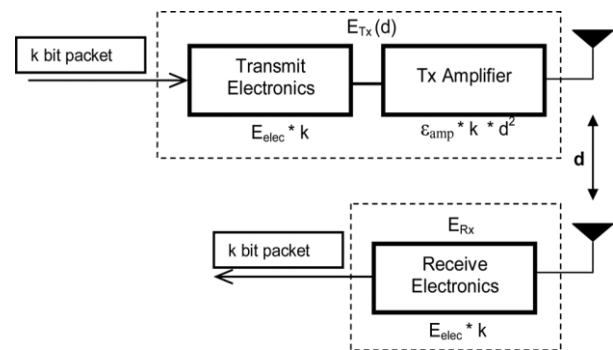


Figure 4. Radio Energy Dissipation Model in WSN [21].

The energy cost of transmission (E_{Tx}) is given as [16]

$$E_{Tx} = \begin{cases} k * E_{elec} + E_{fs} * d^2 & \text{if } d \leq d_0 \\ k * E_{elec} + E_{mp} * d^2 & \text{if } d \geq d_0 \end{cases} \quad (2)$$

Here, 'k' is packet length in bits, 'Elect' is the electronics energy loss per bit, 'd' is the distance up to which the data has to be transferred, 'Efs' is the free space energy loss per bit per m^2 , 'Emp' is the multi-path fading energy loss per bit per m^4 , and d_0 is the crossover distance which is defined as [16]

$$d_0 = \sqrt{\frac{E_{fs}}{E_{mp}}} \quad (3)$$

Therefore, depending upon the transmission distance, both the free space (E_{fs}) and multi-path fading (E_{mp}) models are used in our energy dissipation model. The energy cost for reception (E_{Rx}) is given as [16]

$$E_{Rx} = k * E_{elec} \quad (4)$$

Here, 'Elect' is the electronics energy loss per bit. The energy cost for data aggregation (E_{agg}) is given as [16]

$$E_{agg} = k * E_{da} \quad (5)$$

Here, 'E_{da}' is the data aggregation energy loss per bit.

3.2. Result Analysis

The simulation results obtained from the 4 network environments shows the overall relative behavior of LEACH, PEGASIS and HEED and is compared on metrics such as load balancing, network lifetime, energy consumption, and scalability. The Table 2 shows a summarized result of nodes death and the number of rounds of each protocol in each environment for comparing their behavior.

Table 2. Dead Nodes vs. Number of Round.

Environment No.	Protocols	No. of rounds		
		First Node Dies	Half Node Dies	Last Node Dies
Env.:1	LEACH	1165	1611	2209
	PEGASIS	1877	2090	2362
	HEED	207	947	2384
Env.:2	LEACH	255	669	1729
	PEGASIS	1236	2663	3600
	HEED	63	498	1867
Env.:3	LEACH	22	114	432
	PEGASIS	507	1919	3412
	HEED	6	192	673
Env.:4	LEACH	1	17	80
	PEGASIS	1	324	882
	HEED	1	59	236

3.3. Graph Plots of LEACH, PEGASIS and HEED

The graph plots obtained from the simulation describes the performance of each protocol in the simulated environment and can be interpreted on the following metrics:

Figure 5, 6, 7 and 8 shows the graph of each protocol in the 4 environments. Each figure has 4 sub plots describing the total energy, dead nodes, average energy and variance of nodes energy in the network vs. number of rounds of protocol operations.

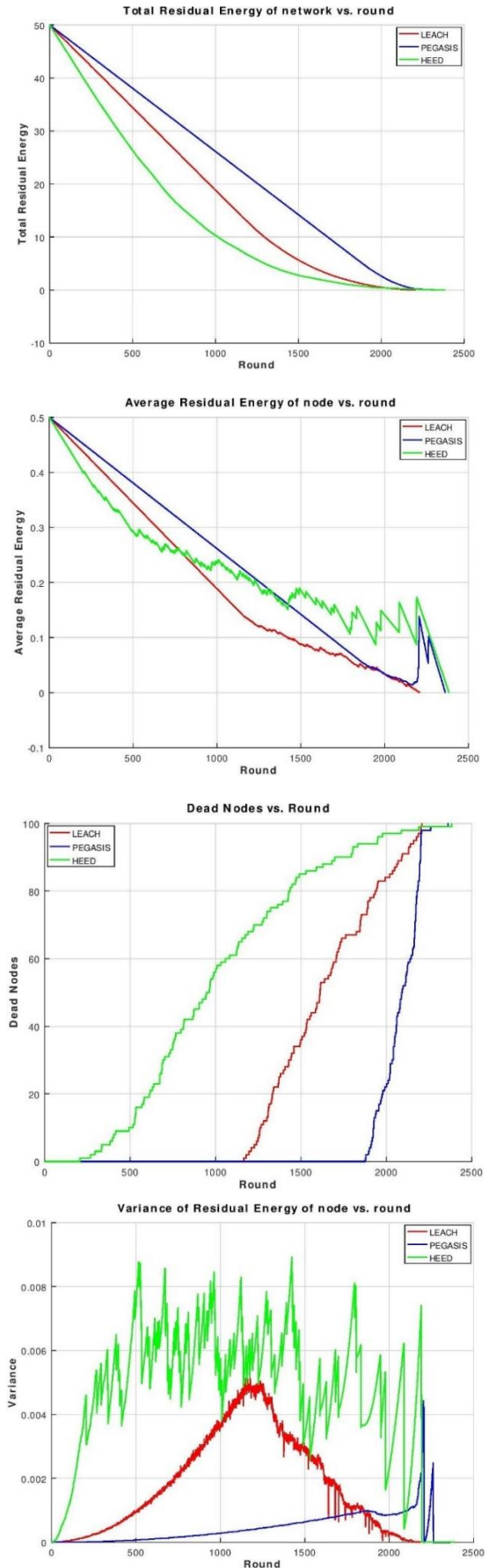


Figure 5. Graphs for Environment: 1

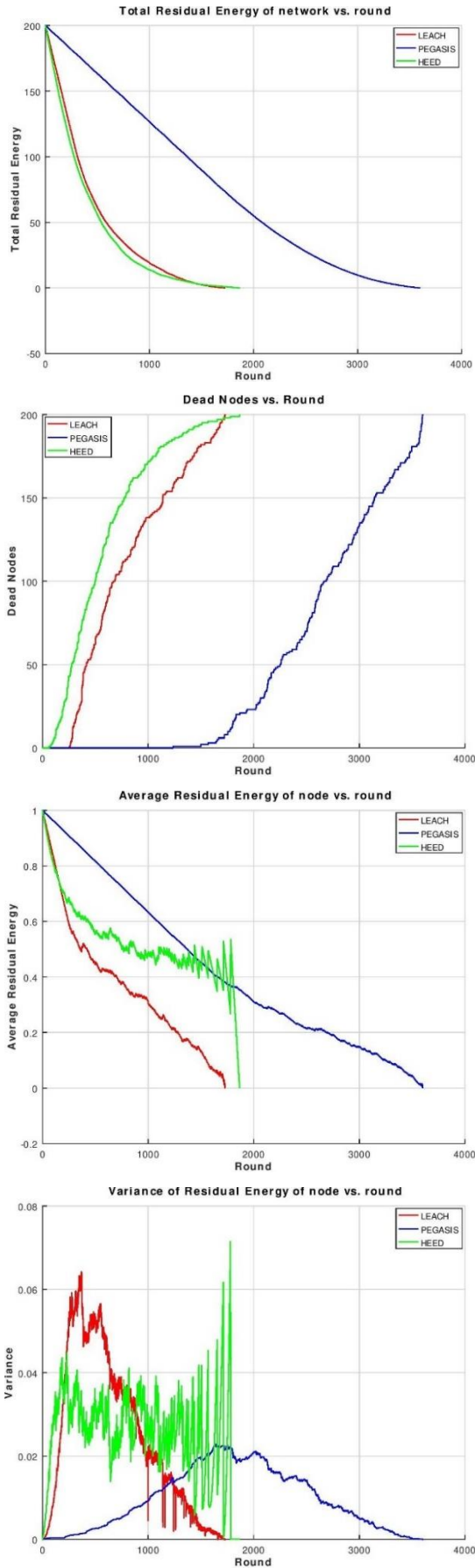


Figure 6. Graphs for Environment: 2

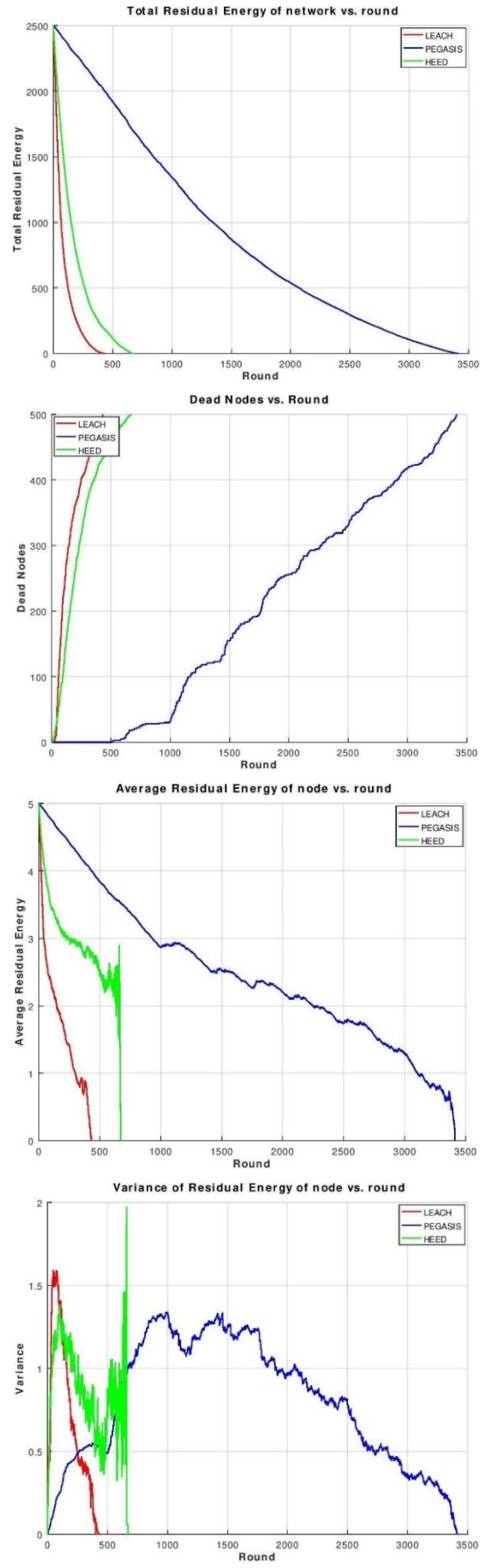


Figure 7. Graphs for Environment: 3

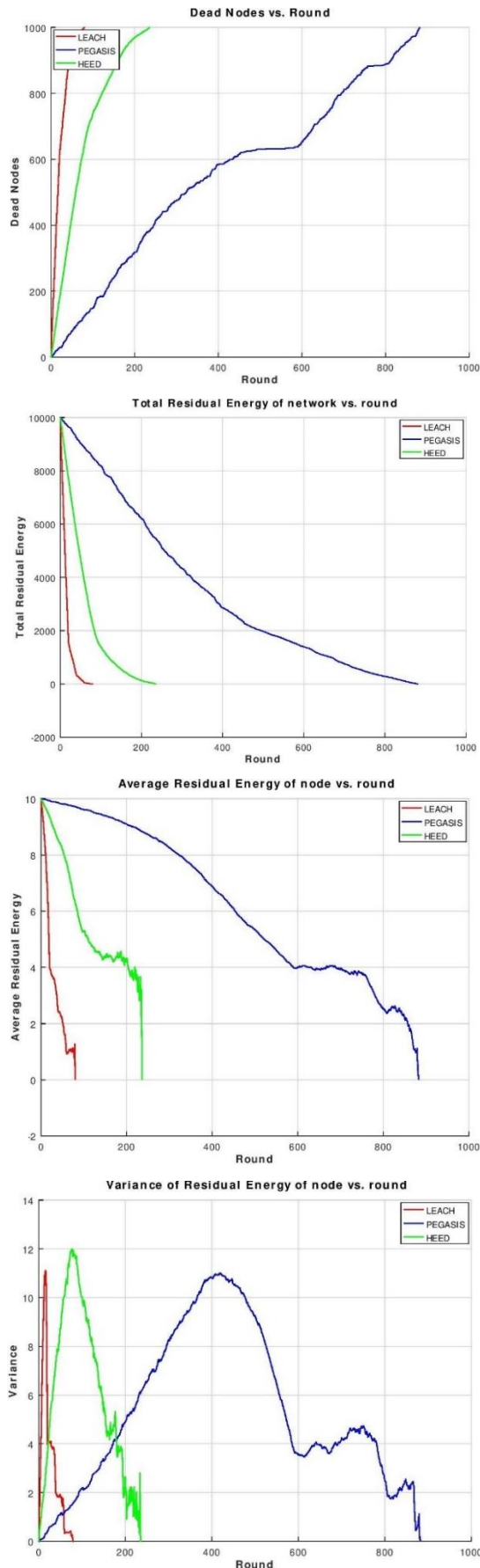


Figure 8. Graphs for Environment: 4

The graph plots obtained from the simulation describes the performance of each protocol in the simulated environment and can be interpreted on the following metrics:

Energy Consumption: The higher the total residual energy of the network for any protocol at any given round, the lower the energy consumption and higher the energy efficiency of the protocol. From the sub plots of Total Residual Energy vs. Round, we can observe that the PEGASIS residual energy curve is above the other two curves in every environment, even when the size of network was increased to 1000 nodes and the network area to 1000 X 1000 m², so it is highly energy efficient as compared to other two protocols. LEACH on the other hand is better than HEED for smaller network like Environment 1 and 2 but, as the network size increases, HEED becomes better than LEACH as we can observe in graph plots of Environment 3 and 4.

Load Balancing: Load balancing in WSN [9] is the act of balancing the network traffic load on the entire network such that most of the nodes survive longer and consume similar amount of energy in transferring of data from one point to the other. From the sub plots of Average Residual Energy vs. Round and the Variance of the Nodes Residual Energy vs. Round, we can observe that the average residual energy of the nodes at any given round is higher in PEGASIS and the variation in each nodes' residual energy is lower, than in LEACH and HEED in every environment i.e. PEGASIS balances the network load better than other two protocols in every environment.

Stability Period: It is defined as the number of rounds from the starting round after which the first node dies [11]. For many applications, the stability period should be higher to cover the entire network for most of the rounds to get better quality of service from the network. From the data shown in table 1 and the sub plots of Dead Nodes vs. Round of each environment, we can observe that the stability period of PEGASIS is far better than the other two protocols.

Network Lifetime: It is defined as the total number of rounds for which the protocol runs until the last node dies [16]. From the sub plots Dead Nodes vs. Round in every graph, we can observe that PEGASIS has the highest network lifetime, followed by HEED and the lowest network lifetime is for LEACH in every environment.

4. Conclusion

This paper presents a comparative study among LEACH, PEGASIS, and HEED protocols. From the simulation results, it is noticeable that PEGASIS is a highly energy-efficient protocol as compared to LEACH and HEED when scalability is also one of the factors or

design issues of WSN. This is because PEGASIS has two main objectives. First, reduce the power required by each node to transmit data per round by using collaborative techniques and spread the power draining uniformly over all nodes. Second, permit just neighborhood coordination between hubs that are near one another so the transmission capacity consumed in correspondence is diminished. Hence, PEGASIS performs better on all the metrics in consideration i.e., load balancing, stability period, network lifetime, and scalability. Furthermore, WSN routing protocol is still a vast field of research and a more scalable and energy-efficient protocol is needed for data gathering in WSNs which includes future research work.

Author's Contributions

Kareem Hameed Ali: Conducted the experiment and result analysis, and then drafted and prepared the article.
A. F. M. Shahen Shah: Assisted and supervised the study, as well as helped in manuscript preparation.



Ethics

After this manuscript's publication, there are no ethical concerns.

References

- [1]. M.A. Matin and M.M. Islam. Overview of wireless sensor network. In Mohammad A. Matin, editor, *Wireless Sensor Networks*, chapter 1. *Intech Open, Rijeka*, 2012. doi: 10.5772/49376.
- [2]. Noman Shabbir and Syed Rizwan Hassan. Routing protocols for wireless sensor networks (wsns). In Philip Sallis, editor, *Wireless Sensor Networks*, chapter 2. *IntechOpen, Rijeka*, 2017. doi: 10.5772/intechopen.70208.
- [3]. H. Guyennet M. Hadjila and M. Feham. A chain-based routing protocol to maximize the lifetime of wireless sensor networks. *Wireless Sensor Network*, 5(5):116–120, 2013. doi: 10.4236/wsn.2013.55014.
- [4]. S. Lindsey and C. S. Raghavendra. Pegasus: Power-efficient gathering in sensor information systems. In *Proceedings, IEEE Aerospace Conference*, volume 3, pages 3–3, March 2002.
- [5]. A. H. Abdulaal, A. F. M. S. Shah, and S. K. Pathan, "NM-LEACH: A Novel Modified LEACH Protocol to Improve Performance in WSN," in *International Journal of Communication Networks and Information Security (IJCNIS)*, vol. 14, no. 1, pp. 1 - 10, April 2022.
- [6]. Bhanu Pratap Singh Jyoti Singh and Subhadra Bose Shaw. A survey on leach-based hierarchical routing protocols in wireless sensor networks. *International Journal of Engineering Research & Technology (IJERT)*, 3(6), JUNE 2014. ISSN 2278-0181.
- [7]. Ali Newaz Bahar Shamim Sardar, Angona Sarker. Hierarchical routing protocol in wireless sensor network a survey. *International Journal of Scientific & Engineering Research*, 6(2), FEB 2015. ISSN 2229-5518.
- [8]. A.E. Narayanan, C.Narmadha, P.Marichamy. A survey on hierarchical-based routing protocols for wireless sensor networks. *International Journal of Pure and Applied Mathematics*, 119(16), 2018. ISSN 663-3676.
- [9]. Yuanchang Zhong, Lin Cheng, Liang Zhang, Yongduan Song, and Hamid Reza Karimi. Energy-efficient routing control algorithm in large-scale wsn for water environment monitoring with application to three gorges reservoir area. *The Scientific World Journal*, 2014:9, 2014. doi: 10.1155/2014/802915.
- [10]. Pu-Tai Yang and Seokcheon Lee. A distributed reclustering hierarchy routing protocol using social welfare in wireless sensor networks. *International Journal of Distributed Sensor Networks*, 8(4), 2012.
- [11]. Georgios Smaragdakis, Ibrahim Matta, and Azer Bestavros. Sep: A stable election protocol for clustered heterogeneous wireless sensor networks. 2004.
- [12]. Li Qing, Qingxin Zhu, and Mingwen Wang. Design of a distributed energy-efficient clustering algorithm for heterogeneous wireless sensor networks. *Computer Communications*, 29(12):2230 – 2237, 2006. ISSN 0140-3664.
- [13]. Satish Kannale Gaikwad Ranjitkumar Sharnappa and Vireshkumar Swamy. Enhanced leach multipath based energy efficient routing for wireless sensor network. *International Journal of Advanced Research in Computer and Communication Engineering*, 4(6):6, 2015. ISSN 2278-1021.
- [14]. D. Dudgeon and R.Mersereau. In *Multidimensional Digital Signal Processing*, chapter 6. Prentice-Hall,Inc., 1984.
- [15]. C.Reed D.Chen K.Yao, R.Hudson and F. Lorenzelli. Blind beamforming on a randomly distributed sensor array system. In *Proceedings of SiPS*, Oct 1998.
- [16]. O. Younis and S. Fahmy. Heed: a hybrid, energy-efficient, distributed clustering approach for ad hoc sensor networks. *IEEE Transactions on Mobile Computing*, 3(4): 366–379, Oct 2004. ISSN 1536-1233.
- [17]. Dong, Q. and W. Dargie. 2013. A survey on mobility and mobilityaware MAC protocols in wireless sensor networks. *IEEE communications surveys & tutorials*. 15(1): 88-100.
- [18]. Migabo, M.E., K. Djouani, A.M. Kurien and T.O. Olwal.2015. Gradient-based Routing for Energy Consumption Balance in Multiple Sinks-based Wireless Sensor Networks. *Procedia Computer Science*. 63: 488-493.
- [19]. Mazinani, S.M. and M. Safari. 2015. Secure Localization Approach in Wireless Sensor Network. *International Journal of Machine Learning and Computing*. 5(6).
- [20]. Migabo, M.E., K. Djouani, A.M. Kurien and T.O. Olwal.2015. Gradient-based Routing for Energy Consumption Balance in Multiple Sinks-based Wireless Sensor Networks. *Procedia Computer Science*. 63: 488-493.
- [21]. M. Razzaq, G. -R. Kwon and S. Shin. Energy efficient Dijkstra-based weighted sum minimization routing protocol for WSN. in *IEEE Third International Conference on Fog and Mobile Edge Computing (FMEC)*, Barcelona, Spain, 2018, pp. 246-251.

Determination of Optimal DC/AC Ratio for Grid-Connected Photovoltaic Systems

Mehmet Fatih Beyoğlu^{1*} , Metin Demirtaş¹ 

¹ Department of Electrical and Electronics Engineering, Balıkesir University, Balıkesir, Türkiye

* fatih.beyoglu@baun.edu.tr

* Orcid No: 0000-0001-8092-7014

Received: 08 November 2022

Accepted: 02 March 2023

DOI: 10.18466/cbayarfbe.1200284

Abstract

Suitability evaluation of a location for solar power generation plant installation requires long-term measurements and calculations. The correct calculation of the project power and energy production values of the solar power plant (SPP) is very important as it directly affects the payback period of the project cost. The effect of the DC/AC ratio used in an inverter selection is a crucial parameter in determining the sizing of SPP. In this study, a model was used to find the closest estimation values. Irradiance values coming to SPP in Balıkesir/Turkey were simulated and DC energy at the inverter input was calculated. The results obtained from the calculation were compared with actual production values. To determine the optimum DC/AC ratio of the existing installed SPP system, calculations were made with two different methods. Estimation of energy production values is calculated for different angles and different DC/AC ratios of inverters. It is vital that the SPP consists of two groups with different directions and the same capacities in terms of comparing the accuracy of the calculation. Energy production calculations, including the hourly meteorological data and catalog values of the system in the developed model, are desired to provide the closest prediction values for energy production of the real system. The optimum DC/AC ratio also varies depending on the coordinates, direction and angle of the PV system. As a result, it has been observed that the direction and location of the PV system affect the selection of inverter power. Thus, it is important to calculate this ratio for efficient working conditions of each system. Optimal values of ratios and efficiencies for Groups 1 and 2 are calculated as 1.28, 1.35, 91.55% and 90.62%, respectively.

Keywords: Clipping, DC/AC ratio, Grid, Performance analysis, Sizing ratio, Solar energy

1. Introduction

Solar energy, one of the most important renewable energy generation sources, is a safe, clean, free, non-polluting and endless energy source. The efficiency of PV systems depends on several climatic factors, such as solar irradiance, ambient temperature and the state of solar panels such as their age and soiling.

For the specified coordinates, the irradiance coming to the surface can be calculated by considering the motion of the earth around the sun and sun angle during the day, the slope and direction angle mounted solar panel system. Karafil et al. [1] examined the effects of panel inclination angle on energy production in Bilecik province. Rustemli et al. [2] compared the solar energy system with a solar tracking system and fixed mounting. Beyoglu [3] compared energy productions of fixed and 2-axis tracking photovoltaic solar energy systems in Balıkesir

province. Beyoglu et al. [4] compared different energy production estimation programs with the actual energy production data of the solar power plant (SPP) established in Balıkesir province. Abot [5] studied calculating sun angles for any time and location using MATLAB code. After that he analyzed the pattern of solar angles and the solar path. Jazayeri et al. [6] studied a simulation model to calculate the sun's position and the incidence angle of sunlight beams on the surface of PV modules with mounted any slope angle and location on the Earth. Demoulias [7] developed a new and simple analytical method to calculate the optimum inverter size for grid-connected PV plants anywhere. Wang et al. [8] introduced the optimum sizing ratio of photovoltaic (PV) array capacity and compared it to the nominal inverter input capacity. The optimum ratio was determined by empirical and analytical approaches. Faranda et al. [9] presented an analytical formulation for annual DC power production by analyzing available solar irradiance data

for some selected locations. A general efficiency characteristic curve fitted for different solar inverter types, using approximated function. A new analytical method is proposed to estimate the optimal size of PV plants from energy production. Pandey et al. [10] presented a new method to calculate inverter power clipping loss because of an oversized PV array, in other words, a high DC/AC ratio. Camps et al. [11] studied a new approach to the experimental validation of the optimal PV to inverter sizing ratio value for the energy yield maximization of an on-grid PV system. They used a custom workbench to simulate a solar array for different technical configurations and environmental data. Azzolini et al. [12] evaluated the expected curtailment associated with Volt-VAr control. Yearlong quasi-static time-series (QSTS) simulations were conducted on a realistic distribution feeder under various PV system design considerations. Overall, this paper found that the amount of curtailed energy is low (<0.55%) when compared to the total PV energy production in a year. Notton et al. [13] studied an optimal sizing methodology based on an energy approach. This method applied on-grid photovoltaic systems and used PV module technology and slope, the inverter type and the location information. Fernandez et al. [14] proposed the use of a fuzzy system evaluating a feature space extracted from the daily power production profile of a photovoltaic solar plant. The fuzzy system proposed is able to detect inverter power-limiting situations, as well as stages where the photovoltaic solar plant is showing steady-state power production. Deschamps et al. [15] studied to perform and analyze the optimum inverter sizing for large-scale on-grid solar photovoltaic. The solar irradiance distribution is analyzed and its potential effects on inverter sizing were performed. Balfour et al. [16] described how performance problems could be "masked" or not readily evident by several causes, PV system configuration, instrumentation design, installation, maintenance, contract clauses, identified management and operational practices. A simple method based on a duration curve is introduced to overcome shortcomings of performance ratio based on nameplate capacity and performance index based on hourly simulation when quantifying masking effects. Inverter clipping and pyranometer soiling were presented as two examples of the new method. Zidane et al. [17] aimed to select the optimum inverter size for large-scale on-grid PV power plants based on the several possible combinations of PV array and inverter. Choi [18] studied the effect of installation location on PV inverter lifetime and DC/AC ratio. Khatib et al. [19] studied a simple iterative method to optimize the inverter size for an on-grid photovoltaic system. The developing models are used hourly solar irradiance and ambient temperature data of the PV systems. Moreover, an optimized inverter and a conventionally sized inverter are compared in this study. In another study, Khatib et al. [20] used the iterative method for optimizing inverter size on five solar power plants in Malaysia. DC/AC ratio was optimized at

different load levels using different commercial inverters models.

In this study, the effects of the DC/AC ratio, which is irradiance a determining parameter in the inverter selection, in the sizing of an SPP were investigated. The incoming irradiance values of a power plant in Balıkesir/Turkey were used to calculate DC energy at the inverter input. The calculation results were compared with the real production values and compatible. The energy productions of PV plants installed at different angles and different inverter powers have been compared. To determine the optimum DC/AC ratio of the existing installed SPP system, calculations were made with two different methods to compare the simulation results.

In this program, the energy production calculations were made using real meteorology data, considering the location of the system, the mounting angle and catalog values. Turkish State Meteorological Service (TSMS) data were used as meteorological data. It was observed that the program gave realistic results.

Nomenclature

η_{norm}	<i>Inverter maximum efficient</i>
η_{ref}	<i>Reference efficient</i>
η	<i>Inverter actual efficient</i>
ξ	<i>DC power ratio</i>
V_{PV}	<i>Output voltage of PV</i>
V_{oc}	<i>Open circuit voltage</i>
I_{sc}	<i>Short circuit current</i>
P_{max}	<i>Maximum power of PV</i>
t	<i>Time</i>
P_{DC}	<i>PV actual input power</i>
P_{DC0}	<i>Inverter maximum input power</i>
P_{ACO}	<i>Inverter maximum output power</i>
P_{irated}	<i>Inverter nominal power</i>
$P_{PV(rated)}$	<i>Total PV nominal power</i>
$P_{mpp.stc}$	<i>PV instant DC power</i>
R_s	<i>Sizing ratio, DC/AC ratio</i>
N_s	<i>Serial PV number</i>
N_p	<i>Parallel PV number</i>

2. Energy Production Estimation Program

An analytical energy generation estimation program that is designed on MATLAB/Simulink was used for the calculations. This program consists of the solar position calculation, surface irradiance calculation, PV system and inverter efficiency calculation modules. A block diagram of the PV system model is given in Figure 1. The designed program needs hourly meteorology data, geographic coordinates with montage info of SPP and some system information for calculation. Output of the

program gives the panel and inverter output energy production values hourly. The program is used to calculate the inverter DC input and AC output power generation data. Since this program uses panel and inverter datasheets, it gives more accurate and detailed results in this calculations.

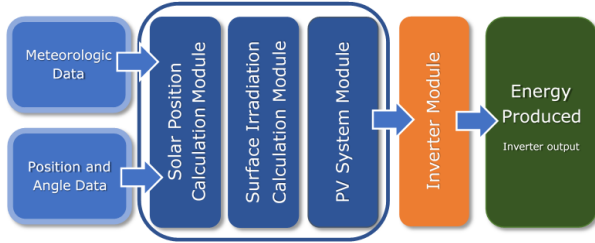


Figure 1. Block diagram of designed program modules

Inverter efficiencies are given as constant values in the datasheet, but in fact, the efficiency decreases rapidly at low power values. Therefore, the inverter efficiency module was used to estimate more realistic results at low power values. The Simulink diagram of the PV system model is given in Figure 2. This diagram consists of three main blocks which are solar position calculation, surface irradiance calculation, PV system and inverter efficiency calculation modules.

2.1. Inverter Efficiency Module

The inverters used in the PV system are designed to convert the DC energy produced by the panels into AC energy with high efficiency. The system follows the maximum power point under all conditions. The fixed losses of the system are also important during low irradiance and the system's efficiency decreases rapidly. Figure 3 shows the efficiency curve of the inverter used in the system. The efficiency curve is calculated by the module shown in Figure 4. The efficiency equation of the inverter can be written as follows:

$$\eta = \frac{\eta_{norm}}{\eta_{ref}} \left(-0.016138 \xi - \frac{0.0059}{\xi} + 0.9858 \right) \quad (1)$$

where,

$$\xi = \frac{P_{DC}}{P_{DC0}} \text{ and } P_{DC0} = \frac{P_{AC0}}{\eta_{norm}}$$

Inverter efficiency is calculated by considering the input power at the optimum operating conditions and instantaneous input power. It is given Equation (1) [21]. Where η , η_{norm} , η_{ref} , P_{DC} , P_{DC0} and P_{AC0} are the instant efficiency, the nominal efficiency, the reference efficiency, the instant input power, the maximum input power and the maximum AC output power of the inverter, respectively.

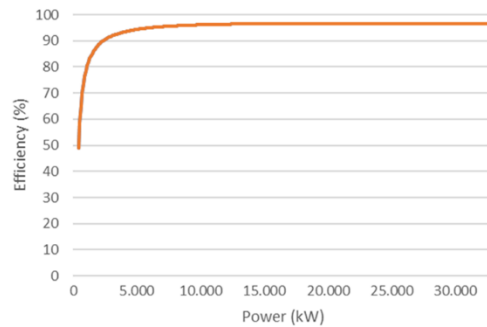
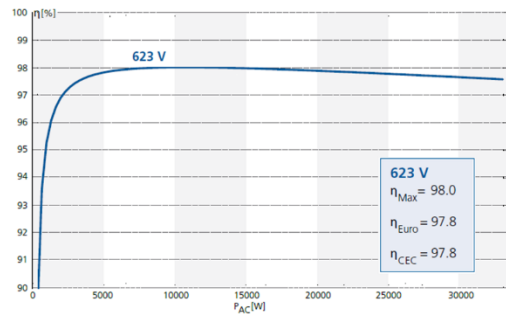


Figure 3. The inverter efficiency curves in catalog and module output

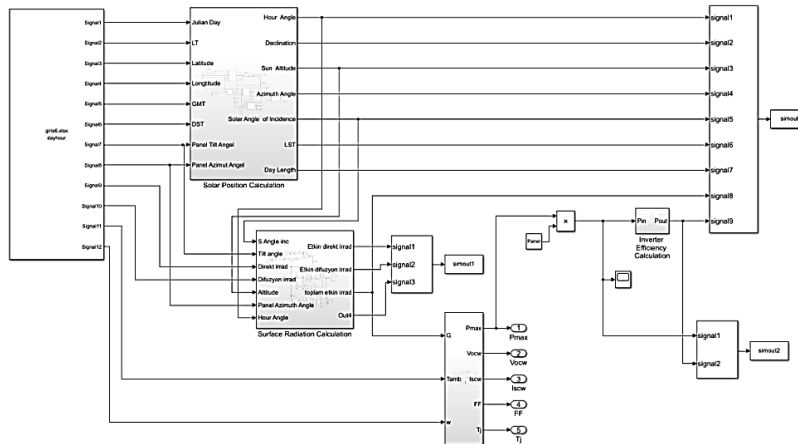


Figure 2. The Simulink diagram of designed program modules

The module that calculates the inverter efficiency and output power to determine input power is shown in Figure 4.

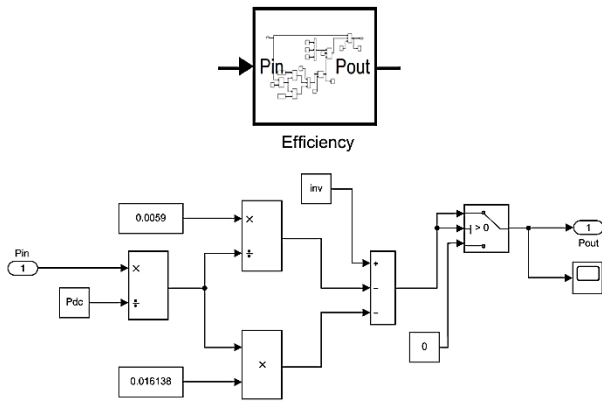


Figure 4. The module calculating inverter efficiency

2.2. DC/AC Ratio Module

The DC/AC or sizing ratio (R_s) is the ratio of the PV array nominal power ($P_{PV(rated)}$) to the nominal power of the inverter ($P_{i(rated)}$) power at the standard test conditions. This ratio is used to express the optimum combination between the PV array and inverter. The sizing ratio is given in Equation (2) [17,19].

$$R_s = \frac{P_{PV(rated)}}{P_{i(rated)}} \quad (2)$$

Table 1. System catalog information.

SYSTEM INFORMATION			
PV DATASHEET		INVERTER DATASHEET	
Model	BYD 250P6-30	Model	POWADOR 33.0 TL3
Voc	38 V	Operation Voltage	200 V-950 V DC
Vmp	30.40 V	Max Input Current	3X34 A
Isc	8.98 A	Efficiency	98%
Imp	8.22 A	AC Rated Output	27500 VA
Pmax	250 W		
Efficiency	15.37%		
		DC/AC Ratio	≈1
PV DC Total Power	27000 W		

Table 2. General comparison table.

INFORMATION	GROUP1 (59°) (kWh)	GROUP2 (239°) (kWh)	TOTAL (kWh)	FAULT RATE (%)
2020 REAL PRODUCTION	24550	30333	54883	
2020 MODEL RESULT	23922	29649	53571	-2.4%

The PV array nominal power ($P_{PV(rated)}$) can be determined using Equation (3).

$$P_{PV(rated)} = P_{mpp,sc} \cdot N_s \cdot N_p \quad (3)$$

Where $P_{mpp,sc}$, N_s and N_p are the PV module nominal maximum power at standard test conditions, the number of PV modules connected in series and parallel, respectively.

If the R_s value is in interval $0 < R_s < 1$ then the inverter is oversized. For $R_s > 1$, the inverter is undersized, and leads to a clipping effect due to power limitation when the daily power generation of the system exceeds the inverter power [8].

3. Program Data

The energy production of a SPP consisting of two independent groups, established in Balıkesir (39.6N 27.9E), was examined. The each group has 108 polycrystalline panels with 250 W and an inverter output power 27500 VA. As shown in Figure 5, it is directed at 59° (Group 1) and 239° (Group 2) symmetrical angles and mounted on 17° angled roof. Circuit diagram of on-grid SPP system with two inverters is given in Figure 6. The inverter has 3 MPPT inputs, and PV arrays consisting of 18 serial modules in 2 parallel strings are connected to each input. PV array voltage-current graph is given in Figure 7.

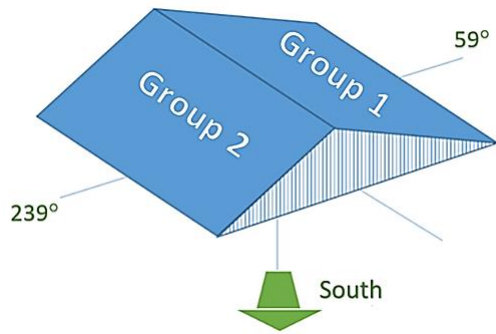


Figure 5. Roof view of the real system.

The real SPP system catalog information is given in Table 1.

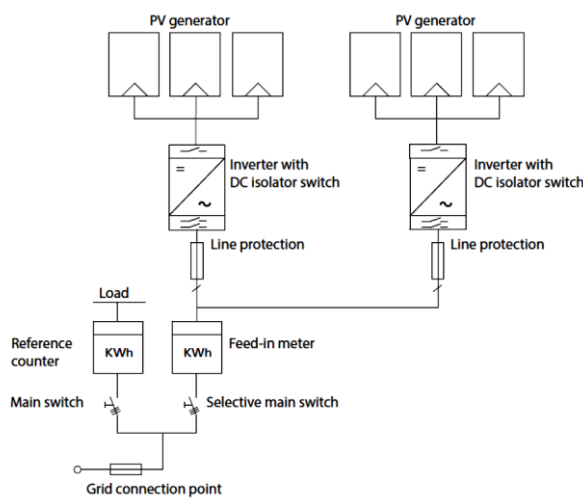


Figure 6. Circuit diagram of a system with two inverters.

When Table 1 is examined, it is seen that the DC power of the real system is 27000 W and the inverter output power is 27500 VA. As a result, the DC/AC ratio is approximately 1. This value is obtained from the catalog information of the real system.

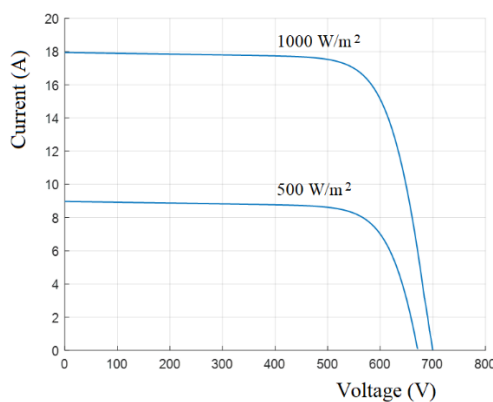


Figure 7. The effect of series/parallel connection of PV arrays on the current-voltage curve.

3.1 Program Calculation

The real SPP annual energy production values were compared with the results of the developed program for Group1 and Group 2. The comparison results are given in Table 2.

The SPP produced 54883 kWh in 2020. The program calculated that the system would produce 53571 kWh by using meteorological data of 2020. In the comparison table, a deviation of 2.4% was observed with the calculation results. The results are stable and realistic at different angle values for both PV groups. DC/AC ratio comparison tables are presented for Group 1 and Group 2 in Table 3 and Table 4, respectively.

Table 3. DC/AC ratio comparison table for Group 1

GROUP 1					
DC/AC RATIO	POWER (W)	INPUT (kWh)	OUTPUT (kWh)	CLIPPING (kWh)	RATIO (%)
0.8	33750	23843	23843	0	0.0%
0.9	30000	23893	23893	0	0.0%
1.0	27000	23929	23926	4	0.0%
1.1	24500	23956	23916	40	0.2%
1.2	22500	23975	23844	131	0.5%
1.3	20750	23988	23714	274	1.1%
1.4	19300	23997	23521	476	2.0%
1.5	18000	24002	23266	736	3.1%

Table 4. DC/AC ratio comparison table for Group 2

GROUP 2					
DC/AC RATIO	POWER (W)	INPUT (kWh)	OUTPUT (kWh)	CLIPPING (kWh)	RATIO (%)
0.8	33750	29544	29544	0	0.0%
0.9	30000	29609	29605	4	0.0%
1.0	27000	29658	29558	100	0.3%
1.1	24500	29693	29369	324	1.1%
1.2	22500	29718	29123	595	2.0%
1.3	20750	29736	28810	926	3.1%
1.4	19300	29748	28483	1265	4.3%
1.5	18000	29755	28152	1603	5.4%

Comparisons of Group 1 and Group 2 for annual energy production at different DC/AC ratios are given in Table 3 and Table 4. For DC/AC=1, it is calculated that Group1 will produce 23926 kWh and Group 2 will produce 29558 kWh. For DC/AC=1.5, it is calculated that Group1 will produce 23266 kWh and Group 2 will produce 28152 kWh. For DC/AC =1.5, it is predicted that Group 1 will produce 3.1% and Group 2 will produce 5.4% energy less than DC/AC=1. Although the system power decreases at DC/AC= 1.5, it is remarkable that the energy production higher than DC/AC=1 due to the more efficient operation of inverter at low power. As shown in Figure 8, the direction of installed system affects the energy production amount. While sizing the system, it should be considered that the transformer power, cross section of cable and connector elements will decrease. As a result, whole system installation cost will decrease with the selection of suitable inverter power.

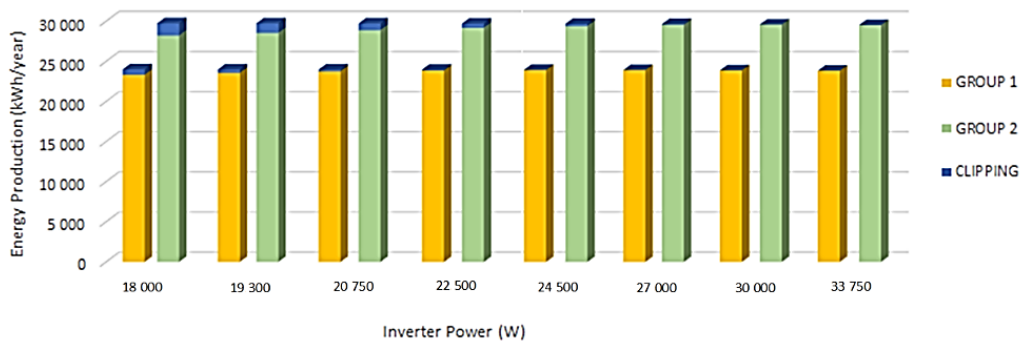


Figure 8. Energy productions of inverter groups.

The energy productions of Groups 1 and 2 for 2020 are shown in Figure 9 in watts/hour. The produced energy data are arranged from the higher values to the lower values so that they can be seen more clearly on the graph. The lines where the production will be clipping for different DC/AC ratios are marked on the Figure 9. As shown from the graph, the clipping sections are at the maximum power production area. This area is a small part of the annual energy production amount. The amount of clipping energy can be seen more clearly on the Figure 9.

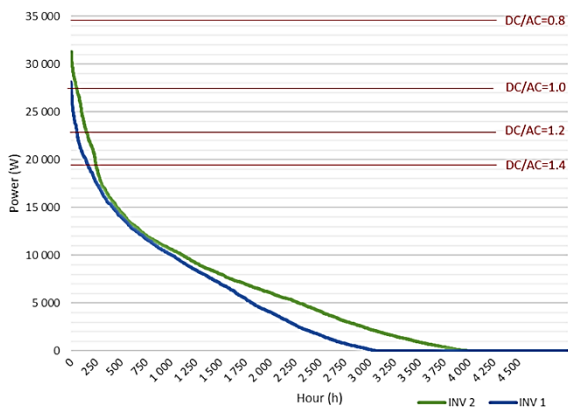


Figure 9. The power production and clipping of inverter groups.

The energy production curve modeled according to the highest power generation day of 2020 for the different inverter powers of SPP is given on the Figure 10.

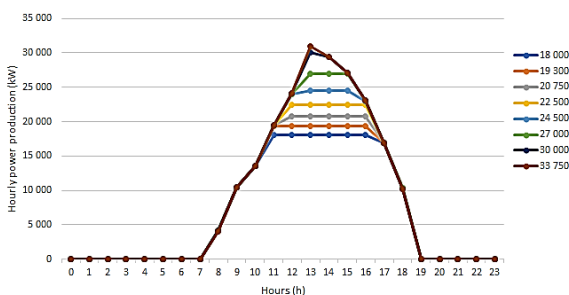


Figure 10. The maximum energy production and clipping values of inverter.

The produced energy according to DC/AC ratio is given Table 5 for the same day and different hours.

Table 5. Energy production according to DC/AC ratio.

DC/AC RATIO	INVERTER POWER (W)	PRODUCED ENERGY (Wh/year)
1.5	18000	163453
1.4	19300	171257
1.3	20750	178679
1.2	22500	187432
1.1	24500	195448
1	27000	202953
0.9	30000	208344
0.8	33750	209246

As seen from the Figure 10 and Table 5, the inverter clipping value ($209246 - 163453 = 45793$ W) is over the rated inverter power 18000W. There is a 22% energy production difference between the highest power and the lowest power. But SPP does not produce the maximum power during the whole year. As a result, the annual energy difference produced by the system is around 5%.

The SPP has two PV system groups with the same power and symmetrically placed. When the energy productions of two groups are analyzed, there is a 19% difference in between them.

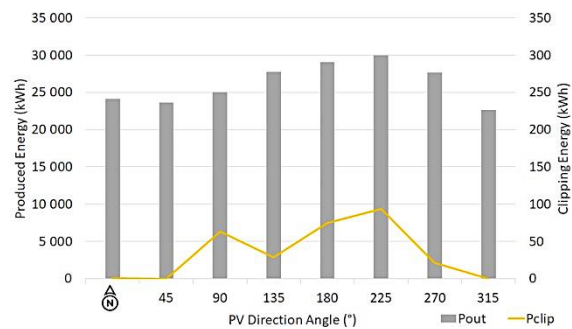


Figure 11. The effect of direction on energy production and clipping.

Calculations were made for different directions to examine the effect of direction of the system on energy production. According to the designed program, if the same panel groups and inverter of real SPP are assembled in the different directions and at same tilt angle, the amount of energy they would generate would be as given in Table 6 and Figure 11.

Table 6. Annual energy production comparisons for different direction angles (DC/AC Ratio = 1).

DIRECTION ANGLE (°)	PV PRODUCED ENERGY E_{pv} (kWh)	INVERTER OUTPUT ENERGY E_{inv} (kWh)	CLIPPING ENERGY E_{clip} (kWh)
0	29407	24159	1
45	28690	23604	0
90	30429	24995	64
135	33667	27713	29
180	35397	29070	75
225	36513	29950	93
270	33740	27692	21
315	27650	22642	0

The PV system energy productions are calculated for DC/AC=1 as given in Table 6 by using different directions and meteorological data for 2020. Program calculates that PV would produce the minimum of 20202 kWh at 335° and the maximum of 30000 kWh at 215° when the system direction is changed. There is a 32% difference between the minimum and maximum energy production.

It is estimated that the highest average annual energy production of existing system will be 30000 kWh in a year if the system operates at 215 degrees by using meteorology data for 2020. This result indicated that the panel's direction was important in selecting inverter power.

4. Calculation of Optimum Sizing Ratio

There are different methodologies to determine the optimal power of an inverter. Of these, DC/AC ratio was calculated with the energy produced in the PV panel and operation method with maximum inverter efficiency. Information about the method and the results obtained are described in detail in the subsections.

4.1. Iterative Conversion Efficiency Method

On-grid inverters are usually sized according to the rated power of the PV array. Inverters usually follow the maximum power point to produce maximum power. However, since solar irradiance varies according to location and meteorological data, the output power of PV panels is also variable. At low solar irradiance levels, the PV array generates less than its rated power. Therefore, the inverter is operated at lower efficiency.

Consequently, it is vital to find the optimal size of inverter for effective energy production using a PV system [19]. An example graph showing the variation of DC/AC ratio with inverter efficiency is presented in Figure 12.

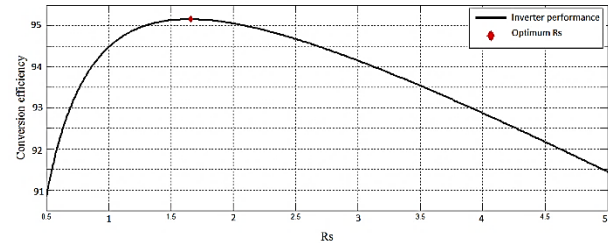


Figure 12. Optimization of the inverter sizing ratio.

Figure 13 shows the proposed optimization algorithm for inverter size in a grid-connected PV system. In the beginning, the PV system parameters such as the rated power of the PV array, the temperature coefficient, location and direction of the PV module are determined. With these parameters, hourly solar irradiance and ambient temperature records are used to obtain the inverter input DC power. Then, DC input power values are used to calculate inverter efficiency with the iteration. Loop of R_s was set in the range of 0.5 to 5.

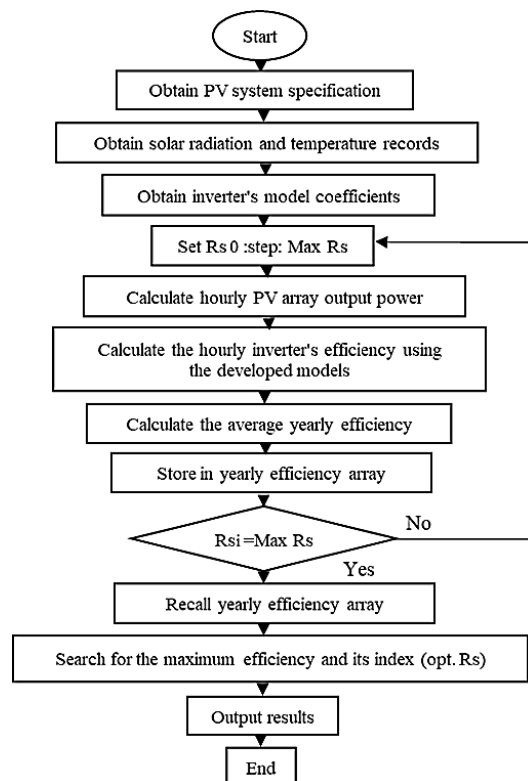


Figure 13. Flowchart for the inverter's optimal efficiency

The PV array output is calculated hourly using the complicated PV model described in Equation (1). After that, the annual average efficiency is calculated. The loop

is being repeated until R_s reaches its maximum value. Finally, when R_s reaches its maximum value, optimum R_s for the maximum efficiency is found.

In Table 7, the conversion efficiency and energy production values are obtained by changing the DC/AC ratio between 0.5 and 5 by using 0.5 steps for Group 1. Change of values was graphed Figure 14(a). For Group 1, the optimum inverter power was calculated as 21094 W and DC/AC ratio is equal to 1.28. For this value, it is predicted that the inverter will operate with an average efficiency of 91.55% and produce 23747 kWh of energy per year.

Table 7. Comparison table of conversion efficiency for Group 1.

GROUP -1			
DC/AC RATIO	INVERTER POWER (W)	CONVERSION EFFICIENCY (%)	PRODUCED ENERGY (kWh)
0.5	54000	87.58%	23531
1.0	27000	91.04%	23926
1.5	18000	91.15%	23266
2.0	13500	89.04%	21628
2.5	10800	85.82%	19743
3.0	9000	82.11%	17901
3.5	7714	78.31%	16264
4.0	6750	74.80%	14847
4.5	6000	71.73%	13633
5.0	5400	68.83%	12601
OPTIMUM DC/AC RATIO FROM CONVERSION EFFICIENCY			
1.28	21094	91.55%	23747

Table 8. Comparison table of conversion efficiency for Group 2.

GROUP -2			
DC/AC RATIO	INVERTER POWER (W)	CONVERSION EFFICIENCY (%)	PRODUCED ENERGY (kWh)
0.5	54000	87.35%	29139
1.0	27000	90.32%	29558
1.5	18000	90.49%	28152
2.0	13500	89.28%	26332
2.5	10800	86.84%	24310
3.0	9000	83.90%	22278
3.5	7714	80.82%	20444
4.0	6750	77.72%	18813
4.5	6000	74.72%	17369
5.0	5400	71.95%	16102
OPTIMUM DC/AC RATIO FROM CONVERSION EFFICIENCY			
1.35	20000	90.62%	28645

In Table 8, the conversion efficiency and energy production values obtained by changing the DC/AC ratio between 0.5 and 5 with 0.5 steps are presented for Group 2. Change in values was graphed in Figure 14(b). For Group 2, the optimum inverter power was calculated as 20000 W and DC/AC ratio is equal to 1.35. For this value, it is predicted that the inverter will operate with an average efficiency of 90.62% and produce 28645 kWh of energy for one year.

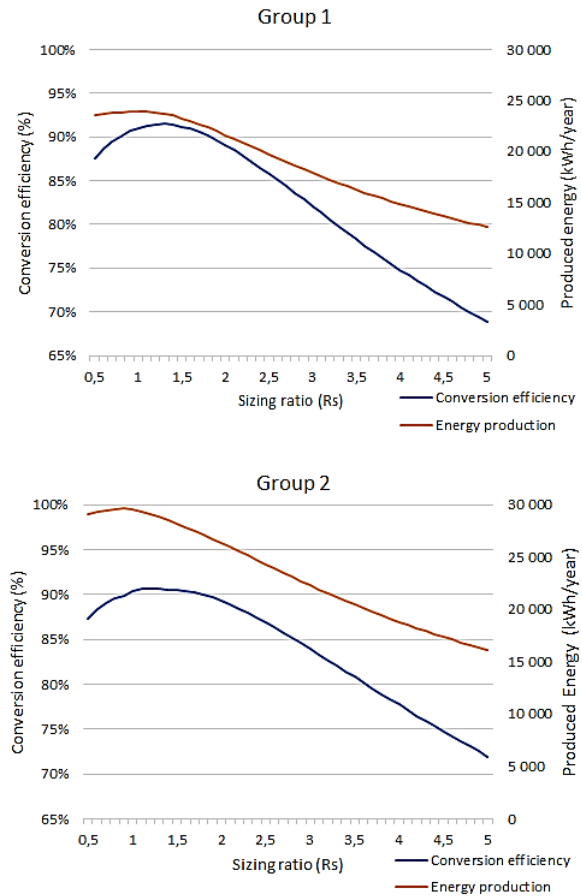


Figure 14. Conversion efficiency and energy productions of groups.

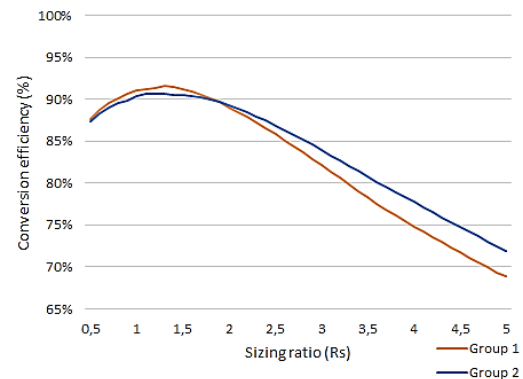


Figure 15. Conversion efficiency of groups

In Figure 15, changes in energy conversion efficiency and produced energies according to sizing ratio for Groups 1 and 2 are presented to compare with each other. Although there is a big difference between the energy productions of groups due to the difference in direction, the efficient working range is between 0.5-2 as shown in Figure 15.

4.2. Energy Production Curve Method

This calculation method determines the optimum inverter power by analyzing the hourly energy production of PV panels.

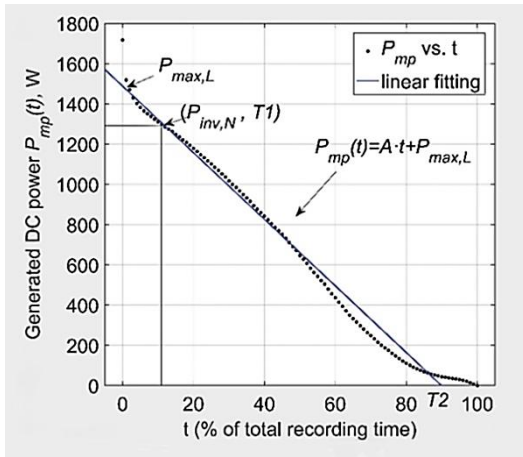


Figure 16. Power duration curve and its linear fitting line.

The first step for the preliminary design of an SPP system with an optimally sized inverter is to create the DC power profile using an appropriate power model with inputs from local climate data. First, the DC energy produced from the irradiance data coming to the panel surface is calculated hourly depending on the direction and angle information. The annual energy production graph is created by placing the produced energy data from high values to low on the time axis. It then offers a suitable realistic inverter sizing based on the DC power-time curve and the line origin intersection of the linear simulation curve.

The DC input instant power of inverter is described in Equation (4). It is the linear fitting line of annual power production graph given in Figure 16.

$$P_{mpp.stc}(t) = A \cdot t + P_{max} \quad (4)$$

The power productions of SPP for Groups 1 and 2 are given for 2020 in Figure 9. Although the power values are the same for the two groups, there is a difference between curves in the graphs for the two groups due to the azimuth angle difference. Linear curves that fit the graphs for the system are calculated and given in Figure 17.

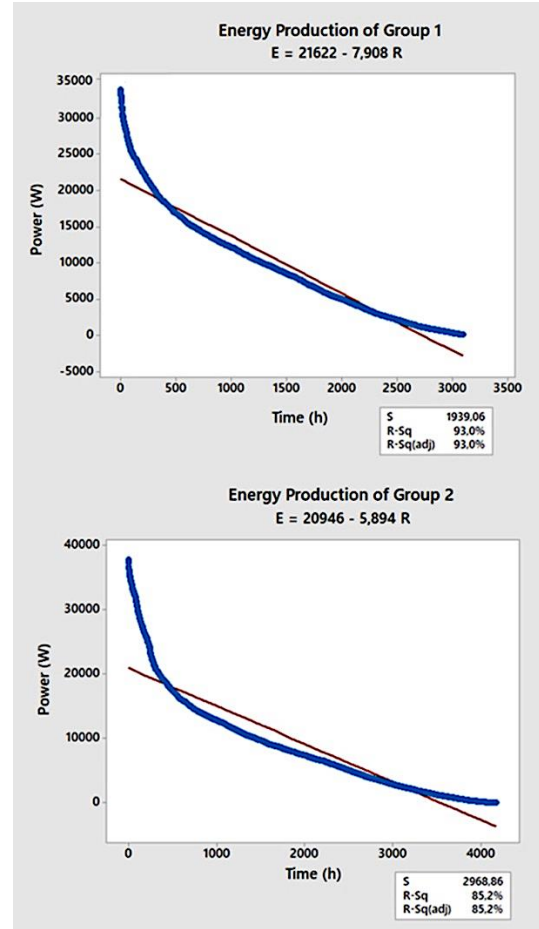


Figure 17. Power duration curve and its linear fitting lines of groups

The parameter values of curves obtained from Figure 17 are given in Table 9. In Equation (4), coefficient A and P_{max} are calculated by using Minitab program.

Table 9. Inverter power equation parameter table for Equation (4).

GROUP	COEFFICIENT A	Pmax (kW)	R ²	R _s
GROUP 1	-7.908	21622	93.0%	1.25
GROUP 2	-5.894	20946	85.2%	1.29

As can be seen from the table, the optimum inverter dimensions are 21622 kW for Group 1 and 20946 kW for Group 2.

When 21622 kW is determined as the optimum inverter power for Group1, the size ratio (R_s) is 1.25. Similarly, the size ratio (R_s) is 1.29 when 20946 kW is determined as the optimum inverter power for Group 2. Depending on the irradiance and angles in SPP location, the DC power value coming to the inverter is lower than DC peak power. It is recommended to choose a lower power inverter for optimum efficiency.

4.3. Comparison Of Optimum Sizing Ratio Calculation Results

The results obtained with both methods, optimum inverter powers, energy conversion ratios and yearly energy productions are compared in Table 10.

For Groups 1 and 2, both methods give close results as given Table 10. If DC/AC ratio is chosen between 1.25 and 1.28, it can be accepted as the optimum value, the system will operate with a clipping loss of about 1%. This

result indicates that when inverter power is selected 21000 W for PV power 27000 W. 1% clipping loss will be experienced although the inverter power is reduced by 28%. If DC/AC ratio is chosen between 1.29 and 1.35 for Group 2, it can be accepted as the optimum value, the system will operate with a clipping of about 3-3.7%. This result indicates that optimal value of inverter power is 21000 W for PV power 27000 W. 3-3.7% loss will be experienced although the inverter power is reduced by 28%.

Table 10. Comparison of optimum sizing ratio for calculation

	INVERTER			ENERGY		
	POWER (W)	DC/AC (-)	EFFICIENCY (%)	PRODUCED ENERGY (kWh)	CLIPPED ENERGY (kWh)	LOSS (%)
EFFICINCY METHOD						
GROUP 1	21094	1.28	91.55%	23747	239	1.0%
GROUP 2	20000	1.35	90.62%	28645	1097	3.7%
ENERGY GRAPH METHOD						
GROUP 1	21622	1.25	93.00%	23789	193	0.8%
GROUP 2	20946	1.29	85.20%	28850	884	3.0%

5. Conclusion

In this study, the effects of the DC/AC ratio, a determining parameter in the inverter selection, in the sizing of an SPP were investigated. The incoming irradiance values of a power plant in Balikesir/Turkey were simulated, and DC energy at the inverter input was calculated. The results obtained from the calculation were compared with the real system production values and were compatible. The effects of the AC/DC ratio on the daily-annual energy production of the system were analyzed numerically and graphically. There are different methodologies to find the optimal value of inverter power. On-grid inverters are usually sized according to the rated power of the PV array. Since solar irradiance varies according to location and meteorological data, the output power of PV panels is also variable. At low solar irradiance levels, the PV array generates less than its rated power. The inverter is operated with lower inverter efficiency. Therefore, calculating the optimal size of the inverter is very important for effective energy production of the PV system. Inverter efficiency is given as a constant in the datasheet, but actually the efficiency decreases rapidly at low power values. The different inverter powers and DC/AC ratios are used to estimate the produced power of a SPP. The high inverter power provides higher system losses and lower clipping losses. Conversely, low inverter power results in lower system losses but higher clipping losses. While sizing the system, if the inverter with lower power is chosen, the transformer power, cable cross-section and connectors dimension will decrease and the system installation cost will also decrease.

As a result of the calculations for the examined SPP, the optimum inverter power for the PV panel system with a DC power of 27000 W was 21000 W, and the size ratio (R_s) was 1.29. When the results for the inverter power 21000 W are examined, it is seen that although the inverter power is reduced by 28%, there will be only 1-3% clipping loss in yearly energy production.

The direction of the installed system affects the amount of energy production. The PV system energy productions are calculated for DC/AC=1 using meteorological data for 2020 and different directions. Program is calculated that change of the system direction will produce the minimum energy 20202 kWh and the maximum energy 30000 kWh. Between the minimum and maximum energy production, there is a 32% difference. This result indicated that the panel's direction was important in selecting inverter power.

The systems operate at maximum power only at certain periods of the year. Systems sized for this situation are forced to operate at lower powers and with lower efficiency throughout the year. Selecting the inverter power for the smallest power that is most efficient for the system while the system is being sized will reduce the installation costs and cross-sections of the system. Since the power panels, conductor sections and substations are sized depending on the inverter power, the inverter power has an important effect on the sizing of the system.

As a result, the effects of inverter power selection and PV panel direction on energy production were studied and analyzed by simulation and real system.

The PV panel direction and inverter power selection are significant parameters to determine the amount of produced energy. Contrary to popular belief, a high-power inverter does not mean more energy generation. A properly sized inverter can make the system more efficient and produce more power, even if it is lower power.

Author's Contributions

Mehmet Fatih Beyoğlu: Drafted and wrote the manuscript, performed the calculation and result analysis.

Metin Demirtaş: Supervised the calculations, result interpretation and helped in manuscript preparation.

Ethics

There are no ethical issues after the publication of this manuscript.

References

- [1]. Karafil, A., Ozbay, H., Kesler, M., & Parmaksiz, H., (2016), Calculation of optimum fixed tilt angle of PV panels depending on solar angles and comparison of the results with experimental study conducted in summer in Bilecik, Turkey. *ELECO 2015*, 971–976, <https://doi.org/10.1109/ELECO.2015.7394517>.
- [2]. Rustemli, S. & Dincadam, F. & Demirtas, M. (2010). Performance comparison of the sun tracking system and fixed system in the application of heating and lighting. *Arabian Journal for Science and Engineering*, 35. 171-183.
- [3]. Beyoğlu, M. F. (2011). Comparison of efficiencies of dual axis solar tracking system and fixed axis PV system in Balıkesir City. Balıkesir University Institute of Science, Master thesis, <https://hdl.handle.net/20.500.12462/2405>.
- [4]. Beyoğlu, M.F., Demirtaş, M. (2019). A comparative evaluation of photovoltaic power plant energy production established in Balıkesir province and production forecasting programs. *International Marmara Sciences Congress (Autumn) 2019 Proceedings Book (Natural and Applied Sciences)*, (November), 401–406.
- [5]. Abood, A., A. (2015). A comprehensive solar angles simulation and calculation using Matlab. *International Journal of Energy and Environment*, 6(4), 367–376, <https://doi.org/10.1177/1098214005283748>.
- [6]. Jazayeri, K., Uysal, S., & Jazayeri, M. (2013). Matlab/Simulink based simulation of solar incidence angle and the sun's position in the sky with respect to observation points on the Earth. *Proceedings of 2013 International Conference on Renewable Energy Research and Applications, ICRERA 2013*, 173–177, <https://doi.org/10.1109/ICRERA.2013.6749746>.
- [7]. Demoulias, C. (2010). A new simple analytical method for calculating the optimum inverter size in grid-connected PV plants. *Electric Power Systems Research*, 80(10), 1197–1204, <https://doi.org/10.1016/j.epr.2010.04.005>.
- [8]. Wang, H. X., Muñoz-García, M. A., Moreda, G. P., & Alonso-García, M. C. (2018). Optimum inverter sizing of grid-connected photovoltaic systems based on energetic and economic considerations. *Renewable Energy*, 118, 709–717, <https://doi.org/10.1016/j.renene.2017.11.063>.
- [9]. Faranda, R. S., Hafezi, H., Leva, S., Mussetta, M., & Ogliari, E. (2015). The optimum PV plant for a given solar DC/AC converter. *Energies*, 8(6), 4853–4870, <https://doi.org/10.3390/en8064853>.
- [10]. Pandey, S., Kumar, R., & Panwar, K. (2019). Calculation of inverter power clipping loss due to PV array oversizing. *International Journal of Electrical Engineering and Technology*, 10(4), 43–46, <https://doi.org/10.34218/IJEET.10.4.2019.005>.
- [11]. Camps, X., Velasco, G., de la Hoz, J., & Martín, H. (2015). Contribution to the PV-to-inverter sizing ratio determination using a custom flexible experimental setup. *Applied Energy*, 149, 35–45, <https://doi.org/10.1016/j.apenergy.2015.03.050>.
- [12]. Azzolini, J. A., Reno, M. J., & Horowitz, K. A. W. (2020). Evaluation of curtailment associated with PV system design considerations. *IEEE Power and Energy Society General Meeting, 2020-August*, <https://doi.org/10.1109/PESGM41954.2020.9281427>.
- [13]. Notton, G., Lazarov, V., & Stoyanov, L. (2010). Optimal sizing of a grid-connected PV system for various PV module technologies and inclinations, inverter efficiency characteristics and locations. *Renewable Energy*, 35(2), 541–554, <https://doi.org/10.1016/j.renene.2009.07.013>.
- [14]. Fernández, F.S., Muñoz-García, M. A., & Saminger-Platz, S. (2016). Detecting clipping in photovoltaic solar plants using fuzzy systems on the feature space. *Solar Energy*, 132, 345–356, <https://doi.org/10.1016/j.solener.2016.03.013>.
- [15]. Deschamps, E.M., & Rütger, R. (2019). Optimization of inverter loading ratio for grid connected photovoltaic systems. *Solar Energy*, 179(November 2018), 106–118, <https://doi.org/10.1016/j.solener.2018.12.051>.
- [16]. Balfour, J., Hill, R., Walker, A., Robinson, G., Gunda, T., & Desai, J. (2021). Masking of photovoltaic system performance problems by inverter clipping and other design and operational practices. *Renewable and Sustainable Energy Reviews*, 145(March), 111067, <https://doi.org/10.1016/j.rser.2021.111067>.
- [17]. Zidane, T. E. K., Zali, S. M., Adzman, M. R., Tajuddin, M. F. N., & Durusu, A. (2021). PV array and inverter optimum sizing for grid-connected photovoltaic power plants using optimization design. *Journal of Physics: Conference Series*, 1878(1), <https://doi.org/10.1088/1742-6596/1878/1/012015>.
- [18]. Choi, U. M. (2020). Study on Effect of Installation Location on Lifetime of PV Inverter and DC-to-AC Ratio. *IEEE Access*, 8, 86003–86011, <https://doi.org/10.1109/ACCESS.2020.2993283>.
- [19]. Khatib, T., Mohamed, A., Sopian, K., & Mahmoud, M. (2012). An iterative method for calculating the optimum size of inverter in PV systems for Malaysia. *Przeglad Elektrotechniczny*, 88(4 A), 281–284.
- [20]. Khatib, T., Yasin, A., Mohammad, A. A., & Ibrahim, I. A. (2017). On the effectiveness of optimally sizing an inverter in a grid-connected photovoltaic power system. *2017 14th International Conference on Smart Cities: Improving Quality of Life Using ICT and IoT, HONET-ICT 2017, 2017-January*, 48–52, <https://doi.org/10.1109/HONET.2017.8102220>.
- [21]. Dobos, A. P. (2014). *PVWatts Version 5 Manual*.

Tissue Mimicking Phantom Design and Characterization for Thermal Imaging Applications on Breast Cancer Diagnosis

Zeynep Ayyıldız^{1,2} , İbrahim Akkaya^{2*} , Mehmet Engin² 

¹ Biomedical Technologies Dept., Graduate School of Natural&Applied Science, Ege University, İzmir/Türkiye

² Dept. of Electrical and Electronics Engineering, Faculty of Engineering, Ege University, İzmir/Türkiye

* ibrahim.akkaya@ege.edu.tr

* Orcid No: 0000-0003-0605-7115

Received: 20 October 2022

Accepted: 02 March 2023

DOI: 10.18466/cbayarfbe.1176244

Abstract

Breast cancer is one of the mortal cancerous for women and an early diagnosis, applying an appropriate treatment and prognosis increases the survival chance of the patients. There are different screening methods and thermal imaging is one of the noninvasive promising diagnosis techniques to detect thermal profile anomalies in breasts. This work includes both simulation and experimental studies for the detection of breast tumors by using thermal images. The first step is the simulation studies based on heat transfer in biological tissues. By using the Bio-Heat transfer theory, temperature differences between the healthy and tumorous tissues are acquired. The second step consists of phantom designs and detection of breast tumor via thermographic imaging in in-vitro. Designing an appropriate phantom is tremendously crucial for the calibration of the thermal imaging system and diagnosis of breast cancer. As a result of the study, it is presented that the detection of temperatures difference especially with asymmetry factor between the tumor and healthy tissue region is feasible. Also, it is shown that the simulation based results are consistent with the experimental as well.

Keywords: breast tumor, cancer, phantom, temperature distribution, thermal imaging thermography.

1. Introduction

Breast cancer is one of the leading deathful cancer types among women. According to the latest report of the International Agency for Research on Cancer (IARC), the most commonly seen cancer is the female breast cancer which is ~11.7% of the total new cases by 2020 [1]. However, early diagnosis is crucial for increasing survival rate. Therefore, there have been employed many studies and techniques to detect and monitor the breast cancer and early diagnosis is still a hot topic. One of the important methods for early breast cancer diagnosis is infrared thermography or in another saying thermal imaging. Infrared thermography of the breast is a promising method to early diagnosis of tumor evaluation [2,3]. The major advantage of the thermography is can detect the cancer cells at least a year earlier than current screening methods such as mammography [4]. While magnetic resonance imaging (MRI), ultrasound, and mammography are looking for a lump or structural changes, the thermography screens for unusual new blood vessel formation which is called angiogenesis. Infrared thermography is a non-invasive functional monitoring technique which detects surface

temperature deviations of an object [2]. Therefore, infrared thermography is totally safe for the patients and there is no ionizing radiation exposure. Another advantage is non-contact and applicable without any pain or stress. Nevertheless, it is worth to mention that thermography is an adjunct to mammography.

Essentially, the history of deployment of infrared thermography to screen breast cancer/tumor goes back 1950s. Ray N. Lawson discovered the breast tumors were relatively warmer than the surrounding healthy breast tissue for the first time in 1956 [5]. The following year in 1957, Lawson proposed to use infrared thermography to detect/monitor breast cancer in his study [6, 7]. After that, many different studies employed and were presented in breast cancer screening by using thermography [6]. One of them is Collett et al. conducted a dynamic imaging technique which is first applying cold air onto the breast, then taking sequential images or video series while the breast warms up to screen breast cancer or abnormalities. They imaged 121 female patients and used 99 of them, but the sensitivity and selectivity results were not promising [8]. However, Wu et al. in 2016 [9], Rassiwal et al. in 2014 [10], and

Delgado [11] et al. in 2010 studied with large groups of patients, 143 in Taiwan, 1,008 in India, and 911 in Mexico, respectively and their conclusions were infrared thermography was a useful and promising tool for prognosis in breast cancer patients. Besides in-vivo studies, many in-vitro based experiments were conducted as well. Levy et al. carried out an in-vitro study where they used inductive heating mechanism and thermal imaging techniques. They were able to detect up to 5 mm diameter size and 14 mm depth tumor structure [4]. Wahab et. al. employed a thermal distribution (TD) analysis into homogenous phantoms and suggested that the TD technique may be applied to detect different tissue structure [12]. Hossain and Mohammadi used temperature profiles to predict physiological, biological, and thermal properties of the tumor. They proposed that skin temperature distribution profile was correlated with tumor structure [13]. In addition, especially some of the recent research have been employed that thermographic breast images are promising non-invasive breast cancer monitoring tool by using machine learning and specifically deep learning algorithms as well [14–17]. Furthermore, infrared thermography is a Food and Drug Administration (FDA) approved supplementary technique to mammography the gold standard for screening breast cancer [6]. Therefore, early breast cancer detection via thermographic imaging is still a trend research field and needs to be investigated further. This work is an early stage study of an in-vitro research of the thermal imaging for early diagnosis of breast cancer detection via manufactured breast phantoms. It is aimed to show the capabilities and effectiveness of the thermography such as tumor size and depth wise. This paper is divided into two main parts. The first part of the study is based on the modelling of a heat transfer simulation in breast tissues. The second part contains manufacturing process of the breast phantoms, mimicking tumors, and then screening the phantoms by a thermal camera. As it is known that the phantom manufacturing has dispensable in medical studies because of ease mimicking the organs and calibration of the device/methods under test. Also, this is the first phase out of three of a medical study which is in-vitro, animal model, and human studies, respectively. In this work, we show that the tumor-wise abnormalities can be detected up to 45 mm depth instead of shallower range. Moreover, we also show that the asymmetry factor is a promising feature to identify the difference between the healthy and cancerous breast.

This paper is organized by following sections. In section 2, simulation and modelling procedures are given. Then, phantom manufacturing process is given in Part 3. In the 4th and last part of the study, the results are presented for thermal imaging analysis of the breast tissue phantoms with and without tumor structure cases under different scenarios such as size and depth location of the tumor.

2. Materials and Methods

2.1. Theory of the Thermal Specification of the Tissue

The prediction of the thermal distribution on biological tissues can be useful for correct evaluation or decision in some cases such as degree of burnt, irregularities, or anomalies. Bio-heat transfer in the tissue is a process contains heat production, heat transfer, heat emission, and heat radiation [18, 19]. Bio-heat transfer is actually a heat transfer procedure between blood perfusion, sweating, bio-heat metabolic heat production, skin tissue and outer surface medium. Many factors affect the bio-heat transfer procedure such as thermal features, temperature, sex, age, damage, or imperfections onto the tissue, and pressure [20, 21]. Tissue is a heterogeneous and anisotropic medium. Also, it is hard to make a theoretical solution for the heat distribution onto the real tissue structure due to the complex geometry of the tissue. Therefore, numerical simulation approach of the bio-heat transfer is more practical.

2.1.1 Bio-Heat Transfer Equation

The most common used heat transfer method on the tissue is the Pennes' bio-heat transfer equation which has been used for breast tumor temperature distribution modeling as well [2, 21]. The Pennes' bio-heat transfer equation solves the tissue temperature distribution as a function of blood perfusion and metabolic heat velocity [22, 23]. In addition, the Pennes equation gives more accurate approximation for the heat transfer process inside the tissue because of using variable metabolic heat generation and also variable blood perfusion instead of assuming constant values [24]. The equation is given by Eq. 2.1 below;

$$\rho C_p \frac{\partial T}{\partial t} - k \nabla^2 T = \rho_b C_b \omega_b (T_b - T) + Q_{met} \quad (2.1)$$

where ρ is tissue density in kg/m^3 , C_p is heat capacity in J/kg.K , T is tissue temperature in K , k thermal conductivity in W/m.K , ρ_b blood density in kg/m^3 , C_b is blood specific heat capacity in J/kg.K , ω_b blood perfusion rate in per second, T_b is blood temperature in the vessel in K , and Q_{met} volumetric metabolic heat generation velocity in W/m^3 .

The Pennes' bio-heat equation is used commonly because of its mathematical simplicity and the superior ability of heat area prediction in use. Additionally, finite element method is employed to simulate the heat reaction onto the biological tissues based on Pennes' equations as well. However, the equation has some limitations due to fact that blood flow direction effect is excluded. Therefore, any convective heat transfer mechanism cannot be defined. [25].

2.2 Model Based Studies

In this study, COMSOL Multiphysics simulation software package, which solves a partial differential equation by using finite element method, was used. Firstly, the breast tissue and tumor structure were modelled. Then, thermal difference between the normal and tumor tissue was calculated with bio-heat transfer module of the software. The temperature profile of the breast tissue with tumor model flowchart is given in Fig. 1. In the first step, what kind of physical problem is handling is defined. In our case, bio-heat transfer solving method is used. The second step is the geometry of the simulated structures is created. The breast model was designed as a hemispherical form with a 12 cm diameter and a tumor-like structure was placed in the hemispherical model. In the third step, physical and thermal parameters for both breast tissue and tumor structure are entered for modeling. Additionally, the features of necessary components such as fat, muscle, bone, etc. are selected and added into the model and they are defined as a function of heat source as well. The parameter selections were done according to Ref. [26]. In the final step, to solve the model, limit conditions, thermal insulation, outer borders of the breast structure, need to be declared. Then, the simulation is numerically solved the problem based on finite element methods.

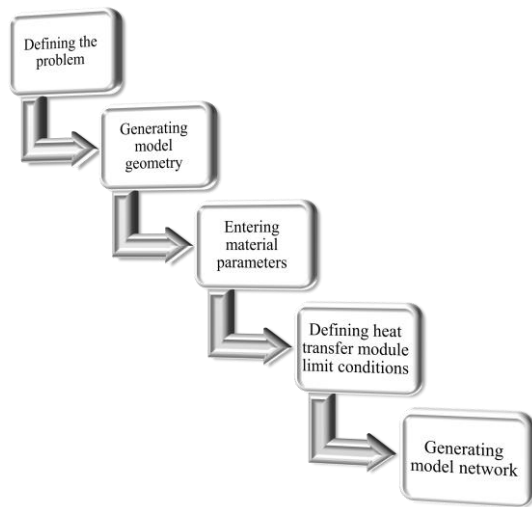


Figure 1. The flow chart of the simulation

To simulate the real cases scenarios, multi-physiology is needed. Therefore, heat transfer model was employed. Bio-heat transfer module is used to model heat transfer via transfer, convection, and radiation. The heat transfer was active in all the fields during biological tissue model. Semi-sphere geometry was designed to model the breast tissue on the simulation software. A semi-sphere geometry whose diameter was set 12 cm is shown in Fig. 2. The initial temperature value was set 36.35 °C after the breast and tumor tissue parameters entered the simulation software.

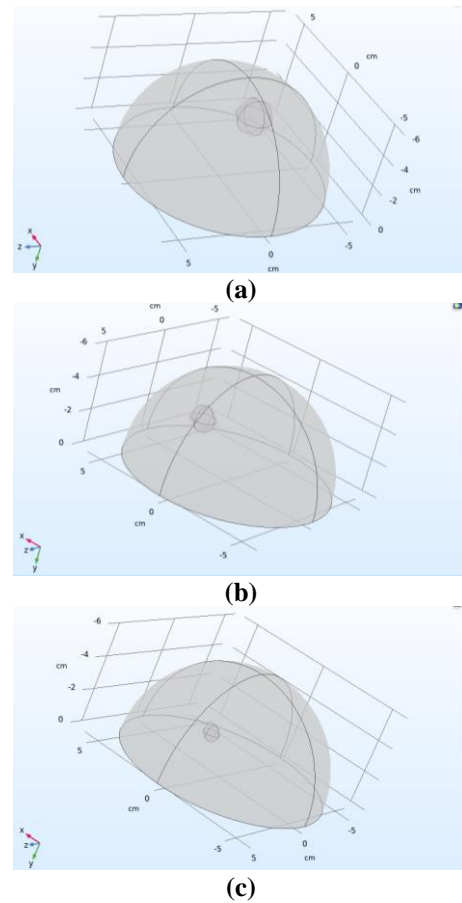


Figure 2. Simulated breast geometries with tumor for different sizes and locations. a) 1.0 cm diameter and 1.5 cm depth; b) 0.75 cm diameter and 3.0 cm depth, and; c) 0.5 cm diameter and 4.5 cm depth.

3. Phantom Design

The phantom manufacturing process is given in two parts. First part is the preparation of the medium. Dragon Skin 10 which is a high performance platinum cure silicone compounds and also are widely used prosthetics in medical fields, was used to mimic the breast tissue. The second part is placing the tumor effect into the medium. A tumor in the tissue causes high metabolic activity and higher blood flow, therefore heat increments are observed. To mimic the tumor effect, different carbon resistances were buried into the medium before pouring the Dragon Skin compounds. To simulate three different tumors, three different resistors whose resistances were 0.47, 1.00, and 1.50 k Ω respectively, were planted at different positions on the frame. The framework and resistor placement are shown in Fig. 3. A DC power supply was used to drive the resistors. The voltages were set to provide the same power to all of the resistors. The framework was fixed into the breast mold and the silicone compounds were poured.

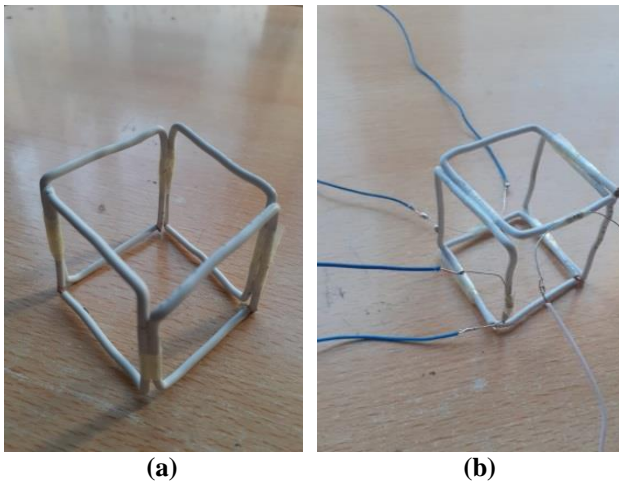


Figure 3. The frameworks for the breast phantoms. a) the framework itself; b) after the resistors planted and wires connected.

The silicone based Dragon Skin 10 poured into semi-hemisphere mold and when it was cured, taken out carefully. An actual view of a final product solid phantom pair is shown in Fig. 4. The electrical wires are for the connection to drive the resistors.



Figure 4. The prepared breast phantoms with buried different resistors as a tumor structure.

4. Results

4.1 Simulation Results

The simulations were modelled based on three different sizes and depths of the tumor. The depth, metabolic speed, and diameter of the simulated tumors were 1.50, 3.00, 4.50 cm, 29,000, 45,000, 80,000 W/m³, and 2.00, 1.50, 1.00 cm respectively. Breast models were created to search the relation between the tumor structure and surface temperature distribution.

The comparison of different metabolic speeds for the tumor had 1.50 cm depth and 2.00 cm diameter is given in Fig. 5. Approximately, 1.0 °C temperature difference from 36.8 to 37.8 °C observed at 29,000 W/m³ metabolic speed (Fig 5(a)). Similarly, 1.40 °C temperature difference from 36.8 to 38.2 °C occurred

while the metabolic speed was 45,000 W/m³ and shown in Fig 5(b). Then, 2.4 °C difference from 36.8 to 39.2 °C measured at 80,000 W/m³ given in Fig. 5(c). The results showed that the surface temperature profile linearly correlated with the metabolic speed of the tumor.

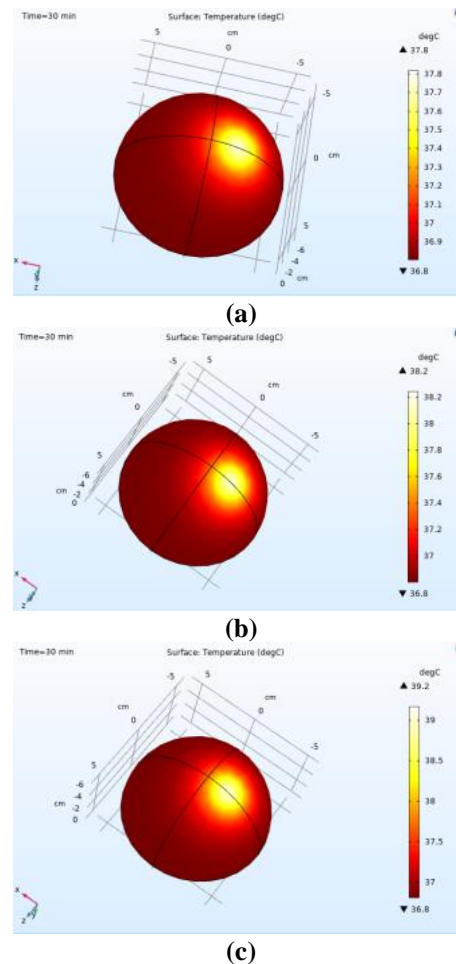


Figure 5. Thermal distribution of 1.5 cm depth and 2.0 cm diameter tumor for (a) 29,000 W/m³; (b) 45,000 W/m³ and; (c) 80,000 W/m³ metabolic speeds.

Moreover, the simulations were conducted while the metabolic speed (80,000 W/m³) and tumor diameter (1.50 cm) kept constant and the depth was variable.

It was reported that the metabolic speeds of a tumor were faster than healthy tissues between the ranges 20 to 200 times [14]. In this study, simulation results showed that 29,000, 45,000, and 80,000 W/m³ metabolic speeds were faster than healthy tissues about 65, 100, and 178 times respectively. In addition, when the ratio of tumor tissue metabolic speeds changes, the temperature gradient between tumor and neighborhood tissue varies as well.

Fig. 6 shows thermal distributions for different positioned tumors with the constant metabolic speed

(80,000 W/m³) and tumor diameter (1.0 cm). When the tumor depth was 4.5 cm, the temperature difference 0.9 °C and the tumor depth was 1.5 cm (Fig. 6(a)), temperature difference increased to 1.1 °C shown in Fig.6(b). Therefore, if tumor is located closer to the breast surface, the temperature difference goes up.

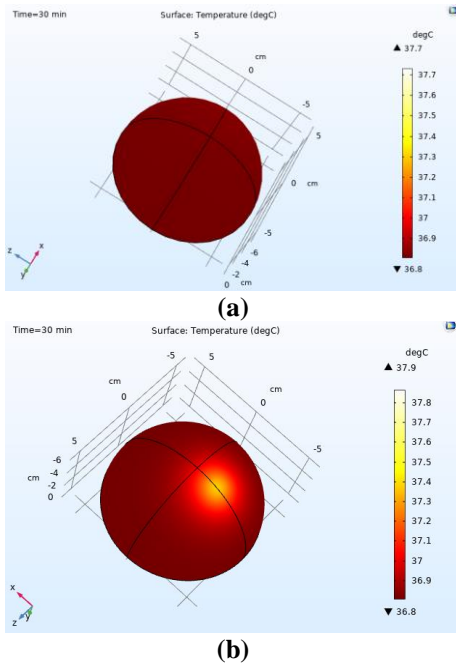


Figure 6. Thermal distribution for 80,000 W/m³ metabolic speed and 1.0 cm diameter tumor placed in (a) 4.5 cm and; (b) 1.5 cm depth.

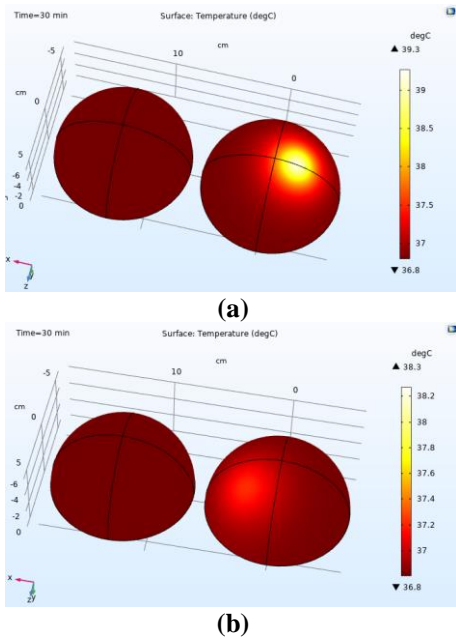


Figure 7. Asymmetry analysis simulation results for thermal distributions of healthy and a) 2.0 cm; b) 1.5 cm diameter tumor.

Moreover, asymmetry is another useful parameter to detect any differences into the breast. To analyze the asymmetry, another breast with the same features was added and is shown in Fig 7. The left hand side breast was healthy and the right one had a tumor. It has been observed that when the temperature difference ≥ 0.5 °C between the breasts, this difference can be used as an indicator parameter for an existence a tumor. In Fig. 7(a) includes a 2.0 cm diameter tumor and the temperature difference with the health one is 2.5 °C. Similarly, 1.5 cm diameter tumor and the temperature difference measured 1.5 °C in Fig. 7(b). Therefore, this is an indicator for thermal features through asymmetric studies can be used to detect tumor existence.

4.2 Experimental Study Results

Breast tumor is related with the temperature difference or deviation of the surrounding tissue. Therefore, by applying an electrical current to the resistors buried into the phantoms, a heat is generated according to the physical size of the resistors. Thermographic images were captured by a thermal camera (Med200 Iris, Meditherm, USA) whose resolution and spectral range was 320 x 240 and 7 – 14 μm respectively.

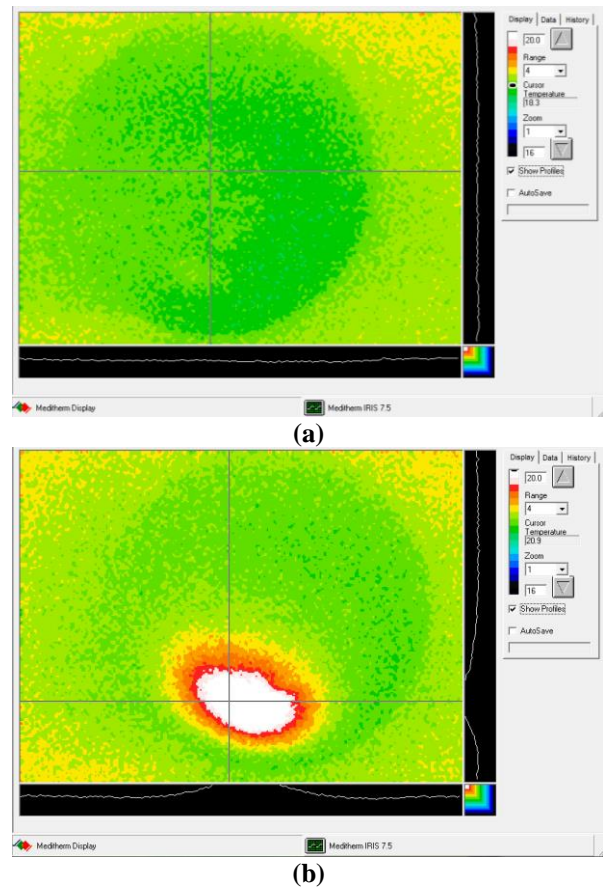
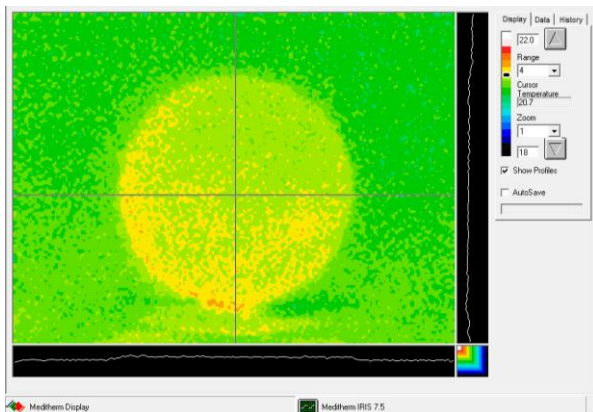


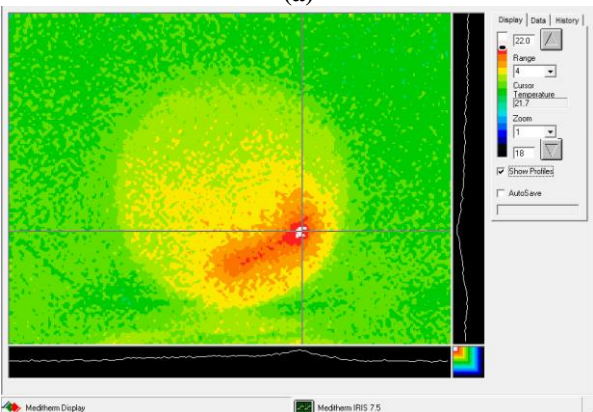
Figure 8. Thermographic image for the tumor structure (a) without tumor; (b) with the tumor in 1.5 cm depth.

The largest size and closest to the surface tumor in the breast phantom where is in 1.5 cm depth was imaged in Fig. 8. The initial condition thermographic image is in Fig 8(a) and the temperature was ~ 18.3 °C. After the resistor was driven, the temperature difference between the tumor region and surrounding tissue reached 20.9 °C and the difference was ~ 2.6 °C which is shown in Fig. 8(b).

The resistor placed in 4.5 cm depth and is given in Fig. 9. While Fig 9(a) shows the initial condition with 20.7 °C initial temperature, Fig. 9(b) shows 1.0 °C difference between the tumor and breast tissue region.



(a)



(b)

Figure 9. Thermographic images for the tumor structure (a) without tumor; (b) with the tumor in 4.5 cm depth.

As it is known that a healthy body temperature distribution is symmetrical. Thermal asymmetry is a distinctive feature abnormality in the thermography. Therefore, infrared thermography has a potential to detect breast cancers by using asymmetrical temperature distribution regions. A pair of breast is given in Fig. 10. While the left hand side one simulates the healthy breast, the right one stands for tumor mimicking. The temperature difference between the breasts was 2.3 °C. When the tumor size bigger or the location is closer to surface, the temperature difference is higher.

5. Conclusions

In this study, breast tumor detection by thermal heat distribution was demonstrated both model based simulation and also experimental in in-vitro. Tumors placed in with different sizes and depths. While the tumor metabolic speed was faster, the temperature difference was higher. In addition, when the tumor location was closer to the surface, the temperature difference was higher as well. For instance, when the tumor was of a depth ~ 1.5 cm, the temperature difference found 2.6 °C experimentally and 2.4 °C in modeled study. Similarly, when the tumor depth was placed at a 4.5 cm depth, it was observed 1.0 °C and 0.9 °C temperature difference experimentally and modeled, respectively. As can be seen, the results are highly correlated with both the simulation and experimental results. Another finding was if the tumor size was bigger, temperature difference can be distinguished better. Furthermore, it is proved that the asymmetry parameter is another promising indicator for anomalies during breast cancer. The asymmetry parameter makes the comparison easier and thermal detection reveals the anomaly detection and makes it more obvious. Therefore, it can be said that thermographic imaging is an encouraging noninvasive breast cancer imaging candidate and a useful tool for screening.

In this study, tumor detection depth was extended to 45 mm with different tumor sizes. Also, the asymmetry factor performance was shown to reveal the tumor structure with ease. In addition for the further studies, in-vitro conditions may extend to mimic more complex breast structure such as vein and capillary networks and fat, muscle, ducts, and lymph nodes, etc. Moreover, it needs to be done to measure sensitivity, specificity, and selectivity performances. Therefore, it can help to differentiate normal, benign, and malignant cases in breast cancer.

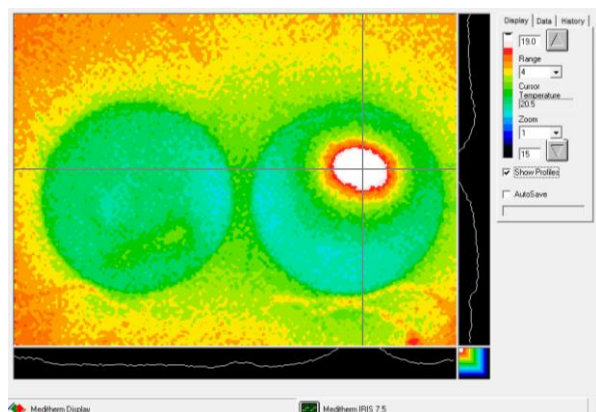


Figure 10. Asymmetric case demonstration for the healthy and tumor breasts. Left had side is healthy, right hand side is cancer case.

Acknowledgments

This study was supported by Ege University grant no. ONAP-FOA-2020-22288.

Authors' contributions

Zeynep Ayyildiz: planned, and conducted all the experiments,
Ibrahim Akkaya: involved in writing original draft, creating, and editing some figures and manuscript,
Mehmet Engin: Obtained support, had conceptualization, and investigation.
All authors read and approved the final manuscript.



Competing interests

The authors declare that they have no competing interests.

References

- [1]. Terrasse V. 2020. Latest global cancer data, Report No: 292, International Agency for Research on Cancer (IARC), 2020.
- [2]. Lin Q. Y., Yang H. Q., Xie S. S., Wang Y. H., Ye Z., Chn S. Q. 2009. Detecting early breast tumor by finite element thermal analysis, *Journal of Medical Engineering & Technology*, 33(4): 274-280.
- [3]. Hernandez J. L. G., Recinella A. N., Kandlikar S. G., Dabydeen D., Medeiros L., Phatak P. 2019, Technology, application and potential of dynamic breast thermography for the detection of breast cancer, *International Journal of Heat and Mass Transfer*, 131: 558-573.
- [4]. Levy A., Dayan A., Ben-David M., Gannot I. 2010, A new thermography-based approach to early detection of cancer utilizing magnetic nanoparticles theory simulation and in-vitro validation, *Nanomedicine: Nanotechnology, Biology, and Medicine*, 6(6), 786 – 769.
- [5]. Lawson R. N. 1956. Implications of surface temperatures in the diagnosis of breast cancer, *Canadian Medical Association Journal*, 75(4): 309 – 310.
- [6]. Lozano A., Hassani pour F. 2019, Infrared imaging for breast cancer detection: An objective review of foundational studies and its proper role in breast cancer scanning, *Infrared Physics & Technology*, 97: 244 – 257.
- [7]. Lawson R. N. 1957. Thermography – a new tool in the investigation of breast lesion, *Canadian Services Medical Journal*, 8(8): 517 – 524.
- [8]. Collet A. E., Guilfoyle C., Gracely E. J., Frazier T. G., Barrio A. V., 2014. Infrared imaging does not predict the presence of malignancy in patient with suspicious radiologic breast abnormalities. *The Breast Journal*, 20(4), 375 – 380.
- [9]. Wu L. A., Kuo W. H., Chen C. Y., Tsai Y. S., Wang J., 2016. The association of infrared imaging findings of the breast with prognosis in breast cancer patients; an observational cohort study, *BMC Cancer*, 16(1).
- [10]. Rassiwala M., Mathur P., Mathur R., Farid K., Shukla S., Gupta P. K., Jain B., 2014. Evaluation of digital infra-red thermal imaging as an adjunctive screening method for breast carcinoma: a pilot study, *International Journal of Surgery*, 12(12): 1439 – 1443.
- [11]. Delgado F. G., Luna J. G. V., 2010. Feasibility of new generation infrared imaging screening for breast cancer in rural communities, *US Oncological Review*, 6(1): 60 – 64.
- [12]. Wahab A. A., Salim M. I. M., Yunus J., Thermal distribution analysis in multi-layers homogenous phantom using infrared technique: A preliminary study, 2014 IEEE Conference on Biomedical Engineering and Sciences (IECBES). IEEE, 2014, 628-633.
- [13]. Hossain S., Mohammadi F., One-dimensional steady state analysis of bioheat transfer equation: tumor parameters assessment for medical diagnosis application, Proceedings 6th International Multi-conference on Engineering and Technological Innovation (IMETI 2013), 2013, pp 26–30.
- [14]. Roslidar, R., Rahman, A., Muharar, R., Syahputra, M. R., Arnia, F., Syukri, M., Pradhan, B., & Munadi, K. 2020. A review on recent progress in thermal imaging and deep learning approaches for breast cancer detection, *IEEE Access*, 8: 116176 – 116194.
- [15]. Galvan J. C. T., Guevara E., Machuca E. S. K., Villanueva A. O., Flores J. L., Gonzalez F. J. 2021. Deep convolutional neural networks for classifying breast cancer using infrared thermography, *Quantitative Infrared Thermography Journal*, DOI: 10.1080/17686733.2021.1918514.
- [16]. Allugunti V. R. 2022. Breast cancer detection based on thermographic images using machine learning and deep learning algorithms, *International Journal of Engineering in Computer Science*, 4(1): 49-56.
- [17]. Resmini R., Silva L., Araujo A. S., Medeiros P., Saade D. M., Conci A. 2021. Combining Genetic Algorithms and SVM for Breast Cancer Diagnosis Using Infrared Thermography, *Sensors*, 21(14), 4802.
- [18]. Bezerra L. A., Oliveira M. M., Rolim T. L., Conci A., Santos F. G. S., Lyra P. R. M., Lima R. C. F. 2013. Estimation of breast tumor thermal properties using infrared images, *Signal Processing*, 93: 2851-2863.
- [19]. Wang H., Qin Q.H. Computational bioheat modeling in human eye with local blood perfusion effect, *Human Eye Imaging and Modeling*, 1st edn. CRC Press, 2012, pp. 311-28.
- [20]. Xu F., Lu T. J., Seffen K. A. 2008. Biothermomechanics of skin tissue, *Journal of the Mechanics and Physics*, 56(5):1852-1884.
- [21]. Gonzales F. J. 2007. Thermal simulation of breast tumors, *Revista Mexicana de Fisica*, 53(4): 323-326.
- [22]. Pennes, HH. 1948. Analysis of tissue and arterial blood temperatures in the resting human forearm. *Journal of Applied Physiology*, 1(2): 93-122.
- [23]. Fung Y. C., *Biomechanics: Motion, Flow, Stress, and Growth*, Springer, New York, USA, 1990.
- [24]. Rai K. N., Rai S. K. 1999. Effect of metabolic heat generation and blood perfusion on the heat transfer in the tissues with a blood vessel, *Heat and Mass Transfer*, 35: 75 – 79.
- [25]. Huang H. W., Horng T. L., *Heat Transfer and Fluid Flow in Biological Processes*, Academic Press, Ch.1, p. 1-42, 2015.
- [26]. Gore J. P., Xu L. U., *Biomedical Photonics Handbook*, CRC Press, USA, Chapter 17, 2003.

Covid-19 Death and Case Numbers Forecasting with ARIMA and LSTM Models

Büşra Çetin^{1*} , Nida Gökçe Narin² 

¹Graduate School of Natural and Applied Sciences, Muğla Sıtkı Koçman University, Muğla, Türkiye

²Department of Statistics, Muğla Sıtkı Koçman University, Muğla, Türkiye

*cetinbusra@gmail.com

* Orcid No:0000-0002-3628-205X

Received: 10 February 2022

Accepted: 15 February 2023

DOI: 10.18466/cbayarfbe.1070691

Abstract

Covid-19, which quickly became a pandemic, has not yet been fully controlled despite the developed vaccines. The pandemic has caused a global economic crisis over the two-year struggle period. Many countries have lifted the restrictions they implemented in the fight against the pandemic to get out of this crisis. Despite the vaccines, the pandemic still poses a significant threat and maintains uncertainty about when life will return to pre-pandemic and when the economic crisis will be under control. Therefore, analyzing the current situation based on the policies followed so far remains a key issue in accurately predicting the future course of the pandemic. In this study, Covid-19 estimation is made with Auto Regressive Integrated Moving Average (ARIMA) and Long-Short-Term Memory (LSTM) models using daily case and death numbers for Germany, France, Italy, Ireland, Poland, Russia, and Turkey. The root mean squared error, mean absolute percentage error, mean absolute error, adjusted R2, Akaike Information Criterion, and Schwarz Information Criterion metrics were used in model selection. The results showed that the ARIMA and the LSTM models could be used to estimate the number of Covid-19 cases and deaths. It has also been observed that the prediction accuracy of the LSTM models for the countries studied is higher than that of the ARIMA models.

Keywords: ARIMA, Covid-19, Forecasting, LSTM

1. Introduction

The sars-Cov-2 virus, which first appeared in Wuhan, China, in December 2019, quickly spread and caused a pandemic by affecting the whole world in a short time. Although countries apply different policies regarding the fight against the virus, almost all countries have switched to online education, implemented curfews, and suspended social activities for a long time. With these measures taken, the virus spread from time to time decreased. Still, with the loosening of the restrictions for economic reasons, the epidemic intensified again, and this process continued as a cycle.

Studies have been started in many countries for the vaccine, which is seen as an effective tool in the fight against the pandemic. In April 2021, there were 14 vaccines on the market that were approved and put into use by at least one country. Sinovac, Johnson&Johnson,

Moderna, Oxford/AstraZeneca, and Pfizer/BioNTech et al. research has proven that the vaccines developed are effective on the virus, but the epidemic remains a threat as the virus mutates.

There are many studies in the literature to predict the progression of the epidemic. Khan F. and Gupta R. estimated the number of cases in India over 50 days using time series and daily case numbers using ARIMA and Nonlinear Auto Regressive (NAR) model-based forecasting [1]. Ozen et al. (2020) used daily validated Covid-19 case data for the United States to predict with machine learning-based Prophet, Polynomial Regression, ARIMA, Linear Regression, and Random Forest models. In the study, mean absolute percent error (MAPE), root means square error (RMSE), and mean absolute error (MAE) metrics were used to compare the performances of the models. The best predictive value according to the MAPE criterion was obtained by

Polynomial Regression [2]. Seveli and Başer (2021) predicted that the prognosis for the future period might be high in the case of estimation with the prophet model [3]. Awan and Aslam (2020) used the automatic ARIMA model in their study and estimated 10-day cases in European countries (Italy, France, Spain, and Germany) [4]. Kirbaş et al. (2020) compared ARIMA, Nonlinear Auto Regressive Neural Networks (NARNN), and LSTM models with estimated confirmed cases of Covid-19 in Denmark, Belgium, Germany, France, the United Kingdom, Finland, Switzerland, and Turkey. They showed that LSTM is the most appropriate approach. They also predicted a decrease in the rate of increase in cases [5]. Hernandez-Matamoros et al. (2020) modeled the spread of Covid-19 to six continents worldwide with ARIMA. They also investigated whether there is a relationship between countries in the same geographical region regarding the virus's behavior [6].

I

Roy et al. (2021) examined the example of India, which has a high number of daily cases, using the ARIMA model based on the data obtained between January 30 and May 11, 2020 [7]. Moftakhar et al. (2020) made new cases estimation with the Artificial Neural Network (ANN) and ARIMA models they created using the Iranian new case numbers observed between February 19 and March 30, 2020. They showed that ARIMA's estimation performance was higher [8]. In their study, Alzahrani et al. (2020) estimated cases with Auto-Regressive (AR), Moving Average (MA), Auto Regressive Moving Average (ARMA), and ARIMA models for the next four weeks using the number of new cases seen in Saudi Arabia between March 2 and April 20, 2020 [9].

Elsheikh et al. (2021) proposed an LSTM model to estimate the total number of confirmed cases, totally recovered cases, and total deaths in Saudi Arabia. The accuracy of the proposed model was compared with ARIMA and nonlinear autoregressive neural network (NARANN) and used to estimate the total number of confirmed cases, total recovered cases, and total deaths for Brazil, India, Saudi Arabia, South Africa, Spain, and the USA [10]. Ala'raj et al. (2021) predicted the development of the Covid-19 outbreak in the United States using SEIRD (Susceptible, Exposed, Infectious, Recovered, and Deceased) and ARIMA models [11]. Eroğlu (2020) used ANN and LSTM models to predict the number of cases 7 days in advance by using the official data of Turkey and concluded that ANN models performed better in predictions [12]. There are many more studies in the literature on the Covid-19 pandemic. However, most of the 2020 studies used relatively fewer data.

Despite the vaccines developed, the fight against the pandemic remains important due to its different variants. As the number of observations increases in

data learning systems, the prediction performance of the models to be created also increases. For this reason, forward-looking predictions are made in this study by examining the course of the epidemic exceeding one year. The daily death and case numbers between March 2020 and October 2021 were modeled using ARIMA and LSTM methods for Germany, France, Ireland, Italy, Poland, Russia, and Turkey. In addition, 10-day cases and deaths are estimated using ARIMA models used in short-term time series estimation and LSTM models based on deep neural networks.

2. Material and Methods

Data collected at certain time intervals are called time series (TS) data. Different models have been developed to make predictions for the future with the help of TS data, which contains the observation values of past periods. The most widely used among these models are the ARIMA models, which can model the linear relationship between the data forming the series without needing any prior knowledge about the structure and general trend of the series. ARIMA models can be successfully applied to stationary series or series that can be made stationary by taking the difference. LSTM is a deep learning model used in solving time series problems. It was developed to solve the gradient descent problem that occurs in the backpropagation process in Recurrent Neural Network. LSTM networks consist of input gate, cell state, forget gate, and output gates, which use sigmoid or tahn activation function to solve short-term memory problems. Thanks to these gates that control and regulate the flow of information, it can receive the information from the previous time and transmit it to the next time. With training, the model can decide which information to remember and which to forget. ARIMA and LSTM models were used in this study due to their widespread use in time series modeling and their successful forecasting performance. The data used in the study were obtained from the Covid-19 dataset published by Our World in Data [13]. For Germany, France, Ireland, Italy, Poland, Russia, and Turkey, the probable number of cases and deaths for the next ten days is predicted with the prediction models created using the daily confirmed deaths and new cases numbers until 30 October 2021.

2.1. Auto Regressive Integrated Moving Average

Auto Regressive Integrated Moving Average (ARIMA) is a univariate time series modeling approach that combines both auto regressive (AR) and moving average (MA) models. The model based on using the autocorrelation structure of the time series was proposed by George Box and Gwilym Jenkins [13]. ARIMA models are defined as ARIMA(p,d,q). AR(p) represents p-order autoregressive process, MA(q) represents a qth degree of moving average process. If the processed time

series is not stationary, d is the number of differencing required to make the time series stationary.

An AR model is assumed to be generated from a linear function of the past values of the time-series. The AR models are named according to the number of past observations they contain, and the model containing p past values is shown as AR(p). In the AR(p) model, the current output x_t is expressed by previous values and parameters, as formulated in Eq. (2.1), where t is the time, p is the order of the parameters, ϕ_i are the autocorrelation coefficients, c is a constant value, and ε_t is the Gaussian white noise series with mean zero and variance σ_ε^2 [14].

$$x_t = c + \sum_{i=1}^p \phi_i x_{t-i} + \varepsilon_t \quad (2.1)$$

The MA models are models in which the observation value in a certain period of the time series is expressed as a linear combination of the error terms of the same period and the error terms of the q number of past periods. In the MA(q) model, the current output x_t is expressed by previous values and parameters, as formulated in Eq. (2.2), where t is the time, q is the order of the parameters, θ_i are the partial autocorrelation coefficients, ε_t is the Gaussian white noise series with mean zero and variance σ_ε^2 [15].

$$x_t = \varepsilon_t + \sum_{i=1}^q \theta_i \varepsilon_{t-i} \quad (2.2)$$

The ARMA models, a combination of AR and MA models, are also frequently used to model stationary time series [14]. The ARMA(p, q) model is defined as in Eq (2.3).

$$x_t = c + \sum_{i=1}^p \phi_i x_{t-i} + \sum_{i=1}^q \theta_i \varepsilon_{t-i} \quad (2.3)$$

Non-stationary time series are made stationary by taking the difference. The models applied to the series converted to stationary by the difference process are called integrated models. For example, if the time series has a linear trend, the first difference series is stationary. On the other hand, if the time series has a curvilinear trend, the second difference series is stationary by retaking the differences. The model used in this case is expressed as ARIMA(p, d, q). Here, “ d ” refers to the stationarization parameter of the series [15,17]. The ARIMA(p, d, q) model is defined as in Eq (2.4).

$$x_t = (1 - x_{t-d}) + \sum_{i=1}^p \phi_i x_{t-i} + \varepsilon + \sum_{i=1}^q \theta_i \varepsilon_{t-i} \quad (2.4)$$

Model selection is based on AIC, SIC, and adjusted R^2 values. The model with the lower absolute values of the AIC and SIC information criteria and the higher adjusted R^2 is the most appropriate model.

2.2. Long Short Term Memory

Long-short-term memory (LSTM) is a deep learning approach with recurrent neural networks (RNN) architecture proposed by Hochreiter and Schmidhuber [18]. RNN is also used to handle long-term dependencies, but it can cause losses by taking into account previous periods' learning. This situation is known as the vanishing gradient problem. The vanishing gradient problem is due to backpropagation optimization used in neural network training.

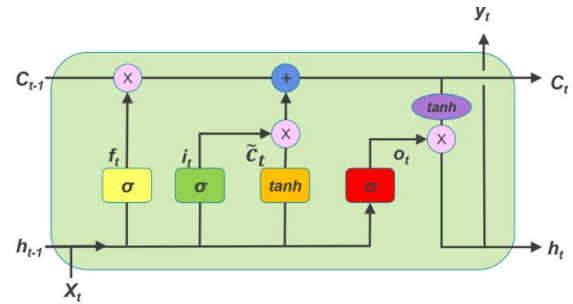


Figure 1. The LSTM Architecture [20]

Backpropagation optimization ensures that the weight and bias values in different layers of a neural network are updated by stepping in the gradient of the weight/bias values for the loss function. However, in the case of the vanishing gradient, it is not possible to update the weights/bias values or perform the learning. LSTM has been developed to solve the gradient vanishing problem encountered in RNNs and is widely used in time series estimation and natural language processing [19].

The LSTM architecture consists of an entry gate, an exit gate, and a forget gate. These gates regulate the flow of information entering and leaving the cell. They also allow cells to enable data to be passed or discarded optionally. The mathematical representation of the LSTM architecture given in Figure 1 is as follows.

$$f_t = \sigma(W_{f,x} * X_t + W_{f,h} * h_{t-1} + b_f) \quad (2.5)$$

$$i_t = \sigma(W_{i,x} * X_t + W_{i,h} * h_{t-1} + b_i) \quad (2.6)$$

$$\hat{c}_t = \tanh \sigma(W_{c,x} * X_t + W_{c,h} * h_{t-1} + b_c) \quad (2.7)$$

$$C_t = (C_{t-1} * f_t + i_t * \hat{c}_t) \quad (2.8)$$

$$o_t = \sigma(W_{o,x} * X_t + W_{o,h} * h_{t-1} + b_o) \quad (2.9)$$

$$h_t = o_t * \tanh(C_t) \quad (2.10)$$

Where, W represents the weight matrix, b represents the bias vector, i_t represents the input gate, f_t represents the forget gate, and o_t represents the output gate. Eq (2.5)

decides what information to enter through the gate using X_t and h_{t-1} as inputs. With the help of the sigmoid activation function (σ) used in the forget gate, it determines whether the information to be entered will pass to the next stage (if its value is 1) or not (if its value is 0).

Eq (2.6) decides which information to update. With Eq (2.7), a vector of new candidate information is created in the tanh layer. Then, with Eq (2.8), new information is created. Finally, using Eq (2.9) and Eq (2.10), the output is obtained. [21, 22].

2.3 Model Selection

The dates of the first cases observed in the countries used in this study differ. In addition, many factors affect the total number of patients and the number of daily cases and deaths, such as countries' health policies, the quarantine measures they take, the restrictive standards they apply, and the hygiene practices. However, all these factors were ignored in the study. The problem is treated as a univariate time series modeling problem using only observed death and case numbers.

The performance of a forecasting model is determined by comparing the observed values with the predicted values. In this study, RMSE, MAPE, MAE metrics, which are frequently preferred, are used to assess the performance of time series forecasting models. The RMSE measures the distance between the actual value and the predicted value, that is, the spread of the prediction error. The MAE is a linear score that measures the mean size of all individual errors in the predictions, regardless of their direction. MAPE expresses the reliability of the estimation methods as a percentage. If there are zeros among the actual values, the MAPE value cannot be calculated due to a division by zero error. The percentage error cannot exceed 100% for very low forecast values, but there is no upper limit to the percent error for very high forecast values. MAPE is biased in that it systematically chooses a method with very low estimates. RMSE, MAPE, and MAE are calculated using the formulas given in Eq (2.11), Eq (2.12), and Eq (2.13) respectively [23].

$$RMSE = \sqrt{\frac{1}{n} \sum_{i=1}^n (y_i - \hat{y}_i)^2} \quad (2.11)$$

$$MAPE = \frac{\sum_{i=1}^n \frac{|y_i - \hat{y}_i|}{y_i}}{n} * 100 \quad (2.12)$$

$$MAE = \frac{1}{n} \sum_{i=1}^n |y_i - \hat{y}_i| \quad (2.13)$$

3. Case Study

As a case study, the daily number of Covid-19 cases and daily deaths in seven countries (Germany, France, Ireland, Italy, Poland, Russia, and Turkey) were examined. Data from March 2020 to October 2021 were used in the modeling performed with ARIMA and LSTM. Then, the 10-day number of cases and deaths between October 31, 2021, and November 9, 2021, for each country was estimated.

3.1 Forecasting with ARIMA

Eviews 10 program was used in ARIMA modeling. First of all, for the number of cases and deaths by country, stability control was carried out with the ADF (Augmented Dickey Fuller) test. ARMA models were applied to the stationary data sets. Non-stationary data sets were made stationary by taking the first and second differences. AR and MA levels in the models were determined by examining the ACF (autocorrelation) and PACF (partial autocorrelation) graphs, respectively. Models selected according to AIC, SIC, and Adjusted R^2 criteria are given in Table 1. The models with the lowest AIC and SIC values and the highest Adjusted R^2 values were selected as the best model among the possible model. Four data sets (France-Death, Ireland-Case, Turkey-Death and Case) are modeled with ARMA as they are stationary at the level. All other data sets are modeled with ARIMA since they become stationary at first difference.

Table 1. Selected Models for Countries

Countries	ARMA/ARIMA	Adj. R^2	AIC	SIC
Germany	Case (4,1,4)	0.57	19.49	19.56
	Death (6,1,2)	0.82	12,11	12,17
France	Case (5,1,7)	0.59	21.25	21.35
	Death (4,4)	0.72	12.57	12.65
Ireland	Case (2,2)	0.84	14.87	14.91
	Death (3,1,2)	0.45	8.09	8.14
Italy	Case (5,1,10)	0.57	17.26	17.38
	Death (5,1,2)	0.94	10.93	10.99
Poland	Case (5,1,4)	0.94	17.76	17.84
	Death (2,1,8)	0.68	11.13	11.22
Russia	Case (6,1,5)	0.35	15.61	15.71
	Death (5,1,2)	0.48	-0.57	-0.50
Turkey	Case (4,0)	0.98	17.90	17.94
	Death (2,0)	0.98	7.80	7.83

3.2 Forecasting with LSTM

Each country's death and case numbers are modeled through the LSTM architecture using the Keras library with the Python programming language. 70% of the datasets are reserved for training and 30% for testing. The LSTM architecture is built with 100 neurons in each hidden layer and one neuron in the output layer.

Table 2. Optimal Values for LSTM Models

Countries		Epoch	Batch Size	Look Back
Germany	Case	100	40	28
	Death	80	100	28
France	Case	100	15	28
	Death	100	30	28
Ireland	Case	100	70	28
	Death	150	80	28
Italy	Case	100	100	28
	Death	100	80	28
Poland	Case	200	18	28
	Death	150	30	28
Russia	Case	130	20	28
	Death	100	50	28
Turkey	Case	180	150	28
	Death	100	50	28

Optimum values of the epoch, batch size, and look-back parameters were determined separately for each model by manual search method. The model was trained with randomly different parameter groups, and the

performances were observed until the best results were obtained by making the prediction error as small as possible. The parameter values determined at the end of trial-and-error execution procedures are given in Table 2.

3.3 Performance Comparison of Models

The number of cases and deaths between 31.10.2021 and 9.11.2021 for all countries was estimated by the models created with ARIMA and LSTM. The prediction performances of the models were compared using RMSE, MAPE, and MAE metrics. The results obtained are given in Table 3. The metrics used can range from 0 to ∞ , but values close to 0 represent better performance.

The results obtained in this study generally showed that the prediction performance of LSTM is higher. According to the RMSE metric, the difference between the performances of the two models was much higher, while it was relatively small compared to the MAE metric. In addition, the daily changes in the forecast values produced by the models are given graphically in Figure 2.

Table 3. Performance Comparison of Models

Countries		RMSE		MAPE		MAE	
		ARIMA	LSTM	ARIMA	LSTM	ARIMA	LSTM
Germany	Case	8494.88	7902.24	289.56	231.77	7347.9	7445.6
	Death	59.22	54.44	310.46	435.31	46.9	48.2
France	Case	3549,14	3012.22	81.36	69.72	3284	2743.3
	Death	28.10	21.14	152.97	73.85	24.2	16.6
Ireland	Case	1330,49	796.48	28.83	14.88	1060.7	546.7
	Death	16,79	16.65	NAN	NAN	12.3	7.1
Italy	Case	983.79	937.64	18.90	19.32	746.7	790.3
	Death	12.31	16.52	32.32	47.88	11.6	14.8
Poland	Case	4538.88	958.17	34.30	24.52	3921.7	2510.2
	Death	78.53	0.95	357.76	205.88	64.1	51.5
Russia	Case	3009.30	991.00	6.55	2.08	2531.5	810.6
	Death	44.97	51.99	3.32	4.35	38.5	50.2
Turkey	Case	3456.58	1874.75	11.41	5,28	3261.1	1517.7
	Death	17.74	17.20	5.75	6.39	12.8	13.9

The solid red line in the graphs shows the actual number of deaths and cases. The green dashed line shows the ARIMA prediction values, and the blue dashed line shows the LSTM values. When the graphs are examined, it is seen that the models are successful in estimating the general trend but cannot catch extreme changes.

4. Conclusion

Despite the vaccines developed and all the precautions taken, the Covid-19 pandemic still continues. This study aims to predict the future values of the number of Covid-19 cases and deaths daily. Many factors affect the spread of Covid-19, the number of cases and deaths,

such as age, chronic diseases, and social relations. It has been effective on the number of cases and deaths in vaccines applied to improve herd immunity, but Covid-19 still poses a significant threat to human and public health due to emerging new variants. In this study, ignoring all other effects, we focused only on the number of cases and deaths and predicted the number of cases and deaths for the next ten days with univariate time series models.

For the purpose of the study, seven countries with the highest number of daily cases and deaths in the first peak period of the pandemic were selected, and their data were modeled using ARIMA and LSTM methods.

In the literature, there are studies carried out with a similar purpose. However, many of these studies were published in the first year of the pandemic. In general, they examined a single country as a case study. However, the course of the epidemic differs from country to country, and as the amount of data used in modeling increases, the performance of time series models increases. Our study differs from those in the

literature regarding both the countries studied and the amount of data used in the modeling. For the seven countries covered in the study, separate estimation models were obtained using the number of cases and deaths from March 2020 to October 2021. These models estimated the 10-day cases and deaths from 31 October 2021.

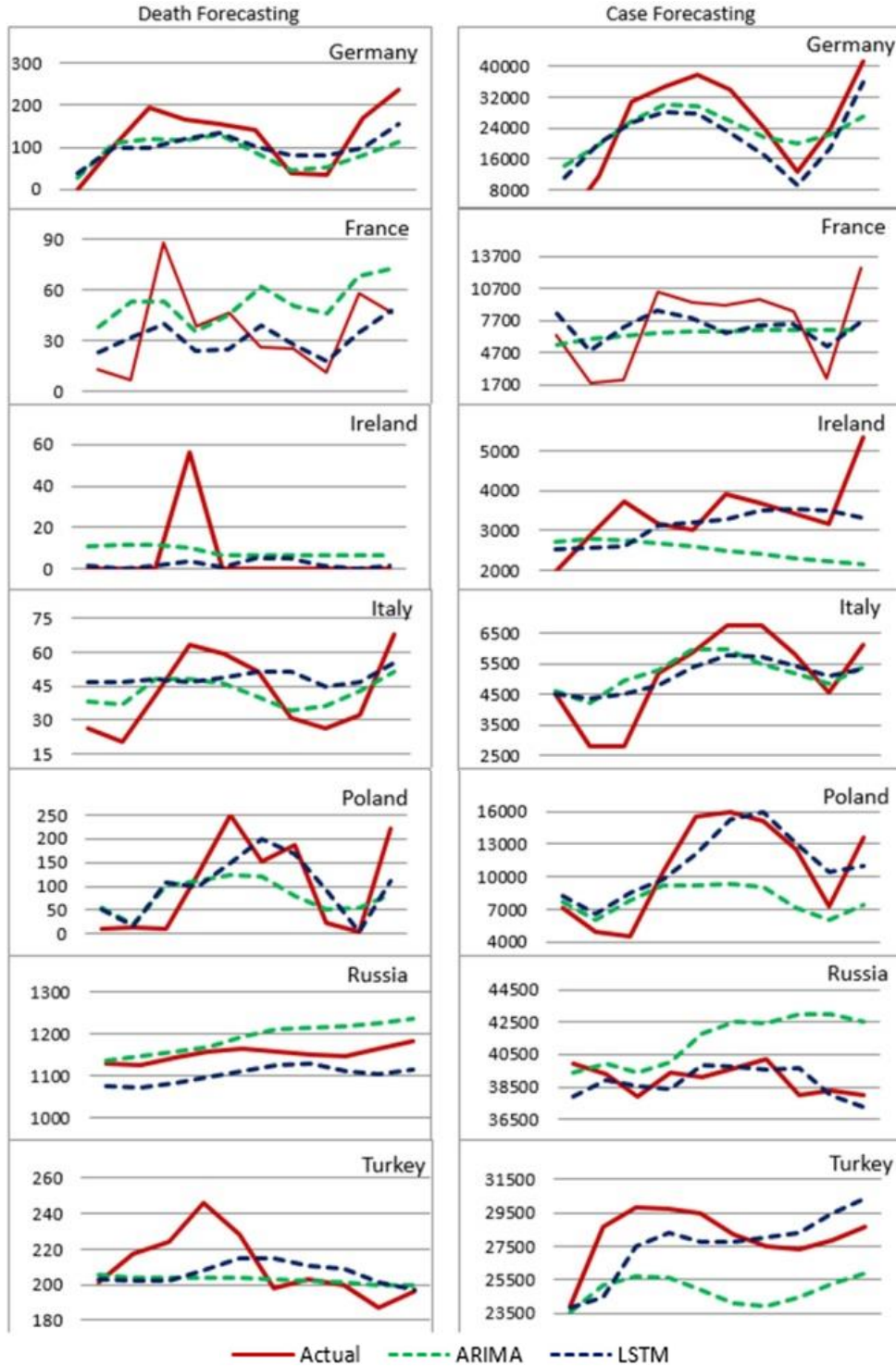


Figure 2. Graph of ARIMA and LSTM forecast versus actual values for 10-days cases and deaths.

In the results in Table 3, while the ARIMA models were more successful in estimating the Italian and Russian death numbers according to the RMSE, the LSTM's prediction success was higher in the remaining twelve models. According to MAPE values, while ARIMA's prediction performance was good for five models, LSTM was more successful in eight models. MAPE values could not be calculated as there were no deaths on some days in Ireland during the forecast period. According to MAE values, LSTM produced successful predictions with six models versus eight models. When the results are evaluated in terms of all metrics, while the prediction performance of LSTM is higher for seven models, ARIMA produced more successful predictions in only two models.

When the actual values and the estimated values of the numbers of deaths and cases given in Figure 1 are examined, it is seen that the LSTM models are more successful than ARIMA in forecasting the structure of the accurate data. However, due to the factors that were not taken into account in the univariate time series analysis, the extreme values occurring in the real data could not be captured in both models. ARIMA models estimated the numbers of deaths and cases for Russia and cases for Turkey and Ireland as far greater than their actual values. The LSTM model, on the other hand, estimated the number of deaths in Russia smaller than their actual values.

The results of the study showed that the ARIMA and LSTM models were successful in predicting the short-term future of the Covid-19 outbreak. In future studies, multivariate time series methods and different deep learning methods can be used to capture shock effects and increase prediction accuracy.

Author's Contributions

Büşra ÇETİN: Drafted and wrote the manuscript, performed the experiment and result analysis.

Nida GÖKÇE NARİN: Assisted in analytical analysis on the structure, supervised the experiment's progress, result interpretation and helped in manuscript preparation.

Ethics

There are no ethical issues after the publication of this manuscript.

References

[1].Khan F, Gupta R. 2020. ARIMA and NAR based prediction model for time series analysis of COVID19 cases in India *Journal of Safety Science & Resilience*, 12-18.

[2].Özen N, Saraç S. ve Koyuncu M. 2021 Prediction of COVID-19 Cases in the United States of America with Machine Learning

Algorithms, *European Journal of Science and Technology Special Issue 22*, pp. 134-139.

[3].Sevli, O. & Başer, V. G. 2020 Machine Learning Based Case Estimation Using Prophet Model with Time Series Data for Covid-19 Outbreak, *European Journal of Science and Technology* No. 19, 827-835.

[4]. Awan T. M., Aslam F. 2020. Prediction of daily COVID-19 cases in European countries using automatic ARIMA model *J Public Health Res.* 9(3),1765.

[5].Kırbaş İ., Sözen A., Tuncer A.D., Kazancıoğlu F.Ş. 2020 Comparative analysis and forecasting of COVID-19 cases in various European countries with ARIMA, NARNN and LSTM approaches *Chaos Solitons Fractals* 110015

[6].Hernandez-Matamoros, A., Fujita, H., Hayashi, T., & Perez-Meana, H. 2020. Forecasting of COVID19 per region using ARIMA models and polynomial functions. *Applied Soft Computing*, 96, 106610.

[7].Roy, S., Bhunia, G. S., & Shit, P. K. 2021. Spatial prediction of COVID-19 epidemic using ARIMA techniques in India. *Modeling earth systems and environment*, 7(2), 1385-1391.

[8]. Moftakhar, L., Mozghan, S. E. I. F., & Safe, M. S. 2020. Exponentially increasing trend of infected patients with COVID-19 in Iran: a comparison of neural network and ARIMA forecasting models. *Iranian Journal of Public Health*.

[9].Alzahrani, S. I., Aljamaan, I. A., & Al-Fakih, E. A. 2020. Forecasting the spread of the COVID-19 pandemic in Saudi Arabia using ARIMA prediction model under current public health interventions. *Journal of infection and public health*, 13(7), 914-919.

[10].Elsheikh, A. H., Saba, A. I., Abd Elaziz, M., Lu, S., Shanmugan, S., Muthuramalingam, T., ... & Shehabeldeen, T. A. 2021. Deep learning-based forecasting model for COVID-19 outbreak in Saudi Arabia. *Process Safety and Environmental Protection*, 149, 223-233.

[11]. Ala'raj, M., Majdalawieh, M., & Nizamuddin, N. 2021. Modeling and forecasting of COVID-19 using a hybrid dynamic model based on SEIRD with ARIMA corrections. *Infectious Disease Modelling*, 6, 98-111.

[12].Eroğlu Y. 2020. Forecasting Models For Covid-19 Cases of Turkey Using Artificial Neural Networks and Deep Learning, *Journal of Industrial Engineering* 31(3), 354-372.

[13]. URL <https://github.com/owid/covid-19-data/tree/master> (accessed at 12.11.2021).

[14]. Box, G.E.P. and Jenkins, G.M. 1970. *Time Series Analysis: Forecasting and Control*. San Francisco: Holden-Day.

[15]. Özmen A., 1986 Zaman Serisi Analizinde Box-Jenkins Yöntemi ve Banka Mevduat Tahmininde Uygulama Denemesi, Anadolu Üniversitesi Yayınları, 207, Eskişehir. (Özmen A.Box-Jenkins Method in Time Series Analysis and Application Trial in Bank Deposit Estimation, Anadolu University Press, 207, Eskişehir 1986)

[16]. Akdi, Y. Zaman Serileri Analiz, *Genelleştirilmiş2. Baskı, Gazi Kitabevi, Ankara.2010* (Akdi, Y. Time Series Analysis, *Generalized 2nd Editioni, Gazi Bookstore, Ankara.2010*)

[17].Hamzaçebi, C. ve Kutay, F., 2004.Electric Consumption Forecasting of Turkey Using Artificial Neural Networks up to Year



2010", Journal of The Faculty of Engineering and Architecture of Gazi University, (19), No 3, 227-233.

[18]. Hochreiter & Schmidhuber, 1997. Long Short-Term Memory, *Neural Computation* 9(8):1735-1780.

[19]. Kara A. 2019. Global Solar Irradiance Time Series Prediction Using Long Short-Term Memory Network *Journal of Science, Gazi University GU J Sci, Part C*, 7(4): 882-892.

[20]. T. W. C. B. Aya Abdelsalam Ismail, 2018. Improving Long-Horizon Forecasts with Expectation-Biased, [arXiv:1804.06776](https://arxiv.org/abs/1804.06776) [cs.LG]

[21]. M. Yuan, Y. Wu, L. Lin, 2016. Fault Diagnosis and Remaining Useful Life Estimation of Aero Engine Using LSTM Neural Network, *IEEE International Conference on Aircraft Utility Systems (AUS)*, 135-140.

[22]. Olah, C. 2015. Understanding LSTM Networks. August 7, 2015, [colah.github.io: colah.github.io/posts/2015-08-Understanding-LSTMs](https://colah.github.io/posts/2015-08-Understanding-LSTMs)

[23]. Emang, D., Shitan, M., Abd Ghani, A. N., & Noor, K. M. 2010. Forecasting with univariate time series models: A case of export demand for peninsular Malaysia's moulding and chipboard. *Journal of Sustainable Development*, 3(3), 157.

Refraction simulation of nonlinear wave for Shallow Water-Like equation

Murat Subaşı¹ , Hülya Durur^{2*} 

¹ Department of Mathematics, Science Faculty, Atatürk University, Erzurum, Türkiye

² Department of Computer Engineering, Faculty of Engineering, Ardahan University, Ardahan, Türkiye

* hulyadurur@ardahan.edu.tr

* Orcid: 0000-0002-9297-6873

Received: 19 July 2022

Accepted: 18 November 2022

DOI: 10.18466/cbayarfbe.1145651

Abstract

The generalized (3+1) dimensional Shallow Water-Like (SWL) equation, which is one of the higher dimensional evolution equations, is successfully constructed with aid of the $(1/G')$ -expansion method, which is one of the analytical solution instruments in mathematics. Solitary waves are depicted by assigning specific values to the parameters in the SWL equation travelling wave solutions, which have a significant place in physical energy transport. Graphics representing the solitary wave at any given moment are displayed in 2D, 3D and contours. A simulation of the wave is created for different values of the velocity of a solitary wave, which is a physical quantity. In addition, by keeping the parameters other than the rupture event of the wave constant, the situation at which the velocity the wave reaches the breakage event is discussed.

Keywords: Exact solution, $(1/G')$ -expansion method, solitary wave.

1. Introduction

When one of the independent variables in the SWL equation depends on the time parameter t , it is defined as the nonlinear evolution equation [1]. Observations of physical phenomena and the resulting nonlinear partial differential equations (NPDEs) corresponding to these observations have always been a subject of research since. These research topics have application areas in fluid dynamics, quantum mechanics, materials science, chemistry and similar situations [2-4]. As a result of the observations in these application areas, models of situations related to physical events are created [5-7]. For this reason, firstly, the mathematical equivalents of these models were determined. In the next process, the exact solutions of these NPDEs were investigated with the help of powerful and effective methods. Generally, the solutions obtained were associated with the soliton concept first defined by Russell [8]. From this starting point, these application areas have been continuously developed and rapid progress has been made. One of the causes for this is that the travelling wave solutions found are of various types, which enabled these studies to continue continuously. When the literature is examined, it has been observed that various methods have been developed.

Some of these methods: modified sub-equation method [9], Lie transformation method [10], sine-Gordon expansion method [11], the first integral method [12], Hirota bilinear method [13] and so on [14-27].

The (3+1)-dimensional equation of generalized SWL is a nonlinear equation of evolution that has recently become very common [28].

$$u_{xxx} + 3u_{xx}u_y + 3u_xu_{xy} - u_{yt} - u_{xz} = 0. \quad (1.1)$$

Recently, there have been several articles on this equation. (G'/G) -expansion method procedure was obtained by Zayed, and travelling wave solutions were obtained with the aid of the generalized binary operator by Zhang [29-30]. With the aid of the Bernoulli sub equation process, wave solutions of Eq. (1.1) were attained by Dusunceli [31].

By using the $(1/G')$ -expansion method, we aim to achieve travelling wave solutions for Eq. (1.1) in this study [32,33].

The $(1/G')$ method is a method inspired by the (G'/G) method. While three different types of solutions are obtained with the (G'/G) method, the solution obtained in the $(1/G')$ method is different from these three solutions. One of the most significant reasons for choosing this method is to shed light on the shock wave phenomenon with nonlinear wave propagation in shallow waters.

2. $(1/G')$ -Expansion Method

This method was introduced to the literature in Yokus' Phd thesis [34]. Let us consider a NPDE as follows:

$$W(u, u_t, u_x, u_y, u_z, u_{xx}, \dots) = 0. \quad (2.1)$$

Where, let

$$u(x, y, z, t) = U(\xi) = U, \quad \xi = x + ky + mz - wt, \quad w \neq 0.$$

Here k, m are numbers of wave and w is a physical quantity and the velocity parameter of the wave. We can transform (2.1) to the following ODE for $U(\xi)$:

$$S(U, U', U'', \dots) = 0. \quad (2.2)$$

Solution of Eq. (2.2) has the form

$$U(\xi) = a_0 + \sum_{i=1}^n a_i \left(\frac{1}{G'} \right)^i, \quad (2.3)$$

here $a_i, (i=0,1,2,\dots,n)$ are constants, $G(\xi) = G$ provides the following quadratic linear ordinary differential equation (ODE)

$$G'' + \lambda G' + \tau = 0, \quad \tau, \lambda \in R. \quad (2.4)$$

The solution format produced by the method is as follows:

$$\frac{1}{G'(\xi)} = \frac{1}{-\frac{\tau}{\lambda} + A \cosh(\xi\lambda) - A \sinh(\xi\lambda)}, \quad A \in R. \quad (2.5)$$

Considering that the solution satisfies the equation, (2.3) substituted in Eq. (2.2). To obtain the polynomial $P(1/G') = 0$. The coefficients of all the powers of $(1/G')$ are set to zero. Thus, a system of equations is created. By solving the system of equations, unknown constants are found.

The resulting constants are substituted in Eq. (2.3) and by applying inverse transform, a travelling wave solution of Eq. (2.1) is achieved.

3. Solutions of SWL Equation

Applying the transform $u = u(x, y, z, t) = U(\xi)$ in Eq. (1.1), we get

$$kU^4 + 6kU'U'' + (kw - m)U'' = 0, \quad (3.1)$$

where w represents the velocity of the wave. After Eq. (3.1) is integrated, the following equation is attained

$$kU''' + 3k(U')^2 + (kw - m)U' = 0. \quad (3.2)$$

The n balancing term is a constant obtained between the highest order linear term and the highest order nonlinear term in any ODE [34]. So, balancing between highest order linear term U''' with highest nonlinear term $(U')^2$ in Eq. (3.2), we find the balancing term $n = 2$ and by considering in Eq. (2.3),

$$U(\xi) = a_0 + a_1 \left(\frac{1}{G'} \right) + a_2 \left(\frac{1}{G'} \right)^2. \quad (3.3)$$

Let us substitute the Eq. (3.3) in the Eq. (3.2) so that the coefficients in the Eq. (3.3) can be calculated. After some mathematical operations, a polynomial equation based on $(1/G')$ is constructed. The coefficient of each term of this polynomial is equal to zero and the following system of equations is created.

$$\begin{aligned} \frac{1}{G'[\xi]}: & -m\lambda a_1 + kw\lambda a_1 + k\lambda^3 a_1 = 0, \\ \frac{1}{G'[\xi]^2}: & -m\tau a_1 + kw\tau a_1 + 7k\lambda^2 \tau a_1 + 3k\lambda^2 a_1^2 - 2m\lambda a_2 + 2kw\lambda a_2 + 8k\lambda^3 a_2 = 0, \\ \frac{1}{G'[\xi]^3}: & 12k\lambda\tau^2 a_1 + 6k\lambda\tau a_1^2 - 2m\tau a_2 + 2kw\tau a_2 + 38k\lambda^2 \tau a_2 + 12k\lambda^2 a_1 a_2 = 0, \\ \frac{1}{G'[\xi]^4}: & 6k\tau^3 a_1 + 3k\tau^2 a_1^2 + 54k\lambda\tau^2 a_2 + 24k\lambda\tau a_1 a_2 + 12k\lambda^2 a_2^2 = 0, \\ \frac{1}{G'[\xi]^5}: & 24k\tau^3 a_2 + 12k\tau^2 a_1 a_2 + 24k\lambda\tau a_2^2 = 0, \\ \frac{1}{G'[\xi]^6}: & 12k\tau^2 a_2^2 = 0, \end{aligned} \quad (3.4)$$

using a software application, obtain the $k, \lambda, \tau, w, a_1, a_2$ and m constants, from Eq. (3.4).

Case 1. If

$$a_1 = -2\tau, \quad a_2 = 0, \quad m = k(w + \lambda^2), \quad (3.5)$$

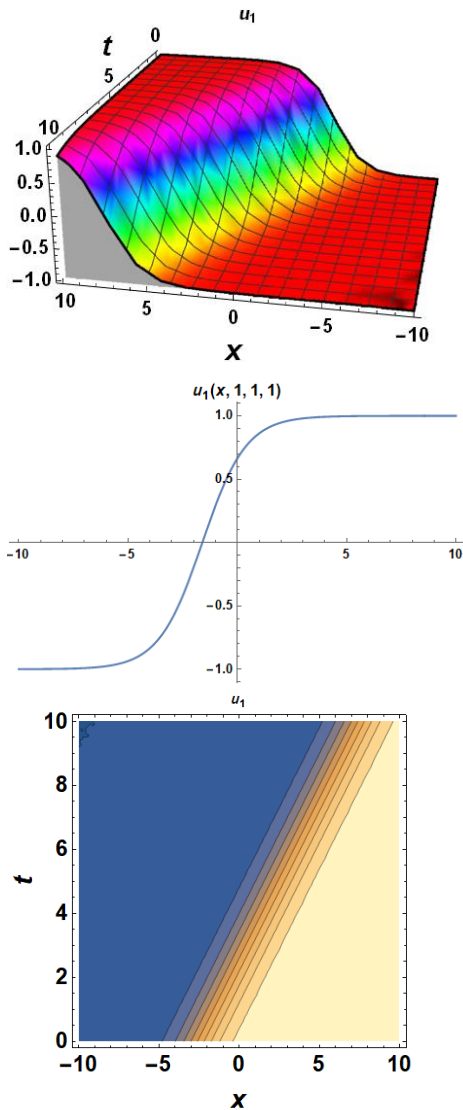


Figure1: Graphs for the Eq. (3.6) for $a_0 = 1, \lambda = -1, \tau = 0.1, w = 1, k = 0.1, y = 1, z = 1, A = 1$.

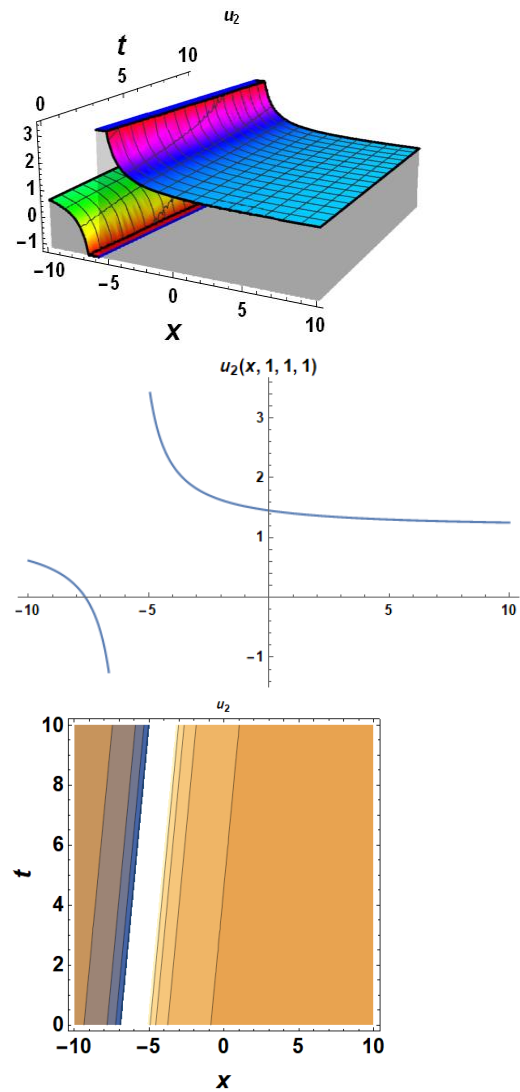


Figure2: Graphs for the Eq. (3.8) for $a_0 = 1, \lambda = 0.1, \tau = 0.1, w = 1, k = 5, y = 1, z = 1, A = 1, m = 1$.

substituting values Eq. (3.5) into Eq. (3.3) and one may have an exact solution of the hyperbolic type for Eq (1.1):

$$u_1(x, y, z, t) = -\frac{2\tau}{-\frac{\tau}{\lambda} + A \cosh[\lambda(-tw + x + ky + kz(w + \lambda^2))] - A \sinh[\lambda(-tw + x + ky + kz(w + \lambda^2))]} + a_0, \quad (3.6)$$

Case 2. If

$$a_1 = -2\tau, \quad a_2 = 0, \quad w = \frac{m - k\lambda^2}{k}, \quad (3.7)$$

substituting Eq. (3.7) into Eq. (3.3), one may have an exact solution of the hyperbolic type for Eq. (1.1):

$$u_2(x, y, z, t) = -\frac{2\tau}{-\frac{\tau}{\lambda} + A \cosh\left[\lambda\left(x + ky + mz - \frac{t(m - k\lambda^2)}{k}\right)\right] - A \sinh\left[\lambda\left(x + ky + mz - \frac{t(m - k\lambda^2)}{k}\right)\right]} + a_0, \quad (3.8)$$

4. Results and Discussion

We have attained the travelling wave solution to the generalized SWL equation by aid of the $(1/G')$ method in this study. While Duran and Kaya produced travelling wave solutions in hyperbolic, trigonometric and rational forms with the sub equation method in their studies [35], in the Yokus study, travelling wave solutions were produced with the modified Kudryashov method [36]. In Yokus et al. studies, complex hyperbolic type solution was obtained with modified $(1/G')$ method [37], and in this study, hyperbolic type

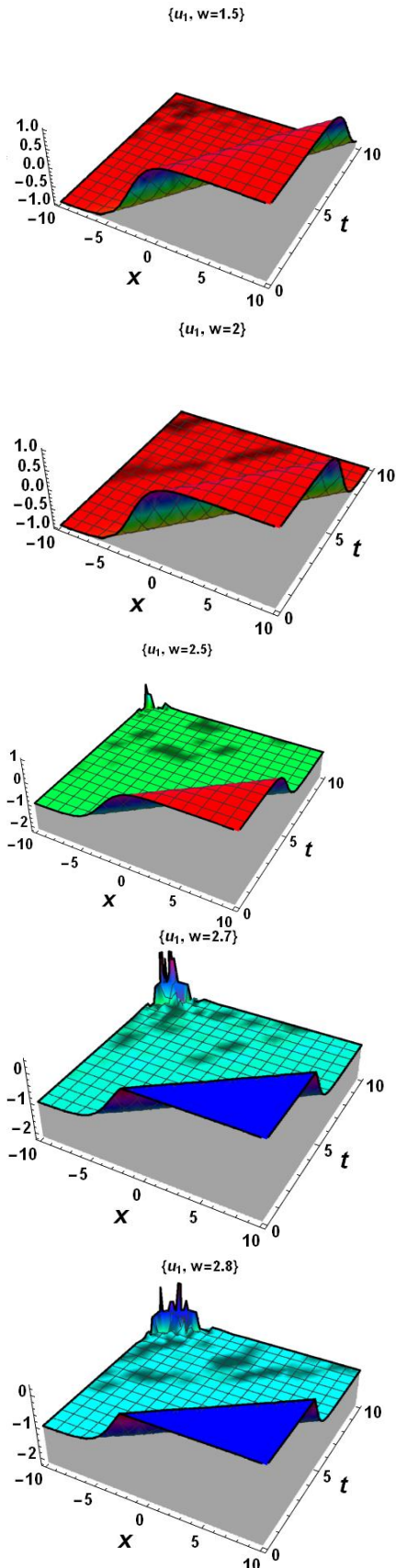


Figure3: Graphs for the Eq. (3.6) for $a_0 = 1, \lambda = -1, \tau = 0.1, k = 0.1, y = 1, z = 1, A = 1$.

solution was produced with the $(1/G')$ method. We especially observed that the $(1/G')$ method is applicable for the SWL equation, which is a high dimensional evolution equation. It was observed that the solution attained by this method supports the solutions obtained in the literature. Solitary wave solutions were created with the aid of particular values given to the travelling wave solutions attained in this article. The effect of changes in the velocity parameter in the solitary solution on wave behavior was analyzed. In this analysis part, other parameters are taken as constant. It has been observed that the change in velocity causes distortions at the extremes of the wave after a certain value. By aid of Mathematica package program, this situation is presented in 3D in the simulation below.

As seen in Figure3, it has been determined that the speed factor is a very effective parameter in solitary wave solutions. As seen in the simulation presented for different values of “ w ” which represents the velocity of the solitary wave, it can be observed that for $w = 2.5$, the wave begins to exhibit behaviors different from the normal behavior at the extreme points. We also observed that the wave was broken for $w = 2.7$. In future studies, taking into account the changes in the coefficients of classical wave transformation, its effect on wave behavior can be examined. When Eq. (3.6) is examined carefully, the velocity parameter w affects the distribution of the travelling wave in the direction z . The wave number in the direction z of the travelling wave cannot be observed in Figure3. Because variable z is considered as constant and $z=1$ is taken. In addition, the parameter λ , which comes from the methodology of the method and is more clearly seen in the Eq. (2.5), plays a significant role in the nonlinear distribution. It is an important parameter that affects both the wave velocity and the wave number.

The theme of discussion in this work is the physical parameter w , which represents the wave velocity. The effects of the wave velocity on the travelling wave solution and the condition that causes the wave to break are a matter of debate. Parameters other than the velocity parameter are out of the scope of this study. In the discussions about the behavior of travelling waves in the future, the k and m parameters, which affect the wave propagation in the y and z directions and represent the wave number, can be taken into account. It is also predicted that these physical discussions are valuable for experimental workers.

5. Conclusion

In this manuscript, the travelling wave solutions of the generalized SWL equation were successfully obtained with the $(1/G')$ method. It was concluded that the $(1/G')$ method for Eq. (1), which is one of the higher

dimensional evolution equations, is applicable according to many methods we have given in the introduction. 2D, contour and 3D graphics of these solitary waves are presented. In Figure 3, the relation between velocity parameter and $u(x, y, z, t)$ is presented in 3D, provided that the other parameters are taken as constant. The velocity values causing the breaking of the wave were investigated and determined. In future studies, many studies can be done on high dimensional nonlinear evolution equations with the help of this method.

Author's Contributions

Murat Subaş: Assistance with the production of the manuscript, result interpretation, and analytical analysis on the structure.

Hülya Durur: Conducted literature search, drafted and authored the manuscript, performed the result analysis.

Ethics

Regarding the publication of this manuscript are no ethical issues.

References

- [1]. Duran, S. 2021. An investigation of the physical dynamics of a traveling wave solution called a bright soliton. *Physica Scripta*, 96(12), 125251.
- [2]. Yokus, A, Yavuz, M. 2021. Novel comparison of numerical and analytical methods for fractional Burger–Fisher equation. *Discrete & Continuous Dynamical Systems-S*; 14(7), 2591-2606.
- [3]. Benetazzo, A, Barbariol, F, Pezzutto, P, Staneva, J, Behrens, A, Davison, S, Cavaleri, L. 2021. Towards a unified framework for extreme sea waves from spectral models: Rationale and applications, *Ocean Engineering*; 219: 108263.
- [4]. Duran, S. 2020. Exact Solutions for Time-Fractional Ramani and Jimbo—Miwa Equations by Direct Algebraic Method, *Advanced Science, Engineering and Medicine*; 12(7): 982-988.
- [5]. Raissi, M, Karniadakis, G, E. 2018. Hidden physics models: Machine learning of nonlinear partial differential equations. *Journal of Computational Physics*; 357: 125-141.
- [6]. Duran, S. 2020. Solitary Wave Solutions of the Coupled Konno-Oono Equation by using the Functional Variable Method and the Two Variables (G'/G, 1/G)-Expansion Method. *Adyaman Üniversitesi Fen Bilimleri Dergisi*; 10(2): 585-594.
- [7]. Yokuş, A. 2018. Comparison of Caputo and conformable derivatives for time-fractional Korteweg–de Vries equation via the finite difference method. *International Journal of Modern Physics B*; 32(29): 1850365.
- [8]. Russell, J. S. 1845. Report on Waves.
- [9]. Duran, S, Yokuş, A, Durur, H, Kaya, D. 2021. Refraction simulation of internal solitary waves for the fractional Benjamin–Ono equation in fluid dynamics. *Modern Physics Letters B*; 35(26): 2150363.
- [10]. Saleh, R, Mabrouk, S. M, Wazwaz, A, M. 2021. Lie symmetry analysis of a stochastic gene evolution in double-chain deoxyribonucleic acid system. *Waves in Random and Complex Media*; 1-15.
- [11]. Nestor, S, Houwe, A, Rezazadeh, H, Betchewe, G, Bekir, A, Doka, S, Y. 2022. Chirped W-shape bright, dark and other solitons solutions of a conformable fractional nonlinear Schrödinger's equation in nonlinear optics. *Indian Journal of Physics*; 96,243-255.
- [12]. Feng, Z. 2002. The first-integral method to study the Burgers–Korteweg–de Vries equation. *Journal of Physics A: Mathematical and General*; 35(2): 343.
- [13]. Alhami, R., & Alquran, M. 2022. Extracted different types of optical lumps and breathers to the new generalized stochastic potential-KdV equation via using the Cole-Hopf transformation and Hirota bilinear method. *Optical and Quantum Electronics*, 54(9), 1-12.
- [14]. Silambarasan, R, Kilicman, A. 2023. Solitons of nonlinear dispersive wave steered from Navier-Bernoulli hypothesis and Love's hypothesis in the cylindrical elastic rod with compressible Murnaghan's materials. *Mathematics and Computers in Simulation*; 203, 699-720.
- [15]. Yokuş, A. 2021. Construction of different types of traveling wave solutions of the relativistic wave equation associated with the Schrödinger equation. *Mathematical Modelling and Numerical Simulation with Applications*, 1(1), 24-31.
- [16]. Kumar, S, Kumar, A, Wazwaz, A, M. 2020. New exact solitary wave solutions of the strain wave equation in microstructured solids via the generalized exponential rational function method. *The European Physical Journal Plus*; 135: 870.
- [17]. Park, C, Khater, M, M, Abdel-Aty, A, H, Attia, R, A, Rezazadeh, H, Zidan, A, M, Mohamed, A, B. 2020. Dynamical analysis of the nonlinear complex fractional emerging telecommunication model with higher–order dispersive cubic–quintic. *Alexandria Engineering Journal*; 59(3): 1425-1433.
- [18]. Duran, S. 2021. Travelling wave solutions and simulation of the Lonngren wave equation for tunnel diode. *Optical and Quantum Electronics*; 53(8): 58.
- [19]. Yokuş, A, Durur, H, Abro, K, A, Kaya, D. 2020. Role of Gilson–Pickering equation for the different types of soliton solutions: a nonlinear analysis. *The European Physical Journal Plus*; 135: 657.
- [20]. Li, Z, Manafian, J, Ibrahimov, N, Hajar, A, Nisar, K, S, Jamshed, W. 2021. Variety interaction between k-lump and k-kink solutions for the generalized Burgers equation with variable coefficients by bilinear analysis. *Results in Physics*; 28: 104490.
- [21]. Zhang, Z, Li, B, Chen, J, Guo, Q. 2021. Construction of higher-order smooth positons and breather positons via Hirota's bilinear method. *Nonlinear Dynamics*; 105(3): 2611-2618.
- [22]. Wang, K, J, Liu, J, H. 2022. On abundant wave structures of the unsteady korteweg-de vries equation arising in shallow water. *Journal of Ocean Engineering and Science*.
- [23]. Seadawy, A, R, Rehman, S, U, Younis, M, Rizvi, S, T, R, Althobaiti, S, Makhlof, M, M. 2021. Modulation instability analysis and longitudinal wave propagation in an elastic cylindrical rod modelled with Pochhammer–Chree equation. *Physica Scripta*; 96(4): 045202.
- [24]. Alotaibi, M, F, Omri, M, Khalil, E, M, Abdel-Khalek, S, Bouslimi, J, Khater, M, M. 2022. Abundant solitary and semi-analytical wave solutions of nonlinear shallow water wave regime model. *Journal of Ocean Engineering and Science*.
- [25]. Yilmaz, E, U, Khodad, F, S, Ozkan, Y, S, Abazari, R, Abouelregal, A, E, Shaayesteh, M, T, ... Ahmad, H. 2022. Manakov

model of coupled NLS equation and its optical soliton solutions. *Journal of Ocean Engineering and Science*.

[26]. Isah, M. A., & Yokuş, A. (2022). The investigation of several soliton solutions to the complex Ginzburg-Landau model with Kerr law nonlinearity. *Mathematical Modelling and Numerical Simulation with Applications*, 2(3), 147-163.

[27]. Özkan, Y. S, Eslami, M, Rezazadeh, H. 2021. Pure cubic optical solitons with improved $\tan(\varphi/2)$ -expansion method. *Optical and Quantum Electronics*; 53(10): 1-13.

[28]. Baskonus, H, M, Eskitascioglu, E, I. 2020. Complex wave surfaces to the extended shallow water wave model with (2+1)-dimensional. *Computational Methods for Differential Equations*; 8(3): 585-596.

[29]. Zayed, E, M, E. 2010. Traveling wave solutions for higher dimensional nonlinear evolution equations using the G'/G-expansion method, *Journal of Applied Mathematics & Informatics*; 28(1_2): 383-395.

[30]. Zhang, Y, Dong, H, Zhang, X, Yang, H. 2017. Rational solutions and lump solutions to the generalized (3+1)-dimensional shallow water-like equation, *Computers & Mathematics with Application*; 73(2): 246-252.

[31]. Dusunceli, F. 2019. Exact Solutions for Generalized (3+1)-Dimensional Shallow Water-Like (SWL) Equation, *In Conference Proceedings of Science and Technology*; 2(1): 55-57.

[32]. Durur, H, Yokuş, A. 2020. Analytical solutions of Kolmogorov–Petrovskii–Piskunov equation. *Bahkesir Üniversitesi Fen Bilimleri Enstitüsü Dergisi*; 22(2): 628-636.

[33]. Yokus, A, Durur, H, Ahmad, H. 2020. Hyperbolic type solutions for the couple Boiti-Leon-Pempinelli system. *Facta Universitatis, Series: Mathematics and Informatics*; 35(2): 523-531.

[34]. Yokus, A. 2011. Solutions of some nonlinear partial differential equations and comparison of their solutions, Ph.Diss., Firat University.

[35]. Duran, S., & Kaya D. (2021). Applications of the Sub Equation Method for the High Dimensional Nonlinear Evolution Equation. *Erzincan University Journal of Science and Technology*, 14(3), 898-906.

[36]. Yokuş, A. (2021). Solitary Wave Solutions of the Generalized (3+ 1)-Dimensional Shallow Water-Like Equation by Using Modified Kudryashov Method. *Adiyaman University Journal of Science*, 11(1), 157-165.

[37]. Yokuş, A., Duran, S., & Durur, H. (2022). Analysis of wave structures for the coupled Higgs equation modelling in the nuclear structure of an atom. *The European Physical Journal Plus*, 137(9), 1-17.

Majority Vote Decision Fusion System to Assist Automated Identification of Vertebral Column Pathologies

Akın Özçift^{1*}, Mehmet Bozuyula²

¹ Department of Software Engineering, Hasan Ferdi Turgutlu Technology Faculty, Manisa Celal Bayar University, Manisa, Türkiye

² Akürün Textile Corporation, Turkey

*akinozcift@mcbu.edu.tr

* Orcid No: 0000-0003-2840-1917

Received: 3 March 2022

Accepted: 2 March 2023

DOI: 10.18466/cbayarfbe.1082067

Abstract

This paper presents a majority vote decision fusion system called AIVCP (Automated Identification of Vertebral Column Pathologies). With this aim, we proposed a three-step decision fusion algorithm: In the first step, a pool of algorithms from different groups is obtained and the number of classifiers is decreased to 10 with the use of prediction accuracy and classifier diversity concept. As a second step, different majority vote combinations of 10 algorithms are searched with a grid search strategy guided on top of 10-fold cross validation evaluation and with prediction error analysis. In the second step, we obtained four base classifiers, i.e., Naïve Bayes (NB), Simple Logistics (SL), Learning Vector Quantization (LVQ) and Decision Stump (DS) whose majority vote decision fusion generate the most accurate diagnosis rate in Vertebral Column Pathologies domain. As the third step, we applied a Support Vector Machine based feature selection to increase prediction performance of the proposed system further. The experiments are evaluated with the use of 10-fold cross-validation, Sensitivity, Specificity and Confusion Matrices. The experimental results have shown that NB, SL and LVQ single classifiers generate 0.780, 0.829 and 0.786 average diagnosis f-scores respectively. On the other hand, majority vote decision fusion of these single predictors produces 0.883 f-score value that is higher than each of the constituents. The resultant diagnosis f-score value of Vote algorithm for Vertebral column pathologies is enhanced.

Keywords: Majority voting, decision fusion, multiple-classifier systems, vertebral column pathologies

1. Introduction

There is a continuous effort to design computer-based clinical decision support systems (CDSSs) to assist clinical decision making. In this concept, CDSSs are designed software for further helping clinical decision-making based on the computerized clinical knowledge base[1].

CDSSs generally makes use of an inductive engine to learn the decision characteristics of a specific disease and then to use the proposed strategy in the diagnosis of unseen instances of the disease [2]. A high-accurate CDDS design normally comprises a three step approach: (i) preprocessing of data, (ii) feature mining in the form of feature selection or feature transformation and (iii) an intelligent decision algorithm proposal. Though, the order and necessity of those steps may change from one application to another, the general workflow is presented in Figure 1.

<p>Step 1: Input raw data with n features, $D_i = \{f_1, f_2, \dots, f_n\}$</p> <p>Step 2: Preprocess input data D_i: else skip this step</p> <p>Step 3: Make feature selection, $D_i = \{f_1, f_2, \dots, f_m\}$ for $m < n$ Or Make feature transformation else skip this step</p> <p>Step 4: Classify D_i</p>
--

Figure1. Basic CDSSs design steps.

Many machine learning (ML) algorithms are used in automated medical diagnosis literature to obtain accurate CDSSs. Taxonomy of these algorithms can be summarized as follows: (i) Logic based algorithms, i.e., decision trees and rule-based classifiers (ii) Perceptron based techniques, i.e., Artificial Neural Networks and Multi-Layer Perceptron (MLP) (iii) Statistical learning algorithms, i.e., Bayesian Networks (BN), Naïve Bayes (NB) classifiers and k-Nearest Neighbor (kNN), and

finally (iv) Support Vector Machine (SVM) classifiers [3]. Design of a CDSS makes use of a single ML algorithm from mentioned groups to apply on a specific disease domain with the most possible diagnosis accuracy. Generally, if the accuracy of the algorithm is irrelevant in terms of disease diagnosis then another strategy called multiple-classifier systems (MCSs) should be preferred to improve classification performance. In this context, a MCS may be defined as the use of multiple learners to obtain better predictive performance than could be obtained from any of the single learners. In clearer terms, human nature consults several experts before making a final decision. Similarly, automated decision making applications weigh opinions of individual members of community to obtain a more accurate final solution. “Also known under various other names, such as committee of classifiers, or mixture of experts, MCSs have shown to produce favorable results compared to those of single-expert systems for a broad range of applications and under a variety of scenarios” [4]. Various MCSs are bagging, boosting, AdaBoost, stacked generalization, mixture of experts, voting based techniques with a range of combination strategies, and decision templates [4, 5]. In particular, voting based multi-classifier algorithms comprise Maximum, Median, Mean, Minimum, and Majority vote rules to fuse individual decisions of classifiers [6]. Accordingly, the aim of this study is to develop a majority vote decision system for automated identification of vertebral column pathologies from Orthopedics field. The vertebral column system is composed by a group of vertebrae, intervertebral discs, nerves, muscles, medulla and joints. The two example dysfunctions of vertebral column are disc hernia (DH) and spondylolisthesis (SP) that may cause intense pain [7]. The analyzed dataset is from UCI repository and it is built by Dr. Henrique da Mota during a medical residence period in the Group of Applied Research in Orthopaedics (GARO) of the Centre Médico-Chirurgical de Réadaptation des Massues, Lyon, France. In the dataset, the two pathologies are defined in terms of six biomechanical attributes of the spino-pelvic system that correspond to the following parameters: angle of pelvic incidence, angle of pelvic tilt, lordosis angle, sacral slope, pelvic radius and grade of slipping [7]. Berthonnaud et al. discusses the correlation between six biomechanical attributes and the two Orthopedic pathologies in [8] with detail. In the literature, there are two significant studies that use this dataset [7–9]: In study [9], authors remove some of the instances from dataset with the help of an outlier analysis and they use 80% train-20% test set divisions for classification. They present three ensembles, i.e., SVM, MLP and GRNN with the average accuracies of 91%, 84.5% and 76.8% respectively. However, study [9] is in Portuguese and this made difficult the interpretation of the results precisely. In their second study, Neto et al. studied an embedded rejection option based SVM algorithm and they obtained 85.9% as

their highest accuracy. More recent studies that used this dataset as machine learning problem are given in [27-30]. The studies in the literature using this dataset focus on single learners. It is confidently known that ensemble learners that constitute single learners may improve the performance of a machine learning problem to some extent. Hence the design of the experiments for identification of vertebral column pathologies were evaluated in this direction [4]. As it is widely known in view of this introduction, the aim of this study is to develop a multiple-classifier algorithm to discriminate three states, i.e. normal, DH and SP, of an Orthopedic patient with an acceptable accuracy.

2. Materials and Methods

2.1 Vertebral Column Dysfunctions

Vertebral column is another term that refers to the spine or backbone, and it is the main structure of the axial skeleton of all vertebrate animals. In humans, vertebral column comprises series of vertebrae, i.e., any of the bones or segments composing the spinal column, extending from the axis bone at base of the skull to the tip of the tail. The main functions of vertebral column are: (i) permit movement of the body, (ii) enclosure and protection of the spinal cord and (iii) providing points of attachment for the ribs (bones) and muscles of the torso. Vertebral column can suffer dysfunctions that cause backaches with very different intensities. The two example pathologies of vertebral column are disc hernia and spondylolisthesis. In general, these pathological cases may originate from several traumas in the column that gradually injures the structure of the intervertebral disc [7].

Disc hernia is the result of the migration of inter-vertebral disc from its place. The other type of vertebral disease, i.e. Spondylolisthesis occurs if one of 33 vertebrae from vertebral column slides [7]. Each patient of the two diseases is defined in terms of six biomechanical features and we present brief information for these attributes in the next section.

2.2 Description of Dataset

The analyzed dataset is prepared by Dr. Henrique da Mota, who collected it during a medical residence in spine surgery at the Centre Médico-Chirurgical de Réadaptation des Massues, placed in Lyon, France. The data is extracted from sagittal panoramic radiographies of the spine of 310 patients. The characteristic of each patient is defined with the help of six biomechanical features. The name of the features defining parameters of spino-pelvic system and the distribution of dataset is provided in Table 1. There is a remarkable correlation between these biomechanical features and the mentioned diseases, and this relation is explained in [8] with detail.

Table 1. Statistical distribution of diseases and their biomechanical characteristics.

No	Distribution of patients	Name of the features
1	100: Normal	Pelvic incidence angle (PI)
2	60: Disc hernia	Pelvic tilt angle (PT)
3	150: Spondylolisthesis	Lumbar lordosis angle (LL)
4		Sacral slope (SS)
5		Pelvic radius (PR)
		Spondylolisthesis degree (SD)

Pelvic and spinal parameters are presented in Figure 2, 3 respectively and we briefly describe these features as follows:

The sacral slope (SS) is the angle between the sacral plate and the horizontal axis. Another mechanic attribute, the pelvic tilt (PT), is defined as the angle between the line connecting the midpoint of the sacral plate to the vertical plane from the centre of femoral head. The pelvic incidence (PI) is an angle between the line perpendicular to the sacral plate and the line through the center of femoral head [10]. Pelvic radius is defined as the distance between center of femoral head to the posterior superior corner of sacral plate. On the other hand, lumbar lordosis is the angle between the superior surface of the second lumbavertebral and the inferior surface of the fifth lumbavertebral [11].

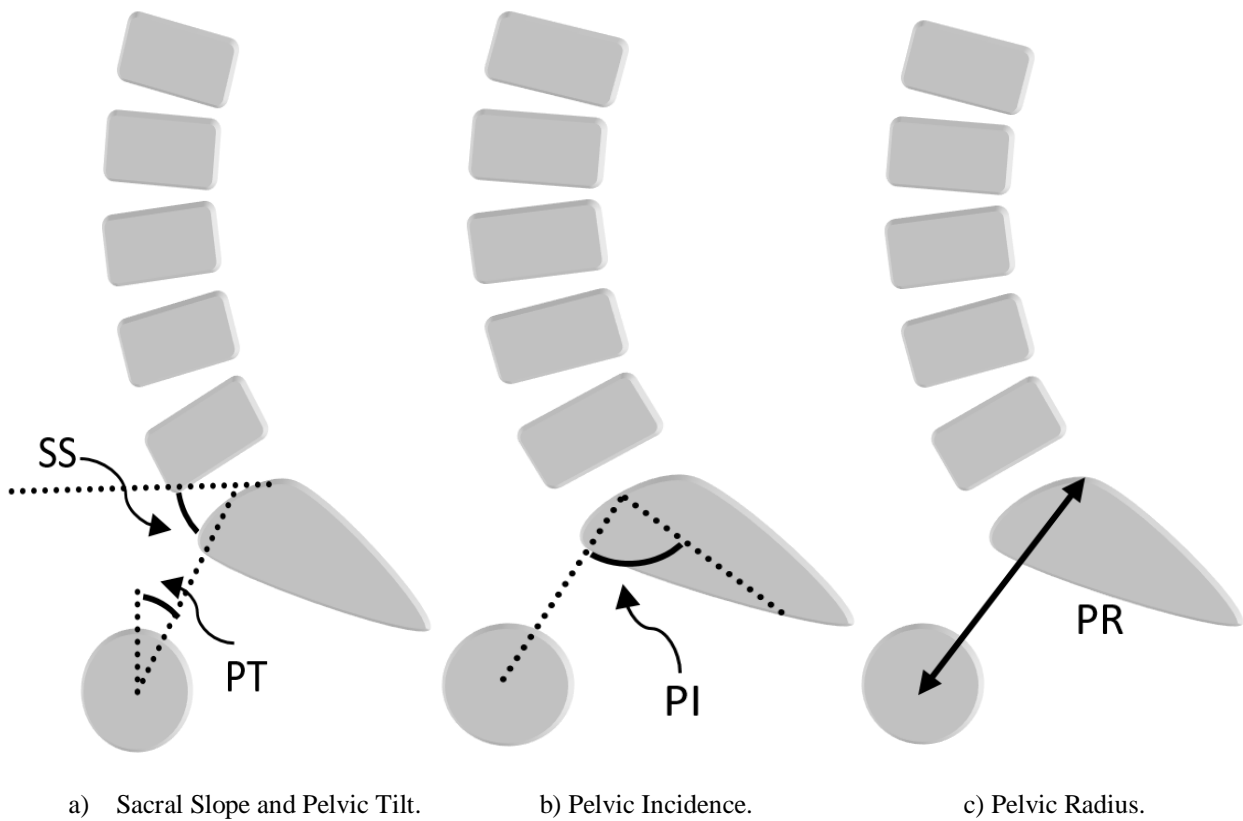


Figure 2. Sacral Slope, Pelvic Tilt (a), Pelvic Incidence(b) and Pelvic Radius(c)

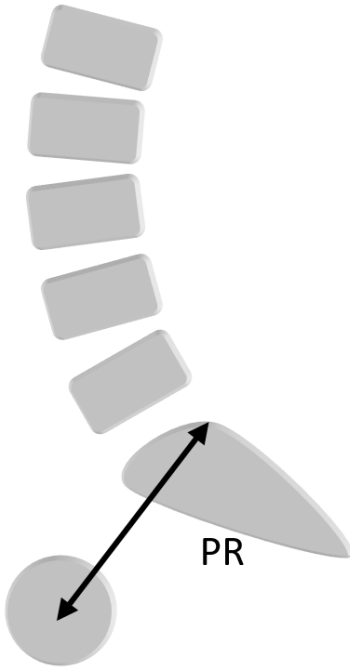


Figure 3. Lumbar Lordosis angle.

2.3 AIVCP Methodology

In this section, we provide design details of the proposed algorithm in two steps: (i) identification of the most relevant features (ii) Design of majority vote decision fusion. Furthermore, we should remind that our dataset is not high-dimensional and feature selection is not a preliminary step in our workflow. Instead, we design majority voting decision system at the first and then we apply SVM-based feature selection as the second step to improve diagnosis accuracy of the overall system.

2.3.1 Feature Selection with SVM

In a classification problem, if the number of input features is relatively larger than the number of instances then the dataset is said to be high-dimensional. There are three main difficulties in the analysis of high-dimensional datasets: (i) high computational cost, (ii) overfitting of classifier algorithm and (iii) risk of low classification accuracy [12]. In this concept, an efficient feature selection algorithm can reduce the computational cost, and increase classifier classification accuracy and efficiency [13]. In particular, feature selection is a search optimization process to identify the smallest and the most valuable features in accordance with class labels of an input dataset. For a large feature space, feature selection strategies often use greedy search rather than exhaustive. Feature-ranking methods are among widely used techniques that are used to select fixed number of top relevant features. This suggests that feature ranking may be used to design a high-accurate class predictor based on a pre-selected (ranked) subset of features.

Though, our dataset is not high-dimensional, for the sake of higher classification accuracy, we make use of a SVM based feature selection strategy while developing the proposed AIVCP system.

In our feature selection scheme, we use a two class approach, i.e., normal, abnormal, to identify the most relevant features. Therefore, for a given set of training instances $\{x_1, x_2, \dots, x_k, \dots, x_l\}$ with class labels $\{y_1, y_2, \dots, y_k, \dots, y_l\}$ for $y_k \in \{normal, abnormal\}$. The test instances \mathbf{x} are classified with respect to sign of the decision function $D(\mathbf{x})$ as follows:

- (i) $D(\mathbf{x}) > 0 \Rightarrow \in$ class *normal*
- (ii) $D(\mathbf{x}) < 0 \Rightarrow \in$ class *abnormal*
- (iii) $D(\mathbf{x}) = 0$, decision boundary

In this context, decision functions are defined as the simple weighted sums of the training instances and additional bias that are called linear discriminant functions [14]. Mathematically, this relationship is shown in equation (2.1).

$$D(\mathbf{x}) = \mathbf{w} \cdot \mathbf{x} + b \quad (2.1)$$

In equation (2.1), \mathbf{w} is weight vector and b is bias. Furthermore, a dataset is *linearly separable* under the condition that a linear discriminant function is found to separate classes of data without error.

Feature ranking coefficients may be used as classifier weights, and reciprocally the weights multiplying the inputs of a classifier may also be used as feature ranking coefficients [14, 15]. In this scheme, linear discriminant functions may be trained with an algorithm such as SVM to provide feature ranking. In this algorithm, the magnitude of weights of the linear function is proportional to the weight (relevancy) of features.

Linear SVMs are suitable to be used as linear discriminant functions, and we used polynomial kernel with training inputs normalization option as feature evaluator to identify the best feature subset from vertebra column dataset. The flow of algorithm is adopted from [14] and the SVM based feature selection process is given in Figure 4.

Step 1: input $\mathbf{x} = \{x_1, x_2, \dots, x_k, \dots, x_l\}$ and $\mathbf{y} = \{y_1, y_2, \dots, y_k, \dots, y_l\}$
Step 2: set $\mathbf{f} = \{f_1, f_2, \dots, f_n\}$ initial feature vector
 set $\mathbf{r} = \{\}$ ranked feature list
Step 3: until $\mathbf{f} = \{\}$ repeat steps from 4 to 8

Step 4: train SVM with \mathbf{f} and \mathbf{x} and obtain classifier parameters α
Step 5: compute weight vector $\mathbf{w} = \sum \alpha_k y_k \mathbf{x}_k$
Step 6: compute ranking criteria $c_i = (w_i)^2$ for all i
Step 7: eliminate feature with smallest ranking criterion, c_i
Step 8: update \mathbf{r}
Step 9: output optimum feature subset

Figure 4. SVM-based feature selection algorithm

The resultant feature subset through the application of SVM feature selection is provided in Table 2.

Table 2. Feature subset of vertebral column dataset based on SVM-feature selection

Subset of features
Sacral slope
Spondylolisthesis degree
Lumbar lordosis angle
Pelvic radius

2.3.2 Multiple Classifier Systems

Multiple classifier fusion may generate more accurate classification than each of the constituent classifiers. Fusion is often based on based combination rules like the median and average.

MCSs, particularly vote decision fusion algorithms, are developed to obtain higher predictive performances compared to each of constituent predictors. Voting based multi-classifier algorithms use miscellaneous classifiers as experts and they fuse individual decisions of these learners to obtain a more accurate final decision. The continuous output provided by each classifier is combined with the help of fusion rules such as Maximum, Median, Mean, Minimum, and Majority voting [6, 16]. From classification perspective, the output provided by a classifier for a given class is interpreted to be the posterior probability estimate for that class. In this interpretation, the outputs are normalized to add up to 1 over all classes [4]. Mathematically, “ $p_j(\mathbf{x})$ is bounded between 0 and 1 computed for test objects \mathbf{x} for each of the c classes. Once the set of posterior probabilities $\{p_{ij}(\mathbf{x}), i = 1, m; j = 1, c\}$ for m classifiers and c classes is computed for test object \mathbf{x} , they have to be combined into a new set $q_j(\mathbf{x})$ that can be used for the final classification” [6]. In general, new confidence $q_j(\mathbf{x})$ for class j depending on a combination rule i is computed with equation (2.2).

$$q_j'(\mathbf{x}) = \text{combinationRule}_i(p_{ij}(\mathbf{x})) \quad (2.2)$$

From equation (2.2), $q_j(\mathbf{x})$ can be rewritten as in equation (2.3).

$$q_j(\mathbf{x}) = \frac{q_j'(\mathbf{x})}{\sum_j q_j'(\mathbf{x})} \quad (2.3)$$

Final classification of instance \mathbf{x} is computed with equation (2.4).

$$\omega(\mathbf{x}) = \arg \max_j (q_j(\mathbf{x})) \quad (2.4)$$

Through equations (2.2), (2.3) and (2.4), we can define combination rules as follows: (i) maximum voting selects the predictor with the highest estimated confidence, however (ii) minimum voting strategy selects the classifier with the least objection. (iii) median, and (iv) mean voting strategies average the posterior probability estimates. In the last voting strategy, (v) maximum voting counts the votes of individual classifier and selects majority class as final decision [6].

2.3.2.1 Majority Vote Decision Fusion Systems

A majority vote decision fusion comprises of n independent classifiers, and each of these predictors produces a unique decision for an unknown pattern. The final decision for the class label of the pattern is obtained with the k number of agreement among the classifiers [17]. Moreover, the relationship between k and n is defined as follows:

$$\text{i) } k = \left\{ \left(\frac{n}{2} \right) + 1 \text{ for even } n \right.$$

$$\text{ii) } k = \left\{ \left(\frac{n+1}{2} \right) \text{ for odd } n \right.$$

In our implementation, we selected four diverse classifiers, i.e., Simple Logistics (SL), Decision Stump (DS), Naïve Bayes (NB), and Learning Vector Quantization (LVQ), to design the proposed majority vote decision fusion system. In the following section, we provide brief information about the classifiers and the classifier selection methodology while designing the proposed fusion algorithm.

2.3.3 Classifier Selection Strategy for Fusion

Design of fusion strategies from a large pool of different classifiers is not a straightforward task. It is almost impossible to define an exact design strategy that will guarantee the optimum solution to a particular problem [18]. However, it is recommended in the literature that a two-step design strategy may be helpful to obtain the optimum combination for a multiple-classifier fusion application: i) creating a limited collection of promising classifiers with diversity, ii) selection of classifiers from the collection recurrently with a search strategy. Furthermore, it should be noted that the best fusion combination is not always guaranteed with the combination of the best individual classifiers [19]. Therefore, to evaluate possible fusion combinations, a search strategy is required. In our implementation, we used a grid-search strategy, i.e., an exhaustive method to obtain possible fusion combinations, on top of the 10-fold cross-validation for the evaluation of models. Since, grid-search for high number of classifiers require a serious computational load, we therefore limited the number classifiers in the collection. Our selection strategy is as follows:

i) At the first step, we wrote a java interface to WEKA suit to evaluate classifiers from diverse groups, i.e., Bayes learners, neural network classifiers, instance-based learners, rule based learners, decision trees and relatively new algorithms based on immune-colony inspired systems.

ii) We made experiments for vertebral column dataset to obtain 2 or 3 significant classifiers from each group and we obtained 10 classifiers in total. The names of the classifiers are provided in Table 3. In selection of classifiers, we used two criteria; a) prediction performance and b) the error analysis regard to predictions of the classifiers. In simpler terms, we examine the output of the classifiers for their predictions, and we choose classifiers making different predictions (either false or true) for the same instance.

iii) We applied a grid-search methodology guided by 10-fold cross-validation strategy to obtain different classifier combinations for majority voting.

iv) We obtained the best fusion combination producing the highest classification accuracy for the SL, LVQ, NB and DS.

Table 3. Classifier pool used in the selection of base classifiers

No	Classifier	No	Classifier
1	Decision Stump	6	Multi-Layer
2	iBk	7	Simple Logistics
3	Naïve Bayes	8	Clonal Selection
4	Hyper Pipes	9	Artificial Immune
5	Learning Vector	10	ZeroR

2.3.3.1 Selected Classifiers

In this section, we provide brief information for Simple Logistics, Decision Stump, Naïve Bayes, and Learning Vector Quantization:

i) *Simple Logistics*: Two popular supervised learning tasks are tree induction methods and linear regression models. The two approaches may be combined into model trees whose leaves are regression functions. In a similar fashion, SL algorithm is implemented with model trees having logistic regression models at the leaves. Linear logistics regression models posterior class probabilities $\Pr(G = j | X = x)$ for the J classes via linear functions of x . The simple form of model is given in equation (2.5).

$$\Pr(G = j | X = x) = \frac{e^{F_j(x)}}{\sum_{k=1}^J e^{F_k(x)}}, \sum_{k=1}^J F_k(x) = 0 \quad (2.5)$$

Linear regression functions, i.e., $F_j(x) = (\beta_j)^T \cdot x$, are usually fit by obtaining maximum likelihood estimates for parameters β_j . These estimates are efficiently computed with the use of LogitBoost algorithm and hence the model in equation (2.5) is simplified as $F_j(x) = \sum_m f_{mj}(x)$. Here, f_{mj} is with the use of simple linear regression summation and this simplified algorithm is called as Simple Logistics by its implementers [20].

ii) *Decision Stump*: A decision stump is a decision tree with one internal node which is immediately connected to the terminal nodes. DS tree makes a prediction based on the value of just a single input feature. In the literature, these 1-level decision trees are also known as 1-rule algorithms [21]. At each given node i of the tree for a subset of training examples D_i , the goal is to select a feature such that the instances are divided into their relevant class. In other words, segmentation of D_i is accomplished with purity, i.e., all instances in a node should be in the same class. In DS, this feature selection is made to maximize information gain. More clearly, DS selects the feature that maximizes information gain in the whole dataset. Decision stumps are often used as components of classifier ensemble algorithms to obtain high accurate systems.

iii) *Naïve Bayes*: A NB classifier is an algorithm that assumes the presence of a particular feature of a class is unrelated to the presence of any other feature, for a given class variable. In other words, even if those features depend on each other, a NB classifier considers all of those properties to independently contribute to the class

variable. A NB classifier uses a small amount of training data to estimate the parameters, i.e., means and variances of the variables, for classification. NB classifier model can be given in equation (2.6) [22, 23].

$$p(C | f_1, \dots, f_n) = \frac{1}{Z} p(C) \prod_i^n p(f_i | C) \quad (2.6)$$

In equation (2.6), $p(C | f_1, \dots, f_n)$ is conditional probability model for NB classifier over a dependent class variable C conditional on feature variables (f_1, \dots, f_n) . And in the equation, Z is a constant depending on features. NB classifier combines this model with a decision rule such as the *maximum a posteriori* rule to make classification [22, 24].

iv) Learning Vector Quantization: LVQ is an algorithm that learns classifiers from labeled data. LVQ, models the class discrimination function with the use of labeled codebook vectors and the nearest neighborhood search between the codebook and data. For classification purposes, an instance is first assigned to the closest codebook vector and then it takes class label of that codebook as its class. LVQ training is accomplished with iterative gradient update of the winner unit. The winner unit m^c is defined by equation (2.7).

$$c = \arg \min_k \|D_i - m^k\| \quad (2.7)$$

In equation (2.7), D_i is the instance to be classified. With the nearest neighborhood search, the update equation for a data sample $D(t)$ is given in equation (2.8).

$$m^c(t+1) := m^c(t) \pm \alpha(t)[D(t) - m^c(t)] \quad (2.8)$$

In equation (2.8), the sign is taken as positive for correctly classified data instances and as negative for a misclassification. In the same equation, $\alpha(t)$ is the learning rate that may take values between 0 and 1. In a classification problem, this procedure is repeated iteratively until convergence is reached [25, 26].

2.3.4 Flow of AIVCP Algorithm

In this section, we provide layout of the proposed algorithm and we present the general flow in Figure 5. However, there are a few reminders about the designed algorithm: (i) expecting a higher accuracy, we applied SVM feature selection after obtaining the best majority vote fusion decision system, (ii) In the case of equality in the votes of four classifiers, we selected the decision of SL as the correct classification label for majority voting evaluation and (iii) we evaluated performance of the whole algorithm on top of a 10-fold cross-validation scheme.

In the Figure 5, we provide two sample instances from the classifier outputs and then we present combination of these two decisions with majority voting scheme: For the first instance, the four classifiers make false predictions and hence majority vote of these decisions produces a false prediction. In the second case, though NB and DS produce false predictions for Hernia, SL and LVQ make true predictions. As we declared, in the case of the equality of votes, the algorithm chooses the vote of SL's group to identify true label of the instance. Hence, voting makes a true prediction for the second instance.

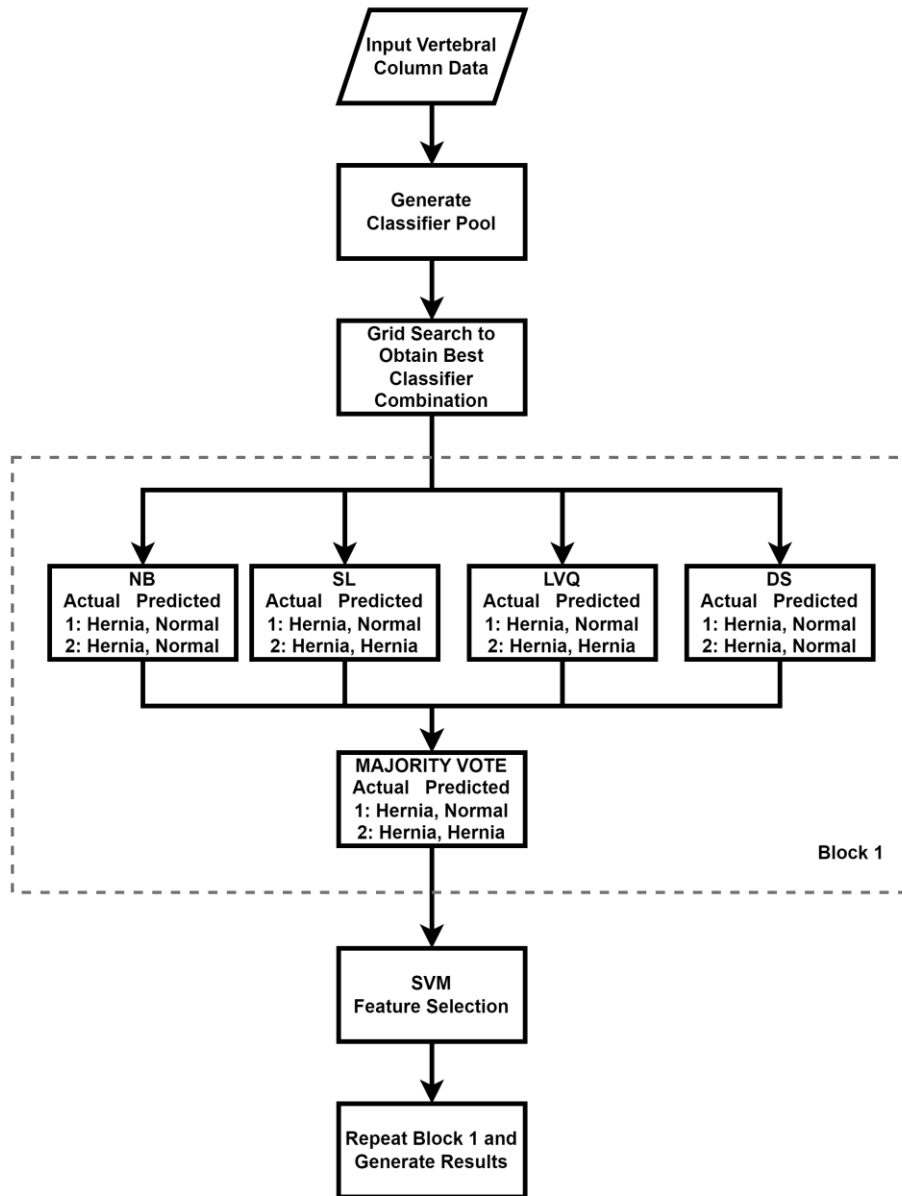


Figure 5. General flow of the AIVCP Algorithm.

3. Experiments

3.1 Statistical Evaluation Metrics

Any classification problem, produces four possible outcomes defined as *true positive* (TP), *false positive* (FP), *true negative* (TN) and *false negative* (FN). These outcomes are related to each other with *confusion matrix*. This matrix is used to derive well known performance metrics such as sensitivity, specificity, accuracy, positive prediction value, f-score, AUC and ROC curve. In our study, we use f-score (FS), Sensitivity (Sn) and Specificity (Sp) to evaluate the results of our experiment. We also make use of confusion matrices to inspect classifier prediction performances in detail. FS, Sn and Sp are defined with the following relations:

Sensitivity (Sn): The number of true positive decisions/number of actual positive cases.

Specificity (Sp): The number of true negative decisions/number of actual negative cases.

F-Score (FS): FS is used to measure the performance of machine learning classifiers and it can be used for balanced or imbalanced problems. The metric is defined in equation (3.1).

$$FS = 2TP / (2TP + FP + FN) \quad (3.1)$$

Table 4. Experimental results of AIVCP algorithm with and without feature selection

		Without Feature Selection					With SVM Feature Selection				
		NB	SL	LVQ	DS	Vote	NB	SL	LVQ	DS	Vote
Diseases	F1-Score	0.786	0.831	0.816	0.744	0.853	0.780	0.829	0.786	0.660	0.883
Hernia	Sn	0.717	0.633	0.750	0	0.717	0.667	0.667	0.683	0	0.800
Spondylolisthesis	Sn	0.973	0.960	0.947	0.953	0.980	0.980	0.960	0.947	0.953	0.973
Normal	Sn	0.690	0.860	0.780	0.970	0.830	0.690	0.860	0.740	0.970	0.860
	Sn (Avg)	0.793	0.818	0.826	0.641	0.842	0.779	0.829	0.79	0.641	0.877
Hernia	Sp	0.991	0.944	0.904	1.000	0.944	0.912	0.948	0.896	1.000	0.956
Spondylolisthesis	Sp	0.912	0.981	0.975	0.750	0.969	0.925	0.981	0.975	0.750	0.975
Normal	Sp	0.929	0.881	0.919	0.686	0.914	0.905	0.886	0.890	0.686	0.929
	Sp (Avg)	0.944	0.935	0.933	0.812	0.942	0.914	0.938	0.921	0.812	0.954

3.2 Experiments and Results

The results of the AIVCP algorithm with and without feature selection are given in Table 4. It is known in advance that a good medical decision support system is

the one producing high f-score, specificity and sensitivity concurrently. With this point in mind, we provide Figure 6 for the results corresponding to without feature selection and we provide Figure 7 for the SVM-based feature selection.

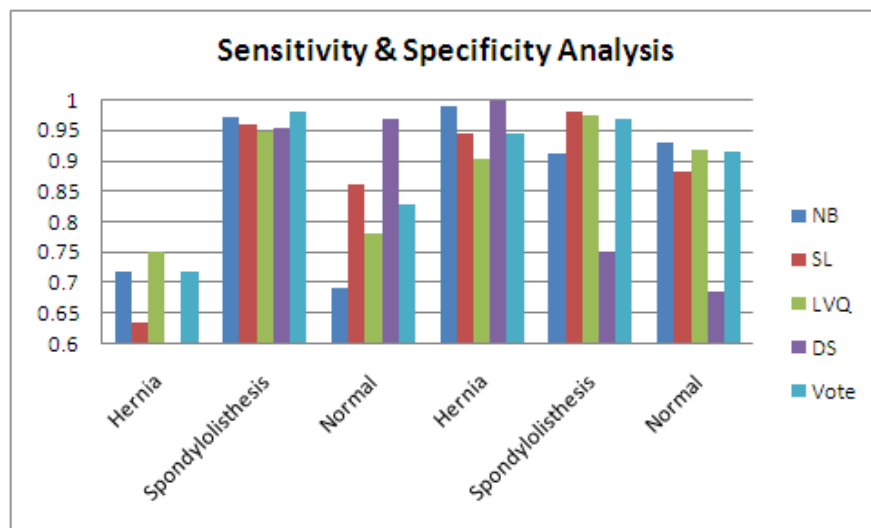


Figure 6. Sensitivity and Specificity analysis with all features used.

It is observed from Table 4 that *FS* of the majority Vote algorithm is higher than from each of the constituents of the decision system. From Table 6, for the case of Sn, the average value of voting algorithm is significantly better from the four of the classifiers. On the other hand, overall inspection of Figure 6 demonstrates that performance of classifiers, i.e., in terms of Sn and Sp, changes relatively in Hernia and Normal cases. For example, LVQ generates the highest Sn for Hernia and in contrast DS produces the worst performance. Furthermore, in Normal case, DS has the most significant Sn value of 0.970

among the classifiers. Additionally, for Sp values, it is observed from the right part of the Figure 6 that the most significant value for Hernia is produced by DS. For the Normal case, whereas DS is the worst predictor, the remaining three classifiers generate acceptable results. Interestingly, though overall classification performance of DS is the lowest among the classifiers, it contributes positively to the performance of the vote algorithm. We will analyze contribution of DS with more detail with the help of confusion matrices and some additional experiments later.

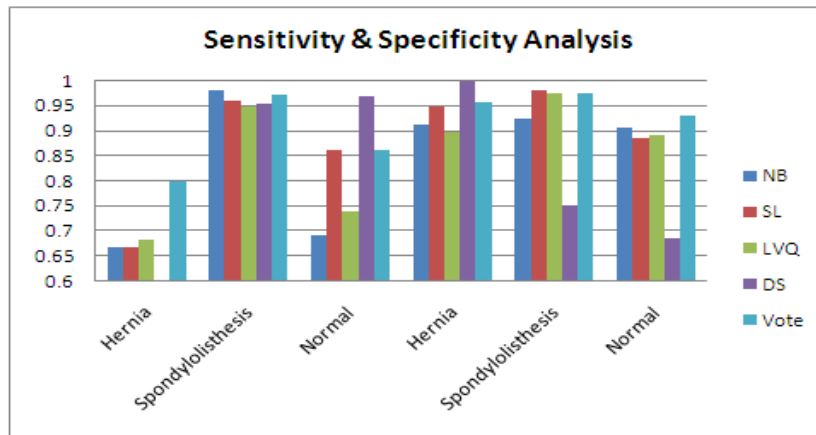


Figure 7. Sensitivity and Specificity analysis for SVM-based feature selection.

From Table 4, it is obviously inspected that vote algorithm generates the highest f-score value of 0.883. For Sn-Sp evaluation, results of Figure 7 are observed to be similar to those of Figure 6. On the other hand, we may observe from Figure 7 that for Hernia-Normal pair, vote algorithm has significantly better Sn-Sp values compared to values of Figure 6. It is furthermore observed from Figure 7 that overall performance of vote is increased significantly.

After this point, we provide some other experimental results to present contributions of classifiers to the community decision. In simpler terms, we observed all classifiers, except DS, more or less produce similar results. Since, overall performance of DS is significantly lower than the three classifiers in terms of f-score values, it is necessary to question the effect of classifiers on the final decision of vote algorithm.

Table 5. Comparison of experimental results of Vote algorithm with DS and without DS.

Diseases	Vote without DS			Vote with DS		
	Sn	Sp	FS	Sn	Sp	FS
Hernia	0.717	0.928	-	0.800	0.956	-
Spondylolisthesis	0.973	0.981	-	0.973	0.975	-
Normal	0.800	0.908	-	0.860	0.929	-
Average	0.830	0.939	0.867	0.877	0.954	0.879

Table 5 evidently shows that, though single overall classification performance of DS algorithm is relatively small compared to LVQ, NB and SL, it has a considerable contribution to the performance evaluation metrics of Vote algorithm. All of the performance metrics are improved obviously. The only exception is Spondylolisthesis whose metrics have a minor decrease. The reason behind the contribution of DS algorithm to the entire decision fusion may be explained in terms of confusion matrices given in Table 6. For the sake of convenience, we make use of abbreviations of three cases as *H* for Hernia, *S* for Spondylolisthesis and *N* for Normal. It is repeated that the original numbers of

instances are 60, 150 and 100 for three class labels respectively. For an intense evaluation, we provide confusion matrices of voting algorithm for two cases: (i) voting without DS (Vote1) and (ii) voting with DS (Vote2).

Table 6. Confusion matrices of classifiers.

Confusion Matrices									
NB	Predicted			SL	Predicted				
	H	S	N		H	S	N		
Expected	H	40	3	17	Expected	H	40	1	19
	S	0	147	3		S	1	144	5
	N	22	9	69		N	12	2	86
LVQ	Predicted			DS	Predicted				
	H	S	N		H	S	N		
Expected	H	41	1	18	Expected	H	0	1	59
	S	3	142	5		S	0	143	7
	N	23	3	74		N	0	3	97
VOTE1 (-DS)	Predicted			VOTE2 (+DS)	Predicted				
	H	S	N		H	S	N		
Expected	H	43	1	16	Expected	H	48	1	11
	S	0	146	4		S	0	146	4
	N	18	2	80		N	11	3	86

As confusion matrices of classifiers are examined in Table 6, the following results can be drawn:

The relative true prediction performances of four base classifiers for class Spondylolisthesis is similar to each other. There are 150 Spondylolisthesis cases in the dataset and the classifiers make true predictions that change from 143 to 147. On the other hand, there are some remarkable results for Hernia and Normal classes. There are 60 Hernia instances in the dataset and classifiers make predictions through 0 to 41. It is interesting to observe that DS in this case has no true prediction at all. Other than DS, base classifiers generate similar true predictions between 40 and 41. In spite of poor prediction performance of DS, Vote1 and Vote2 algorithms combine remaining predictions and they obtain 43 and 48 true predictions respectively. For the

Normal class, it is observed that the most significant true prediction performance, i.e., 97 predictions out of 100, belong to DS algorithm. The second remarkable result for this class is that of SL algorithm with the 86 true predictions. When the two voting algorithms are examined from confusion matrices, it is observed that they have 80 and 86 true predictions for Normal class. In this case, SL and DS contribute to the Vote2 algorithm and they lead to produce an acceptable true prediction. In this context, Vote2 benefits from the fusion of the decisions of DS and SL. From confusion matrices, it is seen that the most successful prediction performances among six classifiers belong to SL and Vote2. Both SL and Vote2 have almost the same prediction ratios in Spondylolisthesis and Normal cases. However, it is seen that SL and Vote2 algorithms have 40 and 48 true predictions in Hernia class. This is the main source of performance increase of Vote2 algorithm. Fusion of predictions of SL, LVQ and NB for different data

instances increases overall performance of Vote2 algorithm.

We provide Figure 8 and 9 to show the contribution of each base classifier to final decision of Vote algorithm.

The procedure to obtain the two figures is as follows:

- i) We first generated the predictions of all classifiers (including Vote algorithm) for all instances of data.
- ii) We excluded predictions for Spondylolisthesis class and we obtained the true and false predictions of all classifiers for Hernia and Normal cases. And then, we divided this outcome into two parts regard to Hernia and Normal cases.
- iii) For each of the two divisions of step (ii), we maintained the outcomes that contain at least one false prediction and we eliminated the instances that are classified correctly by all classifiers. While realizing this step, we kept the order of the instances unchanged to observe coincidence of predictions.
- iv) We obtained false predictions of all classifiers for Hernia and Normal classes as two separate figures.

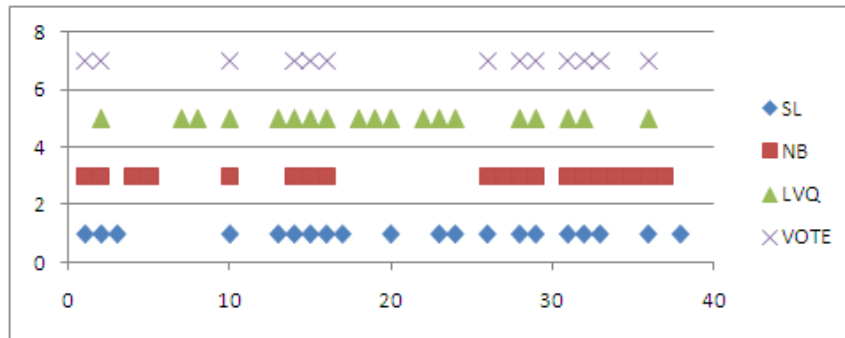


Figure 8. False predictions of base classifiers and Vote algorithm for Hernia class.

Since it has shown in Table 6 that DS produces misclassifications for all Hernia instances, we provide the predictions of SL, LVQ, NB and Vote algorithm in Figure 8 and we disregard DS predictions. As the figure is examined, DS (with having no true prediction), NB, LVQ and SL make misclassifications much more than

Vote algorithm. However, it is observed from the figure that, the base predictors make misclassification in different portions (instances) of dataset. Therefore, the fusion of those decisions with majority vote produces less false predictions compared to the each of the base predictors.

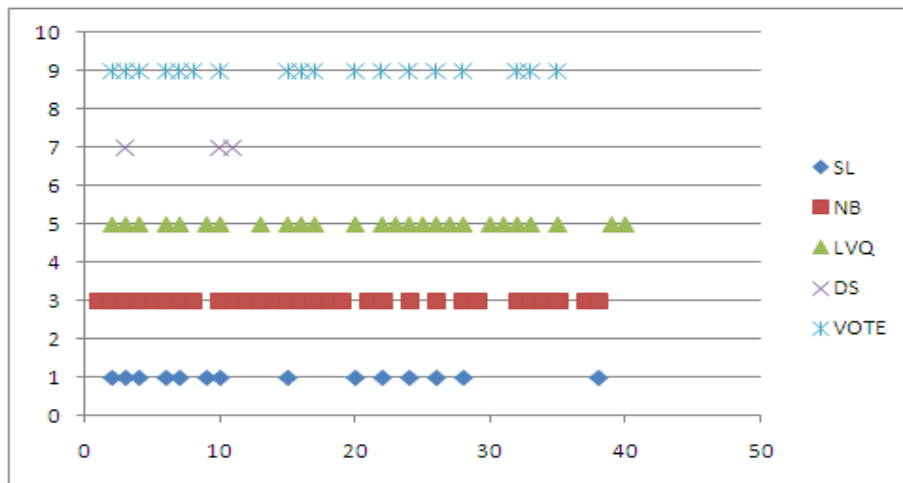


Figure 9. False predictions of base classifiers and Vote algorithm for Normal class.

Figure 9 demonstrates false predictions of base classifiers and their majority vote based fusion counterpart. In this case, though LVQ and NB make more false predictions compared to those of SL and DS, the majority vote combination of the whole predictions decreases chance of false prediction of Vote algorithm. Hence, the misclassification rate of Vote algorithm benefit from DS and SL prediction rate positively.

As a last experiment for SL, LVQ, DS and NB base classifiers, we provide average f-score values for different combination rules of voting algorithms. The respective f-score values for rules, i.e., Average of probabilities, Product of probabilities, Minimum probability, Maximum probability, and Majority voting, are given in respective order as 0.823, 0.513, 0.819, and 0.883.

4. Conclusion

Vertebral column pathologies are diagnosed with the use of a majority vote decision fusion system. The diagnosis of these pathologies is first analyzed with the use of single predictors, NB, SL, LVQ, and DS. The prediction performances of the classifiers with SVM-based feature selection are 0.780, 0.829, 0.786, 0.660 respectively. In order to obtain a higher diagnosis performance, we designed a decision fusion system and therefore we obtained an acceptable f-score of 0.883 compared with the results in the literature.

The proposed AIVCP algorithm is evaluated in terms of fscore, sensitivity, specificity, confusion matrices and prediction error ratios. Through these steps the following significant results are obtained:

- 1) The single base predictor performances may be combined to obtain higher prediction f-score values.
- 2) High performances of the individual classifiers do not guarantee to generate high prediction f-score. Instead, diverse classifiers and different combinations should be evaluated. Different combinations may be generated with the use of limited exhaustive search or with a heuristics algorithm such as Genetic search.
- 3) In the selection of algorithms, an error analysis depending on the predictions of base classifiers may contribute the success of the vote algorithm.
- 4) Analysis of confusion matrices and sensitivity-specificity pairs may also contribute positively to the overall performance of the vote algorithm.
- 5) Though, we obtained majority voting as the best combination rule in this specific problem, other rules may also be searched for a better prediction f-score. The relative success of the proposed algorithm, decision fusion approach in particular, may be used to increase

single classifier based CDSSs with different combination strategies.

As a future direction, we intend to extend the proposed algorithm with the use of heuristics search strategies to obtain higher prediction performances for different medical decision domains.

Author's Contributions

Dr. Akın Özçift designed the algorithm. Dr. Mehmet Bozuyula evaluated experiments and their results. Both authors contributed to the preparation of the whole article.

Ethics

There are no ethical issues after the publication of this manuscript.

References

- [1]. Sim I, Gorman P, Greenes RA et al. 2001. Clinical decision support systems for the practice of evidence-based medicine. *Journal of the American Medical Informatics Association*; 8(6): 527–534. doi: 10.1136/JAMIA.2001.0080527/2/JAMIA0080527.F01.JPEG.
- [2]. Shahmoradi L, Safdari R, Ahmadi H, Zahmatkeshan M. 2021. Clinical decision support systems-based interventions to improve medication outcomes: A systematic literature review on features and effects. *Medical Journal of the Islamic Republic of Iran*; 3527. doi: 10.47176/MJIRI.35.27.
- [3]. Shaikh F, Dehmeshki J, Bisdas S et al. 2021. Artificial Intelligence-Based Clinical Decision Support Systems Using Advanced Medical Imaging and Radiomics. *Current Problems in Diagnostic Radiology*; 50(2): 262–267. doi: 10.1067/J.CPRADIOL.2020.05.006.
- [4]. Polikar R. 2006. Ensemble based systems in decision making. *Circuits and Systems Magazine*; 6(3): 21–44. doi: 10.1109/MCAS.2006.1688199.
- [5]. Hanson CC, Brabyn L, Gurung SB. 2022. Diversity-accuracy assessment of multiple classifier systems for the land cover classification of the Khumbu region in the Himalayas. *Journal of Mountain Science* 2022 19:2; 19(2): 365–387. doi: 10.1007/S11629-021-7130-7.
- [6]. Duijn RPW, Tax DMJ. 2000. Experiments with Classifier Combining Rules. In: *Int. Work. Mult. Classif. Syst.* Springer-Verlag. pp 16–29.
- [7]. Neto ARDR, Sousa R, Barreto GDA, Cardoso JS. 2011. Diagnostic of Pathology on the Vertebral Column with Embedded Reject Option. In: *Iber. Conf. Pattern Recognit. Image Anal. Las Palmas de Gran Canaria, Spain*, Springer, Berlin, Heidelberg. pp 588–595.
- [8]. Berthonnaud E, Dimnet J, Roussouly P, Labelle H. 2005. Analysis of the sagittal balance of the spine and pelvis using shape and orientation parameters. *Journal of Spinal Disorders and Techniques*; 18(1): 40–47. doi: 10.1097/01.BSD.0000117542.88865.77.
- [9]. Neto ARR, Barreto GA. 2009. On the application of ensembles of classifiers to the diagnosis of pathologies of the vertebral column: A comparative analysis. *Latin America Transactions*; 7(4): 487–496. doi: 10.1109/TLA.2009.5349049.
- [10]. Baker JF, Joseph Baker CF, Y W O R D S child KE. 2021. Computed tomography study of the relationship between pelvic incidence and bony contribution to lumbar lordosis in children. *Clinical*

Anatomy; 34(6): 934–940. doi: 10.1002/CA.23756.

[11]. Açar G, Çiçekcibaşı AE, Koplay M, Seher N. 2021. Surface anatomy and lumbar lordosis angle. *Anatomical Science International*; 96(3): 400–410. doi: 10.1007/S12565-021-00602-1/FIGURES/6.

[12]. Jain AK, Duin RPW, Mao J. 2000. Statistical pattern recognition: A review. *IEEE Transactions on Pattern Analysis and Machine Intelligence*; 22(1): 4–37. doi: 10.1109/34.824819.

[13]. Tu C-J, Chuang L-Y, Chang J-Y, Yang C-H. 2006. Feature selection using PSO-SVM. *IAENG Int. J. Comput. Sci.* 33

[14]. Guyon I, Weston J, Barnhill S, Vapnik V. 2002. Gene Selection for Cancer Classification using Support Vector Machines. *Machine Learning*; 46(1): 389–422. doi: 10.1023/A:1012487302797.

[15]. Guyon I, Elisseeff A. 2003. An Introduction to Variable and Feature Selection. *Journal of Machine Learning Research*; 3:1157–1182.

[16]. Rwigema J, Mfitumukiza J, Tae-Yong K. 2021. A hybrid approach of neural networks for age and gender classification through decision fusion. *Biomedical Signal Processing and Control*; 66:102459. doi: 10.1016/J.BSPC.2021.102459.

[17]. Rahman A, Fairhurst M. 2000. Decision combination of multiple classifiers for pattern classification: Hybridisation of majority voting and divide and conquer techniques. In: *Appl. Comput. Vis. Fifth IEEE Workshop*. pp 58–63.

[18]. Wang H, Liang T, Cheng Y. 2021. Evolution and quality analysis algorithm of consumer online reviews based on data fusion and multiobjective optimization. *J Sensors*. doi: 10.1155/2021/6252425

[19]. Ruta D, Gabrys B. 2005. Classifier selection for majority voting. *Information Fusion*; 6(1): 63–81. doi: 10.1016/J.INFFUS.2004.04.008.

[20]. Landwehr N, Hall M, Frank E. 2005. Logistic Model Trees. *Machine Learning*; 59(1): 161–205. doi: 10.1007/S10994-005-0466-3.

[21]. Holte RC. 1993. Very Simple Classification Rules Perform Well on Most Commonly Used Datasets. *Machine Learning*; 11(1): 63–90. doi: 10.1023/A:1022631118932.

[22]. Bhargavi P, Jyothi S. 2009. Applying Naive Bayes Data Mining Technique for Classification of Agricultural Land Soils. *IJCSNS International Journal of Computer Science and Network Security*; 9(8): 117–122.

[23]. Wickramasinghe I, Kalutarage H. 2021. Naive Bayes: applications, variations and vulnerabilities: a review of literature with code snippets for implementation. *Soft Computing*; 25(3): 2277–2293. doi: 10.1007/S00500-020-05297-6/FIGURES/2.

[24]. Domingos P, Pazzani M. 1997. On the Optimality of the Simple Bayesian Classifier under Zero-One Loss. *Machine Learning*; 29(2): 103–130. doi: 10.1023/A:1007413511361.

[25]. Kohonen T. 2001. Self-Organizing Maps. doi: 10.1007/978-3-642-56927-2

[26]. Hollmén J, Tresp V, Simula O. 2000. A learning vector quantization algorithm for probabilistic models. In *Tampere, Finland, IEEE*.

[27]. Reshi, A. A., Ashraf, I., Rustam, F., Shahzad, H. F., Mehmood, A., & Choi, G. S. 2021. Diagnosis of vertebral column pathologies using concatenated resampling with machine learning algorithms. *PeerJ Computer Science*, 7, e547.


[28]. Cruz, A. D., Santhosini, P., Santhini, P., & Shirly, S. 2022. Comparative Study and Detection of Spinal Deformities using Supervised Machine Learning Algorithms. In *2022 International*

Conference on Computing, Communication, Security and Intelligent Systems (IC3SIS) (pp. 1-6). IEEE.

[29]. Handayani, I. 2019. Application of K-nearest neighbor algorithm on classification of disk hernia and spondylolisthesis in vertebral column. *Indonesian Journal of Information Systems*, 2(1), 57-66.

[30]. Riveros, N. A. M., Espitia, B. A. C., & Pico, L. E. A. 2019. Comparison between K-means and self-organizing maps algorithms used for diagnosis spinal column patients. *Informatics in Medicine Unlocked*, 16, 100206

One-Step Fabrication of Silver Nanostructures Decorated Cu-Grid as an Ideal SERS Platform

Menekşe Şakir^{1*} 

¹ ERNAM- Erciyes University Nanotechnology Application and Research Center, Kayseri 38039, Türkiye

*meneksesarihan@erciyes.edu.tr

* Orcid: 0000-0003-3102-0947

Received: 15 February 2023

Accepted: 12 March 2023

DOI: 10.18466/cbayarfbe.1170104

Abstract

Many ways to produce plasmonically-active substrates used for SERS applications, which is a non-destructive and reliable spectroscopy method, have been tried in recent years. Here we have presented an economical and easy procedure for synthesizing Ag NSs on Cu-grid in one step. Structural and elemental characterizations of Ag NSs on the Cu-grid were performed by scanning electron microscopy (SEM), energy-dispersive X-ray spectroscopy (EDX), X-ray diffraction (XRD), and X-ray photoelectron spectroscopy (XPS). Ag NSs on Cu-grids cause a high electromagnetic increase due to having complex morphology. Thus, the determination of R6G is easily realized even at very low concentrations such as 100 pM. It is predicted that different metallic nanostructures can be obtained by applying a similar recipe for different applications.

Keywords: Cu-grid, SERS, silver, rhodamine 6G.

1. Introduction

In recent years, surface-enhanced Raman spectroscopy (SERS) has been widely used in many fields such as chemistry, physics, materials science, and life science, as it is ultra-sensitive, dependable, has no labeling, and a non-destructive spectroscopic technique [1-3]. The developed SERS-active substrates are expected to be produced economically and efficiently, show high sensitivity, and are easy to use. SERS-active solid substrates are generally obtained using lithography and PVD [4-7]. While these production methods consist of long processing steps, they also require expensive and complex devices.

Chemical synthesis methods are a more straightforward and economical option for producing SERS-active materials. It is also possible to obtain more complex and off-hand structures that cause high electromagnetic field concentration. When using colloidal nanoparticles, it would be more appropriate to grow nanostructures in situ on the surface to avoid agglomeration, adversely affecting SERS measurements, and reusable if necessary. For this purpose, varied materials such as Si wafer, Al or Cu foil, and paper were used as solid substrates [8-11]. Silver and gold dendrites produced on commercial Al foil by galvanic replacement route were used as SERS-active substrates [12]. Similarly, Ag/Cu₂O heterostructures

synthesized on Cu foil by the hydrothermal synthesis method were evaluated to determine p-amino thiophenol and 4-pyridinethiol [13]. ZnO nanorods attached to the filter paper were modified with Au nanoparticles by UV-irradiation, and a reusable SERS-active substrate was obtained [14]. These studies showed that chemical synthesis methods could be exercised as high-activity SERS substrates when using plasmonic nanostructures on solid substrates.

Efficaciously, the Cu-grid is utilized to visualize the morphology of nanostructures with electron microscopy. Apart from this purpose, Gao et al. deposited Ag nanodendrites on Cu-grid by electrochemical deposition method and exerted for glucose determination [15]. Dendritic structured Ag nanocrystals on the Cu-grid were obtained with galvanic replacement by immersing in AgNO₃ solution [16]. In another study, the chemically synthesized Ag colloidal solution was dripped onto the Cu-grid and applied as SERS active substrate [17]. Even the silver nanoparticles grafted Ge nanowires were grown onto Cu-grid to achieve the detection limit of 6-aminopenicillins acid and penicillin G [18].

This study obtained Ag nanostructures (NSs) in a single step on the Cu-grid without any preliminary or device. These Ag nanostructures with sharp edges caused a severe enhancement of the electromagnetic field on the

surface and provided the opportunity to determine even very low concentrations of R6G. This procedure can also be performed for the in-situ growth of other metallic nanostructures.

2. Materials and Methods

2.1. Chemicals and Materials

Carbon-coated Cu-grid (400 mesh) was obtained from Electron Microscopy Science. Silver nitrate (AgNO_3 , $M_n=169.87$ g/mol), hydroquinone (HQ, $\text{C}_6\text{H}_6\text{O}_2$, $M_n=110.11$ g/mol), rhodamine 6G (R6G; $\text{C}_{28}\text{H}_{31}\text{N}_2\text{O}_3\text{Cl}$, $M_n=479.01$ g/mol) were purchased from Sigma-Aldrich. All aqueous solutions were prepared by using distilled water.

2.2. Fabrication of Ag NSs on the Cu-grid

In order to grow Ag NSs on Cu-grid, a fresh solution consisting of 0.2 mM AgNO_3 and 0.2 mM HQ in 50 mL of distilled water was prepared. First, the Cu-grids were cleaned with distilled water under sonication for 5 min. The cleaned Cu-grid was thrown into the solution and stirred at certain intervals (0.5, 1, and 2 hours) on the same experimental condition in the dark. Afterward, the Cu-grid removed from the solution was washed with distilled water and left to dry under room conditions.

2.3. Characterizations

The morphology and elemental analysis of Ag NSs on the Cu-grid were performed by scanning electron microscopy (SEM, ZEISS EVO LS10) and energy-dispersive X-ray spectroscopy (EDX, Bruker) attached with SEM at 25 keV. The crystal structure of Ag NSs was operated by an X-ray thin film diffractometer (Rigaku SmartLab) at 40 kV, 30 mA using $\text{Cu K}\alpha$ ($\lambda=0.154$ nm) radiation source. The chemical characterization of Ag NSs was conducted by X-ray photoelectron spectroscopy (XPS, SpecsFlex) using XR 50 M source exciting radiation.

SERS measurements were studied by a confocal Raman microscope (WITec Alpha 300 M+) with a 532 nm laser with a 50x objective (NA=0.85). The power of the laser was adjusted to 3 mW. 100 μM , 100 nM, and 100 pM of R6G solution with water as the probe molecule were prepared for the measurement. Each solution was dropped onto Ag NSs separately and left to dry at room temperature. After drying, SERS measurements were taken over 80x80 μm of area.

The analytical enhancement factor (AEF) was calculated by using the following equation (1) [19]:

$$AEF = \frac{I_{SERS}/C_{SERS}}{I_{Raman}/C_{Raman}} \quad (1)$$

Here, the concentrations of R6G dropped on only Cu-grid and Ag NSs are C_{Raman} and C_{SERS} , respectively. The peak

intensities at 1507 cm^{-1} of the Raman spectra obtained on these surfaces are I_{Raman} and I_{SERS} .

3. Results and Discussion

This study aims to procure plasmonically-active Ag NSs on a solid substrate without any seed in the medium. In Fig. 1, a schematic representation shows how to obtain Ag NSs grown on the carbon-coated Cu-grid. Here, a carbon-coated Cu-grid was added to the distilled water solution consisting of HQ as a reducing agent and, AgNO_3 as metal salt and stirred for two hours in a dark environment. Then, it was washed with distilled water and allowed to dry at room temperature. After this process, it was observed that Ag NSs grew successfully in large areas on the Cu-grid.

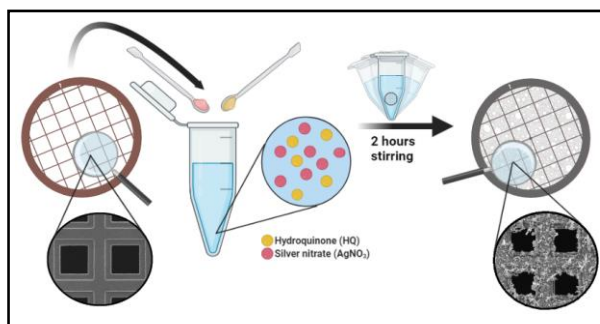


Figure 1. Schematic diagram of fabricating Ag NSs on Cu grid.

The commercially purchased Cu-grid surface is almost smooth in the SEM image (Fig. 2a). It can be an ideal solid substrate for growing Ag NSs without any seed. As shown in EDX analysis of the carbon-coated Cu-grid, although it contains mainly Cu (86.16 %) and relatively C (9.02 %) elements, trace amounts of O (2.58 %) and Al (2.24 %) elements are seen (Fig. 2b).

SEM pictures were taken to see the morphology of Ag NSs that we expect to grow on the Cu-grid after being kept in the appropriate solution medium. In Fig. 3a, it is seen that Ag NSs grow on almost the entire Cu-grid. There is no trace of that smooth surface before Cu-grid growth looking closer at the structures. The grid is wholly covered with Ag NSs (Fig. 3b). While there were nanoplates with smaller formations on the ground, especially the edges of the grid played a more active role, and a more intense Ag growth took place. Since the boundary lines have higher surface energy, reducing Ag ions in these regions is likely denser. For this reason, we come across the existence of highly symmetrical needle-like Ag NSs at the grid edges.

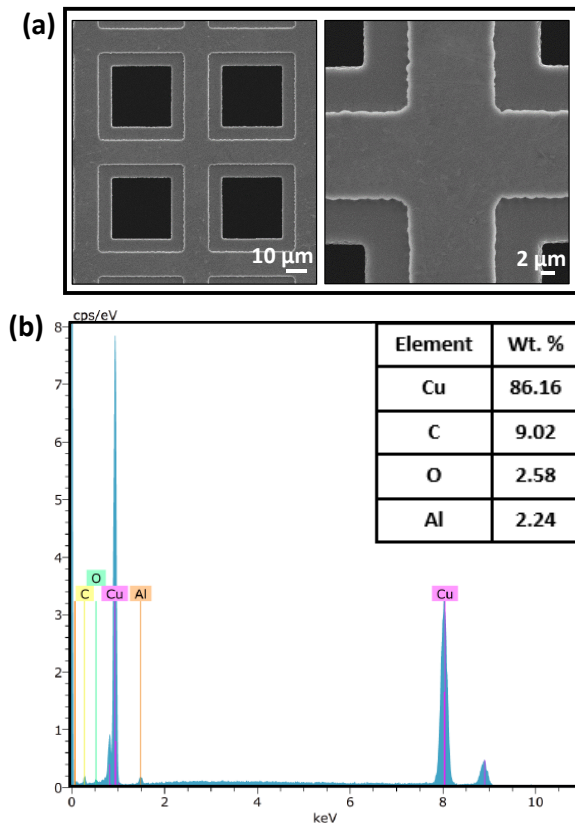


Figure 2. (a) SEM images of the Cu-grid. (b) EDX analysis of the Cu-grid.

In processes where the thermodynamic mechanism is dominant, crystals prefer to grow with a minimum total interfacial free energy. However, in cases where the kinetic mechanism dominates the thermodynamic

mechanism, it is expected to occur in different complex morphologies such as plate and needle-like, just like here. In this study, if the Cu grid in the growth solution is not shaken, there is no intense growth on the surface, as seen in Fig. 3c, and spherical particles tend to form rather than complex structures such as needles. We have also confirmed with the study that stirring is an important parameter affecting the growth mechanism [20].

The chemical composition of Ag NSs on the Cu-grid was characterized by EDX analysis and mapping. The Cu-grid at the base is symbolized with red, while the Ag NSs growing on it are marked with green in Fig. 4a. It is seen from the green color distribution that Ag NSs have grown successfully on the Cu-grid. When the EDX analysis is examined (Fig. 4b), the characteristic peak of Ag observed around 3 keV confirms that Ag NSs grew at a rate of 47.62% on the grid. The crystal structure of Ag NSs was examined with XRD analysis (Fig. 4c). Here, characteristic peaks of Cu at the bottom dominate, and Ag peaks are highly extinguished. The diffractions of (111), (200), and (220) planes of face cubic crystal (fcc) structured metallic Cu have peaks at 43.25°, 50.36°, and 74.06°, respectively. (JCPDS 85-1326). However, the peak around 38.02° belongs to the (111) plane diffraction of the fcc structured metallic Ag (JCPDS 87-0717). Since crystal growth of Ag is dominant in the (111) plane direction, only this peak can be observed. The XPS analysis of Ag NSs was given in Fig. 4d to characterize the chemical composition of Ag NSs further. It exhibited the characteristic peaks over Ag 3d region, which were split into 5/2, and 3/2 states at 367, and 373 eV, respectively. All structural and chemical characterizations support the growth of Ag NSs on the Cu-grid.

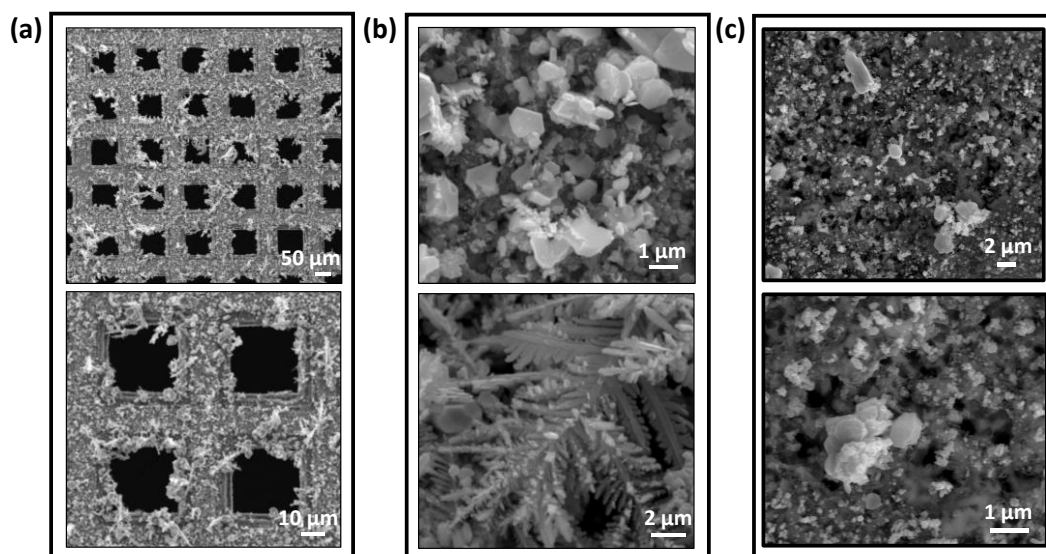


Figure 3. (a-b) SEM images of Ag NSs on Cu-grid at different magnifications. (c) SEM images of Ag NSs on Cu-grid without stirring.

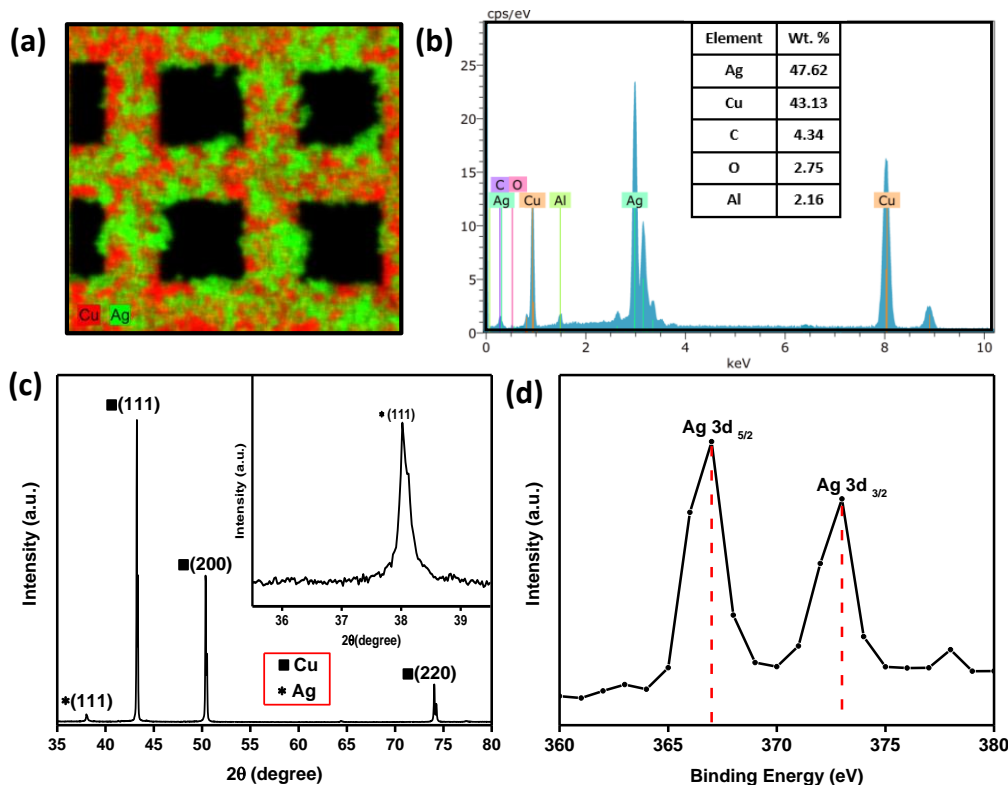


Figure 4. (a) EDX mapping and (b) EDX analysis (c) XRD analysis, and (d) XPS analysis of Ag NSs on the Cu-grid.

The growth of Ag NSs on the Cu-grid requires time. If we keep the reaction time at 0.5 hours (Fig. 5.a), we can see that Ag^{+1} ions are reduced on the Cu-grid, and nucleation begins. At this stage, the particles are relatively spherical and cover the entire surface. When the reaction is continued for 1 hour (Fig. 5.b), the particles grow more, go out of the spherical form, and nanoplates begin to form on the surface. Even needle-like structures are just starting to appear. When the time is completed to two hours, the existence of more complex shaped particles and needle-like structures that allow hot-spot formation becomes possible. According to the results of EDX analysis, it is seen that Ag formation on the surface increases with time (Fig. 5 c-d).

It is known that nanostructures with sharp corners and edges increase the number of hot spots on the surface, resulting in a higher Raman signal [21]. The branched hierarchical nanostructures and complex-shaped nanoparticles we see in Fig. 3b cause the electromagnetic field to intensity on the surface, positively affecting the SERS results. We can observe this clearly in Fig. 6a. Although Cu is a plasmonically-active material [22], since the surface of the Cu-grid is relatively smooth, we obtain a very low Raman signal even from the 100 μM of R6G solution on the Cu-grid. Thanks to the Ag NSs on the Cu-grid, we can get a very high Raman signal from the 100 μM of R6G solution.

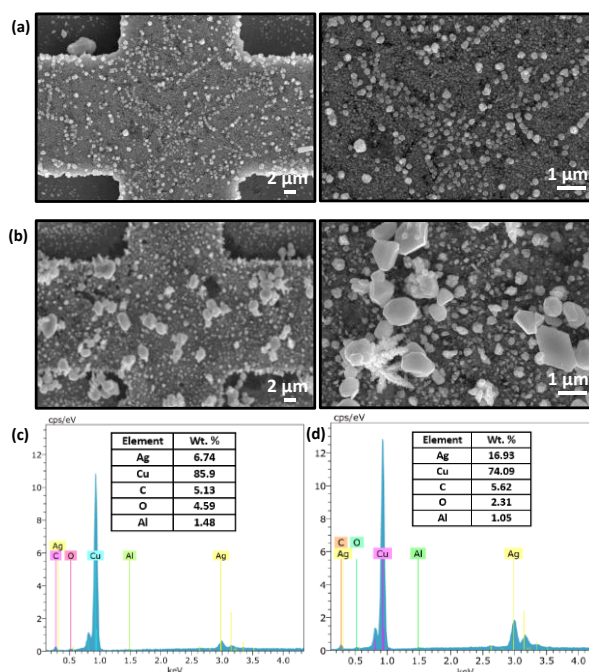


Figure 5. SEM images of Ag NSs on the Cu-grid after (a) 0.5, and (b) 1 hour. EDX analysis of (c) 0.5, and (d) 1 hour.

In Fig. 6b, there is Raman mapping filtered according to the band at 1507 cm^{-1} , which we have taken from the $100\text{ }\mu\text{M}$ of R6G solution on the Ag NSs. Here, we acquire a strong Raman signal over almost the entire area. The solutions prepared at lower concentrations were dropped on the Ag NSs to evaluate the limit of detection (LOD) of the R6G as a probe molecule. We can clearly distinguish the characteristic peaks of R6G at 612 cm^{-1} (C-C-C ring in-plane), 773 cm^{-1} (C-H out-of-plane), 1185 cm^{-1} (C-H in-plane); 1310 , 1363 , 1507 , 1575 , 1648 cm^{-1} (C-C stretching of the aromatic ring) even at a concentration as low as 100 pM (Fig. 6c) [23]. It is very valuable to fabricate a strong SERS substrate for ultra-trace sensing using a one-step, straightforward, low-cost method.

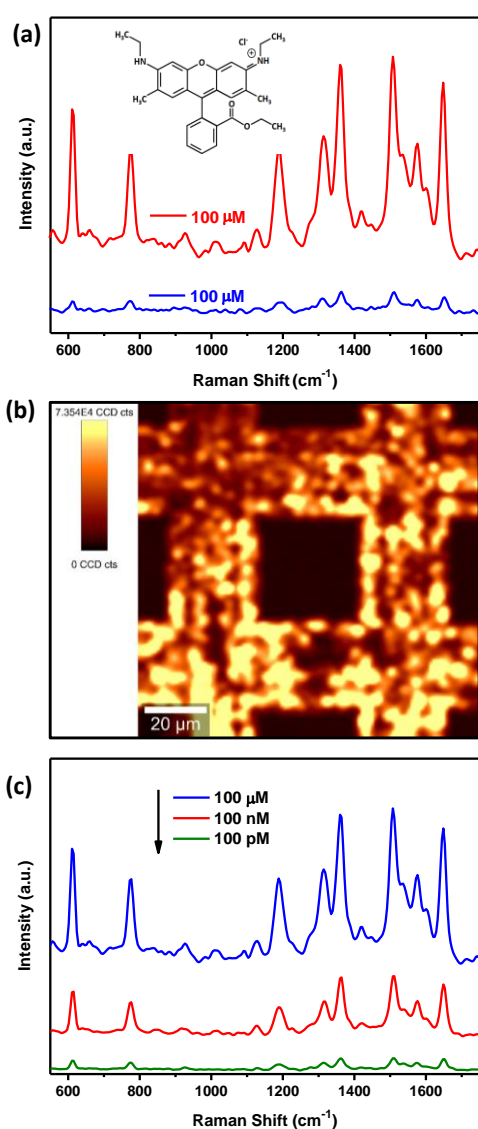


Figure 6. (a) SERS of R6G taken on Ag NSs (red line) and Cu-grid (blue line) (Inset: The chemical formula of R6G molecule). (b) SERS mapping of R6G on Ag NSs.

filtered with respect to the band at 1507 cm^{-1} . (c) Limit of detection of R6G on Ag NSs.

To calculate the AEF, we use the peak intensities at 1507 cm^{-1} of the Raman spectra in Fig. 6a. The peak intensities obtained from $100\text{ }\mu\text{M}$ of R6G solution dropped only on Cu-grid, and 100 pM of R6G solution dropped on Ag NSs are 206 and 193, respectively. When we replace these values in Formula (1), AEF is calculated as high as 9.37×10^6 . This result is quite remarkable compared to similar studies in the literature [15, 17].

4. Conclusion

The SERS-active substrate with a high enhancement factor of 9.37×10^6 has been fabricated using a simple, cheap, and one-step method for ultra-trace sensing applications. This method synthesized needle-like and complex-shaped Ag NSs, causing this superior enhancement in situ on Cu-grid to detect R6G as a probe molecule. Growing nanostructures in situ also avoid the agglomeration problem, which we often encounter in colloidal nanoparticles, and thus, many hot spots are formed with suitable nano-gaps. Herein, we have demonstrated that Ag NSs can be grown in situ on commercially available Cu-grids and be used as a SERS-active substrate. This method can also be applied to grow other metallic nanostructures for different applications.

Author's Contributions

Menekşe Şakir: Drafted and wrote the manuscript, performed the experiment and result analysis.

Ethics

There are no ethical issues after the publication of this manuscript.

References

- [1] Mosier-Boss, P. A. 2017. Review of SERS substrates for chemical sensing. *Nanomaterials*; 7(6): 142.
- [2] Sharma, B., Frontiera, R. R., Henry, A.-I., Ringe, E., Van Duyne, R. P. 2012. SERS: Materials, applications, and the future background and mechanism. *Materials Today*; 15(1-2): 16-25.
- [3] Sharma, B., Fernanda Cardinal, M., Kleinman, S. L., Greeneltch, N. G., Frontiera, R. R., Blaber, M. G., Schatz, G. C., Van Duyne, R. P. 2013. High-performance SERS substrates: Advances and challenges. *MRS Bulletin*; 38(8): 615–624.
- [4] Green, M., Liu, F. M. 2003. SERS substrates fabricated by island lithography: The silver/pyridine system. *Journal of Physical Chemistry B*; 107(47): 13015–13021.
- [5] Nowicka, A. B., Czaplicka, M., Kowalska, A. A., Szymborski, T., Kamińska, A. 2019. Flexible PET/ITO/Ag SERS platform for label-free detection of pesticides. *Biosensors*; 9(3): 111.
- [6] Suresh, V., Ding, L., Chew, A. B., Yap, F. L. 2018. Fabrication of large-area flexible SERS substrates by nanoimprint lithography. *ACS Applied Nano Materials*; 1(2): 886–893.

- [7]. Xu, B. B., Zhang, Y. L., Zhang, W. Y., Liu, X. Q., Wang, J. N., Zhang, X. L., Zhang, D. D., Jiang, H. B., Zhang, R., Sun, H. B. 2013. Silver-coated rose petal: Green, facile, low-cost and sustainable fabrication of a SERS substrate with unique superhydrophobicity and high efficiency. *Advanced Optical Materials*; 1(1): 56–60.
- [8]. Fodjo, E. K., Li, D. W., Marius, N. P., Albert, T., Long, Y. T. 2013. Low temperature synthesis and SERS application of silver molybdenum oxides. *Journal of Materials Chemistry A*; 1(7): 2558–2566.
- [9]. Fu, J., Ye, W., Wang, C. 2013. Facile synthesis of Ag dendrites on Al foil via galvanic replacement reaction with $[\text{Ag}(\text{NH}_3)_2]\text{Cl}$ for ultrasensitive SERS detecting of biomolecules. *Materials Chemistry and Physics*; 141(1): 107–113.
- [10]. Korkmaz, I., Sakir, M., Sarp, G., Salem, S., Torun, I., Volodkin, D., Yavuz, E., Onses, M. S., Yilmaz, E. 2021. Fabrication of superhydrophobic $\text{Ag@ZnO@Bi}_2\text{WO}_6$ membrane disc as flexible and photocatalytic active reusable SERS substrate. *Journal of Molecular Structure*; 1223: 129258.
- [11]. Yuan, J., Lai, Y., Duan, J., Zhao, Q., Zhan, J. 2012. Synthesis of a β -cyclodextrin-modified Ag film by the galvanic displacement on copper foil for SERS detection of PCBs. *Journal of Colloid and Interface Science*; 365(1): 122–126.
- [12]. Ye, W., Chen, Y., Zhou, F., Wang, C., Li, Y. 2012. Fluoride-assisted galvanic replacement synthesis of Ag and Au dendrites on aluminum foil with enhanced SERS and catalytic activities. *Journal of Materials Chemistry*; 22(35): 18327–18334.
- [13]. Ji, R., Sun, W., Chu, Y. 2014. One-step hydrothermal synthesis of $\text{Ag/Cu}_2\text{O}$ heterogeneous nanostructures over Cu foil and their SERS applications. *RSC Advances*; 4(12): 6055–6059.
- [14]. Sakir, M., Salem, S., Sanduvac, S. T., Sahmetlioglu, E., Sarp, G., Onses, M. S., Yilmaz, E. 2020. Photocatalytic green fabrication of Au nanoparticles on ZnO nanorods modified membrane as flexible and photocatalytic active reusable SERS substrates. *Colloids Surf. A*; 585: 124088.
- [15]. Gao, Y., Zhang, C., Yang, Y., Yang, N., Lu, S., You, T., Yin, P. 2021. A high sensitive glucose sensor based on Ag nanodendrites/Cu mesh substrate via surface-enhanced Raman spectroscopy and electrochemical analysis. *J. Alloys Compd.*; 863: 158758.
- [16]. Guo, T. L., Li, J. G., Sun, X., Sakka, Y. 2016. Improved galvanic replacement growth of Ag microstructures on Cu micro-grid for enhanced SERS detection of organic molecules. *Mater. Sci. Eng. C*; 61: 97–104.
- [17]. Sharma, H. S. S., Carmichael, E., McCall, D. 2016. Fabrication of SERS substrate for the detection of rhodamine 6G, glyphosate, melamine and salicylic acid, *Vibrational Spectroscopy*; 83: 159–169.
- [18]. Zhou, Q., Meng, G., Liu, J., Huang, Z., Han, F., Zhu, C., Kim, D. J., Kim, T., Wu, N. 2017. A hierarchical nanostructure-based surface-enhanced Raman scattering sensor for preconcentration and detection of antibiotic pollutants. *Adv. Mater. Technol.*; 2(6): 1700028.
- [19]. Salem, S., Sakir, M., Sahin, K., Korkmaz, I., Yavuz, E., Sarp, G., Onses, M. S., Yilmaz, E. 2020. Low bandgap microsphere-like magnetic nanocomposite: An enhanced photocatalyst for degradation of organic contaminants and fabrication of SERS-active surfaces. *Colloids Surf. A*; 589: 124436.
- [20]. Sakir, Menekse, Yilmaz, E., Onses, M. S. 2020. SERS-active hydrophobic substrates fabricated by surface growth of Cu nanostructures. *Microchemical Journal*; 154: 104628.
- [21]. Sakir, Menekse, Pekdemir, S., Karatay, A., Küçüköz, B., Ipekci, H. H., Elmali, A., Demirel, G., Onses, M. S. 2017. Fabrication of plasmonically active substrates using engineered silver nanostructures for SERS applications. *ACS Applied Materials and Interfaces*; 9(45): 39795–39803.
- [22]. Cejkova, J., Prokopec, V., Brazdova, S., Kokaislova, A., Matejka, P., Stepanek, F. 2009. Characterization of copper SERS-active substrates prepared by electrochemical deposition. *Applied Surface Science*; 255(18): 7864–7870.
- [23]. Zang, L. S., Chen, Y. M., Koc-Bilican, B., Bilican, I., Sakir, M., Wait, J., Çolak, A., Karaduman, T., Ceylan, A., Ali, A., Elbuken, C., Serdar Onses, M., Kaya, M. 2021. From bio-waste to biomaterials: The eggshells of Chinese oak silkworm as templates for SERS-active surfaces. *Chemical Engineering Journal*; 426: 131874.

A Study on Total Phenolic and Flavonoid Content, Antioxidant, Toxicity, and Anthelmintic Activities of Methanol Extract of *Crocus cancellatus* subsp. *lycuis*

Mehlika Alper¹ , Mehmet Özgür Atay¹ , Olcay Ceylan² , Ramazan Mammadov^{1*} 

¹Muğla Sıtkı Koçman University, Molecular Biology and Genetic Department, Muğla, Türkiye

²Muğla Sıtkı Koçman University, Biology Department, Muğla, Türkiye

*rmammad@yahoo.com

* Orcid No: 0000-0003-2218-5336

Received: 29 April 2022

Accepted: 15 February 2023

DOI: 10.18466/cbayarfbe.1111317

Abstract

The present study was planned to assess total phenolic and flavonoid content and some biological properties (antioxidant, toxicity, and anthelmintic) of the methanol extract of *Crocus cancellatus* subsp. *lycuis* from Muğla province (Turkey) for the first time. It was found that the total phenolic (2.08 ± 0.06 mg GAE/g) and total flavonoid (3.63 ± 0.09 mg QE/g) contents of the aerial part extract were higher than the bulb extract. The aerial part extract (IC₅₀ value: 0.86 ± 0.03 mg/mL, IC₅₀ value: 0.26 ± 0.003 mg/mL, 0.77 ± 0.007 mg TE/g, and 5.92 ± 0.30 mg TE/g, respectively) was determined to exhibit the higher activity than that of bulb parts extract in the assays shortly named as DPPH, ABTS, FRAP, and CUPRAC. Both extracts were observed to have anthelmintic activity on brine shrimp. According to these results, *Crocus cancellatus* subsp. *lycuis* can be accepted as a good source for the pharmaceutical and food industries.

Keywords: Anthelmintic, Antioxidant, Brine shrimp, Crocus, Flavonoid, Phenolic

1. Introduction

Natural products are important in the increases of health and avoiding illness and also, they have been known to have several biological features such as antioxidant, anti-inflammatory, and anti-apoptotic activities [1]. Secondary metabolites which are natural products generated and used by organisms for defense or adaptation remain the most significant resource with potential therapeutic properties [2]. Known to be of worldwide medicinal importance, plants have served as an important source of nutrition and also for the development of new treatments for diseases. Secondary metabolites synthesized by plants play important role in the discovery of novel drugs [3,4,5]. The *Crocus* genus which is a member of the large family Iridaceae including a large number of flowering plants is a perennial geophyte. Most *Crocus* species are native to the Mediterranean floristic region and distributed eastwards into the Iran-Turanian region [6,7]. This plant was reported to be widely cultivated in Iran, Morocco, India, Italy, Greece, Italy, Spain, and Afghanistan [7].

The *Crocus* genus has been reported to have biological activities like antimicrobial, anti-fungal, and antiseptic. The pharmacological properties of species belonging to the genus *Crocus* were reviewed by Mykhailenko et al. (2019) and Mohtashami et al. (2021) [6,7]. Turkey is a rich country in terms of *Crocus* species with about 70 *Crocus* taxa 31 of them are endemic to Turkey [8,9] the present study intended to examine the antioxidant, cytotoxic and anthelmintic potential, and to determine the amount of the total phenolic and total flavonoid contents of the methanol extracts of *Crocus cancellatus* subsp. *lycuis* from Muğla province (Turkey) for the first time.

2. Materials and Methods

2.1 Material

Crocus cancellatus subsp. *lycuis* were collected from Muğla province ($28^{\circ}22'34''$ K- $28^{\circ}22'18''$ D, 660 m, Ula-Menteşe) in November 2020 and were identified by Dr. Olcay Ceylan (Muğla Sıtkı Koçman University, Türkiye) in addition, a voucher specimen (O.2120) was kept in his herbarium.

2.2 Chemicals

DPPH, ABTS, BHA, Trolox, FCR, Sodium carbonate, gallic acid, and quercetin were obtained from Sigma-Aldrich (USA).

2.3 Methods

2.3.1 Preparation of plant extracts

For the extraction procedure, the dried samples (aerial and bulb) in shadow at room temperature were extracted with methanol at 50°C for 24 h using a water bath. After filtration, methanol used as solvent was evaporated with a rotary evaporator (Heindolph LABOROTA 4011). The crude extracts were deposited at -20°C [10].

2.3.2 Determination of total phenolic and flavonoid content of extracts

The total phenolic and flavonoid contents of aerial and bulb methanol extract were determined according to the methods described by Singleton and Rossi (1965) and Aryal et al., (2019), respectively [11,12]. The results were calculated as equivalents of gallic acid (mg GAE/g extract) and quercetin (mg QE/g extract), respectively.

2.3.3 Determination of antioxidant activity

For determination of the antioxidant activity of the extract, DPPH (2,2-diphenyl-1-picrylhydrazyl) [10], ABTS (2,2'-azino-bis(3-ethylbenzothiazoline-6-sulfonic acid)) [13] radical scavenging activity assays, FRAP (ferric reducing antioxidant power) assay [14] and CUPRAC (cupric ion reducing antioxidant capacity) assay [15] were carried out. IC₅₀ (half max inhibitory concentration) values were estimated for DPPH and ABTS assays. The results of FRAP and CUPRAC assays were expressed as equivalents of Trolox (mg TE/g extract).

2.3.4 Brine shrimp lethality bioassay

The brine shrimp lethality assay described by Krishnaraju et al. (2005) was carried out with some modifications for evaluation of the cytotoxic potential of the extracts. 10 mg of *Artemia salina* eggs were added to an aquarium with maintaining aeration containing 500 ml of artificial seawater (38 g/L of sea salt) at 28°C and kept for 48 h. 0.5 mL of each extract at different concentrations (0.01-1 mg/mL) were added to 4.5 mL of brine solution including 10 nauplii. Following 24 h, surviving larvae were counted under the light [16].

2.3.5 Determination of anthelmintic activity

The anthelmintic activities of the extracts were performed using a nearly 1-2 cm size of *Tubifex tubifex* (Annelida) according to the method described by Dutta

et al. (2012) [17]. In brief, 20 ml of extract at different concentrations (2.5-20 mg/mL) dissolved in distilled water was transferred to a petri dish and then 6 worms were added. Albendazole as a reference standard (20 mg/mL) and distilled water were positive and negative controls, respectively. The worms were evaluated in terms of motility. When worms without motility were vigorously shaken, the time of paralysis and death were recorded if any movement and if no movement were perceived, respectively.

2.3.6 Data analysis

The results from the assay performed in triplicate were expressed as mean±SE (Standard Error). The IC₅₀ (half maximal inhibitory concentration) values for DPPH and ABTS assay, and also LC₅₀ value (half maximal lethality concentration) for brine shrimp lethality assay were calculated using the Statistical Package for the Social Sciences (SPSS) software version 22.0 for Windows. Analysis of Variance (ANOVA) and Tukey (P<0.05) test was performed to determine the difference in the groups.

3. Results and Discussion

3.1 Total phenolic and total flavonoid contents of the extracts

Phenolic compounds are important in human health due to their biological properties such as antioxidant activity, which helps to eliminate oxidative stress that can be associated with various diseases such as cancer, neurodegenerative, and others [18]. In the present study, the total phenolic and total flavonoid contents were found to be high in an aerial part extract with values of 2,08±0,06 mg GAE/g and 3,63±0,09 mg QE/g, respectively (Table 1).

Table 1. Total phenolic and total flavonoid contents of *Crocus cancellatus* subsp. *lycuis* extracts

Plant Extracts	Total Phenolic Content (mg GAE/g)	Total Flavonoid Content (mg QE/g)
Aerial Part	2,08±0,06 ^a	3,63±0,09 ^a
Bulb Part	0.59±0.02 ^b	0.19±0.007 ^b

The different letters in a column are significantly different (p<0.05)

Our results were showed lower values when compared to those reported by Loizzo et al (2016), who declared that total phenols and total flavonoids for *C. cancellatus* subsp. *damascenus* stigmas extract (Ethanol %70) were 146.8±2.5 mg chlorogenic acid equivalents per g extract and 57.5±1.2 mg quercetin equivalents per g extract, respectively [19]. The total phenolic contents of methanol, ethanol, and boiling water extracts of stigmas

of *C. sativus* from Iran, with values of 6.54, 6.35, and 5.70 mg GAE/g of dry weight (DW), respectively were found to be higher than those of our extracts. In addition, the total flavonoid content of these *C. sativus* stigmas extracts was reported as 5.88, 2.91, and 3.68 mg rutin equivalent/g DW, respectively [20]. On the other hand, Satybaldiyeva et al. (2015) showed that the total phenolic contents of the extracts from aerial and bulb parts of *C. alatavicus* (Kazakhstan) using different solvents (distilled water, 96% ethanol, 99% methanol, and 99% dichloromethane) were ranged from 13.63 to 72.29 mg GAE/g extract and that the ethanolic extract of aerial part contained the highest total phenolic content [21]. Under different brewing conditions, total polyphenol, and flavonoid contents in stamens and tepals of *C. sativus* from Italy were reported to be in the range of 83-186 mg GAE/L and 34-91 mg CE (catechin equivalents)/L, respectively [22]. It was shown that the total phenolic content of the extracts of the different parts of *C. pallasi* was in the range of 13.48-28.92 mg GAE/g, while the total flavonoid content was in the range of 0.50 - 31.44 mg RE (rutin equivalent)/g [23]. According to these results, the total phenolic and total flavonoid content of the *Crocus* species may vary depending on the plant species, the geographical region where it was collected, the parts of the plant used, and the extraction method.

3.2 Antioxidant activities of the extracts

The different assays (DPPH, ABTS, FRAP, and CUPRAC) were applied to evaluate the antioxidant activity of the extracts (Table 2).

Table 2. Antioxidant activity of *Crocus cancellatus* subsp. *lycuus* extracts

Plant Extracts	DPPH (IC ₅₀ , mg/mL)	ABTS (IC ₅₀ , mg/mL)	FRAP (mg TE/g)	CUPRAC (mg TE/g)
Aerial Part	0,86±0,03 ^b	0,26±0,00 ^{3b}	0,77±0,007 ^a	5,92±0,30 ^a
Bulb Part	1,11±0,01 ^c	0,61±0,03 ^{5c}	0,46±0,003 ^b	1,33±0,07 ^b
BHA	0,009±0,0002 ^a	0,008±0,004 ^a		

The different letters in a column are significantly different (p<0.05)

In the DPPH and ABTS radical scavenging assays, the antioxidant activity of both extracts was lower than the BHA as control.

However, when compared to the bulb extract, the extract of the aerial parts was determined to exhibit high activity with the IC₅₀ values of 0,86±0,03 and 0,26±0,003 mg/mL, respectively. In addition, the extract of the aerial parts (0,77±0,007 and 5,92±0,30 mg TE/g) showed higher antioxidant activity than the bulbs extract, in terms of FRAP and CUPRAC assays which were performed to determine the reducing power potentials of the extracts. Phenolic compounds based on plants have been known to show antioxidant activity [24]. The reason why the aerial part shows higher activity than the bulb part maybe it contains more phenolics.

Antioxidants are of great importance in neutralizing the harmful effects of free radicals on human health. Due to the possible negative effects of synthetic antioxidants for example BHA (butylated hydroxyl anisole) and BHT (butylated hydroxyl toluene) on health, the search for natural antioxidants instead them is of great interest. The various plant samples have been reported to be a source of antioxidants with a natural origin [25]. There are various outcomes in the literature displaying the antioxidant activities of the genus *Crocus* [6]. Contrary to the current study, the extract of the bulb of *C. cancellatus* herb. gained from Qarachugh mountain (Erbil) showed better antioxidant activity at all concentrations tested in the DPPH assay compared to the BHT served as control [26]. Stigma extract of *C. cancellatus* subsp. *damascenus* from Iran was reported to cause the DPPH and ABTS radical scavenging activity with IC₅₀ values of 34.6 and 21.6 µg/mL, respectively, and exhibit a good reducing potency (53.9 mM Fe (II)/g) [6]. The DPPH activity of the extracts tested herein is less than the methanol extracts of aerial parts and bulbs of *C. alatavicus* from Almaty (Kazakhstan) because its IC₅₀ values were shown as 510 and 853 µg/mL, respectively [21]. Also, several *Crocus* species for example *C. caspius* [27], *C. sativus* [28], and *C. pallasi* [29] were declared to exhibit antioxidant activity.

3.3 Toxicity of the extracts on brine shrimps

The brine shrimp lethality assay is one of the significant bioassays for the pre-screening of cytotoxicity of the plant extracts and is used for evaluating the preliminary screening of the anti-cancer activity of these extracts [30,31]. The present study revealed that the mortality percentage of shrimp nauplii increased depending on the increasing concentrations of both extracts (Table 3). According to Meyer et al. (1982), the aerial parts and bulb extracts with LC₅₀ values of 0.014 and 0.012, respectively were found to be active, because the LC₅₀ values were recorded as lower than 1000 µg/mL for each extract tested [32].

Table 3. Average mortality rates (%) of *Artemia salina* after 24 h of exposure to *Crocus cancellatus* subsp. *lycuis* extracts at different concentrations

Concentrations	Aerial Part 24 h Later (%)	Bulb Part 24 h Later (%)
0.01 mg/mL	52.77	55.55
0.05 mg/mL	61.11	63.88
0.1 mg/mL	72.22	72.22
0.5 mg/mL	85.55	88.88
1.0 mg/mL	100	100
Negative Control*	11.36	11.36
LC ₅₀ (mg/mL)	0,014	0,012
LC ₉₀ (mg/mL)	0,523	0,423

*Negative Control: Distilled water

Similarly in our study, the ethanolic aerial part extract of *C. alatavicus* was stated to cause a high cytotoxic activity on brine shrimp with an LC₅₀ value of 15.75 µg/ml [21].

3.4 Anthelmintic activities of the extracts

Tubifex tubifex belonging to the same group of annelids as the intestinal roundworm parasites of humans was used in this study due to anatomical and physiological resemblances to those found in human beings. The anthelmintic activity was determined to increase with the increasing concentration of the extract tested (Table 4).

Table 4. Anthelmintic activity of *Crocus cancellatus* subsp. *lycuis* extracts

	Concentration (mg/mL)	P (Min)*	D (Min)**
Aerial Part	2,5	8	12
	5	4	6
	10	2	3
	20	1	2
	2,5	13	23
Bulb Part	5	5	10
	10	2	5
	20	1	3
Positive Control***	20	3	7
Negative Control****	-	-	-

*P=Time taken for paralysis. **D=Time taken for death of worms. ***Positive Control: Albendazole® ****Negative Control: distilled water

The aerial and bulb methanol extracts of the plant showed higher activity than the albendazole used as the control. The aerial extract exhibited a higher anthelmintic activity than the bulb extract. When compared in terms of paralysis and death times, at 20 mg/mL, the anthelmintic activity of both extracts was seen to be better than the standard. Helminth infections and anthelmintic resistance are among considerable health concerns for both animals and humans. Plants as an important resource in the research of new bioactive natural agents may be greatly significant for providing some advantages such as obtaining substances with anthelmintic properties which are safe for animal and human health. Investigations concerning plants that have anthelmintic properties continue to be important [17,33,34].

4. Conclusion

To the best of our knowledge, the properties of the methanol extracts of *C. cancellatus* subsp. *lycuis* from Muğla province (Turkey), which were investigated here, were determined for the first time in the present study. The aerial part extract of *C. cancellatus* subsp. *lycuis* was found to be richer than the bulb part extract in terms of total phenolic and flavonoid contents. In addition, the aerial extract exhibited higher antioxidant activity than the bulb extract. *C. cancellatus* subsp. *lycuis* extracts were observed to exhibit toxicity on brine shrimp, and anthelmintic activities. The results of the present study suggest that the *C. cancellatus* subsp. *lycuis* is capable of being evaluated as a natural source for different applications such as the pharmaceutical and food industry, due to its biological properties determined here. This study will allow its application to further studies for the isolation and identification of substances with bioactive properties from *C. cancellatus* subsp. *lycuis*.

Author's Contributions

Mehlika Alper: Helped with data interpretation and statistical analysis and wrote the manuscript.

Mehmet Özgür Atay: Supported the antioxidant test

Olca Ceylan: Helped write the manuscript

Ramazan Mammadov: Performed the project, researched the design of all experiments, and wrote the manuscript.

Ethics

There are no ethical issues after the publication of this manuscript.

References

- [1]. Rehman, M. U., Wali, A. F., Ahmad, A., Shakeel, S., Rasool, S., Ali, R., ... & Khan, R. (2019). Neuroprotective strategies for neurological disorders by natural products: an update. *Current Neuropharmacology*,17(3),247-267.
- [2]. Bernardini, S., Tiezzi, A., Laghezza Masci, V., & Ovidi, E. (2018). Natural products for human health: an historical overview of the drug discovery approaches. *Natural product research*, 32(16), 1926-1950.
- [3]. Raina, H., Soni, G., Jauhari, N., Sharma, N., & Bharadvaja, N. (2014). Phytochemical importance of medicinal plants as potential sources of anticancer agents. *Turkish Journal of Botany*, 38(6), 1027-1035.
- [4]. Alamgir, A.N.M. (2018). Introduction. In: *Therapeutic Use of Medicinal Plants and their Extracts: Volume 2. Progress in Drug Research*, vol 74. Springer, Cham. https://doi.org/10.1007/978-3-319-92387-1_1
- [5]. Che, C. T., & Zhang, H. (2019). Plant Natural Products for Human Health. *International journal of molecular sciences*, 20(4), 830.<https://doi.org/10.3390/ijms20040830>
- [6]. Loizzo, O., Kovalyov, V., Goryacha, O., Ivanauskas, L., & Georgiyants, V. (2019). Biologically active compounds and pharmacological activities of species of the genus *Crocus*: A review. *Phytochemistry*,162,56-89.
- [7]. Mohtashami, L., Amiri, M. S., Ramezani, M., Emami, S. A., & Simal-Gandara, J. (2021). The genus *Crocus* L.: A review of ethnobotanical uses, phytochemistry and pharmacology. *Industrial Cops and Products*, 171, 113923.
- [8]. P.H. Davis, R. Mill, K. Tan Flora of Turkey and the East Aegean Islands (Supplement I), vol. 10, Edinburgh University Press, Edinburgh (1988) 278pp
- [9]. Verma, S. K., Das, A. K., Cingoz, G. S., Uslu, E., & Gurel, E. (2016). Influence of nutrient media on callus induction, somatic embryogenesis and plant regeneration in selected Turkish crocus species. *Biotechnology Reports*, 10, 66-74.
- [10]. Turan, M., Mammadov, R. 2018. "Antioxidant, Antimicrobial, Cytotoxic, Larvicidal and Anthelmintic Activities and Phenolic Contents of *Cyclamen alpinum*", *Pharmacology & Pharmacy*, 9, 100-116.
- [11]. Singleton, V.L., Rossi, J.A. 1965. "Colorimetry of total phenolics with phosphomolybdic-phosphotungstic acid reagents", *American Journal of Enology and Viticulture*, 16(3), 144-158.
- [12]. Aryal, S., Baniya, M. K., Danekhu, K., Kunwar, P., Gurung, R., Koirala, N. 2019. "Total phenolic content, flavonoid content and antioxidant potential of wild vegetables from Western Nepal", *Plants*, 8(4), 96.
- [13]. Re, R., Pellegrini, N., Proteggente, A., Pannala, A., Yang, M., Rice-Evans, C. 1999. "Antioxidant activity applying an improved ABTS radical cation decolorization assay", *Free radical biology and medicine*, 26(9-10), 1231-1237.
- [14]. Benzie, I. F., Strain, J. J. 1996. "The ferric reducing ability of plasma (FRAP) as a measure of "antioxidant power": the FRAP assay", *Analytical Biochemistry*, 239(1), 70-76.
- [15]. Apak, R., Güçlü, K., Özyürek, M., Karademir, S. E. 2004. "Novel total antioxidant capacity index for dietary polyphenols and vitamins C and E, using their cupric ion reducing capability in the presence of neocuproine: CUPRAC method", *Journal of Agricultural and Food Chemistry*, 52(26), 7970-7981.
- [16]. Krishnaraju, A. V., Rao, T. V., Sundararaju, D., Vanisree, M., Tsay, H. S., & Subbaraju, G. V. (2005). Assessment of bioactivity of Indian medicinal plants using brine shrimp (*Artemia salina*) lethality assay. *International Journal of Applied Science and Engineering*, 3(2), 125-134.
- [17]. Dutta et al. (2012). Dutta, B., Ghosal, M., Chakrabarty, P., & Mandal, P. (2012). Anthelmintic and free radicalscavenging potential of various fractions obtained from foliar parts of *Glinus oppositifolius*(Linn.) *DC.International Journal of Pharmacy and Pharmaceutical Sciences*,4(4), 233–239
- [18]. Cosme et al. 2020. Plant Phenolics: Bioavailability as a Key Determinant of Their Potential Health-Promoting Applications. *Antioxidants* 2020, 9, 1263; doi:10.3390/antiox9121263
- [19]. Loizzo et al. 2016. *Crocus cancellatus* subsp. *damascenus* stigmas: chemical profile, and inhibition of α -amylase, α -glucosidase and lipase, key enzymes related to type 2 diabetes and obesity. *J Enzyme Inhib Med Chem*, 2016; 31(2): 212–218.
- [20]. Karimi, E., Oskoueian, E., Hendra, R., & Jaafar, H. Z. (2010). Evaluation of *Crocus sativus* L. stigma phenolic and flavonoid compounds and its antioxidant activity. *Molecules*,15(9),6244–6256.
- [21]. Satybaldiyeva et al. 2015. Satybaldiyeva, D., Mursaliyeva, V., Rakhimbayev, I., Zayadan, B., Mammadov, R., 2015. Preliminary phytochemical analysis and antioxidant, antibacterial activities of *Crocus alatavicus* from Kazakhstan. *Not. Bot. Horti Agrobot. Cluj-Napoca* 43, 343–348.
- [22]. Bellachioma, L., Rocchetti, G., Morresi, C., Martinelli, E., Lucini, L., Ferretti, G., ... & Bacchetti, T. (2022). Valorisation of *Crocus sativus* flower parts for herbal infusions: impact of brewing conditions on phenolic profiling, antioxidant capacity and sensory traits. *International Journal of Food Science & Technology*.
- [23]. Zengin et al. 2020. Chemical characterization, antioxidant, enzyme inhibitory and cytotoxic properties of two geophytes: *Crocus pallasii* and *Cyclamen cilicium*. *Food Research International* 133 (2020) 109129.
- [24]. Soobrattee et al., 2005. Phenolics as potential antioxidant therapeutic agents: Mechanism and actions. *Mutation Research/Fundamental and Molecular Mechanisms of Mutagenesis*. Volume 579, Issues 1–2, 11 November 2005, Pages 200-213.
- [25]. Lourenço, S. C., Moldão-Martins, M., & Alves, V. D. (2019). Antioxidants of Natural Plant Origins: From Sources to Food Industry Applications. *Molecules* (Basel, Switzerland), 24(22), 4132. <https://doi.org/10.3390/molecules24224132>.
- [26]. Ismael, 2021. Phytochemical screening and anti-candida activities of *Crocus cancellatus* herb. Ethanol extract. *ZANCO Journal of Pure and Applied Sciences* 33 (3): 124-133
- [27]. Khalili et al. 2016. Antioxidant activity of bulbs and aerial parts of *Crocus caspius*, impact of extraction methods. *Pak. J. Pharm. Sci.*, 29(3), 2016, 773-777.
- [28]. Rahaiee, S., Moini, S., Hashemi, M. et al. Evaluation of antioxidant activities of bioactive compounds and various extracts obtained from saffron (*Crocus sativus* L.): a review. *J Food Sci Technol* 52, 1881–1888 (2015). <https://doi.org/10.1007/s13197-013-1238-x>



- [29]. Shakeri et al. 2019. Cytotoxic and Antioxidant Activities of *Crocus pallasii* subsp. *haussknechtii* Corms Extracts Compared with *Crocus sativus*. *Research Journal of Pharmacognosy (RJP)* 6(3), 2019: 51-59
- [30]. Sarah et al. 2017. Brine shrimp lethality assay. *Bangladesh J Pharmacol.* 2017; 12: 186-189.
- [31]. Mianabadi et al., 2015. Comparison of Cytotoxicity and anti-cancer activity, by *Artemia urmiana* Brine Shrimp Lethality Test (BSLT) and Cancer Cell leukemia and Breast Cancer by two species of *Daphne*
- [32]. Meyer, B.N., Ferrigni, N.R., Putnam, J.E., Jacobsen, L.B., Nichols, D.E., McLaughlin, J.L., 1982. Brine Shrimp: A convenient general bioassay for active plant constituents. *Planta Medica.* 45, 31-34.
- [33]. Peixoto E.C.T.M., Andrade A., Valadares F., Silva L.P. and Silva R.M.G. 2013. Phytoterapy in the control of helminthiasis in animal production. *Afr. J. Agric. Res.* 8:2421-2429.
- [34]. Jayawardene, K. L. T., Palombo, E. A., & Boag, P. R. (2021). Natural Products Are a Promising Source for Anthelmintic Drug Discovery. *Biomolecules*, 11(10), 1457.

Adsorption behavior of methylene blue onto four different coffee residues

Ecem Tekne¹ , Yeliz Özüdoğru^{1*} 

¹ Faculty of Education, Chemistry Education, Çanakkale Onsekiz Mart University, Çanakkale, Türkiye

*yelizozudogru@hotmail.com

* Orcid No: 0000-0003-0471-6404

Received: 13 August 2022

Accepted: 06 February 2023

DOI: 10.18466/cbayarfbe.1161567

Abstract

In this study, the adsorption of methylene blue dyestuff in aqueous solution was investigated by using four different types of waste coffee grounds. The four coffee residues were Jacobs Monarch Coffee, Tchibo Professional Special Filter Coffee, Turkish Coffee (Mehmet Efendi), and Anisah Guatemala Coffee. Adsorption mechanisms were investigated by applying different adsorption conditions such as contact time, pH, methylene blue concentration and temperature. The characterization of the samples (before and after adsorption with methylene blue) was performed using FTIR and SEM analyses. The FTIR findings showed that methylene blue bonded with the hydrogen bonds. Langmuir and Freundlich isotherms were preferred to determine the adsorption mechanisms. When the results obtained are examined, it is seen that the maximum adsorption capacity was 67.14 mg/g at 298 K for Turkish coffee. It is understood that waste coffee grounds (especially Turkish coffee) are a cost-effective and environmentally friendly material for the removal of methylene blue in aqueous solution.

Keywords: Adsorption, Coffee Residue, Methylene Blue.

1. Introduction

As a result of increasing industrialization, environmental pollution has been increasing, also creating many problems by affecting living organisms [1]. Dyes are colored with organic compounds that give color to surfaces and fabrics [2]. These wastes can be classified as dyestuffs, heavy metals, organic and inorganic pollutants. Synthetic dyes are preferred in many different industrial areas such as textile, food processing, paper, plastic and cosmetics. [3]. With the discharge of dyes, both terrestrial and aquatic life are endangered. This causes a serious problem [4]. Physical, chemical and biological methods can be used to treat dyes [5]. Among these methods, the adsorption method is the most effective methods for removing many synthetic and organic substances in water. Because it is very high efficiency and adaptability [6]. Adsorption or adhesion is a chemical and physical force related to the surface. Adsorption is a very efficient process for remove pollutants [7]. In adsorption methods, especially activated carbon, some polymer-derived adsorbents and other low-cost (waste) materials are widely preferred [8]. There are many studies that used a variety of materials such as banana peel and orange peel [9], *Terminalia*

catappa Shell [10], corn cub [11], *Ulva lactuca* [12] and *Cystoseira barbata* [13].

The most existing dye's chemical structure is quite complex, but remains stable when exposed to light, heat, and oxidizing agents. To eliminate this complexity, paints maintain their stable form when exposed to factors such as light, heat, and oxidizing agents. One of the water-soluble dyes is methylene blue (MB). Methylene blue is used in many different areas such as cotton, wood, leather and drug dyeing. [14]. Although methylene blue does not cause a very high level of toxic effects in the aquatic system, it still causes negative effects such as rapid or difficult breathing, nausea, vomiting, diarrhea, and gastritis [15].

The aim of this study is to investigate the maximum adsorption capacities of four different waste coffee grounds used as adsorbent for the adsorption of methylene blue in aqueous solution. The study of various factors affecting the adsorption, such as pH, contact time, different concentrations of methylene blue, and three different temperatures, were carried out. Different adsorption conditions have been optimized to achieve maximum adsorption capacity. Freundlich and Langmuir

isotherm models were used to explain the adsorption mechanism. Fourier transform infrared spectroscopy (FTIR) and Scanning Electron Microscopes (SEM) analysis were preferred to understand the bonding structure and surface of the coffee grounds.

Although there are different studies with coffee [16-20] et al., 2021), there is no study on Turkish coffee. Therefore, this study is the first to include Turkish coffee on the comparison of different coffees.

2. Materials and Methods

2.1. Preparation of the Adsorbent

The coffee residues were provided by Jacobs Monarch Coffee Company, Tchibo Professional Special Filter Coffee, Turkish Coffee (Mehmet Efendi), and Anisah Guatemala Coffee, which were used as a filter. Waste coffee grounds were cleaned with distilled water and dried at 60°C for 24 hours.

2.2. Reagent and Equipment

Information about coffee and MB was given in Table 1. For the adsorption experiments, 1000 ppm stock MB solution was prepared and MB solutions (5, 10, 20, 50, 100, 150 and 200 mg/L) were obtained at different concentrations from the stock MB solution. pH adjustments with 0.1 M HCl and 0.1 M NaOH aqueous solutions. The samples were shaken with Mikrotest MSC 30 model shaker. MB concentration in solution was determined at 665 nm with a Specord S 600, Analytical Jena spectrophotometer.

2.3. Batch Biosorption Studies

10 mg of different coffee waste grounds were added to 10 mL of methylene blue (MB) solutions (10 ppm) of different pH standards. It was shaken at 250 rpm at 298 K for 60 minutes and then measured by spectrophotometer. All adsorption experiments were performed in three repetitions. % Removal (R) of MB removed from the aqueous solution was calculated by applying the following equation:

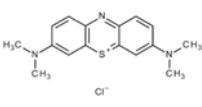
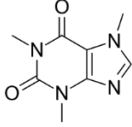
$$\% \text{ Removal (R)} = \frac{(C_o - C_e)}{C_o} * 100 \quad (2.1)$$

where C_o is the initial MB concentration (mg/L) and C_e is the equilibrium MB concentration in the aqueous solution (mg/L).

2.4. Determining the pH Effect

Studies were performed at different pHs (2, 3, 5, 7 and 9) at a fixed initial concentration (10 ppm). The samples were shaken at 250 rpm at 298 K for 60 minutes and the R-value was again calculated using Equation. (2.1).

Table 1. Information on methylene blue and coffee.

Descriptive factor	Methylene blue	Coffee
Chemical formulation	$C_{16}H_{18}N_3SCl$	$C_8H_{10}N_4O_2$
Molecular weight	319.85 $gmol^{-1}$	194.94 $gmol^{-1}$
Chemical structure		

2.5. Determining the time effect

Biosorption studies were performed at room temperature at different contact time from 10 minutes to 300 minutes (10, 25, 50, 100, 150, 200 and 300 minutes). The MB uptake at each time interval, qt (mg/g), was calculated by applying the equation given below:

$$qt = \frac{(C_o - C_e)}{M} * V \quad (2.2)$$

where C_o is the initial MB concentration (mg/L), C_e is the concentration of MB at a given time (mg/L), V is the volume of the MB solution (L), and M is the mass of the coffee (g dry weight).

2.6. Determining the Ion Concentration Effects

In the adsorption process, 100 mg of different percentages of coffee was added and with 10 mL of MB solution at an optimum pH for each coffee at different concentrations (5, 10, 20, 50, 100, 150, and 200 mg/L) at 25, 35, or 45 °C. The quantity of MB was derived from the concentration change at each temperature.

2.7. Characterizing Biomass

FTIR and SEM analysis were preferred for the analysis of the surface structures of the coffee groups. For FTIR and SEM analysis, each of the coffee batches was dried at 60 °C for 24 hours. A scanning electron microscope (Jeol JSM 7100F) was used to understand the changes in the adsorption process.

3. Results and Discussion

3.1. Determining the pH Effect

The pH of a dye solution is important because the performance of adsorption is dependent on the pH. pH affected the surface charge and protonation and deprotonation reaction were occurred [21]. The pH-dependent adsorption of MB with waste coffee grounds in aqueous solution is shown in Figure 1.

With the increasing pH, the proportion of negative charge in coffee molecules increased. As can be seen in Figure 1, with the change of pH, the adsorption capacity changed. The maximum adsorption capacity was 90% for Jacobs (at pH 3), 87% for Tchibo (at pH 5), 90% for Turkish coffee (at pH 9) and 83% for Anisah (at pH 9). A similar behavior has been given by other MB adsorption studies [22-24].

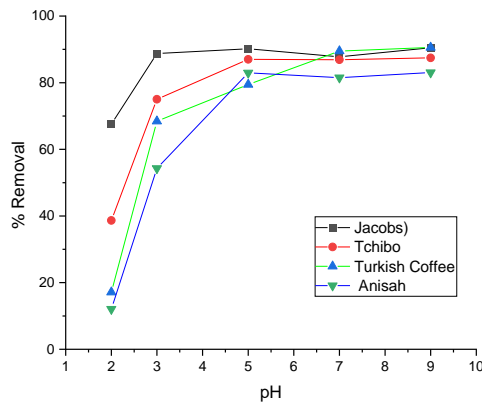


Figure 1. Effect of pH on the biosorption of methylene blue (MB).

3.2. Determining the Time Effects

The contact time has a great influence on the adsorption studies. As seen in Figure 2, adsorption takes place in 100 minutes for Turkish coffee, 150 minutes for Tchibo, and 200 minutes for Anisah and Jacobs coffees. This is stated that methylene blue adsorption occurs mainly on the surface of the waste coffee grounds as given by other studies on adsorption of methylene blue [23].

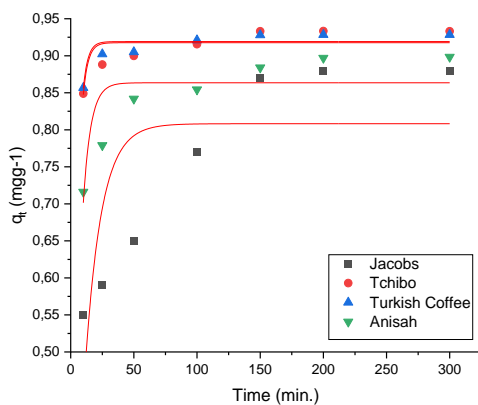


Figure 2. Effects of time on the biosorption of MB (pH 3) by different concentrations of four coffee residues.

3.3. Adsorption isotherms

Langmuir and Freundlich isotherm models were used for equilibrium description. The Langmuir model [25] is shown below:

$$\frac{C_e}{q_e} = \frac{1}{q_m a_L} + \frac{C_e}{q_m} \quad (3.1)$$

where q_e (mg/g) and C_e (mg/L) correspond to the concentration of MB adsorbed per gram of biomass and present in aqueous solution. q_m (mg/g) is the maximum adsorption capacity, and a_L is the Langmuir constant related to the adsorption energy.

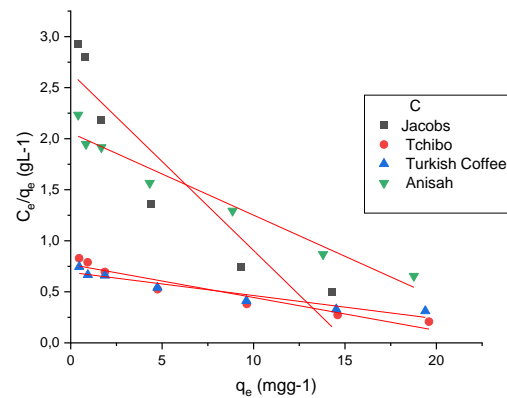
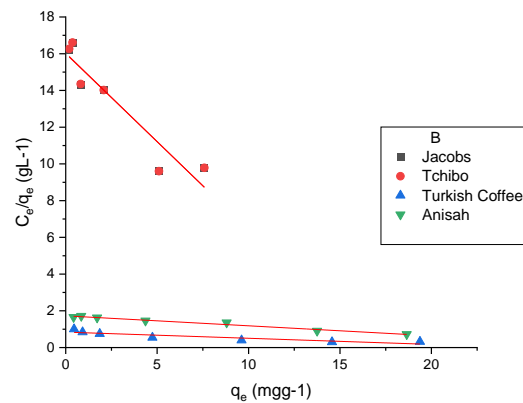
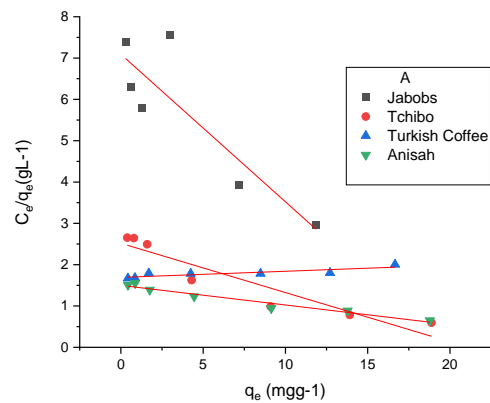


Figure 3. Adsorption isotherm curves for MB at 298 K (A), 308 K (B), and 318 K (C) at different concentrations of four coffee residues.

A linear form of Freundlich's equation is shown below [26] is shown below:

$$\log q_e = \log K_f + 1/n_f \log C_e \quad (3.2)$$

Given in this equation, K_f represents the adsorption capacity and n_f is related to adsorption. Linear regression using Langmuir and Freundlich isotherm models, equilibrium data at different concentrations and at three different temperatures were customized as seen in Figure 3 and Table 2.

As can be seen from Table 2, for all coffee species, for every temperature, the Freundlich adsorption isotherm gave a better fit than the Langmuir model based on the

correlation coefficient (R^2) value (up to 0.93). Looking at these results, it can be understood that MB adsorption belongs to the physical adsorption group.

The highest q_{max} value for Jacobs and Tchibo coffees was at 318 K, and was 5.74 mg/g and 30.96 mg/g, respectively. However, when the temperature increased, the q_{max} value of Turkish coffee first decreased and then increased (67.14 mg/g to 29.85 mg/g and to 44.05 mg/g). For Anisah, the q_{max} value increased with temperature (21.09 mg/g – 18.45 mg/g – 12.41 mg/g). From these results, we can say that the temperature affected the maximum adsorption capacity for each coffee species. The highest adsorption capacity was 67.14 mg/g (at 298 K).

Table 2. Parameters of Langmuir and Freundlich isotherms of MB adsorption at different concentrations of four different waste coffee grounds.

Adsorbent	Temperature(K)	Langmuir isotherm models			Freundlich isotherm models		
		q_{max} (mg/g)	a_L	R_L^2	n_f	K_f (mg/)	R_F^2
Jacobs	298	1.83	0.082	0.7012	0.89	0.128	0.9684
	308	1.04	0.059	0.8867	0.85	0.046	0.9949
	318	5.74	0.066	0.8710	0.54	0.225	0.9312
Tchibo	298	8.34	0.047	0.8870	0.63	0.267	0.9574
	308	1.04	0.060	0.8888	0.85	0.046	0.9949
	318	30.96	0.042	0.9248	0.66	1.584	0.9693
Turkish Coffee	298	67.14	0.009	0.7375	1.04	0.596	0.9995
	308	29.85	0.039	0.8098	0.67	1.325	0.992
	318	44.05	0.033	0.9207	0.77	1.665	0.9917
Anisah	298	21.09	0.032	0.9560	0.79	0.634	0.9889
	308	18.45	0.032	0.9761	0.82	0.556	0.9775
	318	12.41	0.039	0.958	0.73	2.44	0.9722

Table 3. Comparison of adsorption capacities of MB in various adsorbents

Adsorbent	q_m (m/g)	Reference
Coffee grounds	18.73	[23]
Banana peel	21.0	[9]
Orange peel	20.5	[9]
Wheat shells	16.6	[27]
Coffee husk	20.95	[28]
Ipomoea carnea	83.87	[29]
Corn stigmata	106.3	[30]
<i>Sargassum latifolium</i>	8.54	[31]
Jacobs Coffee	5.74	This study
Tchibo Coffee	30.96	This study
Turkish Coffee	67.14	This study
Anisah Coffee	21.09	This study

3.4. Characterizing Biomass

3.4.1. FTIR Study

The functional groups of different coffee residues were shown in Table 4 and Figure 4. The peak around 3300 cm^{-1} is the stretching band of OH in water [32]. The sharp peak at 1744 cm^{-1} is attributed to the stretching of the carbonyl groups [1]. The OH peak is seen at around 2360 cm^{-1} . The CH-OH bending peak is seen at 1455 cm^{-1} [33].

It can be seen that when coffee species adsorbed MB, the peaks shifts were observed in these peaks. As a result, the hydrogen bonds were responsible for the adsorption of MB.

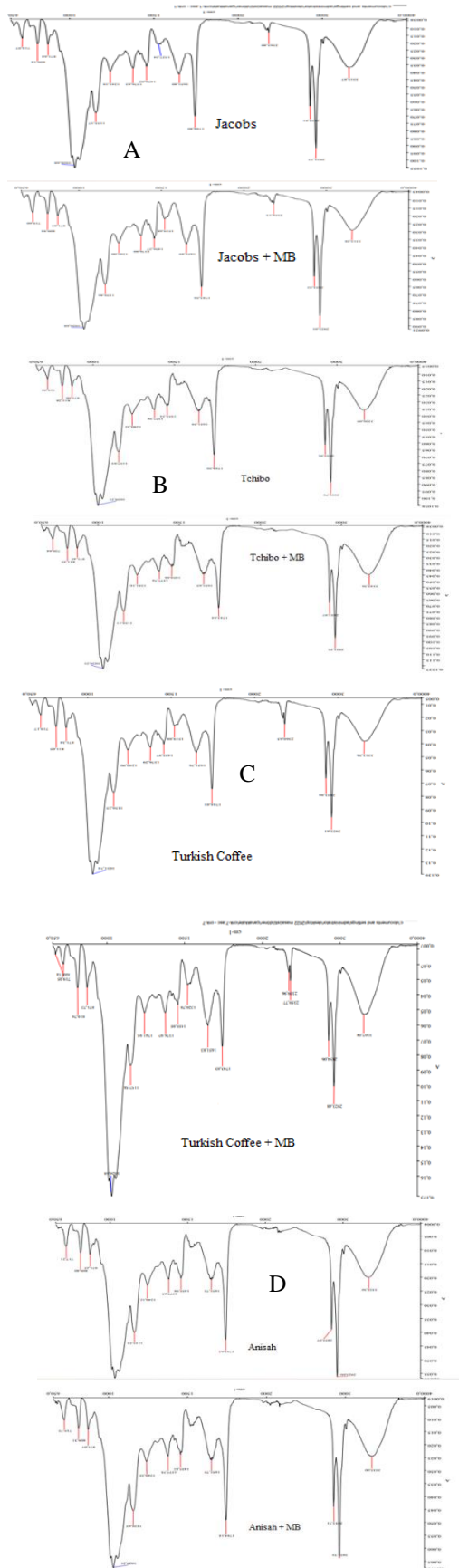


Figure 4. FTIR spectra of (A) Jacobs, (B) Tchibo, (C) Turkish Coffee and (D) Anisah.

Table 4. Functional groups in the FTIR analyses of the waste coffee grounds.

Functional group	Wavenumber (cm ⁻¹)			
	Jacobs	Tchibo	Turkish Coffee	Anisah
-OH groups in water molecule	3315	3366	3313	3332
-CH stretching	2923	2923	2923	2923
-OH	2363	2358	2360	2360
C = O carbonyl groups	1744	1744	1744	1746
Amide C=N and C=C stretches	1651	1651	1651	1651
CH-OH bending	1456	1455	1455	1455
Amide C-N	1376	1377	1367	1377
C-O carboxyl	1241	1240	1240	1240
Symmetric stretching vibration of the C-O-C	1155	1157	1156	1155

3.4.2. SEM study

The SEM and EDX micrographs of the four species of coffee residues before and after the adsorbed MB dye were presented in Fig. 5. In Figure 5, a is Jacobs, b is Jacobs after MB adsorption, c is Turkish coffee, d is Turkish coffee after MB adsorption, e is Anisah, f is Anisah after MB adsorption, g is Tchibo, and h is Tchibo after MB adsorption. For the SEM analysis, it was seen that the surface of each coffee was different. It was understood that the coffee with the most indented surface was Turkish coffee.

Considering the EDX analyses, the elemental analyses of the coffee varieties were also different. Considering the EDX analyses, the elemental analyses of the coffee varieties were also different. It was observed that there was a change in the elemental analysis as a result of MB adsorption. It was thought that the adsorption capacity of Turkish coffee was higher due to its structure and surface being more protruding.

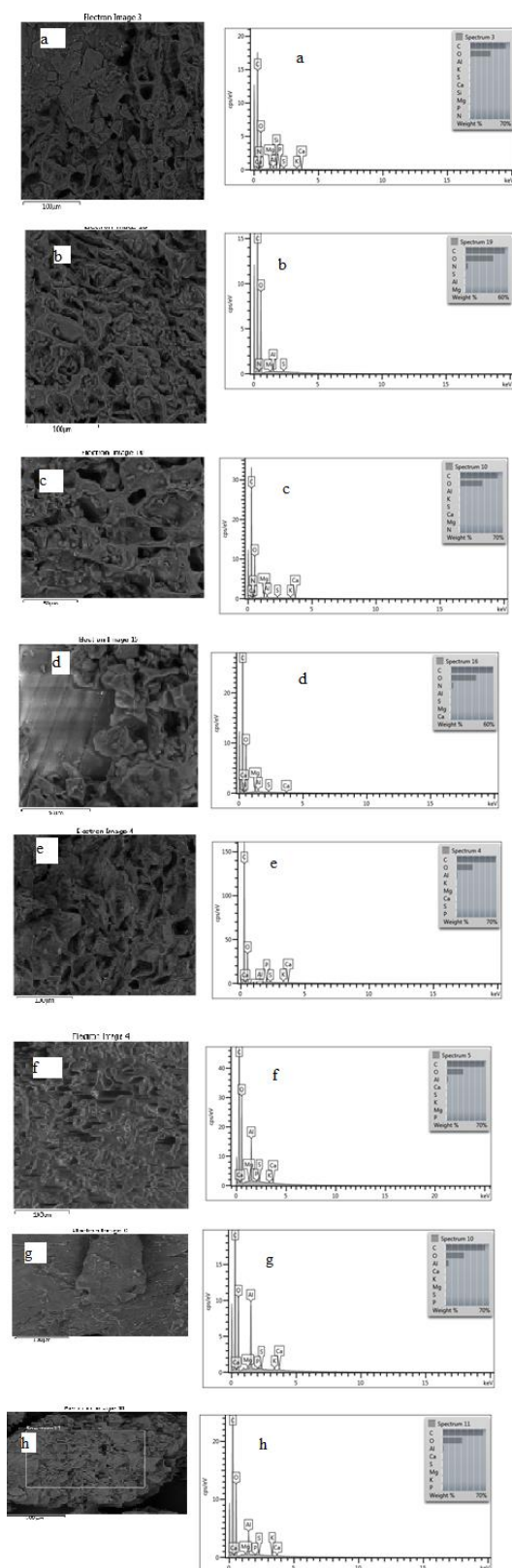


Figure 5. SEM and EDX micrographs of the four species of coffees, before and after adsorbed MB.

4. Conclusion

The residues of four different coffee species were prepared and applied to remove methylene blue (MB) from aqueous solution. The adsorption efficiency, such as, pH, contact time, concentration and temperature, were investigated. For each group of coffee, the removal % of MB was increased with pH and the maximum adsorption capacities were, pH 3 for Jacobs, pH 5 for Tchibo and pH 9 was Turkish and Anisah. Adsorption rate was fast, arrived adsorption balance within about 1000 min. The maximum adsorption capacity was 67.14 mg/g at 298 K for Turkish coffee. The Freundlich model was appropriate to represent the equilibrium data. The coffee surfaces of the adsorbent were confirmed by the FTIR analysis. For the FTIR analysis, the hydrogen bonds were responsible for MB adsorption. Moreover, the SEM revealed that the surface heterogeneity of the coffees was reduced after the adsorption of MB. Briefly, we can say that especially Turkish coffee is a readily available and eco-friendly adsorbent for removing MB.

Acknowledgement

This study was supported by the Çanakkale Onsekiz Mart University research foundation (BAP, project no: FBA-2021-3746). This study was derived from the master thesis of the first author

Author's Contributions

Ecem Tekne, Yeliz Özüdoğru: Drafted and wrote the manuscript, and performed the experiment and result analysis.

Ecem Tekne, Yeliz Özüdoğru: Assisted in analytical analysis on the structure, supervised the experiment's progress and result interpretation, and helped the manuscript preparation.

Ethics

There are no ethical issues regarding the publication of this manuscript.

References

- [1]. Dinçer A, Aydemir T. 2021. Adsorptive Removal of Tartrazine Dye by Poly(N-vinylimidazoleethylene glycol dimethacrylate) And Poly(2-hydroxyethyl methacrylateethylene glycol dimethacrylate) Polymers. *Celal Bayar University Journal of Science*; 17 (4): 397-404.
- [2]. Kausar A, Iqbal M, Javed A, Aftab K, Nazli ZH, Bhatti HN, Nouren S. 2018. Dyes adsorption using clay and modified clay: A review. *Journal of Molecular Liquids*; 256: 395-407.
- [3]. Yagub MT, Sen TK, Afroze S, Ang HM. 2014. Dye and its removal from aqueous solution by adsorption: A review. *Advances in Colloid and Interface Science*; 209: 172-184.
- [4]. Saxena M, Sharma N, Saxena R. 2020. Highly efficient and rapid removal of a toxic dye: Adsorption kinetics, isotherm, and mechanism

- studies on functionalized multiwalled carbon nanotubes. *Surfaces and Interfaces*; 21: 100639:1-10.
- [5]. Ghoreishi SM, Haghghi R. 2003. Chemical catalytic reaction and biological oxidation for treatment of non-biodegradable textile effluent. *Chemical Engineering Journal*; 95(1):163–169.
- [6]. Adeyemo AA, Adeoye IO, Bello OS. 2017. Adsorption of dyes using different types of clay: a review. *Applied Water Science*; 7: 543–568.
- [7]. Dabrowski A. 2001. Adsorption - from theory to practice. *Advances in Colloid and Interface Science*; 93 (1-3) 135-224.
- [8]. Qui H, Lv L, PAN B, Zhang Q, Zhang W, Zhang Q. 2009. Critical review in adsorption kinetic models. *Journal of Zhejiang University-Science A*; 10(5):716-724.
- [9]. Annadurai G, Juang RS, Lee DJ. 2002. Use of cellulose-based wastes for adsorption of dyes from aqueous solutions. *Journal of Hazardous Materials*; B92: 263–274.
- [10]. Hevira L, Ighalo JO, Zein R. 2020. Biosorption of indigo carmine from aqueous solution by *Terminalia catappa* Shell. *Journal of Environmental Chemical Engineering*; 8(5), 104290, 2020.
- [11]. Berber-Villamar NK, Netzahuatl-Muñoz AR, Morales-Barrera L, Chávez-Camarillo GM, Flores-Ortiz CM, Cristiani-Urbina E. 2018. Corn cob as an effective, eco-friendly, and economic biosorbent for removing the azo dye Direct Yellow 27 from aqueous solutions. *Plos One*; 13(4): 1-30.
- [12]. El-Naggar NEA, Rabei NH, El-Malkey SE. 2020. Eco-friendly approach for biosorption of Pb²⁺ and carcinogenic Congo red dye from binary solution onto sustainable *Ulva lactuca* biomass. *Scientific Reports*; 10(1): 1-22.
- [13]. Ozudogru Y, Merdivan M. 2017. Metilen mavisinin modifiye edilmiş *Cystoseira barbata* (stackhouse) C. Agardh kullanılarak biyosorpsiyonu. *Trakya University Journal of Natural Sciences*; 18 (2): 81-87.
- [14]. Meili L, Lins PVS, Costa MT, Almeida RL, Abud AKS, Soletti JL, Dotto GL, Tanabe EH, Sellaoui L, Carvalho SHV, Erto A. 2019. Adsorption of methylene blue on agroindustrial wastes: Experimental investigation and phenomenological modelling. *Progress in Biophysics and Molecular Biology*; 141: 60-71.
- [15]. Ghosh D, Bhattacharyya KG. 2002. Adsorption of methylene blue on kaolinite. *Applied Clay Science*; 20 (6): 295-300.
- [16]. Ahmad MA, Rahman NK. 2011. Equilibrium, kinetics and thermodynamic of Remazol Brilliant Orange 3R dye adsorption on coffee husk-based activated carbon. *Chemical Engineering Journal*; 170(1): 154-161.
- [17]. Cheruiyot GK, Wanyonyi WC, Kiplimo JJ, Maina EN. 2019. Adsorption of toxic crystal violet dye using coffee husks: equilibrium, kinetics and thermodynamics study. *Scientific African*; 5 (e00116): 1-11.
- [18]. Shen K, Gondal MA. 2017. Removal of hazardous Rhodamine dye from water by adsorption onto exhausted coffee ground. *Journal of Saudi Chemical Society*; 21 (1): 120-127.
- [19]. Ayalew AA, Aragaw TA. 2020. Utilization of treated coffee husk as low-cost bio-sorbent for adsorption of methylene blue. *Adsorption Science & Technology*; 38(5–6): 205-222.
- [20]. Vairavel P, Rampal N, Jeppu G. 2021. Adsorption of toxic Congo red dye from aqueous solution using untreated coffee husks: kinetics, equilibrium, thermodynamics and desorption study. *International Journal of Environmental Analytical Chemistry*; 1-19.
- [21]. Manzar MS, Zubair M, Khan NA, Khan AH, Baig U, Aziz MA, Blaisi NI, Abdel-Magid HIM. 2020. Adsorption behaviour of green coffee residues for decolorization of hazardous congo red and eriochrome black T dyes from aqueous solutions. *International Journal of Environmental Analytical Chemistry*; 1-17.
- [22]. Dai, Y., Zhang, K., Meng, X., Li, J., Guan, X., Sun, Q., Sun, Y., Wang, W., Lin, M., Liu, M., Yang, S., Chen, Y., Gao, F., Zhang, X., Liu, Z. 2019. New use for spent coffee ground as an adsorbent for tetracycline removal in water. *Chemosphere*; 215: 163-1172
- [23]. Franca, AS, Oliveira LS, Ferreira ME. 2009. Kinetics and equilibrium studies of methylene blue adsorption by spent coffee grounds. *Desalination*; 249: 262-272.
- [24]. Oliveira, L.S., Franca, A.S., Alves, T.M., Rocha, S.D.F. 2008. Evaluation of untreated coffee husks as potential biosorbents for treatment of dye contaminated waters. *Journal of Hazardous Materials*, 155 (3): 507–512
- [25]. I. Langmuir. 1918. The adsorption of gases on plane surfaces of glass, mica and platinum, *Journal of American Chemical Society*, 40: 1361–1403.
- [26]. H. Freundlich. 1906. Over the adsorption in solution, *Journal of Physical Chemistry*, 57: 385.
- [27]. Bulut Y, Aydın H. 2006. A kinetics and thermodynamics study of methylene blue adsorption on wheat shells. *Desalination*; 194–267.
- [28]. Ronix A, Pezoti O, Souza LS, Souza IPAF, Bedin KC, Souza PSC, Silva TL, Melo SAR, Cazetta AL, Almeida VC. 2017. Hydrothermal carbonization of coffee husk: Optimization of experimental parameters and adsorption of methylene blue dye. *Journal of Environmental Engineering*; 5: 4841-4849.
- [29]. Mathivanan M, Syed Abdul Rahman S, Vedachalam R, Karuppiah S. 2021. Ipomoea carnea: a novel biosorbent for the removal of methylene blue (MB) from aqueous dye solution: kinetic, equilibrium and statistical approach. *International Journal of Phytoremediation*; 1-19.
- [30]. Mbarki F, Kesraoui A, Seffen M, Ayrault P. 2018. Kinetic, thermodynamic, and adsorption behavior of cationic and anionic dyes onto corn stigmata: nonlinear and stochastic analyses. *Water, Air, & Soil Pollution*; 229(3): 1-17.
- [31]. Fawzy MA, Gomaa M. 2021. Low-cost biosorption of Methylene Blue and Congo Red from single and binary systems using Sargassum latifolium biorefinery waste/wastepaper xerogel: an optimization and modeling study. *Journal of Applied Phycology*; 33: 675-691.
- [32]. Saxene M, Sharma N, Saxene R. 2020. Highly efficient and rapid removal of toxic dye: Adsorption kinetics, isotherm, and mechanism studies on functionalized multiwalled carbon nanotubes. *Surface and Interfaces*; 21 (100639):1-10.
- [33]. Kusmono IA. 2019. Water sorption, antimicrobial activity, and thermal and mechanical properties of chitosan/clay/glycerol nanocomposite films. *Heliyon*; 5(e02342): 1-7.

Comparison of Microwave, Ultrasonic Bath and Homogenizer Extraction Methods on the Bioactive Molecules Content of Green Tea (*Camellia Sinensis*) Plant.

Hafize Dilek Tepe^{1*} , Fatma Doyuk² 

^{1,2} Manisa Celal Bayar University, Application Science and Research Center (ASRC), Manisa, Türkiye

*hafize.dilek@hotmail.com

* Orcid No: 0000-0002-6035-6901

Received: 01 September 2022

Accepted: 02 March 2023

DOI: 10.18466/cbayarfbe.1169751

Abstract

In this study, the effects of three different extraction methods on the antioxidant capacity, phenolic component, volatile organic molecule and amino acid contents of green tea (*Camellia sinensis*) leaves were compared. Microwave digestion assisted extraction (MDAE), ultrasonic bath assisted extraction (UBAE) and homogenizer assisted extraction (HAE) methods were used as extraction methods. When the MDAE, UBAE and HAE extraction methods were compared according to the ferric reducing antioxidant power (FRAP) antioxidant activity results, 51.95, 50.9 and 13.8 TE/g dry weight (DW) results were obtained in green tea plant, respectively. DPPH activity in green tea was found to be 94.65, 69.7 and 36.35 TE/g dry weight in microwave extraction, ultrasonic bath and homogenizer extractions, respectively. Analysis in green tea leaves as a result of gas chromatography-mass spectrometry (GC-MS), caffeine, phytol, palmitic acid, beta.-monoglyceride, 13-docosenamide, (z)- and phytol were identified in all three extractions. Fourteen amino acid types were determined in green tea leaves by liquid chromatography-diode array detection (HPLC-DAD). Especially asparagine, glutamine, alanine, serine and L-theanine were determined in very high amounts. When the analysis data were compared, it was determined that the best results were in MDAE>UBAE>HAE, respectively.

Keywords: Extraction, green tea, HPLC-DAD, amino acid, phenolic compounds, LC-MS/MS.

1. Introduction

Extraction is defined as the whole process of separating bioactive components from plant or animal tissues from inert or inactive parts using selective solvents [1]. An ideal extraction method should be simple, inexpensive, fast and environmentally friendly, and should ensure that the desired component is obtained in high yield [2]. As a result of the extraction, the bioactive components should be obtained pure and should not be lost or decomposed. Efficiency in solid-liquid extraction based on the principle of obtaining one or a part of the components of a solid substance using a suitable solvent; it is affected by factors such as solvent type, pH, solid/liquid ratios, particle size, temperature and time [3]. Extraction of bioactive components from plant materials is of particular interest to the cosmetics, herbal medicine and food industries [4]. Modern extraction methods are encountered in classical extraction; efforts to eliminate the negativities such as long extraction time, high cost,

high purity solvent requirement, the necessity of evaporation of large amounts of solvent, low extraction selectivity and thermal degradation of temperature-sensitive components have led to the development of new extraction techniques [3, 5]. The basic properties sought in extraction techniques developed today are use of more reliable chemicals, energy efficiency design, and use of renewable raw materials, prevention of pollution, shortened extraction time, low cost and prevention of accidents [5]. Methods such as, supercritical flow, pressurized liquid extraction, ultrasound, enzyme, microwave, accentuated electric field, homogenizer assisted extraction have been developed as modern extraction methods. These methods are referred to as 'green techniques' as they conform to standards set by the US Environmental Protection Agency [6]. Microwave Assisted Extraction is known as a new method that can be used for the extraction of components dissolved in the liquid from the material using microwave energy [3]. Microwaves are electromagnetic fields in the range of

300 MHz to 300 GHz. Pan et al. (2003) stated that in the microwave assisted extraction process they applied for the extraction of polyphenols and caffeine from green tea leaves, they obtained higher yields than other extraction methods applied in 20 hours at room temperature [7]. The Ultrasound Assisted Extraction method is a technique that uses ultrasonic waves, which are mechanical waves that propagate in an elastic medium, to degrade the plant cell wall and accelerate mass transfer, enabling the desired bioactive components to be obtained in a shorter time and with higher efficiency compared to classical techniques. In addition, it is an environmentally friendly technology with lower energy consumption and less solvent use [8,9]. Homogenizer Assisted Extraction is generally used to homogenize samples at high speed. At high cutting speed, it allows the plant to break in a few seconds and, as a result, to release the components. Since it has a high shear rate, it is faster to pass the bioactive components into the solution compared to other extraction methods. Once the mechanism is evaluated, the ultra-homogenizer can be used for the extraction of total phenolic compounds [6, 10, 11].

Tea is one of the most popular beverages worldwide. According to the production process, tea; It is classified as green and white tea (unfermented), oolong tea (semi-fermented), black tea (fully fermented) and puerh tea (post fermented). It has been observed that tea has very important physiological and pharmacological activities due to characteristic components such as caffeine, polyphenol/flavonoids, amino acids (AA) and carbohydrates [12]. Green tea has various biological activities such as anti-tumor, anti-oxidation and anti-obesity. Therefore, it helps to reduce cancer and cardiovascular diseases [13,14]. According to the information in the literature, green tea is very rich in amino acids, polyphenols and purine alkaloids. The pharmacological effects of theanine and γ -aminobutyric acid (GABA) include nutritional role for essential amino acids. Theanine is an essential amino acid with important functions found in green tea. It is neuroprotective and strengthens cognition by lowering the levels of norepinephrine, serotonin and blood pressure in the brain. [15,16].

In this study, green tea leaves were extracted by three different methods. Three methods were used: microwave digestion, ultrasonic bath and homogenizer assisted. Methanol was used as solvent in all three extraction methods. In the obtained extracts, volatile organic compounds, phenolic and amino acids were determined by chromatographic methods. The antioxidant contents of the extracts were also analyzed. When all analysis data are compared, it was determined which of these three different extraction methods used was more efficient.

2. Materials and Methods

2.1. Chemicals and reagents

Green tea leaves were purchased from an herb market in Manisa city (38.749444°N 28.122778°E), Türkiye in August of 2020. The leaves were washed to remove impurities and then air-dried in the shade before extractions. All standards included chlorogenic acid (>99.0%), D-(+)-catechin (>99.8%), rutin (>99.7%), hyperoside (>99.8%), kaempferol-3-O-rutinoside (>99.7%), astragaloside (>99.8%), rosmarinic acid (>99.7%), polydatin (>99.8%), quercetin (>99.8%), apigenin (>99.8%), kaempferol (>99.8%) were purchased from Sigma-Aldrich Chemical Co., Ltd. (St. Louis, Missouri, USA). ABTS (2,2'-Azino-bis (3-ethylbenzothiazoline-6-sulfonic acid) diammonium salt), 1,1-diphenyl-2-picrylhydrazyl (DPPH), 2,4,6-tris(2-pyridyl)-s-triazine (TPTZ), and Trolox (6-hydroxy-2,5,7,8-tetramethylchroman-2-carboxylic acid) were purchased from Sigma-Aldrich Chemical Co., Ltd. (St. Louis, Missouri, USA). Methanol, ethanol, acetonitrile ($\geq 99.9\%$, (for HPLC) from Merck operates as Millipore Sigma, US. Amino acid standards 10X1 mL, Sigma/AAS18, Fmoc chloride (FMOC-Cl) ($\geq 99.0\%$) from Sigma-Aldrich Chemical Co., Ltd. (St. Louis, Missouri, USA), OPA (o-phthalaldehyde) from Alfa Aesar, Thermo Fisher Scientific Chemicals, Germany.

2.2. Extraction methods of green tea leaves

2.2.1. Microwave digestion-assisted extraction (MDAE)

Dried leaves samples of 0.5 g were weighed, and 20 mL of pure methanol (Sigma-Aldrich) was added. Extraction was performed in a Microwave digestion device (Cem, Mars 6 version, NC, USA.), setting the temperature to 55 °C, 15 min ramp, 25 min hold and 20 min cooling program. The obtained extract solution was filtered, and kept at +4 °C in amber glass vials until the other analysis.

2.2.2. Homogeniser- assisted extraction (HAE)

Dried leaves samples of 0.5 g were weighed, and 20 mL of methanol was added. Extraction was performed by using an Ultra-turrax (IKA T25, Staufen, Germany) at 5000×g for 3 min at room temperature. The extracts were then centrifuged (Hettich- universal 320, Tuttlingen, Germany) at 10.000×g for 10 min at 4 °C. Finally, the resulting solutions were collected in amber glass containers until the other analysis.

2.2.3. Ultrasound bath- assisted extraction (UBAE)

Dried leaves samples of 0.5 g were weighed, and 20 mL of methanol was added. Extraction was performed by using an ultrasonic bath device (Wised, Wisd WiseClean,

Germany), for 30 min at 45 °C. The obtained extract solution was filtered and kept at +4 °C in amber glass vials until the other analysis. For calculate the yield %, the obtained extract was filtered and the methanol was completely evaporated by rotary evaporator (IKA RV8, Germany). The yield % was calculated from the dry extract mass. The percentage yield % of extraction was calculated as:

Percentage yield = weight of dry extract/weight of dry plant material X 100%;

Percentage yield of microwave digestion - assisted extraction (MDAE): 22.96

Percentage yield of homogeniser- assisted extraction (HAE): 17.24

Percentage yield of ultrasound bath- assisted extraction (UBAE):15.48

2.3. Antioxidant activity assays

The FRAP analysis was performed according to the following procedure with some modifications [17]. Stock solutions in the experiment: 300 mM acetate buffer (3.1 g $C_2H_3NaO_2 \cdot 3H_2O$, 16mL $C_2H_4O_2$), pH 3.6, 10 mM TPTZ (2, 4, 6-tripyridyl-s-triazine) in 40 mM HCl and 20 mM $FeCl_3 \cdot 6H_2O$. The fresh FRAP solution was prepared as follows: 25 mL acetate buffer, 2.5 mL TPTZ solution, and 2.5mL $FeCl_3 \cdot 6H_2O$ solution and then warmed at 37 °C before use. Leaf extract (150 μ L) and 2850 μ L of FRAP were mixed in the dark for 30 minutes at room temperature conditions. Then, absorbance was taken at 593 nm using the spectrophotometer (TECAN, Männedorf, Switzerland). The standard curve was linear between 25 and 600 mM Trolox. Results were expressed in mM Trolox equivalents (TE)/g dry mass (DM).

The DPPH analysis was performed according to the following procedure with minor modifications [18]. Stock DPPH solution was prepared by weighing 24 mg of DPPH and dissolving it in 100 mL of methanol. The working solution was obtained by taking 10 mL of the stock solution and diluting it with 45 mL of methanol. Leaves extracts (150 μ L) were allowed to react with 2850 μ L of the DPPH solution for 2 h in a dark condition. Then, absorbance was taken at 515 nm using the spectrophotometer (TECAN, Männedorf, Switzerland). The standard curve was linear between 25 and 800 mM Trolox. Results are expressed in mM Trolox equivalents (TE)/g dry mass. In all measurements, additional dilution was needed if the analysis value measured was over the linear range of the standard curve.

For ABTS assay of leaf extracts was performed according to the following method with some modifications [19]. A stock solution containing 7.4 mM ABTS and 2.6 mM potassium persulfate was prepared. The prepared stock solution was kept at room temperature for 12 h and then 1 mL was taken and diluted

with 60 mL of methanol before the analysis. Leaves extracts (150 μ L) were allowed to react with 2850 μ L of the ABTS solution for 2 h in a dark condition. Then, absorbance was taken at 734 nm using the spectrophotometer (TECAN, Männedorf, Switzerland). The standard curve was linear between 25 and 600 mM Trolox. Results were expressed in mM Trolox equivalents (TE)/g dry mass.

2.4. Determination of phenolic compounds by LC-MS/MS

Phenolic profiles of leaf extracts were determined with Agilent 1260 Triple Quadrupole MS/MS. Separation was performed with a C18 ODS (25x4.6 mmx5 μ m) analytical column. Analyzes were performed in three replications. Aqueous solution (0.1% formic acid) (A) and methanol (B) were used as mobile phase. The gradient method for chromatographic separation is as follows: 3 min 2% B, 6 min 25% B, 10 min 50% B, 14 min 95% B, 17.5 min 2% B. The method injection volume is 2 μ L and flow rate 0.4 ml/min. The identification of compounds was achieved in positive and negative modes [20]. LC-MS/MS total ion chromatogram of phenolic compounds was given in figure 1.

2.5. Determination of volatile organic molecules by GC-MS

Methanol extracts were filtered with a 0.45 μ m filter and analyzed in GC-MS. Volatile components in the extract were analyzed qualitatively by Agilent Technology 7890A GC-MS electron ionization method. Chromatographic separation was achieved with Agilent HP-5 MS, capillary column (30 mx0.25 mm, 0.25 mm film thickness). The oven temperature was started at 40°C and held at 40°C for 5 minutes, then increased to 280°C in increments of 5°C min⁻¹ and held at this temperature for 5 minutes. Method flow rate is 1.5 mL min⁻¹, injector temperature is 250°C. Helium gas (99.999%) was used as carrier gas. Extract injection was performed in splitless mode with 1 μ L. Interpretation of the mass spectrum was done according to the National Institute of Standards and Technology (NIST) and the Wiley Mass Spectral database.

2.6. Determination of amino acid contents by HPLC-DAD

2.6.1. Derivatization of samples and amino acid standards

Before HPLC-DAD analysis, amino acid (AA) standards and samples were derivatized using o-phthaldehyde (OPA) for primary AA and 9-fluorenylmethyl chloroformate (FMOC) for secondary AA according to the method of Henderson et al. (2000), modified to optimize the parameters for green tea plant leaves extraction analysis [21]. The derivatization solution was

freshly prepared every day as follows: Borate Buffer: 0.4 M in water (pH 9.2), FMOc reagent, 0.2 mg/mL in acetonitrile, OPA reagent, 5 mg dissolved in 0.05 mL of methanol was added 0.45 mL of 0.4 M boric acid buffer (pH=9.5). Then 25 µL of β-mercapto ethanol was added. Derivatization of amino acids and samples was achieved by preparing a mixture of boric acid buffer/OPA/amino acid or sample/FMOc (5v/v/v/v). The mixture was vortexed for 2 min.

2.6.2. HPLC-DAD analysis

HPLC-DAD analysis was performed according to Wang et al. (2010) with some minor changes [22]. Agilent 1200 Infinity series HPLC system (Agilent Technologies, CA, USA) was used for the determination of amino acids. The separation was completed on a Zorbax Eclipse Inertsil ODS-3 column (250x4.6 mm, 5 µm, Agilent). The temperature of the column oven was set at 40 °C. The mobile phase consisted of methanol/acetonitrile/water (45/45/10, A) and phosphate buffer (pH 7.5, B). Elution was performed with following gradient as: 0–1.9 min, 100% A; 1.9–18.1 min, 0–58% B; 18.1–18.6 min, 58% B; 18.6–22.3 min, 58–70% B; 22.3–22.4 min, 70–100% B; 22.4–22.6 min, 100% B and 22.6–24 min, 100–0% B. The flow rate was 2.0 ml/min. The DAD was set at 338 nm to monitor the derivatized amino acids. The injection volume was 20 µL. Except for L theanine amino acid, 13 amino acids could be separated simultaneously with HPLC-DAD. Since the retention times of L- theanine and tyrosine are the same, a separate chromatogram was created for L theanine. Standard addition procedure was applied for each amino acid and validation was performed. Chromatograms of amino acids and samples were shown in figure 2.

Statistical analysis

Data were analyzed by two-way analysis of variance (ANOVA) using the GraphPad Prism 8.4.2 program. Means were separated from each other using Bonferroni's multiple comparison test ($p < 0.05$). All analyzes were achieved in triplicate.

3. Results and Discussion

3.1. Antioxidant activity results

Antioxidant activities measured in methanol extract of green tea leaves obtained using FRAP, DPPH and ABTS assays from a single extract were measured three times to test the reproducibility of the assays. Differences were observed according to the three different extraction methods and the results were shown in **Table 1** as TE/g dry mass (DM).

Table 1. Antioxidant activity results of three extraction methods of green tea leaves.

Extraction methods	FRAP mM TE/g DM	DPPH mM TE/g DM	ABTS mM TE/g DM
MDAE	51.95±0.7	94.65±11	47±2.4
UBAE	50.9±1.5	69.7±0.7	44.1±4.5
HAE	13.8±0.2	36.35±0.07	14.9±0.1

$P < 0.05$, DM: dry mass

In green tea leaves ABTS antioxidant activity was obtained as 47.2, 44.1 and 14.9 TE/g dry weight, MDAE, UAE and HAE, respectively. When the three extraction methods were compared according to all analysis results, it was observed that the highest antioxidant activity was in microwave digestion extraction. Afterwards, it was determined that the ultrasonic bath and homogenizer extractions were respectively (Table 1). Some studies have listed the antioxidant properties of different teas as following order: green tea > oolong tea > black tea > puerh tea [23].

3.2. LC-MS/MS phenolic compound content results

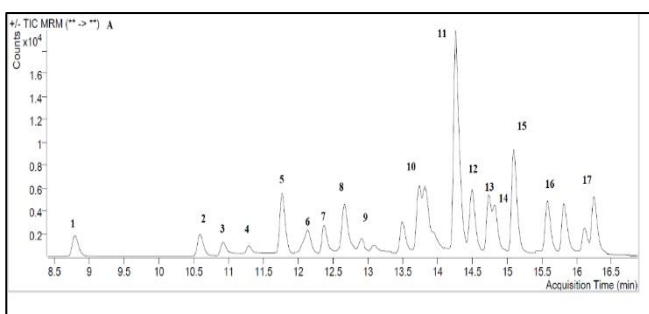


Figure 1. Total ion chromatograms of LC-MS/MS phenolic compounds. (1: Gallic acid, 2: Protocatechin acid, 3: 3,4-Dihydroxyphenylacetic acid, 4: (+)-Catechin, 5: Chlorogenic acid, 6: 4-Hydroxybenzoic acid, 7: (-)-Epicatechin, 8: Caffeic acid, 9: Vanillic acid, 10: p-Coumaric acid, 11: Hesperidin, 12: Rosmarinic acid, 13: Apigenin 7-glucoside, 14: Pinoresinol, 15: Eriodictyol, 16: Quercetin, 17: Kaempferol.

A total of 31 phenolic compounds were determined qualitatively by LC-MS/MS device. Gallic acid, catechin, epicatechin, hesperidin, hyperocyt were detected at a higher rate than other phenolic compounds.

When the total phenolic amounts were compared among the methods, it was seen that the most effective method was microwave decomposition (**Table 2**). Previous studies have found that catechins, chlorogenic acid, kaempferol-3-o-glucoside are the main antioxidants in tea leaves [24]. Catechins are natural antioxidants due to their free radical scavenging effects [25, 26]. The antioxidant activity of catechins differs

from each other according to the plant species. Salman et al. (2022) when green tea was compared with other types of tea, they determined that the total catechin content was at the highest level. Accordingly, DPPH and ABTS antioxidant activities were determined more than other tea types [27].

Table 2. LC-MS/MS phenolic contents of three extraction methods of green tea leaves.

Phenolic content (µg/g Dry weight)	MDAE	UBAE	HAE
Gallic acid	366.21±1.16	250.64±0.16	200.39±1.69
Protocatechuic acid	75.44±0.66	45.92±0.26	31.11±0.02
Pyrocatechol	25.09±17.54	27.34±21.89	5.65±2.51
3,4-Dihydroxyphenylacetic acid	0.49±0.01	0.37±0.02	0.33±0.04
(±) -Catechin	320.30±2.47	229.24±4.33	202.94±7.67
chlorogenic acid	32.09±0.87	27.41±1.49	23.08±7.09
2,5-Dihydroxybenzoic acid	19.69±1.20	13.87±0.29	11.05±0.02
4-Hydroxybenzoic acid	5.99±1.00	5.62±0.50	4.07±0.26
(-) - epicatechin	3182.75±33.47	2265.61±231.6	2044.06±7.77
caffeic acid	0.32±0.05	ND	0.37±0.07
vanillic acid	2.88±2.62	3.17±4.46	7.87±4.57
syringic acid	1.40±0.31	1.26±0.15	1.12±0.32
3-Hydroxybenzoic acid	ND	1.06±0.66	0.49±0.56
Vanillin	1.24±0.10	1.33±0.32	0.81±0.19
verbascoside	4.17±0.38	0.69±0.06	1.31±0.21
Taxifolin	0.41±0.04	ND	0.11±0.01
sinapic acid	ND	ND	ND
p-kummeric acid	10.23±0.03	8.22±0.02	6.05±0.17
ferulic acid	1.94±0.27	1.21±0.08	1.02±0.04
Luteolin 7-glucoside	3.34±0.04	2.38±0.10	3.01±0.07
hesperidin	641.90±28.36	413.43±8.39	361.99±0.94
hyperocyte	357.12±15.52	224.87±4.45	195.99±0.35
Rosmarinic acid	16.75±0.42	13.64±0.36	89.71±1.60
Apigenin 7-glucoside	2.32±0.11	1.44±0.66	1.47±0.08
2-Hydroxycinnamic acid	0.15±0.01	0.18±0.02	0.17±0.04
pinoresinol	2.89±0.58	2.38±2.07	2.12±0.71
Eriodictyol	0.49±0.03	ND	0.11±0.07
Quercetin	34.68±3.73	18.03±0.83	11.72±0.36
Luteolin	ND	0.11±0.07	0.62±0.10
kaempferol	12.93±3.38	7.16±0.30	6.75±1.20
apigenin	ND	ND	ND
Total Phenolic	5123.21±114.36	3566.58±283.54	3215.49±38.73

P<0.05, ND: not defined.

3.3. GC-MS/MS Volatile organic compounds content

Three different extraction samples were introduced into the instrument and the results were compared according to their percentage similarity from the library in the database. The cas numbers, names, formulas and

retention times (RT) of the determined volatile organic molecules with more than 80% similarity are shown in the tables (**Tables 3, 4, 5**). According to the GC-MS results obtained, similarities were obtained in the organic volatile molecules within the plants in three different extractions. The same molecules were identified as a

result of all three extractions. The most notable among these molecules is the squalene molecule. It has been reported that sharks are a rich source of squalene and that more than 40% of shark liver contains squalene, and therefore the absence of cancer in sharks is related to these high squalene levels [28, 29]. Squalene is a powerful antioxidant thanks to its wide electron exchange capability without undergoing molecular

degradation. Experimental studies have shown that the use of squalene in the diet improves the performance of the immune system and increases macrophage function. Studies have shown that squalene keeps immune cell bio-membranes against oxidative stress during phagocytosis. [30].

Table 3. GC-MS volatile organic molecules of microwave-digestion extraction of green tea leaves.

CAS No	Name	Formula	Score	RT
64-19-7	Acetic acid	C ₂ H ₄ O ₂	97.54	3.719
87-66-1	1.2.3-Benzenetriol	C ₆ H ₆ O ₃	92.39	21.62
58-08-2	Caffeine	C ₈ H ₁₀ N ₄ O ₂	96.1	32.80
23470-00-0	Hexadecanoic acid. 2-hydroxy-1-(hydroxymethyl)ethyl ester	C ₁₉ H ₃₈ O ₄	89.83	44.11
123-94-4	Octadecanoic acid. 2.3-dihydroxypropyl ester	C ₂₁ H ₄₂ O ₄	92.56	47.19
112-84-5	13-Docosenamide. (Z)-	C ₂₂ H ₄₃ NO	82.53	48.09
7683-64-9	Squalene	C ₃₀ H ₅₀	86.36	48.78

+: Determined compound, Score: Similarity%, RT: Retention time

Table 4. GC-MS volatile organic molecules of ultrasound-bath extractions of green tea leaves

CAS No	Name	Formula	Score	RT
64-19-7	Acetic acid	C ₂ H ₄ O ₂	97.53	3.70
87-66-1	1.2.3-Benzenetriol	C ₆ H ₆ O ₃	92.87	21.59
58-08-2	Caffeine	C ₈ H ₁₀ N ₄ O ₂	89.7	32.73
150-86-7	Phytol	C ₂₀ H ₄₀ O	93.57	37.53
23470-00-0	Palmitin. 2-mono-; Palmitic acid .beta.-monoglyceride	C ₁₉ H ₃₈ O ₄	90.59	44.10
123-94-4	Octadecanoic acid. 2.3-dihydroxypropyl ester	C ₂₁ H ₄₂ O ₄	92.93	47.21
112-84-5	13-Docosenamide. (Z)-	C ₂₂ H ₄₃ NO	82.61	48.11
7683-64-9	Squalene	C ₃₀ H ₅₀	85.75	48.78

+: Determined compound, Score: Similarity%, RT: Retention time

Table 5. GC-MS volatile organic molecules of homogeniser extractions of green tea leaves

CAS No	Name	Formula	Score	RT
64-19-7	Acetic acid	C ₂ H ₄ O ₂	97.51	3.705
87-66-1	1.2.3-Benzenetriol	C ₆ H ₆ O ₃	93.53	21.58
58-08-2	Caffeine	C ₈ H ₁₀ N ₄ O ₂	96.19	32.69
150-86-7	Phytol	C ₂₀ H ₄₀ O	93.23	37.53
23470-00-0	Hexadecanoic acid. 2-hydroxy-1-(hydroxymethyl)ethyl ester;	C ₁₉ H ₃₈ O ₄	90.66	44.11
123-94-4	Octadecanoic acid. 2.3-dihydroxypropyl ester	C ₂₁ H ₄₂ O ₄	93.21	47.20
112-84-5	13-Docosenamide. (Z)-	C ₂₂ H ₄₃ NO	82.77	48.11
7683-64-9	Squalene	C ₃₀ H ₅₀	86.66	48.78

: Determined compound, Score: Similarity%, RT: Retention time.

3.4. HPLC-DAD amino acid content results

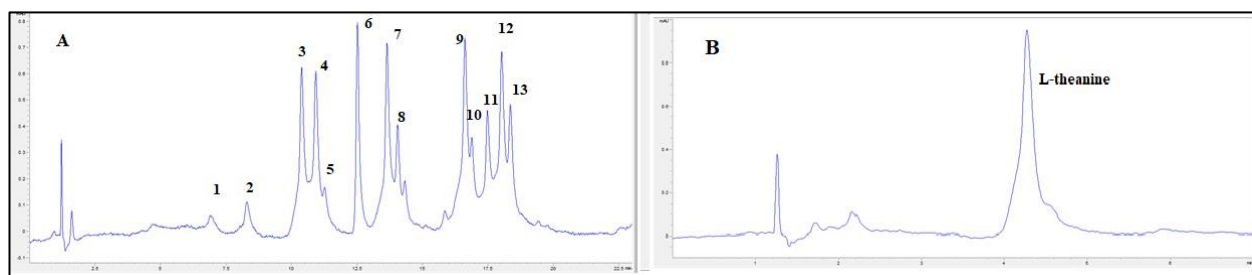


Figure 2. A: HPLC-DAD chromatogram of amino acid standards, B: HPLC-DAD chromatogram of L-theanine standard.

(1: Aspartic acid, 2: glutamic acid, 3: asparagine, 4: serine, 5: glutamine, 6: arginine, 7: alanine, 8: tyrosine, 9: valine, 10: tryptophan, 11: phenylalanine, 12: isoleucine, 13: leucine)

Table 6. Amino acid contents of three extraction methods of green tea leaves.

Amino Acid Content (µg/g kuru ağırlık)	MDAE	UBAE	HAE
Aspartic Acid	12.60±0.22	4.20±0.02	7.00±0.13
Glutamic acid	12.20±0.04	1.00±0.04	0.80±0.03
Asparagine	113.80±0.07	66.40±0.54	46.00±0.44
Serine	33.80±0.32	7.20±0.01	13.60±0.16
Glutamine	69.80±0.42	49.80±0.50	45.00±0.35
Arginine	10.00±0.14	24.80±0.07	16.20±0.32
Alanine	50.80±0.14	56.00±0.41	33.60±0.06
tyrosine	10.00±0.11	23.60±0.28	13.60±0.17
Valine	0.80±0.03	ND	ND
tryptophan	ND	ND	ND
Phenyl alanine	ND	ND	ND
isolaucine	ND	ND	ND
leucine	4.80±0.01	4.40±0.00	4.40±0.00
L-Theanine	57.80±0.16	49.80±0.01	52.40±0.08

P<0.05, ND: not defined

Amino acid analysis was performed with high performance liquid chromatography (HPLC) and diode array detector (DAD) detector. In MDAE, UBAE and HOME extractions, the amount of glutamine in green tea leaves was determined as 69.80, 49.80 and 45.00 µg/g dry weight, respectively. Asparagine, glutamine, alanine and L-theanine were determined at high levels in the green tea plant (**Table 6**). Theanine is one of the essential amino acids found in green tea due to its positive effects on the brain. Some of these effects include increasing neuroprotective and cognitive power by lowering levels of norepinephrine, serotonin and blood pressure. [16,17]. When three different extraction methods were compared from the results obtained, it was observed that the most effective extraction method was microwave decomposition extraction. Pan et al. (2003) stated that they obtained higher yields from the microwave assisted extraction process for the extraction of polyphenols and caffeine from green tea leaves compared to other extraction methods.

4. Conclusion

Extraction is the pre-treatment that must be done before bioactive component analysis. With an efficient extraction process, product loss, amount of solvent and wasted time must be minimized. Phytochemical analyzes were carried out on the extracts obtained with various chromatographic modern devices. There is no similar study in the literature yet. The detailed determination of antioxidant capacities and phytochemical contents of green tea leaves after extractions allowed comparison of extraction efficiency. The importance of natural products rich in bioactive components is increasing day by day. Therefore, this study may guide similar studies in the future.



Acknowledgements

The authors grateful Manisa Celal Bayar University Scientific Research Project Coordination Unit for their financial support (project numbered 2020-089) and Applied Science and Research Centre for allowing the study to be conducted.

Author's Contributions

Hafize Dilek Tepe: Drafted and wrote the manuscript, performed the experiment and result analysis.

Fatma Doyuk: Assisted in analytical analysis on the structure, supervised the experiment's progress, result interpretation and helped in manuscript preparation.

Ethics

There are no ethical issues after the publication of this manuscript.

References

- [1]. Handa, S.S, Khanuja, S.P.S, Longo, G, Rakesh, D.D. Extraction technologies for medicinal and aromatic plants; Trieste (Italy): *Earth Environmental and Marine Sciences and Technologies*, 2008.
- [2]. Chemat, F, Zill-E-Huma, Khan, MK. 2011. Applications of ultrasound in food technology: Processing, preservation and extraction. *Ultrasonics Sonochemistry*. 18 (4) : 813-835. <https://doi.org/10.1016/j.ultsonch.2010.11.023>.
- [3]. Azmir, J, Zaidul, ISM, Rahman, MM, et al. 2013. Techniques for extraction of bioactive compounds from plant materials: A review. *Journal of Food Engineering*. 117 (4) :426–436. <https://doi.org/10.1016/j.jfoodeng.2013.01.014>.
- [4]. Vinatoru, M, Mason, T.J, Calinescu, I. 2017. Ultrasonically assisted extraction (UAE) and microwave assisted extraction (MAE) of functional compounds from plant materials. *TrAC - Trends in Analytical Chemistry*. 97: 159–178. <https://doi.org/10.1016/j.trac.2017.09.002>.
- [5]. Wen, C, Zhang, J, Zhang, H, et al. 2018. Advances in ultrasound assisted extraction of bioactive compounds from cash crops – A review. *Ultrasonics Sonochemistry*. 48 : 538–549. <https://doi.org/10.1016/j.ultsonch.2018.07.018>.
- [6]. Dai, J, Mumper, R.J. Plant Phenolics: Extraction, Analysis and Their Antioxidant and Anticancer Properties. 2010. *Molecules*. 15(10): 7313–7352. <https://doi.org/10.3390/molecules15107313>.
- [7]. Pan, X, Niu, G, Liu, H. Microwave-assisted extraction of tea polyphenols and tea caffeine from green tea leaves. 2003. *Chemical Engineering and Processing: Process Intensification*. 42 (2) :129–133. [https://doi.org/10.1016/S0255-2701\(02\)00037-5](https://doi.org/10.1016/S0255-2701(02)00037-5).
- [8]. Vilku, K, Mawson, R, Simons, L, Bates, D. Applications and opportunities for ultrasound assisted extraction in the food industry - A review. 2008. *Innovative Food Science and Emerging Technologies*. 9 (2) :161–169. <https://doi.org/10.1016/j.ifset.2007.04.014>.
- [9]. Jadhav, D, B. Rekha, B.N, R, Gogate, P.R, et al. Extraction of vanillin from vanilla pods: A comparison study of conventional soxhlet and ultrasound assisted extraction.2009. *Journal of Food Engineering*. 93 (4) :421–426. doi:10.1016/j.jfoodeng.2009.02.007
- [10]. Low-Pressure Solvent Extraction (Solid–Liquid Extraction, Microwave As [Internet]. [cited 2022 Jun 22]. Available from: <https://www.taylorfrancis.com/chapters/mono/10.1201/9781420062397-11>.
- [11]. Bilgin, M, Sahin, S, Dramur, M,U, et al. Obtaining scarlet sage (*salvia coccinea*) extract through homogenizer- and ultrasound-assisted extraction methods. 2013. *Chemical Engineering Communications*. 200: 1197–1209. doi:10.1080/00986445.2012.742434.
- [12]. Thippeswamy, R, Mallikarjun Gouda, K,G, Rao, D,H, Martin, A, Gowda, L, R. Determination of theanine in commercial tea by liquid chromatography with fluorescence and diode array ultraviolet detection. 2006. 54 (19) : 7014-7019. <https://doi.org/10.1021/jf061715+>.
- [13]. Gupta, S, Hastak, K, Ahmad, N, et al. Inhibition of prostate carcinogenesis in TRAMP mice by oral infusion of green tea polyphenols.2001. *Proceedings of the National Academy of Sciences of the United States of America*. 98 (18) :10350–10355. doi: 10.1073/pnas.171326098.
- [14]. He, R,R, Chen, L, Lin, B,H, et al. Beneficial effects of oolong tea consumption on diet-induced overweight and obese subjects. 2009. *Chinese Journal of Integrative Medicine*. 15: 34–41. doi: 10.1007/s11655-009-0034-8.
- [15]. Yokogoshi, H, Kato, Y, Sagesaka, Y,M, et al. Reduction effect of theanine on blood pressure and brain 5-hydroxyindoles in spontaneously hypertensive rats. 1995. *Bioscience, biotechnology, and biochemistry*. 59 (4) :615–618. doi: 10.1271/bbb.59.615.
- [16]. Nathan, P,J, Lu K, Gray, M, et al. The Neuropharmacology of L-Theanine (N -Ethyl-L-Glutamine) . 2006. *Journal of Herbal Pharmacotherapy*. 6:21–30.
- [17]. Benzie, I,F, Strain, J,J. The Ferric Reducing Ability of Plasma (FRAP) as a Measure of“Antioxidant Power”: The FRAP Assay. 1996. *Analytical Biochemistry*. 239 (1) :70–76. doi: 10.1006/abio.1996.0292.
- [18]. Brand-Williams, W, Cuvelier, M,E, Berset, C. Use of a free radical method to evaluate antioxidant activity. 1995. *LWT - Food Science and Technology*. 28 (1) :25–30. [https://doi.org/10.1016/S0023-6438\(95\)80008-5](https://doi.org/10.1016/S0023-6438(95)80008-5).
- [19]. Arnao, M,B, Cano, A, Acosta, M. The hydrophilic and lipophilic contribution to total antioxidant activity. 2001. *Food Chemistry*. 73 (2) :239–244. [https://doi.org/10.1016/S0308-8146\(00\)00324-1](https://doi.org/10.1016/S0308-8146(00)00324-1).
- [20]. Gören, A,C, Çikrikçi, S, Çergel, M, et al. Rapid quantitation of curcumin in turmeric via NMR and LC-tandem mass spectrometry.2009. *Food Chemistry*. 113 (4) : 1239–1242. doi:10.1016/j.foodchem.2008.08.014
- [21]. Henderson, J,W, Ricker, R,D, Bidlingmeyer, B, et al. Rapid , Accurate , Sensitive , and Reproducible HPLC Analysis of Amino Acids. Amino Acids. Amino Acid Analysis Using Zorbax Eclipse-AAA Columns and the Agilent 1100 HPLC. 2000. 1–10.
- [22]. Wang, L, Xu, R, Hu, B, et al. Analysis of free amino acids in Chinese teas and flower of tea plant by high performance liquid chromatography combined with solid-phase extraction. 2010. *Food Chemistry*. 123 (4) :1259–1266. doi:10.1016/j.foodchem.2010.05.063
- [23]. Karori, S,M, Wachira, F,N, Wanyoko, J,K, et al. Antioxidant capacity of different types of tea products. 2007. *African Journal of Biotechnology*. 6 (19) : 2287–2296. doi:10.5897/AJB2007.000-2358.
- [24]. Wu, H, Shang, H, Guo, Y, et al. Comparison of different extraction methods of polysaccharides from cup plant (*Silphium perfoliatum* L.).2020. *Process Biochemistry*. 90 : 241–248. <https://doi.org/10.1016/j.procbio.2019.11.003>.
- [25]. Ng, K,W, Cao, Z,J, Chen, H,B, et al. Oolong tea: A critical review



of processing methods, chemical composition, health effects, and risk. 2018. *Critical Reviews in Food Science and Nutrition*. 58 (17) : 2957–2980. <https://doi.org/10.1080/10408398.2017.1347556>.

[26]. Bancirova, M. Comparison of the antioxidant capacity and the antimicrobial activity of black and green tea. 2010. *Food Research International*. 43 (5):1379–1382. <https://doi.org/10.1016/j.foodres.2010.04.020>.

[27]. Salman, S, Öz, G, Felek, R, et al. Effects of fermentation time on phenolic composition, antioxidant and antimicrobial activities of green, oolong, and black teas. 2022. *Food Bioscience*. 49:101884. <https://doi.org/10.1016/j.fbio.2022.101884>.

[28]. Nakagawa M, Yamaguchi T, Fukawa H, et al. Potentiation by squalene of the cytotoxicity of anticancer agents against cultured mammalian cells and murine tumor. 1985. *Japanese Journal of Cancer Research*. 76 (4):315-20. https://doi.org/10.20772/cancersci1985.76.4_315.

[29]. Liu, G,C, Ahrens E,H, Schreiberman, P,H, et al. Measurement of squalene in human tissues and plasma: validation and application. 1976. *Journal of Lipid Research*. 17 (1) : 38–45. [https://doi.org/10.1016/S0022-2275\(20\)37014-0](https://doi.org/10.1016/S0022-2275(20)37014-0).

[30]. Owen, R,W, Mier, W, Giacosa, A, et al. Phenolic compounds and squalene in olive oils: the concentration and antioxidant potential of total phenols, simple phenols, secoiridoids, lignans and squalene. 2000. *Food and Chemical Toxicology*. 38 (8) : 647–659. [doi:10.1016/S0278-6915\(00\)00061-2](https://doi.org/10.1016/S0278-6915(00)00061-2).

An Approach For Determination of Risky Buildings And Building Energy Performance Concerning Urban Renewal In Türkiye

Ebru Alakavuk^{1*} , Hande Odaman Kaya² 

¹ Yasar Üniversitesi Architecture Faculty, Department of Architecture, İzmir, Türkiye

² Kayapın Mimarlık, Mansuroğlu Mah. 286/7 sok. No:10/11 Bayraklı, İzmir, Türkiye

*ebru.alakavuk@yasar.edu.tr

* Orcid No: [0000-0001-7482-8116](https://orcid.org/0000-0001-7482-8116)

Received: 25 April 2022

Accepted: 09 December 2022

DOI: 10.18466/cbayarfbe.1108873

Abstract

In May 2012 “Urban Renewal Law” for reducing the expected seismic risk for existing buildings was published. Depending on this law, existing old buildings should have stability tests for the decision; if it should be demolished or strengthened. This article is mainly concentrating on the earthquake stability and energy performance of a case building regarding the physical and environmental dimensions of urban renewal. Case building is a deficient structure that couldn't catch the static regulations and so demolished. Regarding the urban renewal process a new building was constructed following the energy performance regulations. In this framework structural and energy performance analysis of the existing deficient building are done to present the conditions first. Then the energy performance of the new building is analyzed to be compared with the demolished building. For the static analysis of the existing building ideCAD, for the energy performance analysis BEP-TR 2 programs are used. As a result of this study, the structural performance of the case building is examined to display the need of a new construction and then the development of the energy performance is presented by the comparison between demolished and new buildings.

Keywords: Urban Renewal, Building Energy Performance, Building Structural Analysis

1. Introduction

Urban renewal, apart from being a periodic definition, it is proposed to be a process of changes affecting the physical structure and fabric of urban areas [1]. In other words, it is a particularly physical change, as the inevitable “outcome” of the action of economic and social forces upon urban areas, especially as a powerful force for urban change and predominantly a market-led process [1]. According to conceptual terminology, urban renewal is a continuous process of remodeling older parts of urban areas, including their central business district (CBD) areas by means of rehabilitation, conservation, and redevelopment [2]. With urban renewal, particular sections of the city change their nature and its structure being evolved [3]. In Eurocities (1996) it is noted that urban renewal is about the sustainable development of cities which is holistic in approach, and targeted at economic and cultural redevelopment, social cohesion and physical rehabilitation of cities [4].

Five basic laws that comprise the legal framework regarding urban transformation in Turkey can be cited.

- “Mass Housing Law” no 2985
- “Municipality Law” no 5393
- “North Ankara Entrance Urban Transformation Project Law” no 5104 (Special Law)
- “Law no 5366 on the Renewal and Preservation and Usage by Sustenance of Worn-out Urban Fabric”
- “Law no 6306 on the Transformation of Areas under Disaster Risk”

Turkey's urban regeneration projects emerged with the approval of law 5366, called “Renovation, Protection, Cherishing, and Use of Worn Historical and Cultural Immovable Properties”. This law gives extensive authorization to municipalities for implementing projects, including the declaration of areas as regeneration areas, expropriation, eviction, and demolition of properties in case of disagreement between municipality and house owners (Turkish Grand National Assembly, 2005). (1)

Turkey is located on a seismically active zone stroked by Alpine-Himalayan Belt, which generates 17% of all earthquakes in the world. Turkey faced Marmara earthquake in 1999 that caused the demolition of many buildings and death of more than 10000 people. After this big disaster lot of changes in the construction sector are done by the government for reducing the vulnerability of possible future earthquakes.

In our country, the issue of urban transformation has become one of the most discussed and disputed topics with the problems of urbanization and settlement that became more visible specifically following the catastrophes in 1999 Marmara and Düzce earthquakes, (5). The "Disaster Law", which is the latest legislation in the context of urban renewal policies, is also shown as a solution to the disaster risk reduction by creating better physical environment and better housing, (6).

It is known that a single structure-based transformation approach is acted upon by the fact that it forms the body of Law No. 6306, and a method is built on the relation of strength. Urban transformation in Turkey; the structures in existing built environments are destroyed and new structures are made in accordance with the 2007 Earthquake Regulation due to the fact that natural disasters play a dominant role [9].

Law No. 6306 refers to the buildings at a risk of damage or serious damage. According to the Law 6306; the structures that either have completed their economic life or under risk of collapse and heavy damage within or outside risky area, determined on the basis of scientific and technological evidence is called as a risky building. The risky buildings cannot resist physical or geological disasters. So, for reducing the risk of risky buildings from being collapsed these buildings must be replaced with new ones according to the Law 6306.

Urban renewal has physical, social, economic, and environmental dimensions. Physical dimensions of the urban renewal are about the physical conditions of the building such as infrastructure, resistant to the forces like earthquake and also urban fabric. Social dimension of the urban renewal is about demography concerning the profile, education level, income, health of the people and is for improving community in that region. Economical dimension of the urban renewal is about the effects of urban renewal on the people's profit and loss in case of urban renewal and also new generation of employment. Environmental dimension of the urban renewal is about the ecological effects of the buildings. Physical and environmental dimensions of urban renewal are taken into account in this paper.

2. Materials and Methods

In order to reduce probable losses under the risk of physical and geological disasters, the risky buildings

must be determined so that they can be replaced with new ones or can be retrofitted according to the regulations. So that the buildings can stand still against natural hazards.

This research is based on determination of risky buildings through directive of Law 6306 and designing a new building instead of the risky one. After that energy performance analysis of both risky building and newly built one is done by using the national energy performance certification tool of Turkey; BEP-TR. Therefore, benefits of constructing new building in respect to energy performance is put forward. The steps for the approach of this research are defined as follows;

- Risky building detection,
- Energy performance analysis,
- Design of the new building,
- Comparison of existing and new buildings.

2.1. Risky Building Detection

For risky building detection analysis general information about the building must be collected. These are; the construction date, address, layout, geographic coordinates, earthquake zone, dimensions of the building, structure information and also load bearing element of the building.

If the static and architectural project of the building cannot be found, then existing building's dimensions of the columns and beams, opening dimensions, width and length of the wall, dimensions of the building and height of the floor can be measured on the existing building on site and the architectural project can be drawn.

After that core sampling and reinforcement evaluation is done for the critical floor for determining the concrete elements quality. According to the regulations, core sampling must be applied to more than 20% of all columns and strength tests should be done on these core samples. By using stripping and monitoring methods stirrup frequency and reinforcement are defined. The next step is preparing soil survey report of the building site which is showing the load carrying capacity analysis of the soil. Based on the RBTYE regulations accepted 2 July 2013, for the performance analysis of the current situation ideCAD building performance analysis program can be used than.

2.2. Building Energy Performance Analysis

'Code for Energy Efficiency' was published on 2nd of May 2007 by Turkish Government. Ministry of Environment and Urbanisation first published 'Building Energy Performance Regulations' on 5th of December 2008; based on 'Energy Performance of Buildings Directive (EPBD) 2002/91/EC' of the European Union and 'Code for Energy Efficiency' of Turkey. National energy performance calculation tool: Bep-TR was

presented as a certification system grounded on EN ISO 13790 and national specifications. (ISO, 2008) To present the energy certificate level; whole building's total energy consumptions are calculated according to the primary energy usage and CO₂ emissions caused by climate conditions, indoor environment needs, regional priorities, and boundary conditions. The online software had been in use from July 2010 till November 2017 by registered professionals under a governmental network. Ministry of Environment and Urbanisation published repeating "Declaration on Building Energy Performance Calculation Methodology" on 1st of November 2017 to present the new calculation tool.

For energy performance analysis of the buildings firstly the building is identified in the offline operation platform of BEP-TR 2 by entering general location and construction information. Than in the two-dimensional drawing interface building energy model is generated as a plan geometry. After that all the details for floors and thermal zones are defined as; construction materials, mechanical systems and lighting systems. When the energy model is completed software runs the offline simulation to calculate the energy consumptions of the building. In this process the system generates a reference building to compare and give an energy consumption class to the evaluated building. Energy classes are determined according to the energy performance (E_p) range as; A: 0-39; B: 40-79; C: 80-99; D: 100-119; E: 120-139; F: 140-174; G: 175-... Generated reference building is accepted as it is over the energy class D. So if the evaluated building has the same results with the reference building, then the E_p value is 100. At the end of all this process, the software requires username and password for the server connection to create an 'Energy Identity Certificate' (Figure 1). Regarding to the regulations; all the new buildings constructed after 01.01.2011; should have an energy identity certificate with minimum energy class C.



Figure 1. Energy identity certificate (Republic of Turkey Ministry of Environment and Urbanization, 2017)

If the building's energy class is lower than C that means more precautions concerning energy savings must be taken into account. And also, it shows that the building's energy expenses are too much. For

decreasing the energy expenses heating methods with lower greenhouse emission, such as thermal insulation can be done according the climate, lighting systems can be energy efficient and façade elements such as windows must have high insulation.

3. Examination of the existing building

The existing building (Figure 2) was constructed in 1970 in Karaçam, Bornova, İzmir (latitude: 38.5156766° N, longitude: 27.2702750° E). It is a single floor reinforced concrete building as one independent living space. It has totally 58.26 m² closed area (6.00 m*9.71 m) with a 2.72 m floor height.



Figure 2. Existing building

Since the building has no application projects; each element of the building such as; column and beam section dimensions, door- window openings, wall thickness, floor plan dimensions and building height are measured for the architectural relieve drawings. (Figure 3)

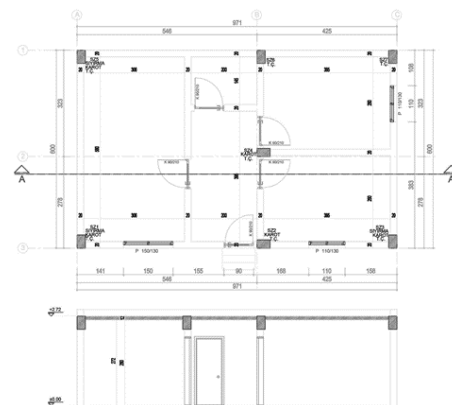


Figure 3. Plan and section relieve drawings, existing building

3.1. Risky Building Detection

The required information about the existing building is collected through site visits. According to the analysis; building's structural system is reinforced concrete. The load bearing system consists of 7 (*) columns with a 12 cm reinforced concrete flat slab which is the roof of the building. Exterior walls are composed of 0.19 m brick elements. (Table 1).

Table 1. Construction elements, existing building

Construction Element	Material	Thickness (m)
Slab (Basement)	Reinforced Concrete (L:2.500-05.01.01)	0.12
	Gypsum Plaster (L:0.510-04.04)	0.02
	Concrete (L:1.650-05.01.02)	0.03
	Lime, Lime- Gypsum Mortar (L:1.000-04.01)	0.02
	Phanerocrystalline Volcanic and Metamorphic Stone (L:1.650-05.01.02)	0.02
Column-Beam	Gypsum Plaster (L:0.510-04.04)	0.03
	Reinforced Concrete (L:2.500-05.01.01)	0.25
	Gypsum Plaster (L:0.510-04.04)	0.02
Exterior Wall	Gypsum Plaster (L:0.510-04.04)	0.03
	Brick_TS EN 771-1 (L:0.810-07.01.01.01)	0.19
	Gypsum Plaster (L:0.510-04.04)	0.02
Flat Roof	Reinforced Concrete (L:2.500-05.01.01)	0.12
	Gypsum Plaster (L:0.510-04.04)	0.02
	Concrete (L:1.650-05.01.02)	0.05
	Bitumen Waterproofing Sheet (L:0.190-09.02.02.01.01)	0.05

Following the RBYTE regulations (02.07.2013); core sampling and reinforcement evaluation for defining stirrup frequency and reinforcement is done for the critical floor (basement) (figure 4). 5 different columns' sections and reinforcements were evaluated.

More than 20% of all the columns were reinforced but not with the ribbed iron (S220) and also [used stirrups](#) were not tightened as it should be done (Table 2). Existing concrete endurance was also lower than the accepted standards.

Table 2. Defining coloumn's and beam's reinforcement with stripping method

NO	Coloumn	Longitudunal Reinforcement (S220)	Stirrup Reinforcement (S220)	Densifi-cation
1	SZ01	4Ø14	Ø8/21-25	-
2	SZ03	4Ø14	Ø6/24-28	-
3	SZ05	4Ø14	Ø8/24-45	-



Figure 4. Column stripping and core concrete, existing building

Core concrete samples from 5 columns located at the ground floor are taken and strength tests are done. The results of unconfined compressive strength are given at Table 3. According to RBYTE regulation accepted on 2nd July 2013, the average strength of core concrete samples should be *85*85.

Table 3. Compressive strength

Ground Floor					
Columns	SZ01	SZ02	SZ03	SZ04	SZ05
Compressive Strenght	16,90	11,13	12,16	9,14	12,83
Average	12,43	12,43	12,43	12,43	12,43
*0.85*0.85	8,98	8,98	8,98	8,98	8,98
Selected concrete strength (Mpa)	10	10	10	10	10

Location of the case building is within the earthquake region 1, so the structural importance coefficient of the building is accepted as Z1 and the parameters used for the calculations are given in Table 4.

For the structural analysis of the building all the collected data is used as input data for IdeCAD simulation (Figure 5). IdeCAD database is based on "Mod Merge Calculation Method" which is compatible with RBYTE regulations. Using the output data of IdeCAD simulation process, structural elements can be examined by their collapse failure value.

Table 4. Parameters for the calculation

Building importance coefficient	1	Earthquake region	1 st degree
Movable Loads	0,5/0,35/0,2 t/m ²	Knowledge level (Min)	0,90
Structural System	Frame	Local Floor Class	Z1
Construction System	Reinforced concrete	Floor group	A
R behaviour coefficient	8	Ground bearing strength	
Spectrum characteristic periods	Ta=0.10 s Tb=0.30 s	Coefficient of soil reaction	
Bearing columns compressive strength		Ao	0,4

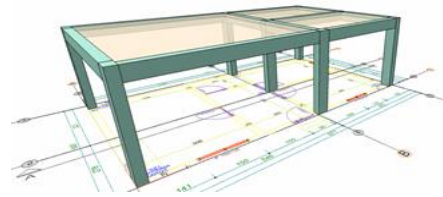


Figure 5. Structural analysis model, existing building

3.2. Energy performance analysis of the existing building

For energy performance analysis of the buildings firstly the building is identified in the offline operation platform of BEP-TR 2 by entering general location and construction information. Than in the two-dimensional drawing interface building energy model is generated first as a plan geometry. After that all the details for floors and thermal zones are defined as; construction materials, mechanical systems and lighting systems. At the end of the process building energy performance is calculated and 'Energy Identity Certificate' (Figure 1) is obtained through the server of the ministry.

Through the results of the structural performance analysis, existing building seems not to be able to provide the safety requirements of earthquake regulations. So that it may collapse under the risk of any moderate earthquake and it may cause loss of lives. This situation may affect our country's and also surrounding societies' sociology, economy and psychology in negative way and so may cause damages. Consequently, the existing building is defined as "risky". floor is entered with the height of 2.72, the only thermal zone is defined as a climatized residential zone with a 27m² kitchen and living room space. Than 5 glow lamps with 40 W are entered as the lighting detail of this thermal zone and the only mechanical system is defined as a coal burning stove for heating. Following the information given in Table, walls, columns, beams, slabs and roof are defined by their materials and thickness. Also, the metal entrance door and 3 openable PVC windows (U-value: 3.3) are defined. After the completion of the building energy model (Figure 6) with no errors, simulation is started for the energy performance calculations.

First the case building is identified in BEP-TR 2 as a detached low-rise residential building located in Bornova, İzmir. Than the plan geometry is generated regarding to the relief drawings given in Figure. According to the outline given in BEP-TR 2; ground

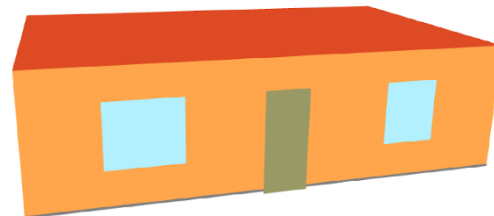


Figure 6. Energy model, existing building

Table 5. Energy performance analysis results, existing building.

Systems	Annual Electricity Consumptions				Renewable Energy/ Cogeneration Energy		Energy Class
	Final (kWh/year)	Primary (kWh/year)	Per Unit Area (kWh/m ² .year)	Per Unit Area (kgCO ₂ /m ² .year)	Primary (kWh/year)	Per Unit Area (kWh/m ² .year)	
Total	12035,11	14021,28	240,67	69,69	0	0	F 147
Heating	9431,70	9431,70	161,89	47,05	0	0	F 144
Hot Water	763,53	777,34	13,34	3,15	0	0	D 104
Cooling	1565,06	3242,80	55,66	16,57	0	0	F 160
Lighting	274,83	569,45	9,77	2,91	0	0	G 300

As a result of the calculations, annual electricity consumptions of heating, hot water and cooling system usages are given in kWh and kgCO₂ units (Table 5). Since there is no renewable energy usage there is no value calculated. Through the evaluation of BEP-TR 2 database, case building is qualified in F energy class.

4. Design of the new building

As the existing building cannot provide requirements of the earthquake regulations, it can collapse under the stress of a probable moderate earthquake. So that there are two actions to be taken; to strengthen the construction and retrofit or to demolish and construct a new building.

Considering the energy performance analysis and the spatial requirements of the householder, constructing a new building is preferred and new building is designed. It is a detached house with ground and first floors as seen in (Figure 7). It has totally 220 m² closed area with a 2.73 m ground and 3.22 m first floor height.

The building has a timber frame construction designed with 20*20 cm columns, 20*15 cm beams carrying the suspended hipped roof and Osb slab seated on 10*15 cm minor beams. The interior walls are 10 cm and exterior walls are 20 cm matched timber. The details of all the construction elements are given in Table 6.

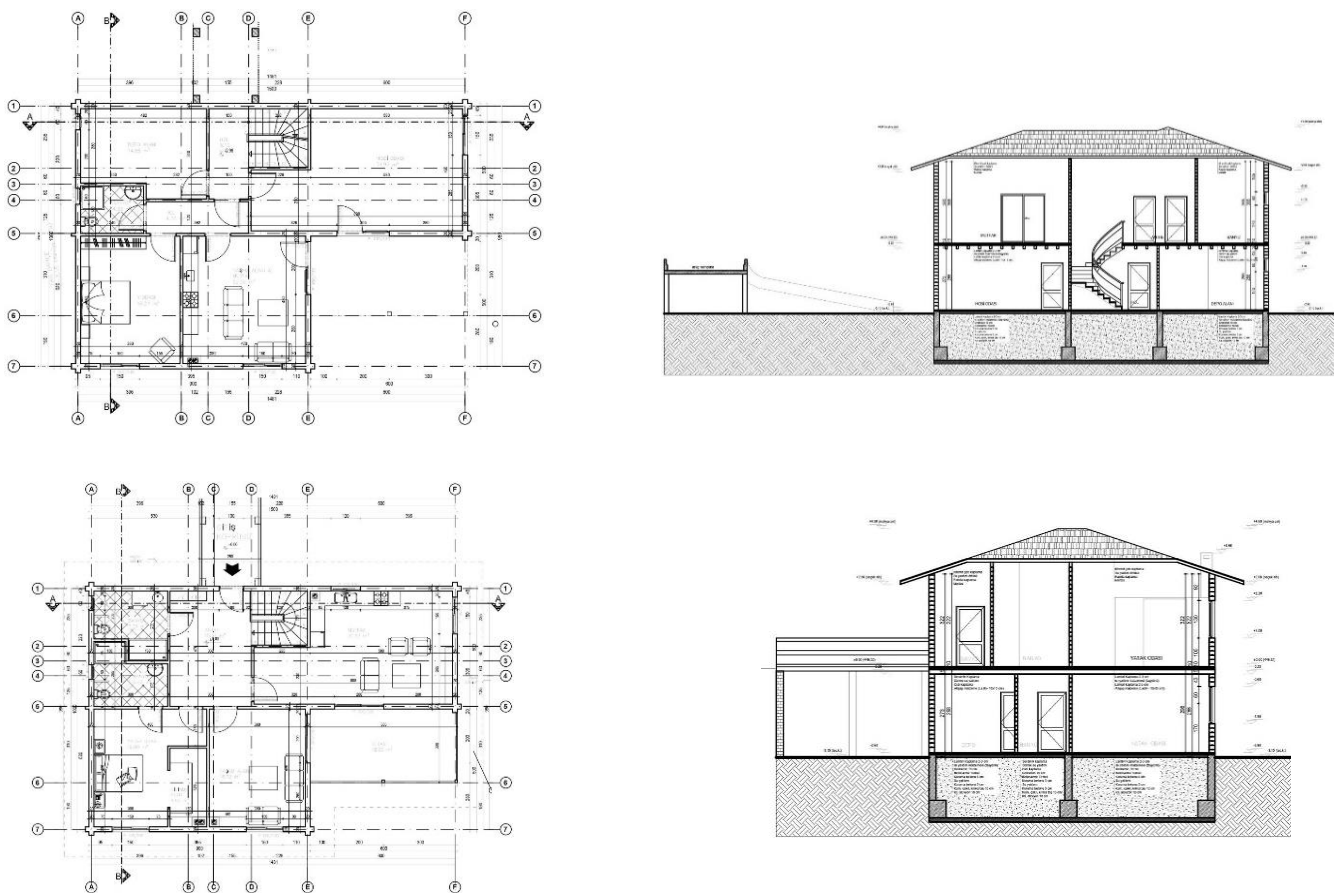


Figure 7. Architectural drawings, new building

Table 6. Construction elements, new building

Construction Element	Material	Thickness (m)
Slab (Basement)	Cast Stone (L: 1.300-01.08)	0.01
	Cement Screed (L: 1.400-04.06.01)	0.03
	Reinforced Concrete (L:2.500-05.01.01)	0.12
	Cement Screed (L: 1.400-04.06.01)	0.05
	Extruded Polystyrene Foamboard (L: 0.030-10.03.02.01.01)	0.05
	Bitumen Waterproofing Sheet (L:0.190-09.02.02.01.01)	0.003
	Concrete (L:1.650-05.01.02)	0.1
	Gravel (L: 0.700-03.01)	0.1
	Clay, Alluvion (L: 1.500-02.02.01)	0.1
Slab (First floor)	Coniferous Sawn Timber (L: 0.130-08.01.01)	0.03
	Mineral and Plant Fiber Heat Insulation Materials (L: 0.035-10.05.01)	0.05
	Coniferous Sawn Timber (L: 0.130-08.01.01)	0.03
Column- Beam	Coniferous Sawn Timber (L: 0.130-08.01.01)	0.20
Exterior Wall	Coniferous Sawn Timber (L: 0.130-08.01.01)	0.20
Hipped Roof Covering	Brick (L: 1.500-02.02.01)	0.03
	Bitumen Waterproofing Sheet (L:0.190-09.02.02.01.01)	0.002
	Beech Wood (L: 0.200- 08.01.02)	0.05
	Mineral and Plant Fiber Heat Insulation Materials (L: 0.035-10.05.01)	0.5
Hipped Roof Slab	Coniferous Sawn Timber (L: 0.130-08.01.01)	0.03
	Bitumen Waterproofing Sheet (L:0.190-09.02.02.01.01)	0.03
	Mineral and Plant Fiber Heat Insulation Materials (L: 0.035-10.05.01)	0.07



Figure 8. New building photos

New building is completed on July 2018. It stands as a good example for the sustainable structures with its all timber construction elements and all timber finishings. Also it is compatible with the site by using the slope to create different levels. (Figure 8)

The new building is identified in BEP-TR 2 as a detached low-rise residential building located in Bornova, İzmir. CAD drawings (Figure 7) are imported for creating the plan geometry. The floor height is entered; as 2.73 m for ground floor, 3.22 m for first floor. 2 thermal zones are defined for the for the ground and first floor of the whole building with totally 50m² kitchen and living room space. Than 9 led lamps with 20 W power are entered as the lighting detail of these thermal zones. The building has a heat pump system with a 21 kW power heating and 10 kW power cooling capacity. Materials and thickness of the walls, columns, beams, slabs and roof are defined in the system as given in Table. Timber doors and timber framed windows with reflected insulated glass (U:2.6) are also defined and the building energy model is completed. (Figure 9)

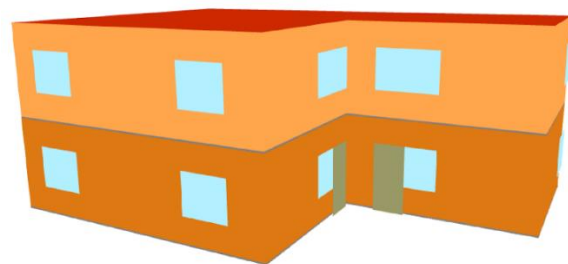


Figure 9. Energy model of new building

Table 7. Energy performance analysis results, new building

Systems	Annual Electricity Consumptions				Renewable Energy/ Cogeneration Energy		Energy Class
	Final (kWh/year)	Primary (kWh/year)	Per Unit Area (kWh/m ² .year)	Per Unit Area (kgCO ₂ /m ² .year)	Primary (kWh/year)	Per Unit Area (kWh/m ² .year)	
Total	9994.26	17217.67	71.74	20.50	8857.57	36.91	B 65
Heating	3771.21	7813.96	32.56	9.70	8857.57	36.91	B 50
Hot Water	3311.89	3371.80	14.05	3.32	0	0	D 105
Cooling	2517.97	5217.24	21.74	6.47	0	0	B75
Lighting	393.18	814.68	3.39	1.01	0	0	D 100

Calculated values for the annual electricity consumptions of heating, hot water and cooling system usages are given in kWh and kgCO₂ units. Also, the renewable energy usage through the heat pump system is calculated. (Table 7) As a result of the evaluation, the new building is qualified in B energy class in total.

5. Results and comparisons

Existing building is a single floor reinforced concrete structure. According to the structural analysis, it is seen that the existing building cannot provide the safety requirements and it is classified as a 'risky building'. Besides the structural analysis energy performance analysis of the existing building is also done. The results show that the building is the energy class F. So, it is decided to design a new building which is structurally resistant and energy efficient.

Instead of reinforced concrete structure system as in the existing building, timber framed structure system is preferred to be used in the newly designed building. The new building is designed according to the structural regulations up to date as it is stable and safe. And from the energy performance point of view, the new designed building is qualified in energy class B. That means building is energy efficient and sensitive to the environment.

The comparison of two buildings according to the building materials, structural performance and energy performance can be seen on Table 8.

6. Conclusion

Urban renewal from an economic, physical, functional or environmental point of view of a degraded urban area, the state, policy, plan, implemented for improvement with integrated approaches, is an implementation process that covers all of the programs and projects. This implementation process has effect on the people living there and structure of the city therefore it is a multi-disciplinary integrated work.

Within this framework both structural and energy deficient building is demolished and instead of it new building is designed and constructed. And a method put forward. According to this method both structural and energy performance of the existing building is evaluated. For structural performance analysis site visits were done and by sampling methods the stability of the building is tested. For this purpose, in the laboratory pressure tests for taken samples were done and also after relief of the building was drawn by using simulation program called ideCAD the structural performance of the building was analysed. Besides the structural performance analysis, energy performance analysis was also done by using BEP-TR programme.

This paper gives recommendations to urban renewal professionals which they can use all through the process of urban renewal. In this concept besides structural improvement energy efficient approaches are taken in account.

Author's Contributions

Ebru Alakavuk: Drafted and wrote the manuscript and interpreted analysis.

Hande Odaman Kaya: Drafted and wrote the manuscript and interpreted analysis.

Ethics

There are no ethical issues after the publication of this manuscript.

Table 8. Comparison of existing and new buildings

		Construction Element	Existing Building		New Building	
			Material	Thickness (m)	Material	Thickness (m)
Structural performance	Construction Element	Slab (Basement)	Reinforced Concrete (L:2.500-05.01.01)	0.12	Cast Stone (L: 1.300-01.08)	0.01
			Gypsum Plaster (L:0.510-04.04)	0.02	Cement Screed (L: 1.400-04.06.01)	0.03
			Concrete (L:1.650-05.01.02)	0.03	Reinforced Concrete (L:2.500-05.01.01)	0.12
			Lime, Lime- Gypsum Mortar (L:1.000-04.01)	0.02	Cement Screed (L: 1.400-04.06.01)	0.05
			Phanero-crystalline Volcanic and Metamorphic Stone (L:1.650-05.01.02)	0.02	Extruded Polystyrene Foamboard (L: 0.030-10.03.02.01.01)	0.05
					Bitumen Waterproofing Sheet (L:0.190-09.02.02.01.01)	0.003
				Concrete (L: 1.650-05.01.02)	0.1	
				Gravel (L: 0.700-03.01)	0.1	
				Clay, Alluvion (L: 1.500-02.02.01)	0.1	
		Slab (First floor)		Coniferous Sawn Timber (L: 0.130-08.01.01)	0.03	
				Mineral and Plant Fiber Heat Insulation Materials (L: 0.035-10.05.01)	0.05	
				Coniferous Sawn Timber (L: 0.130-08.01.01)	0.03	
		Column-Beam	Gypsum Plaster (L:0.510-04.04)	0.03	Coniferous Sawn Timber (L: 0.130-08.01.01)	0.20
			Reinforced Concrete (L:2.500-05.01.01)	0.25		
			Gypsum Plaster (L:0.510-04.04)	0.02		
		Exterior Wall	Gypsum Plaster (L:0.510-04.04)	0.03	Coniferous Sawn Timber (L: 0.130-08.01.01)	0.20
			Brick TS EN 771-1 (L:0.810-07.01.01.01)	0.19		
			Gypsum Plaster (L:0.510-04.04)	0.02		
		Roof	Reinforced Concrete (L:2.500-05.01.01)	0.12	Brick (L: 1.500-02.02.01)	0.03
			Gypsum Plaster (L:0.510-04.04)	0.02	Bitumen Waterproofing Sheet (L:0.190-09.02.02.01.01)	0.002
Concrete (L:1.650-05.01.02)	0.05		Beech Wood (L: 0.200- 08.01.02)	0.05		
Bitumen Waterproofing Sheet (L:0.190-09.02.02.01.01)	0.05		Mineral and Plant Fiber Heat Insulation Materials (L: 0.035-10.05.01)	0.5		
			Coniferous Sawn Timber (L: 0.130-08.01.01)	0.03		
			Bitumen Waterproofing Sheet (L:0.190-09.02.02.01.01)	0.03		
			Mineral and Plant Fiber Heat Insulation Materials (L: 0.035-10.05.01)	0.07		
Structural stability	Risky Building		Complying with regulations			
Energy Performance	Energy Class	Total	F 147	B 65		
		Heating	F 144	B 50		
		Hot Water	D 104	D 105		
		Cooling	F 160	B75		
		Lighting	G 300	D 100		

References

- [1]. Couch, C., (1990) Urban Renewal: Theory and Practice, Macmillan.
- [2]. Aslam, A.B. (2009). Introduction to Urban Renewal and Conservation: Definitions, Concepts, Policies/Approaches. Pakistan: University of Engineering and Technology, Department of City and Regional Planning, Lecture Notes.
- [3]. Tekeli, İ., 2003. Kentleri Dönüşüm Mekanı Olarak Düşünmek, Kentsel Dönüşüm Sempozyumu (11-13 Haziran 2003), TMMOB Şehir Plancıları Odası İstanbul Şubesi Yayını, ISBN: 975-395-602-9, İstanbul, s: 2-7.
- [4]. Onkar, P., Dhote, K.K., Sharma, A. "Exploring The Concept Of Urban Renewal In The Indian Context", *ITPI Journal* 5 : 2 (2008) 42 –46
- [5]. Kalağan, G., Çiftçi, S. (2012). Public-Private Sector Cooperation in Urban Space Reflections: Urban Transformation Example and New Actors, *Journal of Social and Humanities*, Volume 4, No 2, 2012 ISSN:1309-8012.
- [6]. IPKB (2014a), Afete Dirençli Şehir Planlama ve Yapılaşma, <https://istanbul.afad.gov.tr/upload/Node/9562/files/ADSPY.pdf>.
- [7]. CINA, M. M., (2016) A Critical Analysis of Urban Regeneration Projects in Turkey: Displacement of Romani Settlement Case.. *Procedia - Social and Behavioural Sciences*.
- [8]. IPKB (2014b), Kentsel Risklerin Azaltılması, ISMEP Proje Rehber Kitapları. URL: <https://istanbul.afad.gov.tr/upload/Node/9562/files/KENTSEL+1.pdf>.
- [9]. Roberts P.W., & Sykes, H. (2000). Urban Regeneration. A Handbook. London. SAGE. Retrieved from <http://dx.doi.org/10.4135/9781446219980>.
- [10]. İzmir Büyükşehir Belediyesi (2006). 1/25000 Ölçekli İzmir Kentsel Bölge Nazım İmar Plan Revizyonu (IKBNIPR) Raporu. İzmir.
- [11]. Bal, Ö.H. (2008). İzmir’de Kentsel Dönüşüm Sürecinin İzmir Cennetçeşme Mahallesi Üzerinden İrdelenmesi. İzmir: Dokuz Eylül Üniversitesi, Fen Bilimleri Enstitüsü, Yüksek Lisans Tezi.
- [12]. Kösten, Y. Ö., (2016) Kentsel Dönüşümün Tek Alternatifi mi var? YIK-YAP, Mimarlık Journal, Number:387.
- [13]. Urban Renewal Activities in Turkey: The Trabzon Experience. Available from: https://www.researchgate.net/publication/269079148_Urban_Renewal_Activities_in_Turkey_The_Trabzon_Experience [accessed Jul 18 2020].
- [14]. Kılıç, S., Karataş, N., The Role of the Urban Renewal Projects on the Reshaping of the Cities: İzmir (Turkey) Case, *World Academy of Science, Engineering and Technology International Journal of Architectural and Environmental Engineering* Vol:9, No:3, 2015.